This is to certify that the

dissertation entitled

CYCLIC THERMAL SHOCK IN CERAMICS
AND CERAMIC MATRIX COMPOSITES

presented by

Youngman Kim

has been accepted towards fulfillment
of the requirements for

Ph.D. degree in Materials Science

Eldon Case
Major professor

Date May 14, 1991

CYCLIC THERMAL SHOCK IN CERAMICS AND CERAMIC MATRIX COMPOSITES

By

Youngman Kim

A DISSERTATION

Submitted to
Michigan State University
in partial fulfillment of the requirements
for the degree of

DOCTOR OF PHILOSOPHY

Department of Metallurgy, Mechanics and Materials Science

1991

ABSTRACT

CYCLIC THERMAL SHOCK IN CERAMICS AND CERAMIC MATRIX COMPOSITES

By

YOUNGMAN KIM

Thermal fatigue damage for SiC fiber/Aluminosilicate composites, Macor glass-ceramics, and polycrystalline titanium diboride was monitored by Young's modulus and internal friction changes. A fatigue-like power law relation between the damage saturation level and ΔT, the quench temperature difference, was observed. A similar power law fatigue relation was observed in previous studies of SiC whisker/alumina composites and unreinforced alumina. The results also suggest the existence of a fracture toughness (or strength) threshold above which thermal shock damage will not accumulate for a given ΔT.

A measurement technique for the surface heat transfer coefficient was developed. The maximum surface tensile stress developed during quenching was calculated from the measured surface heat transfer coefficient as a function of temperature.

A modulus-microcracking model was presented for surface limited microcrack distributions based on the concept that a specimen containing a surface-limited population of microcracks could be viewed as a composite. The microcrack damaged regions act as layers of reduced modulus, ideally bonded to an undamaged substrate.

The modulus of the individual damaged layers was modeled in terms of the damage parameter, $\Lambda = fGN$, which accounts for the spatial

orientation of the cracks, the crack geometry, and the number density of the microcracks. A Rule of Mixtures model and a dynamic modulus model developed in the present study were used to calculate the moduli of the damaged layers. For the particular case of model indentation crack distributions, corrections were made to the crack perimeter and area calculations to account for the ligament bridging the two crack faces in an indentation crack.

For the Vickers induced indentation cracks, the measured normalized Young's modulus changes, $(E_0-E)/E_0$, increased linearly with increasing microcrack number density N. The observed crack-induced modulus changes were compared to a number of microcracking models. The surface-limited damage model based on the dynamic beam vibration theory and on a modified half-ellipse crack shape fit the experimental data well.

ACKNOWLEDGEMENTS

I would like to thank my adviser, Professor **Eldon D. Case** for his continuous guidance, encouragement, and support throughout this work. It was a joy to work together with Dr. Case. In addition to academical advice, he gave me a good researcher's attitude, **honest** and **hard working**. My thanks are extended to the other members of my Ph.D. committee, Professor K. Mukherjee, Professor N. Altiero and Professor W. Pratt. I also would like to thank my collegues for their helpful discussion.

I would like to acknowledge the financial support by the National Science Foundation under grant number MSM-8706915 and by the State of Michigan's Research Excellence Fund.

Grateful thanks should go to my parents and wife (Eunju) for their love, care and support. Especially my parents who gave me life and wisdom should be gratefully acknowledged.

TABLE OF CONTENTS

LIST OF FIGURES

LIST OF TABLES

1. INTRODUCTION

Thermomechanical stress developed by rapid ambient temperature changes [1] can result in microcracking or catastrophic failure for brittle materials such as ceramics and ceramic matrix composites [2-9]. Many engineering applications of ceramics involve ambient temperature changes, thus thermal shock damage characterization must be an integral part of the effort to improve the reliability of ceramics and ceramic matrix composites in a number of technical applications [10, 11].

A measurement technique for the surface heat transfer coefficients of specimen was presented to calculate the maximum surface tensile stress during quenching. Since a tensile stress develops on the surface for plate cooled from the surface (figure 1), microcracking damage due to thermal shock cyclings is expected to be surface limited. Modulus-microcracking composite models which based on a rule of mixtures and a dynamic beam vibration theory were developed for the surface limited microcrack distribution. A specimen containing a surface-limited population of microcracks was viewed as a composite, with the microcracked damaged region as layer(s) of reduced modulus ideally bonded to an undamaged layer.

In this study the thermal fatigue damage of ceramics and ceramic matrix composites was investigated in terms of non-destructive Young's modulus and internal friction measurements, maximum tensile surface stress during quenching, and modulus-microcracking composite models.

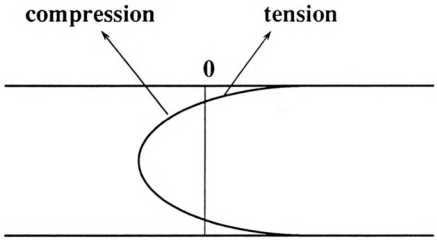

Figure 1. Temperature and stress distributions for plate cooled from the surface (after Kingery et al. [12]).

1.1 Thermal Fatigue

1.1.1 Thermal Shock Resistance Parameters

Although a number of thermal shock resistance parameters appear in the literature, the thermal shock resistance parameters are not quantitative measure of thermal shock resistance. At best, these parameters serve to rank the relative thermal shock resistance of brittle materials. To characterize the thermal stress resistance of ceramic materials, Kingery [12, 13] proposed thermal shock resistance parameters R and R'

$$R = \sigma_f (1 - \nu)/(E\alpha) \quad (1)$$

$$R' = k\sigma_f (1 - \nu)/(E\alpha) \quad (2)$$

where σ_f = strength

k = thermal conductivity

ν = Poisson's ratio

E = Young's modulus

α = thermal expansion coefficient

A high numerical value of R or R' represents a tendency to avoid crack initiation. For example, a material with high strength, high thermal conductivity, low Young's modulus, low thermal expansion coefficient,

and Poisson's ratio minimize crack initiation by thermal shock. Thus the reliability of ceramic components under thermal shock is improved if the surface of the component is smooth enough that crack initiation is a major factor of failure.

If there are many flaws present in the ceramic (such as is the case in a porous refractory brick), then crack initiation is not the issue since many initial flaws are already present. For materials with a significant number of initial flaws, crack propagation rather than initiation becomes the focus of thermal shock resistance parameters. In the context of crack propagation, the thermal shock resistance parameters, R''' and R'''' are defined as [12, 13]

$$R''' = E/(\sigma_f^2(1 - \nu)) \tag{3}$$

$$R'''' = E\lambda_{eff}/(\sigma_f^2(1 - \nu)) \tag{4}$$

where λ_{eff} = fracture surface energy of the ceramic

The parameter R''' represents the minimum available elastic energy for crack propagation. R'''' is the minimum crack propagation distance before catastrophic thermal stress failure. To minimize crack propagation under thermal shock, a material which has high Young's modulus, fracture surface energy, Poisson's ratio and low strength is required.

Thus, the roles of Young's modulus, strength and Poisson's ratio in thermal shock resistance parameters are opposite in nature depending on whether thermal shock resistance is being determined from the viewpoint of avoiding thermal crack initiation or whether one is concerned with avoiding thermal crack propagation. Thus thermal shock resistance parameters should be selected on the basis of whether crack initiation or crack propagation is dominant for a given ceramic.

Thermal shock resistance parameters are contradictory themselves depending on thermal shock damage mechanism. Furthermore thermal shock damage parameters do not predict repeated thermal shock behavior of ceramics. Thus in this study thermal fatigue parameters from Young's modulus and internal friction measurements were related with material parameters, such as fracture toughness.

1.1.2 Thermal Fatigue

Single quench thermal shock testing (single quench-fracture test) [5-9] does not directly model the thermal shock damage induced in many industrial applications. If a component is severely damaged after the first thermal shock cycle, then the design, the material (or both) are judged to be unsatisfactory.

For example, if a ceramic turbine rotor develops severe cracks after the first thermal shock, then the rotor must be redesigned to allow the rotor to survive the several hundred or several thousand thermal shock cycles expected of a functioning turbine rotor. Even in

less severe thermal shock situations, such as in computer substrates [14, 15], the designer still is concerned with repetitive thermal loading that degrades the substrate after a great number of thermal cycles. Thus, in order to address the type of damage involved in many industrial applications of ceramics, one must deal with cyclic thermal shock (thermal fatigue).

While most of the thermal shock studies on ceramics have employed the "single quench-fracture test" protocol, several studies have addressed cyclic thermal shock damage in ceramics [16-20]. However, even cyclic thermal shock studies [16-20] are typically based solely on residual strength testing. Thermal shock damage characterization via fracture testing alone is somewhat limited by the nature of brittle fracture itself, regardless of whether the specimens are subjected to single or multiple thermal shocks. Fracture of monolithic ceramics depends on the details of the length and spatial distributions of maximal flaws in the test specimen [21], as well as the details of the stress distribution. Strength data can exhibit considerable scatter, where the uncertainty in strength values can easily exceed 10 to 15 percent of the measured mean strength [6, 7]. According to Bradt et. al [2-4], a fatigue experiment would likely include a sufficient number of specimens to guarantee good statistics for residual strength testing. Also, for residual strength testing, as for any destructive test, one must account for statistical fluctuations in the measured property (strength) among the many individual specimens measured.

Ceramics can exhibit significant specimen to specimen variations in strength for specimens taken from a single billet, and even more significant variations between different batches of a given material.

In addition to the statistical difficulties, technical ceramics can be expensive, difficult to process and machine. Thus a cyclic thermal shock study involving a thousand strength specimens would be unwieldily and expensive at best.

In contrast, monitoring cyclic thermal shock damage by elasticity and internal friction measurements overcomes many of the shortcomings of the single quench-fracture test methodology [22-25]. Elasticity and internal friction tests are nondestructive so the evolution of thermal shock damage during repeated thermal shocking can be straightforwardly determined for each specimen. In addition, for a specimen having Young's modulus E, the uncertainty in the modulus measurement is at most about 0.01E, which is an order of magnitude or more improvement in precision, when compared to fracture tests.

In this study, thermal fatigue damage was monitored non-destructively by elastic modulus and internal friction measurements on SiC fiber reinforced aluminosilicate composites [22], Macor glass-ceramics [23], SiC whisker/alumina composites [24], polycrystalline titanium diboride, and polycrystalline alumina [25].

1.2. Time-dependent Elastic Modulus Recovery Measurement on Thermally Shocked SiC fiber/Aluminosilicate Composites, Machinable Glass Ceramics and Polycrystalline Alumina

Microcracks in monolithic ceramics and ceramic composites may be generated by many mechanisms including thermal expansion mismatch [26, 27], thermal shock [1], phase changes [28, 29], grinding and mechanical impact [30-32]. Experimental studies have documented microcrack-induced changes in a diverse range of properties such as strength [6, 7], elastic modulus [22-25, 33, 34], internal friction [22-25, 33, 34], and optical transparency [34].

In addition to microcrack-generation studies, numerous studies show that microcracks also can be healed [35-58]. However, microcrack healing typically is observed in terms of high-temperature diffusive healing, that is, for temperatures above a homologous temperature of about 0.6 [36-48]. Microcrack and macrocrack healing in ceramics have been observed at or near room temperature, mainly in glass [51-53, 55-57] and mica [49, 50, 55], and only recently for a polycrystalline ceramic [58]. This study considers partial room-temperature microcrack healing in three different thermally shocked ceramic materials.

1.3. The Measurement of the Surface Heat Transfer Coefficient for Ceramics Quenched into a Water Bath

The thermal stresses that develop in a ceramic during thermal

quenching can be expressed as a function of the quench temperature difference*, the Young's modulus, the coefficient of thermal expansion, Poisson's ratio, and Biot's modulus [12, 59, 60], where Biot's modulus is defined as

$$B = ah/k \tag{5}$$

where h = surface heat transfer coefficient

k = thermal conductivity of the quenched specimen

a = specimen half-thickness.

Calculations of thermal stresses are complicated by the fact that most of the parameters involved are also functions of temperature. While measurement techniques are available and relatively well known for determining the temperature dependence of Young's modulus [35, 61], Poisson's ratio [61], thermal expansion [62], and thermal conductivity [63], materials scientists typically resort to calculations for the temperature dependence of h, the surface heat transfer coefficient [8, 64, 66]. For a quench into a water bath the surface heat transfer coefficient expressions that are available are semi-empirical and dependent on a host of thermophysical properties [8, 64-69]. Furthermore, the forms of the h models change dramatically if boiling occurs or if (at higher temperatures) a vapor

---

* The quench temperature difference is the difference between the specimen's maximum temperature and the temperature of the quench bath.

film forms around the quenched specimen [67-69]. As a further complication, models of h for the boiling regime are still very sketchy [67-69]. In spite of the difficulties in calculating h, such values are crucial to thermal stress calculations, since for a water quench, the value of h is predicted to change by well over an order of magnitude as the quench temperature difference ranges over a few hundred degrees Celcius [8, 64-66, 70].

In this study, we present a technique for measuring the heat transfer coefficient for ceramics thermally quenched into a room temperature water bath. The technique combines a parameter estimation technique for h developed by mechanical engineers but (to the authors' knowledge) not previously utilized by materials scientists, with the fast-response capabilities of recently developed thin film thermocouples.

1.4. Effects of Surface Abrasion on the Thermal Fatigue of Ceramics

In addition to introducing surface flaws, surface abrasion of ceramics may introduce significant surface compressive stresses [71, 72]. For example, such stresses may increase the strength of abraded glass ceramic specimens by up to 46 percent above the strength of unabraded specimens [71]. In thermal shock tests, surface abrasion has been observed to decrease the critical quench temperature

difference, ΔT_c, for retained strength measurements for glasses [73] and glass ceramics [74].

However, the ceramics literature does not discuss another significant and potentially important effect of surface abrasion, which is the increase in the surface heat transfer coefficient for the boiling nucleation regime [75]. Since the Biot modulus is a linear function of h, and quench-induced surface stresses can be sensitive functions of the Biot modulus, increases in h imply increases in the surface tensile stresses experienced by a specimen during quenching.

In this study, changes in Young's modulus monitor the effect of surface abrasion on cyclically thermal shocked specimens of abraded and unabraded alumina and glass ceramics. In addition, estimates are made of the net surface stresses induced by thermal quenching of abraded specimens.

1.5. The Effect of Surface Limited Microcracks on the Effective Young's Modulus of Ceramics

1.5.1. Analysis

Microcracks decrease the effective Young's modulus [22-25, 76-78] of materials. Theories relating the average microcrack size, microcrack geometry, and the number density of microcracks to the decrement in Young's modulus typically describe either three-

dimensional distributions of microcracks in a material [76-78] or two-dimensional distributions such as through cracks in plates [79-81]. The three dimensional theories treat either randomly oriented or aligned microcracks [76-78], where the the centroid of the crack surfaces are homogeneously distributed in three dimensions. Thus, such theories [76-81] do not treat nonuniform spatial distributions of the microcrack spatial distributions, such as the case of a microcrack population limited to a layer near the surface of a brittle specimen.

In ceramics, surface-limited microcrack distributions (that is, distributions of microcracks that occur preferentially in a layer near the specimen's surface) are experimentally observed in: (a) machining damage [31, 32, 82-86], (b) indentation [87-92] and (c) impact damage [93-96]. For example, microcracks generated by machining typically appear as two arrays of semi-elliptical cracks with one set parallel to the grinding direction and the other set normal to the grinding direction [82].

We consider microcracking-modulus relationships for microcrack damage distributed uniformly within a surface layer or layers. Within the damaged layer, the cracks may be either randomly oriented or aligned, but beneath the surface damaged layer(s) the specimen is microcrack free.

1.5.2 Crack Geometry Modification

In this paper, we extend generalized expressions for the modulus of brittle materials subjected to surface limited microcracking [97]. To model changes in elastic moduli for surface limited microcrack damage, the authors converted the problem of characterizing the damage state of a surface-microcracked bar to an elasticity problem [97]. Microcracking decreases the elastic modulus of either one or two of the long transverse faces of a bar-shaped specimen (figure 2). Thus the bar can be viewed as a two or three layer composite, with the microcracked layer(s) having a reduced elastic modulus. The authors modeled the overall, effective modulus of the composite via (bonded damaged and undamaged layers) in the following ways: (1) via a rule of mixtures formulation, which implies a static, tensile measurement of modulus and (2) by the Bernouli-Euler beam equation, which is appropriate to a dynamic elastic modulus measurement of the overall modulus. The ROM and dynamic modulus expressions were thus functions of E_ℓ, the elastic modulus of the microcracked layer. To express the composite (overall) modulus explicitly in terms of microcrack parameters, E_ℓ was expressed directly in terms of microcrack orientation, geometry, and number density.

In this study we consider the effect of particular crack geometries and crack orientations, including a "model" crack field produced by a distribution of indentation cracks.

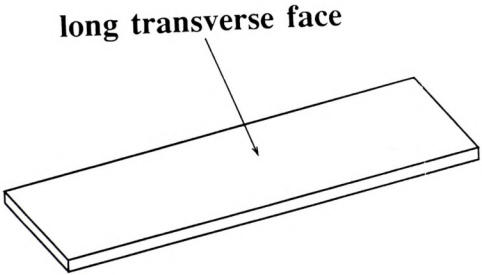

Figure 2. Illustration of long transverse surface of prismatic bar-shaped specimen.

1.5.3. Model System of Indentation Cracks

Aligned Vickers indentation cracks in polycrystalline alumina bars served as a model population of surface-limited microcracks. The ability to control and measure the number, location, and size of the indentation-induced surface cracks facilitates the comparison between theory and experiment. Changes in the Young's modulus were measured as a function of the number and size of Vickers indentation cracks placed on the specimen surfaces.

Two types of composite layer models for surface-limited microcracking damage were considered: (1) dynamic beam theory models and (2) rule of mixtures (ROM) models. In both types of models, the modulus of the crack-damaged layer(s) is reduced according to the number, size and geometry of indentation cracks present on the specimen surface [76-78, 97]. A realistic description of the indentation cracks, namely a half ellipse crack modified to account for the indentation-induced plastic zone models the experimental results well.

2. EXPERIMENTAL PROCEDURE

2.1 Thermal fatigue

2.1.1 Materials Tested and Specimen Characterization

Uniaxially reinforced SiC fiber (Nicalon)/lithium aluminosilicate (LAS) glass ceramic composites having a fiber volume fraction of 35% were fabricated by Corning Glass Works. The fiber diameter was approximately 10 μm (figure 3). The as-received composites, which had a mean mass density of about 2.24 grams per cubic centimeter, were cut into prismatic bar specimens approximately 0.15 cm x 1.2 cm x 4.9 cm (table 1). After cutting, specimens were annealed at 500 degree C in air for 10 hours to relieve residual stresses.

Macor (Corning code 9658) machinable glass-ceramics containing a dispersed phase of randomly oriented fluoromica platelets of approximately 10 μm long and a few micrometer wide (figure 4) may be considered to be a particulate reinforced ceramic composite. As-cut specimens were annealed at 500 °C for 10 hours to eliminate residual stresses that may have been generated during specimen preparation. The dimensions and density of Macor specimens are given in table 2.

Hot-pressed titanium diboride (Eagle-Picher Industries, Inc., Quapaw, Oklahoma) has grain size approximately 15 μm and a density of 98 to 99 percent of theoretical density (figure 5). Specimens were cut into prismatic bars using a surface grinders/slicers (Leematic

Table. 1. Dimensions and densities of prismatic bar-shaped SiC fiber-Aluminosilicate composites.

Specimen	Thickness (cm)	Width (cm)	Length (cm)	Density (g/cm^3)	Fiber content (volume %)
RLA 5.14	0.1425	1.5	4.712	2.475	35
RLA 5.21	0.150	1.16	4.92	2.536	35
RLA 5.22	0.152	1.137	4.92	2.386	35

Table 2. Dimensions and Density of Macor Glass-ceramic Specimens

Specimen	Thickness (cm)	Width (cm)	Length (cm)	Density (g/cm^3)
MA-1	0.1785	1.396	7.8	2.493
MA-2	0.1785	1.29	7.79	2.522
MA-3	0.1785	1.325	7.79	2.519
MA-4	0.1785	1.343	7.79	2.524
MA-5	0.1785	1.359	7.79	2.512
MA-6	0.1765	1.169	7.83	2.498

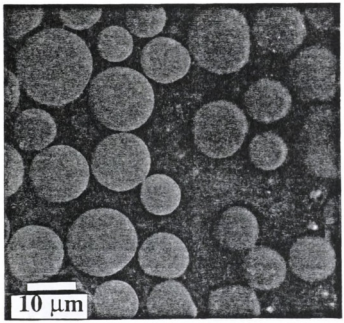

Figure 3. SEM Micrograph of SiC fiber-Aluminosilicate Composite.

Figure 4. SEM Micrograph of Macor Machinable Glass-Ceramic (x 2000).

Figure 5. SEM Micrograph of Polycrystalline Titanium Diboride.

2000, K. O. Lee Company). The as-cut specimens were annealed in Ar atmosphere high temperature horizontal muffle tube furnace (Thermtec, MRL industries) at 1000 °C for 10 hours to reduce residual stresses that generated during specimen preparation. The dimensions of TiB_2 specimens are given in table 3.

2.1.2 Thermal Shock Treatment

Thermal fatigue tests were performed using the apparatus shown in figure 6. During thermal shock testing, the specimen was held at a predetermined temperature for at least 30 minutes in a vertical muffle tube electric furnace. The specimen was quenched into a container of room temperature deionized water. The quenched specimen remained in the deionized water for 10 minutes, then the specimen was pulled back into the furnace for the next thermal shock cycle. After a preselected number of thermal shock cycles, the specimen was dried with a paper towel and allowed to dry in room temperature air for 10 hours prior to measuring the elastic modulus and internal friction.

The furnace used in this study was an electric resistance furnace controlled by a temperature controller (CN5001K2, Omega Engineering, Inc., Stamford, CT) with the heated chamber of 32 cm long and 3.5 cm in diameter. The furnace was allowed to approach thermal equilibrium before operating the thermal fatigue equipment. Temperature measurement was made with a K type thermocouple with its hot junction located to the side of the sample near its middle. An electronic ice

Table 3. Dimensions and densities of prismatic bar-shaped TiB_2 specimens.

Specimen	Thickness(cm)	Width (cm)	Length (cm)	Density (g/cm^3)
T-200	0.169	0.610	6.423	4.42
T-250	0.160	0.607	6.455	4.43
T-300	0.161	0.605	6.453	4.46
T-400	0.158	0.611	6.429	4.40
T-500	0.168	0.611	6.448	4.48

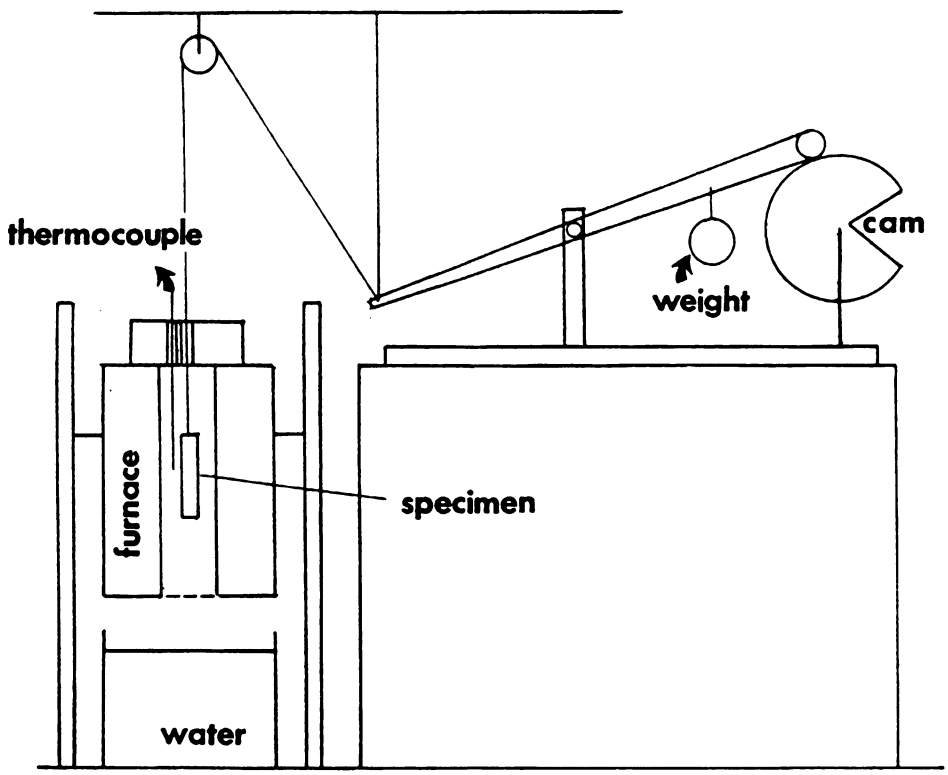

Figure 6. Schematic of Thermal Fatigue Apparatus.

point (Model MCJ, Omega Engineering, Inc.) was used with the thermocouple.

The plastic container for the water bath was rectangular with dimensions 26cm x 26cm x 14cm. Approximately 9.5 liters of deionized water were used for the water bath. The temperature of the water bath was measured by a mercury-in-glass thermometer.

2.1.3 Elastic Modulus Measurement

2.1.3.1 Room Temperature Elasticity Measurement

2.1.3.1.1 Static Elastic Modulus testing

Macor specimens of rectangular cross section were tested in four point fixture using a hydraulic mechanical testing machine (MTS 810 System, MTS Systems Co.). The bars rested on two supports and were loaded at the two quarter points, each an equal distance from the adjacent support point. The load span was 20 mm and support span was 40 mm. The specimen was loaded at a at a strain rate of 0.01 mm/mm min until fracture. A crosshead speed equivalent to a strain rate of 0.01 mm/mm min was calculated using the following equation [98]

$$R = ZL^2/6d \qquad (6)$$

where R = rate of crosshead motion (mm/min)

Z = rate of straining of outer fibers (mm/mm min), shall equal 0.01

L = support span (mm)

d = depth of beam (mm)

For a beam loaded in four point bend at two central points and supported at two outer points (figure 7), the maximum stress, σ_m, is given,

$$\sigma_m = 3PL/4bd^2 \qquad (7)$$

where P = load at a given point on the load deflection curve(N)

L = support span

b = width of specimen

d = thickness of specimen

The maximum strain in the outer fiber occurs at midspan and may be calculated as follows,

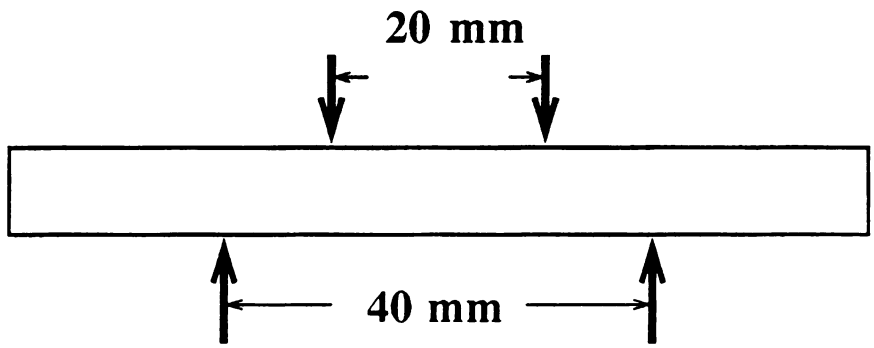

Figure 7. Schematic of Four Point Bend Loading.

$$\epsilon = 6Fd/L^2 \qquad (8)$$

where F = deflection at load fixture at position L/4 or 3L/4 (mm)

The elastic modulus in bending may be calculated by the following equations,

$$E = 5PL^3/384ID \quad \text{or} \quad E = PL^3/96I\phi \qquad (9)$$

where E = elastic modulus (MPa)

I = moment of inertia, In this case, $I = bd^3/12$ (mm^4)

D = corrected deflection at the center of sample

For four point bend, $D = \epsilon L^2/4.363d$ (mm)

ϕ = corrected deflection at load fixture (mm)

Using a low-speed diamond saw the Macor specimens used in this study were cut into prismatic bars shape 1.77 mm wide, 11.48 mm wide, and 78 mm long. As-received surfaces of specimens were used without further surface treatment. The edges of the specimens were beveled with 600 grit abrasive paper to prevent premature fracture caused by stress concentration along edges. Prior to the static modulus measurement, specimens were annealed at 500 °C for 10 hours. To maintain the straining rate of outer fiber, Z, as 0.01 mm/mm min, the rate of cross section motion, R, was maintained as 0.0251 mm/sec

(equation 5). The data acquisition of load and deflection was done by IBM personal computer.

2.1.3.1.2 Dynamic Elastic Modulus Measurement (The Sonic Resonance Method)

The Young's modulus of the specimens before and after a preselected number of thermal shock cycles was measured non-destructively using the sonic resonance method [99]. A prismatic bar-shaped specimen is suspended to a "driver" piezoelectric transducer (model 62-1, Astatic Corp., Conneaut, OH)and to a "pickup" transducer by cotton threads (figure 11) horizontally. Electronic signals from the frequency synthesizer (3325A Synthesizer/Function Generator, Hewlett-Packard) is converted into mechanical vibrations by the driver transducer (figure 8). The "pickup" transducer converts the specimen response to mechanical vibration from the "driver" transducer into an electronic signal, which is in turn amplified, filtered (4302 Dual 24DB/Octave Filter-Amplifier, Ithaco, Ithaca, N.Y.), and shown on an oscilloscope (V-100A 100 MHz Oscilloscope, Hitachi, Japan).

For the Young's modulus calculation, not only resonant frequencies of specimens but also indentifications of the vibration mode and type are required [100, 101]. Resonant frequencies of prismatic bar-shaped specimen were determined as frequencies where the maximum amplitude of the vibration were detected. The vibrational type and mode were identified by probing the nodal and anti-nodal point of the prismatic bar-shaped specimen with a sewing needle along

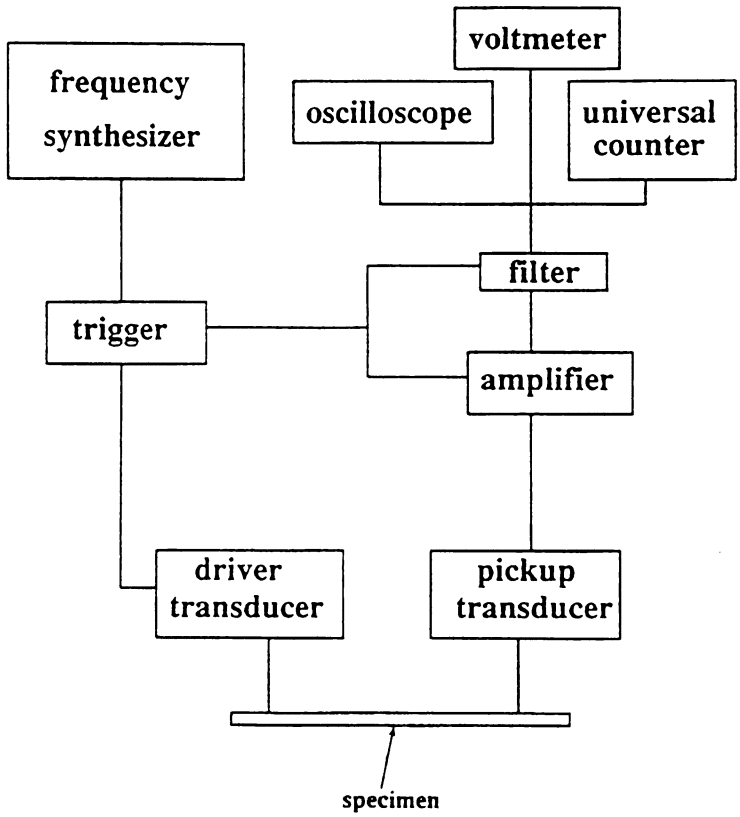

Figure 8. Schematic of the Sonic Resonance Apparatus.

the length direction. While the amplitude of specimen's response shows little change when the needle is located on a nodal line, that of specimen's response shows a reduced value when the needle is located on a anti-nodal line because the needle dampens the amplitude of specimen vibration.

Throughout all the experiments, the resonant frequencies of specimens were measured at least five times, and the average of five or more resonant frequency measurements was used to obtain elastic modulus values using the equations derived by Pickett [102] and later modified by Hasselman [103].

Shear modulus, G, was calculated from the equation

$$G = \rho\,(2L \cdot F/N)^2 \cdot R \qquad (10)$$

where N = an integer (unity for the fundamental mode)

F = torsional resonance frequency

L = specimen length

ρ = mass density

R = a shape factor.

For prismatic specimens of rectangular cross section, R can be approximated by an equation as follows;

$$R = \frac{\{1 + (w/b)^2\}\cdot\{1 + (0.0085N^2w^2/L^2)\}}{[4 - 2.521(b/w)\{(1 - 1.991)/(\exp(w/b) + 1)\}] - 0.06(Nw/L)^{1.5}(w/b - 1)^2} \quad (11)$$

where b = thickness of specimen

w = width of specimen.

Young's modulus, E, for a rectangular specimen can be calculated from the following equation

$$E = \frac{0.94642\ L^4\ f^2\ \rho\ T}{b^2} \quad (12a)$$

$$= \frac{0.94642\ L^4\ f^2\ m\ T}{b^3 w} \quad (12b)$$

where L = specimen length

f = flexural resonant frequency

ρ = specimen density

b = specimen thickness

w = specimen width

m = specimen mass

T = shape factor for the prismatic specimen.

The shape factor T for the prismatic specimen is the following function of the specimen dimensions and Poisson's ratio [101]

$$T = 1 + 6.585(1 + 0.0752\nu + 0.8109\nu^2)\,(b/L)^2 - 0.868(b/L)^4 - \frac{8.34(1 + 0.2023\nu + 2.173\nu^2)\,(b/L)^4}{1 + 6.338(1 + 0.14081\nu + 1.536\nu^2)\,(b/L)^2}$$

where ν = Poisson's ratio.

Poisson's ratio, ν, of the specimen can be obtained from the measured Young's modulus, E, and shear modulus, G on the condition that the specimen is isotropic and homogeneous macroscopically.

$$\nu = E/2G - 1 \qquad (13)$$

2.1.3.2 Elevated Temperature Elastic Modulus and Internal Friction Measurement

For the elevated temperature elastic modulus measurements, the specimen was suspended in an electric resistance furnace by 0.13 mm diameter platinum wire (Ted Pella. Inc., Tustin, CA) instead of cotton wire in the case of room temperature measurements. The fundamental flexural resonance frequency was measured at an interval of 40 to 50 °C increment on heating from room temperature to 950 °C and on cooling from 950 °C to room temperature. Measurements of resonance frequency were made after holding the specimen for at least 20 minutes at that

temperature to allow to reach thermal equilibrium. The elevated Young's modulus was obtained from the equation [101] as following,

$$E^T/E^{298} = (f^T/f^{298})(1 + \alpha\ \Delta T) \qquad (14)$$

where E^T, E^{298} = elastic modulus at elevated temperature and room temperature respectively

f^T, f^{298} = resonance frequency at elevated temperature and room temperature respectively

α = linear thermal expansion coefficient

ΔT = elevated temperature - room temperature.

Internal friction at elevated temperature was measured for unshocked specimen using one suspension position. The internal friction at elevated temperature, $(Q_s^{-1})^T$ was normalized by the specimen room temperature internal friction.

$$(Q_s^{-1})^T = (Q_s^{-1})^{298} \{(Q_m^{-1})^T/(Q_m^{-1})^{298}\} \qquad (15)$$

where $(Q_s^{-1})^{298}$ = specimen internal fiction at room temperature

$(Q_m^{-1})^T$ = measured internal friction at elevated temperature with platinum wire in air

$(Q_m^{-1})^{298}$ = measured internal friction at room temperature with platinum wire in air.

2.1.4 Internal Friction Measurement

The internal friction was determined by the free decay method [104], in which the specimen is driven at a mechanical resonance, then the driving signal is turned off with trigger and the number of cycles, N, required for the signal amplitude to decay from amplitude A_1 to amplitude A_2 is measured with electronic counter (Model 5314A Universal Counter, Hewlett-Packard) (figure 9). The measured internal friction, Q^{-1}, is given by

$$Q_m^{-1} = \frac{\ln(A_1/A_2)}{\pi N} \qquad (16)$$

where Q_m^{-1} = measured internal friction

A_1 = amplitude of driving signal

A_2 = preset amplitude

N = number of cycles required for a driving signal to decay from driving amplitude to preset amplitude.

The measured internal friction, Q_m^{-1}, has two contributions; one from the specimen internal friction, Q_s^{-1}, and the other from the apparatus internal friction, Q_a^{-1}. The specimen and apparatus contributions may be separated by measuring internal friction as a function of suspension position [104]. An equation introduced by Watchman and Tefft [104] which can separate the Q_s^{-1} and Q_a^{-1} was used

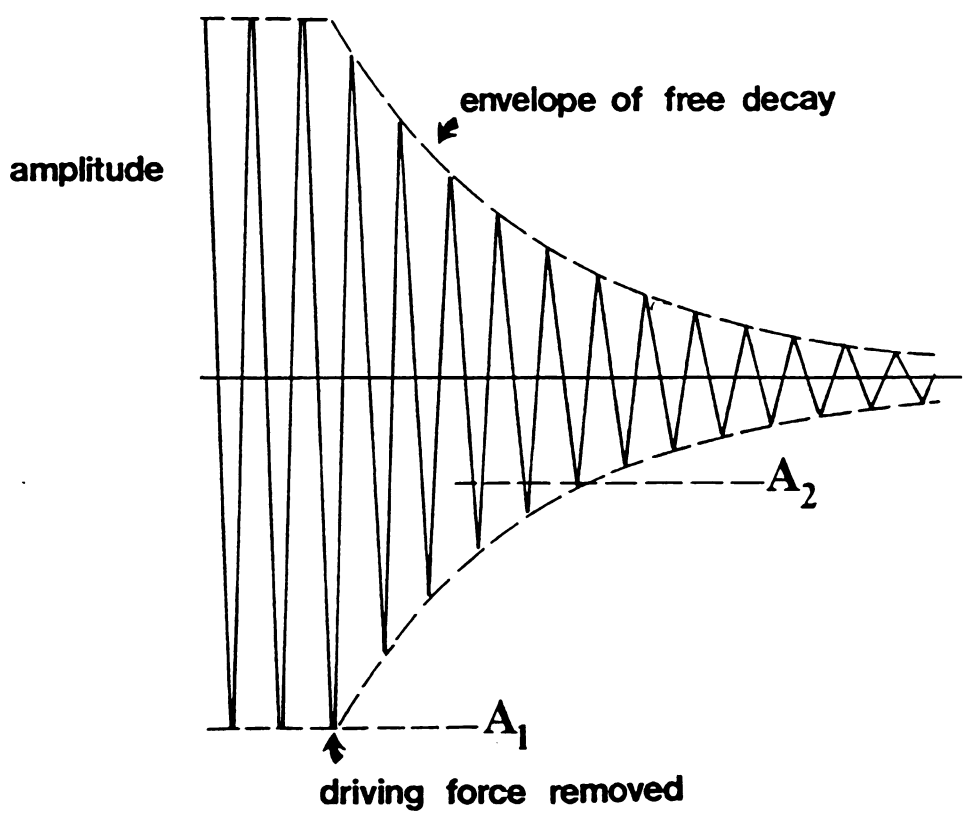

Figure 9. Logarithmic Decrement Method of Determining Internal Friction.

to get the Q_s^{-1}.

$$Q_m^{-1} = \frac{\{Q_a^{-1} + kQ_a^{-1}(y/y_0)^2\}}{\{1 + k(y/y_0)^2\}} \qquad (17)$$

where k = an empirical constant

y = the vertical displacement of the suspension position from equilibrium

y_0 = the vertical displacement of the end of the specimen

Ralyleigh [105] gave the equation describing y/y_o in terms of specimen length, L, and x, the distance from the suspension position to the end of the specimen

$$y/y_0 = \{1.018\ (\cosh 4.730\ x/L + \cos 4.730\ x/L) - (\sinh 4.730\ x/L + \sin 4.730\ x/L)\} / 2.036 \qquad (18)$$

Internal frictions of the specimen and apparatus were suspension position dependent.

Internal frictions were measured at five pairs of suspension positions on each condition of the specimen in air neglecting air damping effect. Internal friction measurement was performed at least eight times at a given pair of position repeatedly. The average values were considered as the measured internal friction values for that suspension position. The non-linear least square best fit

program which was developed by E. D. Case was used to determine the internal friction of the specimen.

2.2. Time-dependent Elastic Modulus Recovery Measurement on Thermally Shocked SiC fiber/Aluminosilicate Composites, Machinable Glass Ceramics and Polycrystalline Alumina

2.2.1 Materials Tested

The three materials employed in this study included an SiC fiber reinforced aluminosilicate, a commercial glass ceramic, and a polycrystalline alumina. The SiC fiber reinforced aluminosilicate (AS) glass ceramic composites were fabricated by Corning Glass Works using a 35 volume percent loading of Nicalon fibers (Nippon Carbon Co.) (figure 3). The glass-ceramic specimens were prepared from commercial Macor machinable glass ceramic (Corning code 9658) with the microstructure of randomly dispersed fluoromica platelets (approximately 10 μm across and 1 μm thick) in a glass-ceramic matrix (figure 4). The polycrystalline alumina (AD-96 Coors Ceramics) specimens had an average grain size of approximately 6 to 7 μm and a density of 86.7 to 93.5 percent of the theoretical density (figure 10).

Specimens of each of the three materials were cut into prismatic bars using a low speed diamond saw (table 4). Prior to testing, the as-cut specimens of SiC fiber reinforced aluminosilicate and

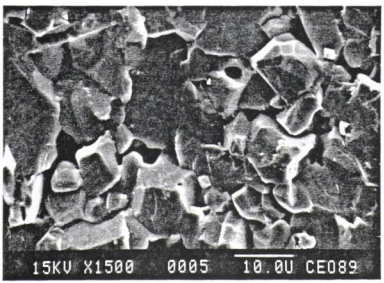

Figure 10. SEM Micrograph of Polycrystalline Alumina.

Table 4. Dimensions and Densities of Materials used in this Study.

Material		Thickness (cm)	Width (cm)	Length (cm)	Density (g/cm^3)
SiC/As	RLA 5.22	0.152	1.137	4.92	2.39
	RLA 5.14	0.142	1.510	4.71	2.47
Macor	MA-2	0.179	1.290	7.79	2.52
	MA-3	0.179	1.325	7.79	2.52
	MA-4	0.179	1.337	7.79	2.52
	MA-5	0.179	1.359	7.79	2.51
	MA-6	0.177	1.169	7.83	2.49
Alumina		0.105	1.20	7.01	3.49

the commercial Macor glass ceramic specimens were thermally annealed in air at 500 °C for approximately 12 hours. The polycrystalline alumina specimens were annealed in air at 850 °C for approximately 12 hours. The thermal anneals helped to reduce residual stresses that may have been generated during specimen preparation.

2.2.2 Young's modulus measurement as a function of time elapsed after the thermal shock

The Young's modulus of the specimens before and after thermal shock was measured via the sonic resonance method [101, 102], in which a specimen is suspended by cotton threads (figure 11). One of the threads is attached to a "driver" piezoelectric transducer, while the other thread is attached to a "pickup" transducer. The driver transducer converts electronic signals from the frequency synthesizer into mechanical vibrations (figure 8). Tuning the frequency synthesizer allows one to find a resonant condition of the specimen, which is then sensed by the pickup transducer. The Young's modulus of the prismatic bar-shaped specimens was calculated from the measured resonant frequencies [101, 103].

An unshocked Macor glass ceramic specimen was used as a control specimen to guard against a possible systematic "drift" in the transducer response. The modulus of the Macor control specimen was remeasured after every five to six modulus recovery runs. During the entire study, the measured modulus of the control specimen varied by

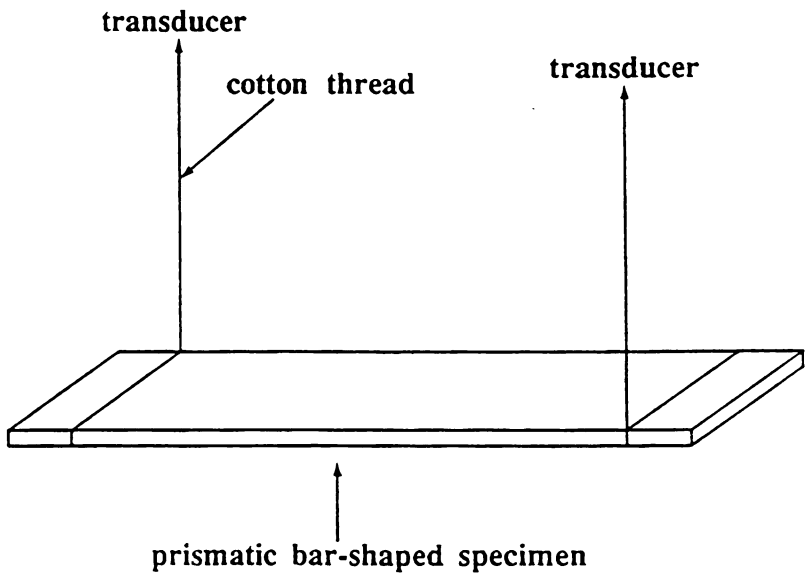

Figure 11. Method of Specimen Suspension for the Sonic Resonance Measurement.

less than ±0.0075 GPa (the average modulus of the control specimen was 62.70 GPa), which indicated negligible change in the transducer response over the course of the study.

To induce thermal shock damage, specimens were first held at a preselected temperature for at least 30 minutes in a vertical-muffle tube electric furnace. The specimens were then quenched into a room-temperature deionized water bath. After drying the quenched specimens with a paper towel, the elastic modulus of the specimens was measured (in air at room temperature) as a function of time for times up to 600 minutes following the quench. Modulus readings were taken at time intervals of about 15 to 20 minutes during the first 150 minutes after the quench and then at intervals of 60 to 90 minutes during the remainder of the modulus recovery measurement. During the time intervals between the actual modulus measurements, the specimen and suspension threads were supported on a block, so that the transducer would not be subjected to a dead weight load during the extended period over which the modulus measurements were conducted.

Since the calculation of Young's modulus requires that the specimen mass be known, specimen mass was determined by an electronic analytical balance (Sartorius Analytic A 210P). In order to assess errors in the mass measurements, a working standard was used whenever the mass of the specimen was measured. During the mass determinations and the modulus measurements, the specimens were handled using tweezers in order to minimize mass change by contamination.

2.3. The Measurement of the Surface Heat Transfer Coefficient for Ceramics Quenched into a Water Bath

2.3.1 Experimental Procedure

Thin foil "cement-on" K-type thermocouples (CO2-K, Omega Engineering, Stamford, CT) with a very rapid response time (2-5 msec) were bonded with high temperature cement (Omega Engineering) onto prismatic bar-shaped specimens (figure 12). The thermocouples were connected to an electronic ice point (Model MCJ, Omega Engineering) which was connected in turn to a digital storage oscilloscope (Model PM 3365, Philips, figure 13). The thermocouple-bonded specimen was held in a vertical muffle tube electric furnace at a preselected temperature for 30 minutes. The specimen was then quenched into a room temperature water bath. The height difference between the specimen's position in the furnace and the surface of the water bath was approximately 40 cm. During the thermal quench, the oscilloscope recorded the thermocouple voltage as a function of time (figure 13).

The materials tested in this study included a machinable glass ceramic (Macor, Corning code 9658), a polycrystalline alumina (AD-96, Coors Ceramics, Inc.) and a hot-pressed titanium diboride (Eagle-Picher Industries, Inc.). The specimens' dimensions and densities are given in table 5.

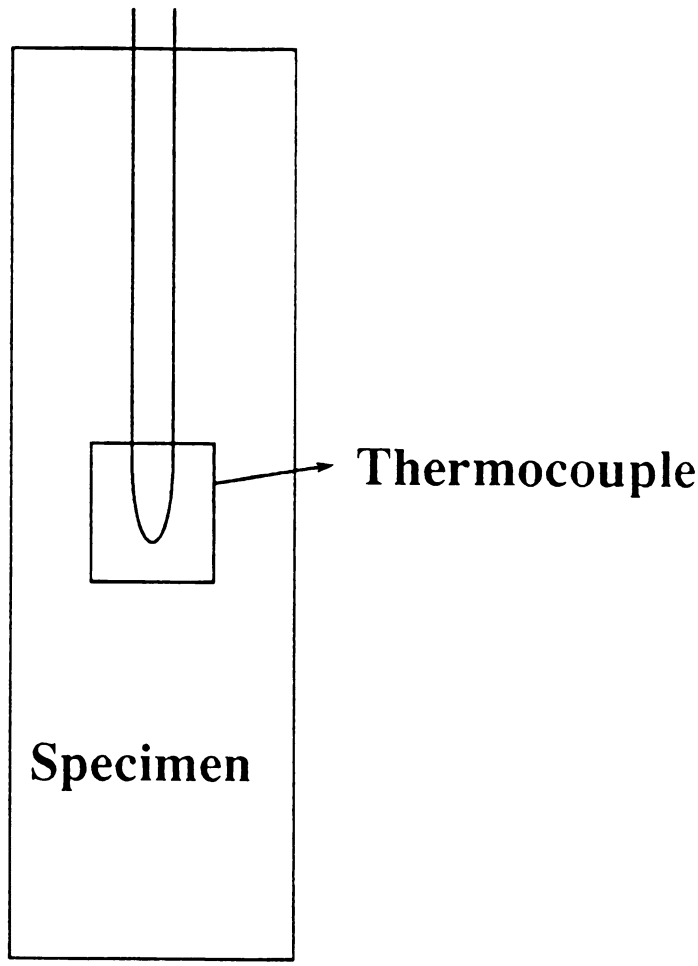

Figure 12. Prismatic Bar Specimen bonded with Thin Film Thermocouple.

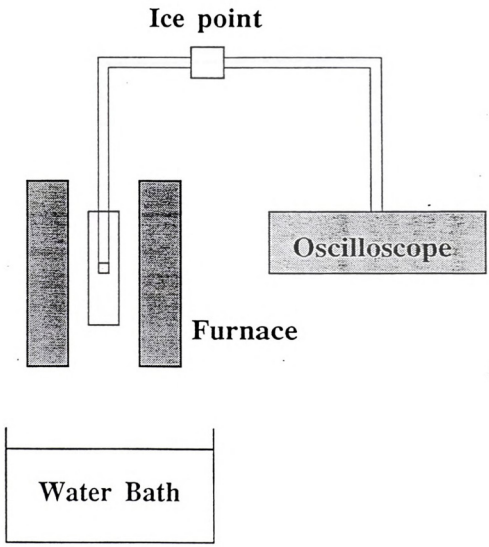

Figure 13. Schematic of experimental setup for surface heat transfer coefficient measurement.

Table 5. The dimensions and densities of the materials tested

Material	width(cm)	length(cm)	thickness(cm)	density(g/cm^3)
Macor	1.005	7.57	0.18	2.52
Alumina	1.20	6.97	0.10	3.70
TiB_2	0.66	6.53	0.20	4.45

2.3.2 Background

The surface heat transfer coefficient was calculated using a parameter estimation method [106, 107] which assumes that temperature is a function of time only. If we model the specimen as a lumped body which is suddenly exposed to a fluid at a temperature T_∞, the governing differential equation is [106, 107]

$$\rho c_p V \cdot \frac{dT}{dt} = hA(T_\infty - T) \tag{19}$$

where h = heat transfer coefficient

ρ = density of the specimen

c_p = specific heat of the specimen

V = volume of the specimen

t = time

A = heated surface area of the specimen

T = true specimen temperature.

Following Beck's procedure [106, 107], we used a polynomial form in the regression of the temperature-time data,

$$T = \beta_1 + \beta_2(t/\Delta t) + \cdots + \beta_p(t/\Delta t)^{p-1} + \epsilon \tag{20a}$$

$$\hat{T} = \beta_1 + \beta_2(t/\Delta t) + \cdots + \beta_p(t/\Delta t)^{p-1} \tag{20b}$$

where $\hat{T}$ = estimated temperature

Δt = time interval between readings of the thermocouple voltage

ϵ = residue of the polynomial

In this study, fourth order polynomials (p = 5) were used to obtain $\hat{T}$ from the time-temperature data. The derivative of estimated temperature, $\hat{dT}/dt$, was obtained from equation 20, such that

$$\hat{dT}/dt = \{\beta_2 + 2\beta_3(t/\Delta t) + 3\beta_4(t/\Delta t)^2 + 4\beta_5(t/\Delta t)^3\} / \Delta t \qquad (21)$$

Using equations 19, 20, and 21 we obtain the estimated heat transfer coefficient $\hat{h}$ [106, 107], where

$$\hat{h} = \frac{\rho c_p V}{A(T_\infty - \hat{T})} \cdot \frac{\hat{dT}}{dt} \qquad (22)$$

In addition to $\hat{T}$ and $\hat{dT}/dt$, the temperature dependence of the other parameters in equation 22 should be considered. For a given material, an expression for $c_p(T)$, the specific heat as a function of temperature may be taken (if available) directly from the literature. Otherwise, (as in this study) $c_p(T)$ may be obtained by regression on available c_p versus temperature data. From the definition of mass density, the product ρV is the specimen mass, which is temperature independent. The change in the surface area, A, with temperature will be proportional to 2α, where α is the linear thermal expansion coefficient. Since A is a rather weak function of temperature compared to the other temperature dependent terms in equation 22, A was considered to be constant in this study.

2.4. Effects of Surface Abrasion on the Thermal Fatigue of Ceramics

Prismatic bar-shaped specimens of a machinable glass-ceramic (Macor, Corning Code 9658) and polycrystalline alumina (AD 96 Coors Ceramics Inc.) were cut from commercial plates using a low speed diamond saw. The as-cut specimens of polycrystalline alumina were annealed in air at 850 °C for approximately 12 hours. The glass ceramic specimens were annealed in air at 500 °C for approximately 12 hours. The purpose of the thermal anneals was to reduce residual stresses that may have been generated during specimen preparation. After annealing, alumina and glass-ceramic specimens were abraded along the width direction using a 240 grit SiC abrasive paper. The dimensions and densities of the specimens tested in this study are given in Table 6.

During thermal shock testing, the abraded and unabraded specimens were held at 270 °C at least 30 minutes in a vertical muffle tube electric furnace. The specimens were quenched into a room temperature deionized water bath where they remained for 10 minutes. The specimens then were returned to the furnace for the next thermal shock cycle. After a preselected number of thermal shock cycles, the specimens' Young's modulus was measured by the sonic resonance technique [102].

Table 6. Dimensions and Densities of Macor and Alumina Specimens.

Material		Thickness(cm)	Width(cm)	Length(cm)	Density (g/cm^3)
Macor	unabraded	0.176	1.102	7.83	2.50
	abraded	0.173	1.105	7.50	2.52
Alumina	unabraded	0.105	1.20	7.01	3.49
	abraded	0.102	1.20	6.17	3.63

2.5. The Effect of Surface Limited Microcracks on the Effective Young's Modulus of Ceramics

2.5.1 Material Preparation and Characterization

Polycrystalline alumina (AD-96, Coors Ceramics Co.) billets were cut into prismatic bars using a low speed diamond saw (Buehler Isomet). The specimens were polished with 3 micron diamond paste to a mirror finish before annealing at 850 °C in air for 12 hours. The purpose of the anneal was to relieve the residual stresses which may have been generated during the cutting and polishing of the specimens. The mass densities of the specimens were determined from measured mass and specimen dimensions (Table 7). The mean grain size of 6 to 7 microns was determined by the linear intercept technique on SEM micrographs of fractured surfaces.

2.5.2 Microindentation and Fractography

Aligned microcracks were generated on the long transverse surfaces of the alumina bars (figure 2) by Vickers microindentation (Digital Semimacrohardness tester, Buehler, Ltd.). Loads of 49 N, 98 N and 196 N were used with a loading speed of 70 μm/sec and a loading time of 10 seconds. The indentation crack field for each specimen consisted of two subgroups of cracks, with one subgroup oriented longitudinally and the other subgroup oriented transversely on the specimen surface (figure 14).

Table 7. Dimensions and densities of the prismatic bar shaped alumina specimens

Indentation load	thickness(cm)	width(cm)	length(cm)	density(g/cm^3)
49 N (S*)	0.1000	1.20	6.390	3.758
49 N (B*)	0.1010	0.612	6.870	3.680
98 N (S*)	0.1014	1.20	6.943	3.734
98 N (B*)	0.1000	1.20	7.070	3.757
196 N (S*)	0.1005	1.20	6.970	3.755
196 N (B*)	0.1000	1.20	6.850	3.742

* B = indented both top and bottom surface, S=indented only single surface.

For each of the three indentation loads (49 N, 98 N and 196 N), pairs of nominally identical specimens were indented. One specimen of the pair was indented on a single long transverse surface only and the other specimen of the pair was indented on both of the long transverse surfaces. Specimens indented on both long transverse surfaces were indented alternatively on the top and bottom surfaces. The spatial arrangement of indentation cracks is illustrated in figures 14 (a), (c) and (e). Specimens indented on a single surface were indented as specified in figures 14 (b), (d) and (f). The average spacing between the indentations was 2.2 mm.

Radial crack lengths were measured using an optical microscope mounted on the indenter, which utilized a digital readout accurate to within ± 0.1 microns.

To directly observe the geometry and depth of the indentation-induced cracks without causing the cracks to extend under an applied load, this study employed a fractographic technique used by Kirchner, et al. [31, 32] and Lawn, et al. [108]. In Kirchner's [31, 32] and Lawn's [108] studies, specimens abraded on a single surface were fractured in four point bend. The specimens were oriented in the bend test fixture so that the undamaged surface of the specimen was the tensile surface, and the compression surface was the abrasion-damaged face. The macrocrack which caused catastrophic failure thus grew from the tensile surface driven by the four-point loading stresses. The macrocrack thus intersected the damaged surface (compression surface) only slightly before the final instant of specimen failure. Thus a

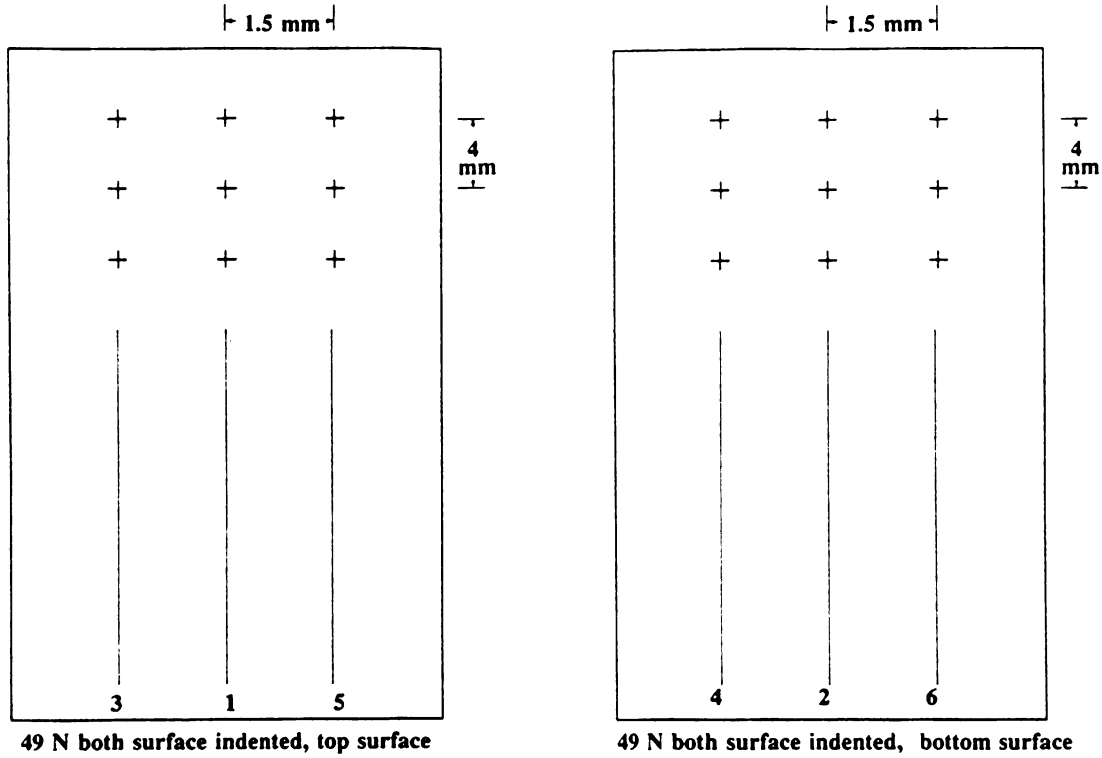

Figure 14. (a) Spatial Arrangements of indentation crcaks for both surface indented at 49 N load.

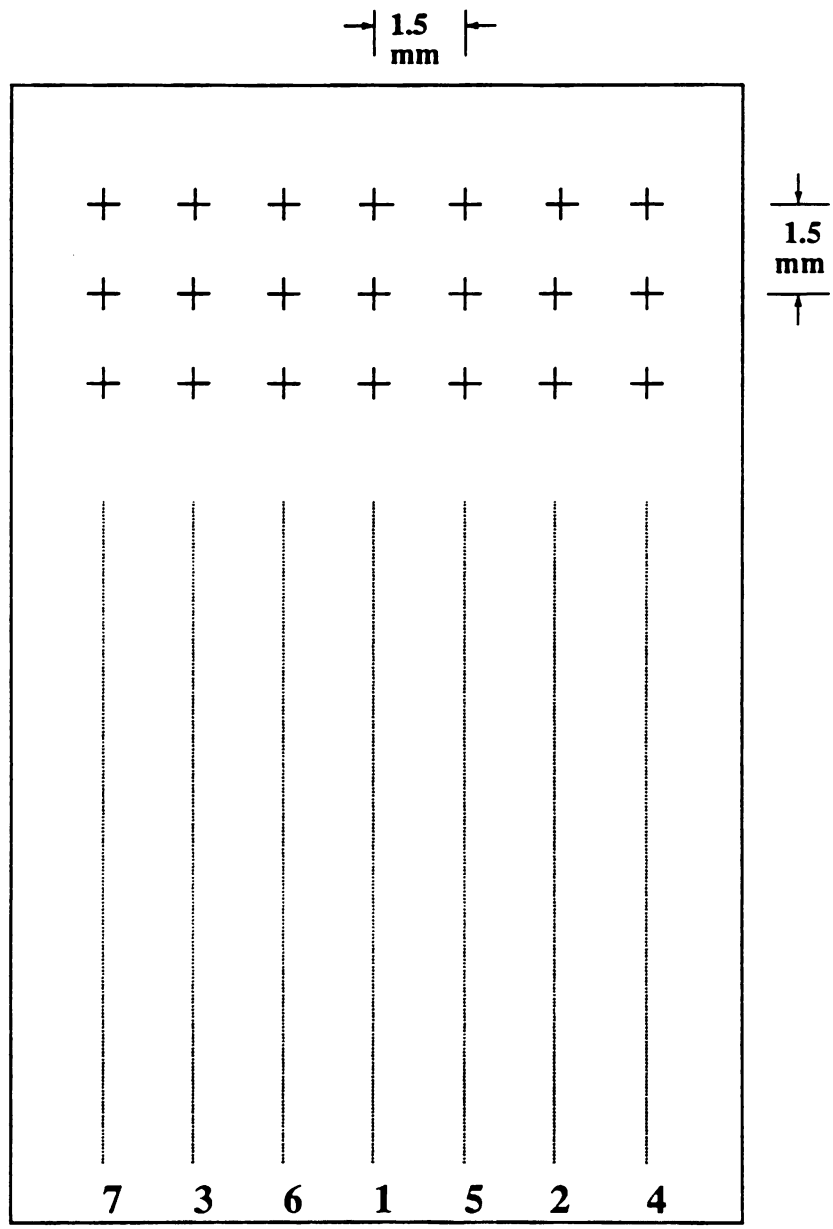

Figure 14. (b) Spatial Arrangements of indentation crcaks for single surface indented at 49 N load.

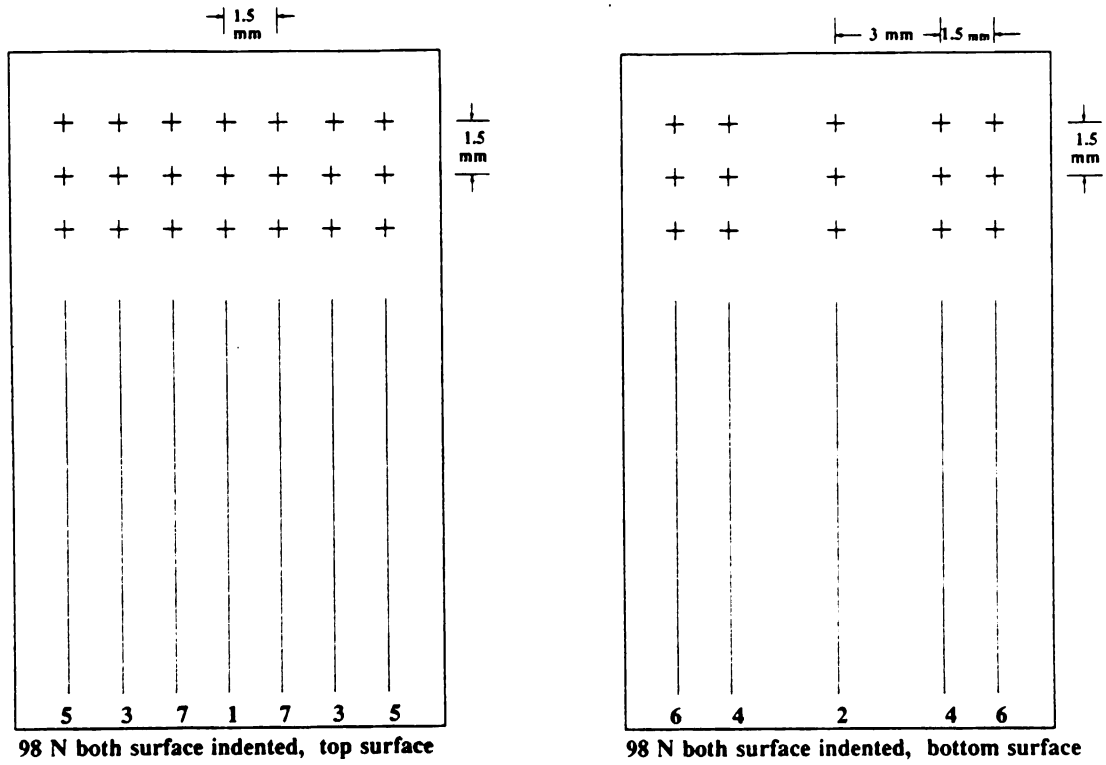

Figure 14. (c) Spatial Arrangements of indentation crcaks for both surface indented at 98 N load.

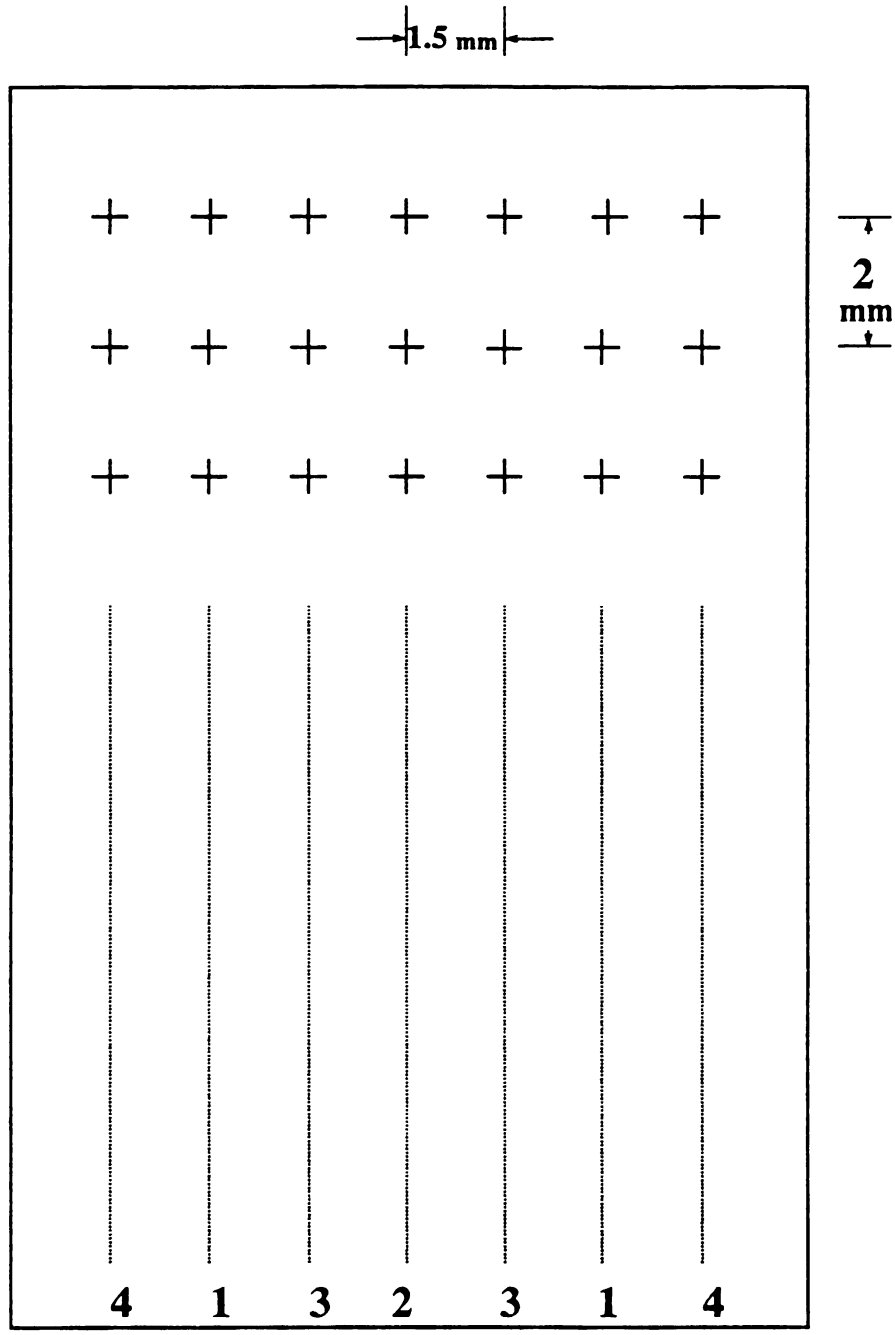

Figure 14. (d) Spatial Arrangements of indentation crcaks for single surface indented at 98 N load.

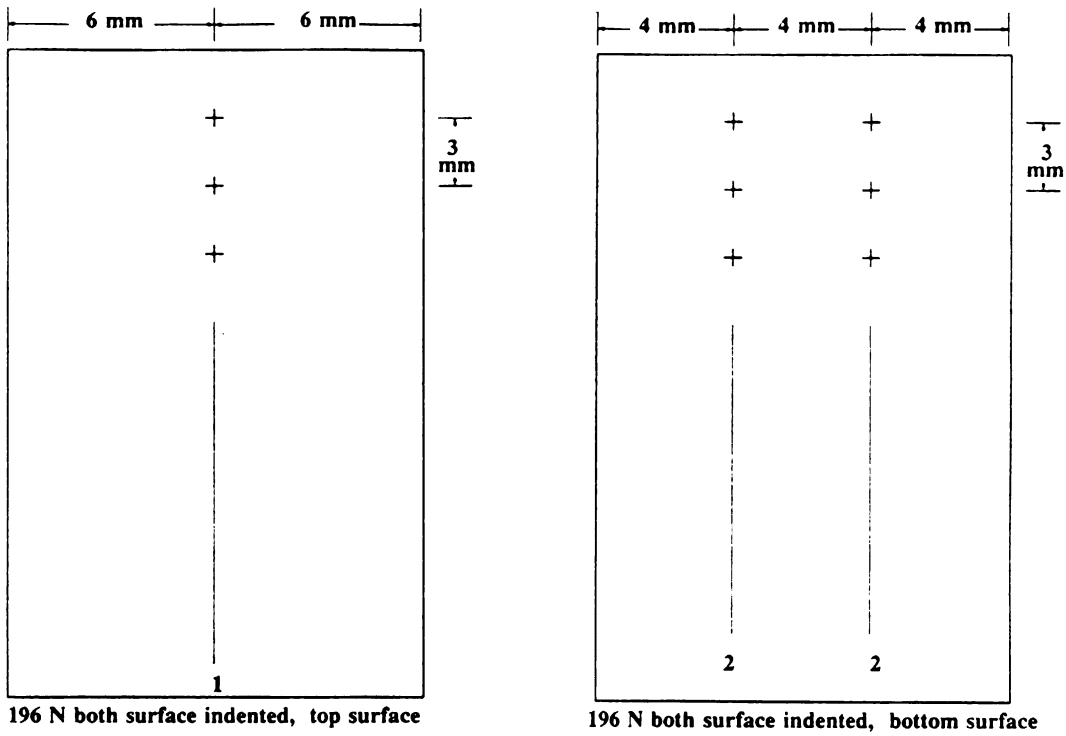

Figure 14. (e) Spatial Arrangements of indentation crcaks for both surface indented at 196 N load.

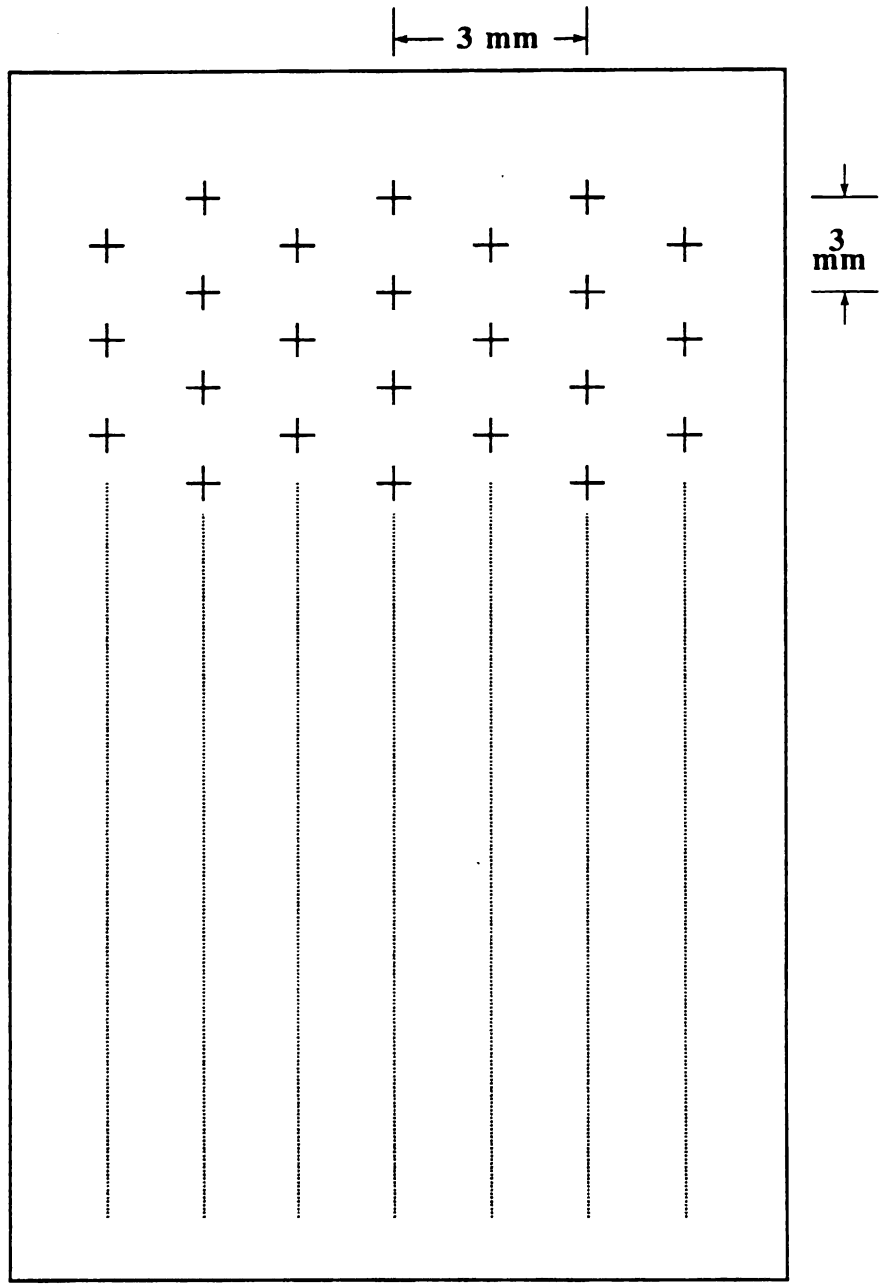

Figure 14. (f) Spatial Arrangements of indentation crcaks for single surface indented at 196 N load.

set of relatively unperturbed surface microcracks were revealed by intersection with the plane of the advancing macrocrack [31, 32, 108]. The success of this technique, of course, depends on the surface crack number density on the specimen's compression face. If the surface cracks are too sparse, then the advancing macrocrack may not intersect one of the microcracks of interest.

Following the indentation-modulus measurements, indent damaged specimens in this study were oriented in a four-point bend fixture with an indented surface on the compression side of the bend bar. (The four-point bend fixture had an upper span of 20 mm, a lower span of 40 mm, and a roller diameter of 3.1 mm). Specimens indented at each of the three different loads (49 N, 98 N, 196 N) were then fractured in four point bend, which allowed a macrocrack from the bar's tensile surface to propagate down and intercept an indented surface. The geometry of indentation cracks (as revealed on the fracture surface of the bend bars) was then studied via optical and scanning electron microscopy.

In addition to serving as a model array of surface cracks, the Vickers microindentations also were used to determine the hardness and fracture toughness of the specimens [89, 90, 109].

2.5.3 Elastic Modulus Measurements

The sonic resonance technique and apparatus used for the modulus measurements are described in detail elsewhere [11-19]. The Young's

modulus and Poisson's ratio of the undamaged alumina specimens were measured after annealing and prior to indentation [11-14]. Also modulus measurements were made immediately after finishing a preselected number of indentations at each load. For example, for the specimen indented on both surfaces at 98 N load, the elastic modulus was measured prior to indentation and was then remeasured after 46, 92, 184, 368, 460, and 552 cumulative indentations.

3 RESULTS AND DISCUSSION

3.1 Thermal Fatigue

3.1.1 Brief Review of Mechanical Fatigue Behavior in Ceramics and Ceramic Matrix Composites

The fatigue failure of any structure consists of three stages; 1) crack initiation, 2) crack propagation, and 3) catastrophic failure. The information of the life of high performance engineering structures is essential. Most of the lifetimes of engineering structures is mostly attributed to the crack propagation. Therefore crack propagation laws have been a very important subject for design engineers. The existing crack propagation laws in metals and alloys are briefly reviewed in four different categories for the purpose of comparing and analyzing the future fatigue data of ceramics and ceramic matrix composites. Some of fatigue results and plausible fatigue mechanisms are reported.

3.1.1.1 Brief Review of Various Crack Propagation Law in Metals and Alloys

3.1.1.1.1 Empirical Crack Propagation Laws

Paris and Erdogan[111] introduced a simple empirical propagation equation after comparing fatigue data of 2024-T3 Al-alloys widely.

$$da/dN = C(\Delta K)^n \tag{23}$$

where a = half crack length

N = number of cycles of applied load

ΔK = range of stress intensity factor(corresponding to stress range

C = material constant

n = numerical exponent

Foreman, et al.[112] modified Paris and Erdogan's law to include the load ratio, R (ratio of minimum K to maximum K in a given cycle) and instability when the stress intensity factor approaches the fracture toughness of the material.

$$da/dN = [C(\Delta K)^n]/[(1-R)K_c - \Delta K] \tag{24}$$

where R = ratio of minimum K to maximum K in a given cycle

K_c = critical stress intensity factor

Foreman, et al. [112] also used numerical integration technique using a computer to analyze the crack propagation and time to failure.

Pearson[113] modified Forman, et al.'s law to fit Aluminum alloy data. For high toughness alloys, fatigue crack growth rate was not affected by increasing R, but the rate increased rapidly with increasing R at high value of ΔK.

$$da/dN = [C(\Delta K)^n]/[(1-R)K_c-\Delta K]^{1/2} \qquad (25)$$

3.1.1.1.2 Crack Propagation Laws Based on Deformation ahead of crack tip

Liu[114] derived a expression for the crack length, a, in a semi-infinite sheet of 2024-T3 Al-alloy under repeated loading in terms of number of loading cycles, N, and a stress dependent factor, C, to account for the effect of an increasing stress range and mean stress as crack propagated.

$$da/dN = Ca \qquad (26)$$

where C = crack propagation factor in a semi-infinite sheet which depends on the initial value of the stress range and the mean stress

Thomkins[115] treated the crack propagation as a continuum mechanics problem by considering the crack tip plastic zone and the

net section microplastic range, which is a part of the strain range applied to the uncracked section.

$$da/dN = \Delta\epsilon_p \, (D_{max}-D_{min}) \qquad (27)$$

where $\Delta\epsilon_p$ = applied plastic strain range

D_{max}, D_{min} = deformation zone size associate with maximum and minimum stress respectively.

This model is mostly based on Manson-Coffin relationship which predicts fracture when the cyclic plasticity build up to a critical value.

$$\Delta\epsilon_p N_f^{\alpha} = C \qquad (28)$$

where N_f = number of cycles to fracture

α = fracture ductility exponent

C = fracture ductility coefficient which is an experimentally obtainable value

Raju[116] derived a crack propagation law by considering the energy of plastic deformation at the tip of the crack growing under sinusoidal loading with constant amplitude, such that

$$da/dN = [C(1-R)^{4-m} K_{max}^{4}] / (K_c^2 - K_{max}^2) \quad (29)$$

where C = material constant

R = minimum stress/maximum stress

m = numerical exponent

K_{max} = stress intensity factor corresponding to the maximum stress in the cycle

K_c = fracture toughness

Duggan[117] developed a continuum mechanics model to predict fatigue crack propagation rate. Fatigue crack growth was controlled by the fatigue ductility exponent, the fatigue ductility coefficient, the elastic modulus and fracture toughness, such that

$$da/dN = 1/\alpha \ (\pi/32)^{1/2\alpha} \{2[1-\Delta K_I/K_c]/[\epsilon_f' E(K_c - K_{max})]\}^{1/\alpha} \Delta K_I^{2/\alpha} \quad (30)$$

where α = fatigue ductility exponent

ϵ_f' = fatigue ductility coefficient

E = elastic modulus

ΔK_I = stress intensity range(mode I)=$K_{max} - K_{min}$

Duggan's model implies that fatigue crack growth is critically dependent on the condition of crack tip as expressed in terms of the stress intensity range. Equation 30 showed good agreement with the fatigue data of a creep resistant stainless steel, FV535, 2.5% Ni-Cr-

Mo direct hardening steel, Ni-based heat resistant alloy,INCO901, and a ferrous alloy containing TiC in medium alloy tool steel matrix.

3.1.1.1.3 Crack Propagation Laws Considering Crack Tip Geometry

Frost and Dixon [118] considered the changes in crack profile during loading cycle to produce crack propagation law.

"a) crack is closed under no load (slit)
b) as the load is increased to maximum stress, crack tip opens and blunts (elliptical profile)-crack tip blunting can occur by both elastic and plastic deformation at the crack tip and by 'unbonding of atoms' at the crack tip
c) as the load is reduced the blunted tip resharpens and crack closes completely at zero load."

$$da/dN = \sigma^2 a[\ln(4E/\sigma)-1]/E^2 \approx 8(K_I/E)^2/\pi \qquad (31)$$

where σ = applied stress

E = elastic modulus

In this model (equation 31) Frost and Dixon [118] thought that fatigue crack growth to occur via a process where the crack tip is blunted and resharpened repeatedly during cyclic loading.

Pook and Frost[119] derived a crack propagation law directly from the stress and displacement field around a crack or sharp notch.

$$da/dN = K_I^2 [1+\ln(4E/\sigma_y)/(\pi E^2) \qquad (32)$$

where σ_y = yield stress

E = elastic modulus

The value of E/σ_y for common engineering materials is of the order of 10^3. If we set $E/\sigma_y = 10^3$ then Pook and Frost's equation becomes

$$da/dN = 9(K_I/E)^2/\pi \qquad \text{for plane stress}$$
$$= 9[K_I(1-\nu^2)/E]^2 \qquad \text{for plane strain}$$

Equation 32 is similar to Frost and Dixon's law but it is derived from the general geometry of the cracks.

3.1.1.1.4 Crack Propagation Law Considering Crack Closure

Paris and Erdogan's law [111] is inadequate since residual stress may hold the crack closed as external stress is applied to open the crack. Ebler[120] introduced a modified fatigue crack growth law,

$$da/dN = C(U\Delta K)^n \qquad (33)$$

where U = effective stress range factor given by

$$(\sigma_{max}-\sigma_{op})/(\sigma_{max}-\sigma_{min})$$

σ_{max}, σ_{min} = maximum and minimum stress respectively

σ_{op} = stress at which the crack starts to open along its length

Ebler [120] introduced the hypothesis that crack propagation can occur only a portion of the cycle where the crack is fully open at the crack tip.

3.1.1.2 Mechanical Fatigue in Ceramics

For polycrystalline alumina, Krohn and Hasselman [121] found that cyclic loading in four point bend resulted in lower time to failure than static loading with maximum cyclic load. Krohn and Hasselman [121] suggested possible cyclic fatigue mechanisms, such as the defects created by dislocation motion at the crack tip and thermally activated processes such as softening of grain boundary phases by heat generated from microcrack friction. The thermally activated processes were also reported in glass cloth reinforced epoxies during cyclic loading [34]. Guiu [122] reported a reduced time to fracture for cyclically loaded 'Lucalox' alumina using the direct push-pull test. Time to failure was in static fatigue about 10 times greater than under 5-10 Hz cyclic loading conditions for a given maximum stress value of 195±5 MPa. In order to eliminate static fatigue effects and study only cyclic mechanical fatigue effects on the sintered silicon nitride specimens, the specimen with indentation-induced flaws was applied a static load which was the maximum stress of loading cycle for a sufficient period of time before cyclic loading [123]. The specimens were loaded in four-point bend cyclically at a frequency of 1 to 20 Hz. By doing this, Horibe [123] reported a clear increase in

radial crack length of indentation-induced flaws as a function of loading cycles. Ewart and Suresh [124, 125] showed cyclic compression applied to notched polycrystalline and single crystal alumina leads to stable mode I crack growth at room temperature. Dislocation plasticity, microcracking, martensitic transformation in some ceramics, or creep at elevated temperatures are plausible sources of the residual tensile stress required to produce stable crack growth even in brittle materials [124, 125]. Ewart and Suresh [124, 125] suggested plausible mechanisms of cyclic fatigue, such as a progressive failure due to grain boundary cracking. Debris particles trapped between crack surfaces caused additional contact forces which slowed down the fatigue crack growth, as observed in an SEM [124, 125]. Kawagubo and Komeya [126] investigated the static and cyclic fatigue of sintered silicon nitride specimens with indentation induced flaws using four point bending at room temperature in air. For the mechanical cyclic loading, loading frequencies of 0.01 to 10 Hz were used. When a relatively high stress is applied, the lower limit of cyclic fatigue lifetime is almost the same as that of static fatigue lifetime, while the upper limit of cyclic fatigue lifetime increases (approaches the upper limit of static fatigue lifetime) with lowering frequency. When relatively low stresses were applied, observed cyclic fatigue lifetime was shorter by two orders of magnitude than predicted lifetime, which means that cyclic load accelerates the fatigue crack growth. Semicircular markings on surfaces fractured in static fatigue gave evidence of crack arrest and repropagation [126]. The arrested

crack may continue to grow by cyclic loading. Fatigue failure occurred mostly by intergranular cracking with some transgranular cracking. The crack growth rate versus stress intensity factor plateaued at values of about 70 to 90 percent of fracture toughness. Stress corrosion cracking of glassy materials along the grain boundaries in sintered silicon nitride is a possible fatigue mechanism [126].

In other cases, mechanical fatigue effects were found to be either non-existent or existent only in a very restricted ranges and loading conditions [127-131]. Chen and Knapp [127] observed that cyclic effects were limited only in a range from room temperature to 216 °C in polycrystalline alumina; decreasing with increasing temperature. Evans and Fuller[128] who also reported non-existence or limited existence of cyclic effects in soda lime glass and electrical porcelain, presented an analysis which predicted crack propagation rate under cyclic load from static crack propagation parameters. Evans[129] proposed two categories of plausible fatigue mechanisms for tension-compression fatigue: macrocrack and microcrack growth. For macrocrack growth, large stresses developed from an applied compression stress at the crack surface asperities may have stress high enough to induce plasticity. Plasticity near crack surface asperities may induce the lateral crack formation on unloading (figure 15). Crack surface asperities may influence crack closure during unloading and subsequent compressive loading by contacting crack surface asperities near the crack tip. This nonclosure of asperities

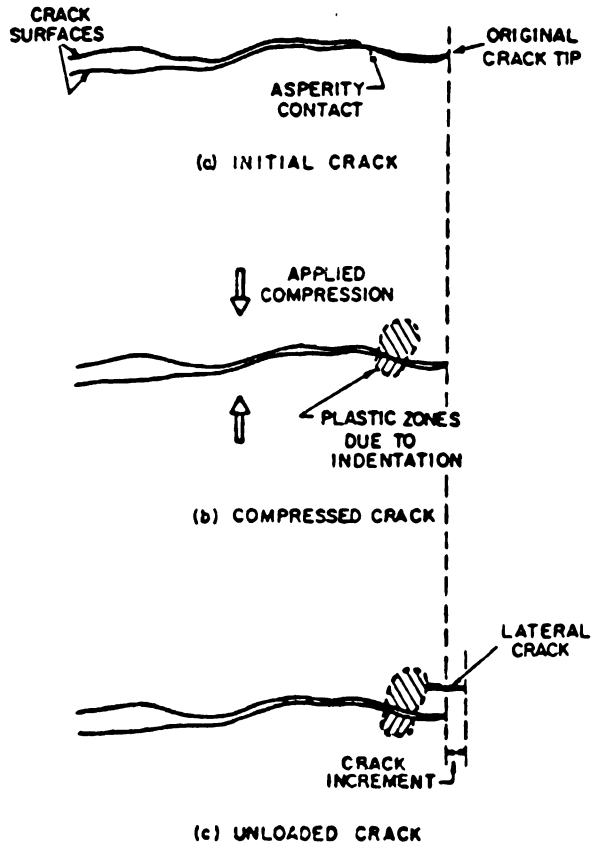

Figure 15. The Formation of lateral cracks at crack surface asperities (after Evans [129]).

could result in a tensile opening force at the crack tip throughout the tension and compression cycle (figure 16). Fatigue mechanisms includes grain boundary crack formation by thermal expansion anisotropy (coarse grained material), microcrack extension and coalescence to form critical size crack.

As a summary, cyclic fatigue effects appears to be existent in ceramics. Static fatigue is mostly controlled by environmentally assisted stress corrosion cracking. Fatigue crack growth via cyclic loading may occur by (1) softening of grain boundary phases by heat generated by friction of microcrack surfaces [34, 121], (2) coalescence of thermal expansion anisotropy induced grain boundary microcracks (figure 17) [129], (3) lateral crack growth on unloading due to the compression load induced plasticity near crack surface (figure 15) [129], (4) a tensile stress at the crack tip (figure 16) [129] induced by the non-closure of asperities near the crack tip, and (5) stable crack growth [124, 125] due to residual tensile stress at the crack tip induced by unloading (far-field compression-compression loading). Also cyclic fatigue crack growth was observed to be mostly intergranular and partially transgranular [126].

3.1.1.3 Mechanical Fatigue in Ceramic Matrix Composites

The fatigue characteristics of ceramic matrix composites (CMC) are very complex because composites exhibit inhomogenieties and anisotropies in mechanical properties. Even though the fatigue

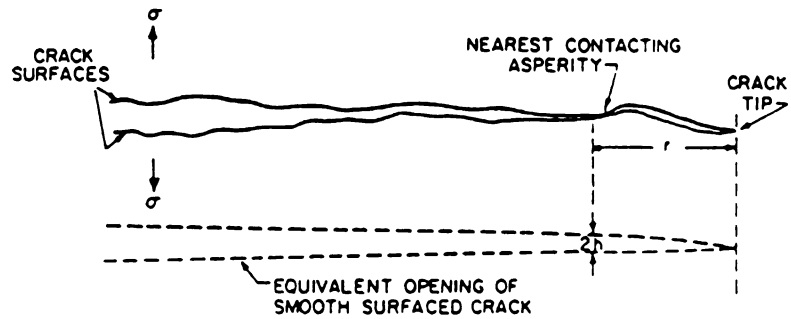

(a) CRACK AT PEAK APPLIED TENSILE STRESS

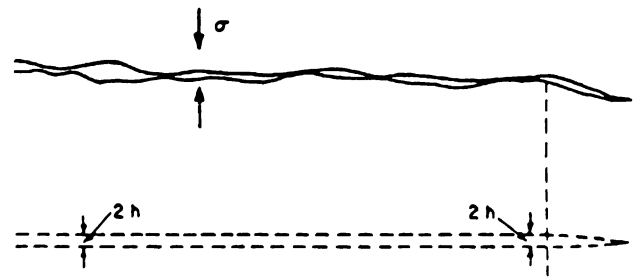

(b) COMPLETE ASPERITY CONTACT UNDER APPLIED COMPRESSION

Figure 16. The limitation on crack closure provided by the crack surface asperities (after Evans [129]).

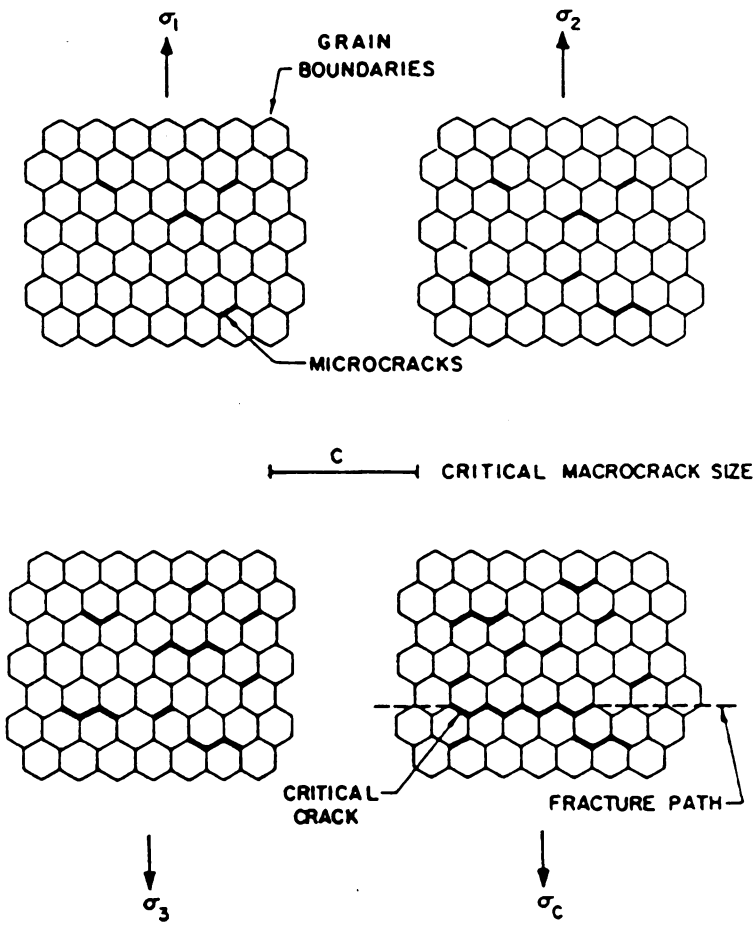

Figure 17. The sequence involved in failure by microcrack formation and coalescence (after Evans [129]).

response of CMC is critical in many engineering applications, little work has been done on fatigue of CMC.

Lewis [132] proposed a cyclic fatigue failure mechanism in ceramic matrix-fiber reinforced composites based on irreversibility in the process of matrix cracking and fiber pull-out. According to Lewis [132], fatigue failure occurs in five basic steps (1) Matrix cracking because of lower strain to failure of the matrix, (2) Crack arrest and deflection at the fiber-matrix interface which leads to fiber-matrix debonding, (3) Further loading entails stress transfer from the matrix to the fiber, (4) Fibers break at the ultimate strength and slide out of the matrix, (5) Ideally, unloading reverses of the process. However the non-ideal frictional restraint at the fiber-matrix interface causes unloading to exert a compressive stress on the fiber being forced into the cavity created by the pull-out. Depending on the fiber length, this eventually leads to fiber buckling and consequent fiber failure in compression.

Prewo [133] performed tensile fatigue testing on two different LAS-SiC fiber composites. LAS I-SiC uniaxially reinforced fiber composite showed a linear stress-strain curve with no change in stress-strain behavior during fatigue maximum load lower than the fracture stress. While uniaxially reinforced LAS II-SiC fiber composite which showed higher strength exhibited a portion of non-linear stress-strain curve at higher stress region (than the proportional limit) at 22 °C. Repeated cyclic loading with maximum loading higher than the proportional limit reduced the proportional

limit and another linear stress-strain region appeared above the reduced proportional limit. The cause of this changes in stress-strain curve was thought to be matrix microcracking and matrix microcrack closure on unloading.

LAS II-SiC were fatigued at up to 10^5 cycles with 0.5 Hz frequency at temperatures 22, 600, 900 °C. At room temperature, most of composites survived up to 10^5 cycles. Residual strengths were not changed and increased in some specimens.

At 600 °C the LAS II-SiC specimens exhibited a flexural strength of 1000-1100 MPa for a single loading cycle. The strength then deteriorated as the number of fatigue cycles increased such that the specimens failed at one third of their room temperature strength after 10^5 cycles. A gradual decrease in the stiffness was observed in the load-deflection behavior. The gradual reduction in stiffness was accompanied by visible interlamella shear cracks in addition to the major tensile cracks. The LAS II-SiC composite exhibited stable fatigue behavior without catastrophic failure, therefore the composite is preferred to the matrix alone.

The strength of the LAS II-SiC composites did not change significantly with increasing number of cycles for fatigue testing at 900 °C. The only anomaly observed was a non-linear load-deflection behavior. As in the case of the specimen fatigued at 600 °C, fracture was non-catastrophic. The resultant fracture features were also non-fibrous(brittle).

Suresh, et al. [134] applied far-field compression cyclic loading on silicon nitride and silicon nitride-SiC whisker composites to investigate stable mode I fatigue crack growth in CMC. Suresh and co-workers [134] used single notched specimens of Si_3N_4 and Si_3N_4-SiC whisker composites loaded with at frequency of 20 Hz and load ratio (= maximum compressive stress/minimum compressive stress) of 10. Threshold stress ranges to initiate a fatigue crack increased and the resultant crack lengths after 10^5 cycles were 2.5 and 2.2 times longer than Si_3N_4 matrix for the 10 volume percent and 20 volume percent SiC whisker composites respectively. However, the threshold stress range was lower than Si_3N_4 by 20 percent. The crack length after $5x10^5$ cycles was as short as 0.05 mm for 30 volume percent SiC whisker composite under maximum stress 318 MPa and minimum stress 31.8 MPa, while the crack length for 20 volume percent SiC whisker composite was 0.22 mm under maximum load 422 MPa and minimum load 42.2 MPa. Suresh, et al. [134] observed that the crack growth rate gradually decreased with fatigue cycles because of the presence of debris and whiskers trapped in the crack wake. Whisker pull-out and debris during cycling were observed from fractography of fatigue failure surface. Sursh et al. [134] assumed a relatively flat and smooth fracture surface due to the severe abrasion between crack surfaces during cycling from fractography of fatigue failure surfaces without presenting unfatigued crack surface. Larger crack opening in the composites appeared to result from the removal of material (caused by high frequency contact of 'pulled-out and broken whiskers' with crack surfaces) from the

crack. SiC whisker reinforcement in Si_3N_4 appeared to deteriorate the cyclic fatigue behavior upto 20 volume percent whisker reinforcement even though the reinforcement produced higher toughness. For 30 volume percent whisker composite, the crack growth rates were smaller but a fatigue crack initiation threshold stress is 20 percent lower than unreinforced Si_3N_4 matrix.

Morrone, et al.[135] used a similar method to Suresh's [134] to study Al_2O_3-SiC whisker composite. Single and double edge notched specimens with different notch root radii were used to monitor the edge crack propagation under cyclic compression loading [124, 125, 134]. The length of self arrested crack increased from 182 to 835 μm as the notch root radius increased from 130 to 1050 μm after 10^6 cycles. The changing root radius did not affect the maximum compressive stress at the notch tip during cyclic loading. As observed previously [134], the crack closure force which can slow down the fatigue crack growth can be supplied by the presence of the debris and pulled-out whiskers trapped in the crack wake. However, fatigue behavior does not seem likely to be improved very much by whisker reinforcement.

3.1.2 Thermal Shock Fatigue

3.1.2.1 Thermal Fatigue in SiC Fiber Reinforced Aluminosilicate Glass-Ceramic Composite

Unshocked (annealed) Young's modulus values (Table 8) measured in this study agree reasonably well with data reported by Prewo [136] for

Table 8. The non-linear regression results of thermal fatigue data of SiC fiber/AS composite

Specimen Label	5.21	5.22	5.14	5.21	5.22	5.14
ΔT (C)	300	370	450	300	370	450
E_0[GPa], Q_0^{-1}[x10^{-5}]	142.2	125.5	132.7	23.06	23.25	25.82
A[GPa], B[x10^{-5}]	0.288	0.514	0.956	14.00	19.98	39.38
A/E_0	0.00202	0.00409	0.00720	*	*	*
B/Q_0^{-1}	*	*	*	0.5422	0.8594	1.7077
α, β	0.097	0.1136	0.193	0.096	0.158	0.207

longitudinal Young's moduli of uniaxially reinforced SiC fiber (44-46 vol percent)/LAS composites at room temperature; 128-136 GPa measured by tension test, 132-172 GPa from four point flexural test. Internal friction data for unshocked specimens are also listed in table 8.

For SiC fiber reinforced LAS, the Young's modulus, E, decreased and internal friction, Q^{-1}, increased monotonically with n, the cumulative number of thermal cycles (figures 18 and 19), as described by the equations

$$E(n) = E_0 - A \{ 1 - \exp(-\alpha n) \} \tag{34}$$

$$Q^{-1}(n) = Q_0^{-1} + B \{ 1 - \exp(-\beta n) \} \tag{35}$$

where $E(n)$, $Q^{-1}(n)$ = Young's modulus and internal friction as a function of n, the cumulative number of thermal shock cycles

E_0, Q_0^{-1} = Young's modulus of unshocked specimen

A, B = damage saturation constants

α, β = rate of decrement and increment (rate constant).

Parameters A, α, B and β (Table 8) were calculated via non-linear regression on the E and Q_0^{-1} data. For a given ΔT, A and B represent a steady state level of damage (damage saturation) for a large number of cumulative thermal shock cycles, n. The constants α and β measure the

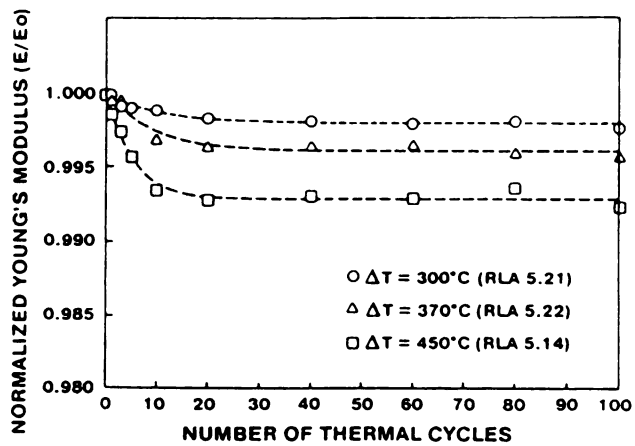

Figure 18. Young's modulus of SiC fiber/AS composites as a function of the cumulative number of thermal shock cycles.

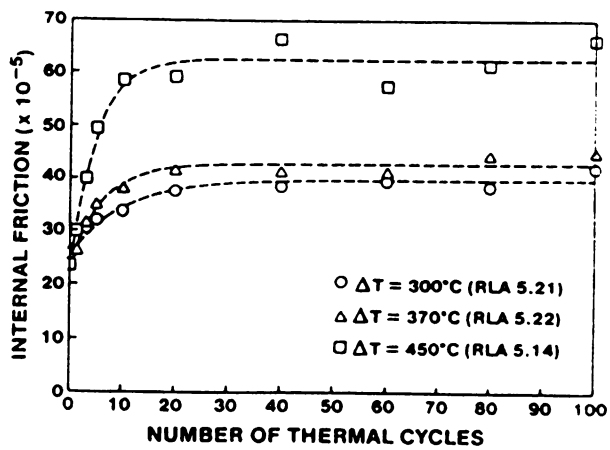

Figure 19. Internal friction of SiC fiber/AS composites as a function of the cumulative number of thermal shock cycles.

rate of decrease in Young's modulus and that of increase in internal friction. The values of α, β and those of A, B increased as ΔT increased. The most probable cause for this thermal fatigue is the microcracking and its coalescence induced by the superposition of microscopic thermal expansion mismatch between the matrix and fiber, thermal expansion anisotropy of crystal, and macroscopic thermal gradient stress present during the quenching in deionized water [137]. Crystalline beta-eucryptite, a major crystalline phase in LAS matrix, has a severe thermal expansion anisotropy (thermal expansion coefficient along the c-axis is $-17.6 \times 10^{-6}\ C^{-1}$, whereas along the a-axis, it is $+8.2 \times 10^{-6}\ C^{-1}$) [138, 139]. Beta-eucryptite grains in glass ceramics are usually submicron in size, thus depending on the critical grain size [35] microcracking due to thermal expansion anisotropy may not be significant. The effective, macroscopic thermal expansion coefficient of beta-eucryptite is $-8 \times 10^{-6}\ C^{-1}$ and the thermal expansion coefficient of SiC fiber is 3.2×10^{-6} [140], thus the thermal expansions may partially cancel each other during heating and cooling. This is consistent with the very low level of thermal shock damage obtained in this study even after 100 thermal shock cycles.

3.1.2.2 Comparison of thermal cycling damage in SiC fiber/LAS composites with polycrystalline alumina and SiC whisker/alumina composites

A simple linear relationship between the change in internal friction and the "crack damage parameter", as defined by Salganik [141] and by Budiansky and O'Connell [76]* was demonstrated. Young's modulus decreases as a function of the microcrack damage parameter**, ϵ, according to

$$E = E_o \{1 - f(\nu)\epsilon\} \tag{36}$$

with the empirical equations 34 and 35, one obtains a relation of the form

$$\Delta Q^{-1}/Q_o^{-1} = C_1[1 - \{1 - C_2 f(\nu)\epsilon\}^{C_3}] \tag{37}$$

where C_1, C_2 and C_3 are constants [24]. For a sufficiently small $C_2 f(\nu)\epsilon$, the term $\{1 - C_2 f(\nu)\epsilon\}^{C_3}$ in equation 37 becomes $\{1 - C_2 C_3 f(\nu)\epsilon\}$ using the binomial expansion theorem. Equation 37 then can be approximated by the linear equation, $\Delta Q^{-1} = D\epsilon$, where D is constant.

For both the SiC fiber/LAS and the SiC whisker/alumina

---

* The crack damage parameter ϵ is defined as the product, $N\langle a^3 \rangle$, where N is microcrack density (number of microcracks per unit volume) and $\langle a \rangle$ is mean microcrack radius.

** $f(\nu)$ is a weak function of Poisson's ratio ν. For most materials, $f(\nu)$ is approximately 1.7. $f(\nu)$ may differ depending on the distribution of cracks and orientations [77, 19].

composites, the ΔQ^{-1} versus ϵ plots were linear, corresponding to $\Delta Q^{-1} = D\epsilon$. Each of the internal friction versus cumulative shock curves (figure 19) corresponds to thermal shock damage evolution at a different ΔT. However, in terms of ΔQ^{-1} versus ϵ, all of the thermal shock damage curves collapse onto a single line (figure 20). For the polycrystalline alumina specimens, the deviation from linearity in the ΔQ^{-1} versus ϵ plot is thought to be due to extensive linkup of microcracks in the unreinforced specimen, where such linkup is limited in the composite specimens [25].

For the SiC fiber/LAS composite, the SiC whisker/alumina composite [24], and the polycrystalline alumina [25], log-log plots of the normalized saturation values (A/E_o and B/Q_o^{-1}) in figure 21 showed a power law relationship with nondimensional temperature difference, $\Delta T/T_r$ namely

$$A/E_o = j1(\Delta T/T_r)^{p^1} \tag{38}$$

$$B/Q_o^{-1} = j2(\Delta T/T_r)^{p^2} \tag{39}$$

where T_r, is a reference temperature (293 K). ΔT, the temperature difference between the furnace temperature and the water bath temperature, was expressed in terms of degrees K (figure 21). A comparison of the slopes of $\ln(A/E_0)$ and $\ln(B/Q_0^{-1})$ versus $\ln(\Delta T/T_r)$ (where the slopes correspond to the exponents p^1 and p^2 in equations 38 and 39, respectively) show that the slope for the SiC fiber/LAS

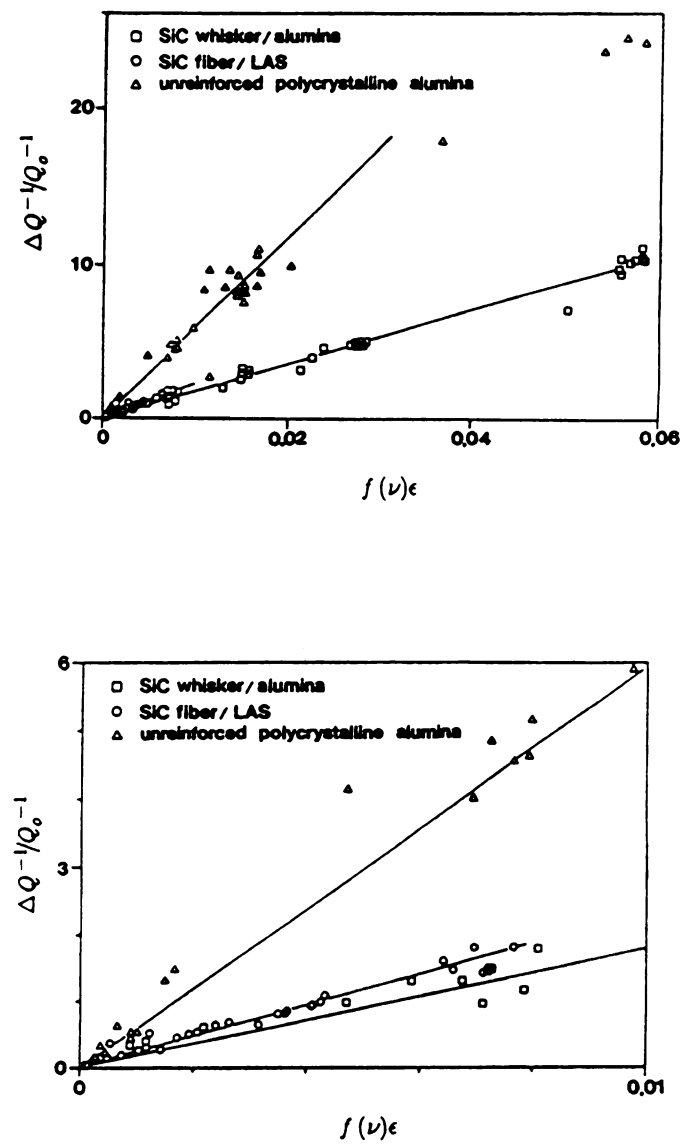

Figure 20. ΔQ^{-1} as a function of crack damage parameter for the SiC fiber/LAS composites, the SiC whisker/alumina composites and unreinforced alumina. The figure (b) represents the less damaged region of figure (a).

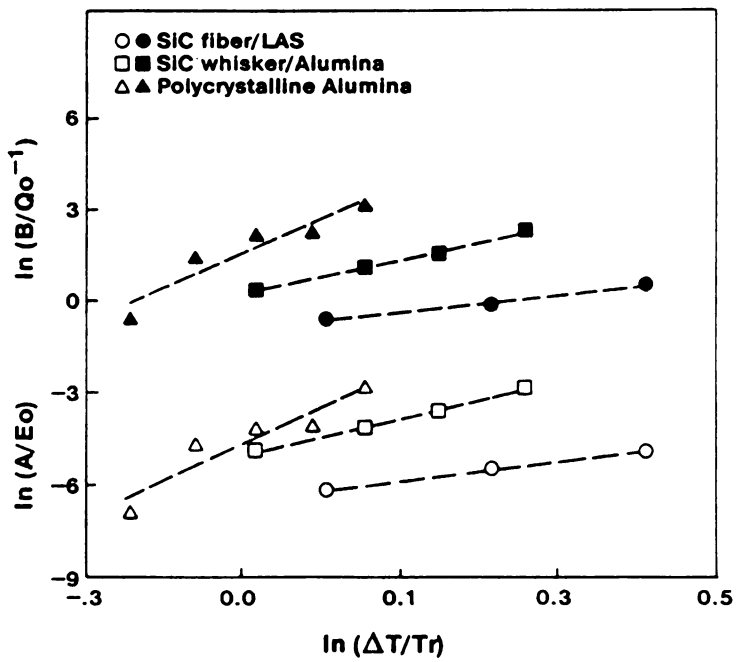

Figure 21. Logarithm of the normalized saturation damage parameters (A/E_0) and (B/Q_0^{-1}) versus logarithm of the normalized temperature.

Table 9. Least-squares best fit results of log-log plots of the normalized saturation values (A/E_o and B/Q_o) with $\Delta T/T_r$

Specimen Label	SiC fiber/AS	SiC whisker/alumina	Alumina
j1	0.002	0.012	0.030
j2	0.510	2.225	14.795
p_1	3.13	5.97	11.83
p_2	2.82	5.69	11.32
A/E_0 (ΔT=300)	0.0022	0.0138	0.0397
A/E_0 (ΔT=400)	0.0053	0.0770	1.1920
B/Q_0^{-1} (ΔT=300)	0.545	2.545	19.328
B/Q_0^{-1} (ΔT=400)	1.227	13.079	501.756

composite is approximately half that of the SiC whisker/alumina and approximately quarter that of the polycrystalline alumina (Table 9). Using equation 38 and the parameters j1 and p^1 (obtained via non-linear least-square fit of E versus ΔT data), A/E_0 can be compared for the three materials at a given ΔT. Equation 38 likewise can predict B/Q_0^{-1} for the three materials for fixed ΔT. For a ΔT of 300 K, the relative moduli decrease by 0.22 %, 1.38 % and 3.97 % for SiC fiber/LAS, SiC whisker/alumina and unreinforced alumina, respectively (Table 9), while the internal friction increases by 54.5 %, 254.5 % and 1932.8 % for the same three materials (Table 9). Changes in E and Q^{-1} for the three materials were also calculated for a ΔT of 400 K (Table 9). All changes in E and Q^{-1} were calculated with respect to the saturation damage levels at the given ΔT. This data provides a quantitative measure of the improvement in thermal shock resistance offered by fiber and whisker reinforcement of ceramics.

The j2/j1 ratio represents the relative sensitivity in internal friction compared to the changes in Young's modulus for a given thermal shock damage level. The j2/j1 ratio is approximately 250 for the SiC fiber/LAS composites, 200 for the SiC whisker/alumina composites [24] and 500 for the polycrystalline alumina [25].

The power law relationship between the saturation damage level and thermal shock difference implies a fatigue-like power law relation in stress, since for brittle materials, ΔT is linearly related to the induced thermoelastic stress [24, 25]. Thus equations 38 and 39 are, equivalently, power law functions of the applied

thermal stresses. Such power law functions are common in the fatigue of metals [111], where instead of stress the power law relation is expressed in terms of stress intensity, such that $da/dn = W \Delta K^q$ where a is the length of the fatigue crack, n is the cumulative number of stress cycles, ΔK is the stress intensity range $K_{max} - K_{min}$, and the parameters W and q depend on the material, the test temperature, etc. Thus, equations 38 and 39 (which as stated above may be rewritten in terms of a power law in stress or stress intensity) demonstrate the existence of fatigue-like behavior for thermal shock loading of ceramics. Macrocrack extension due to repeated purely mechanical cyclic loading of ceramics also recently has been described by similar power-law type fatigue equations [142-144].

3.1.2.3 Static Young's Modulus Measurement of unshocked Macor Glass-Ceramic

The load versus displacement curve of Macor specimen with thickness of 1.77 mm and width of 11.48 mm is shown in figure 22. From the maximum load of 107.42 N, the fracture strength of Macor was 89.60 MPa (equation 7). Chyung et al. [145] reported 100 MPa for the flexural strength of Macor. The tensile strength of 103 MPa was reported for Macor [147]. The maximum strain in outer fiber at midspan was calculated as 1.426×10^{-3} from the maximum displacement value of 0.215 mm in load versus displacement curve (equation 8). The maximum deflection of specimen at midspan was calculated as 0.295 mm (equation 9). The static Young's modulus of Macor specimen was

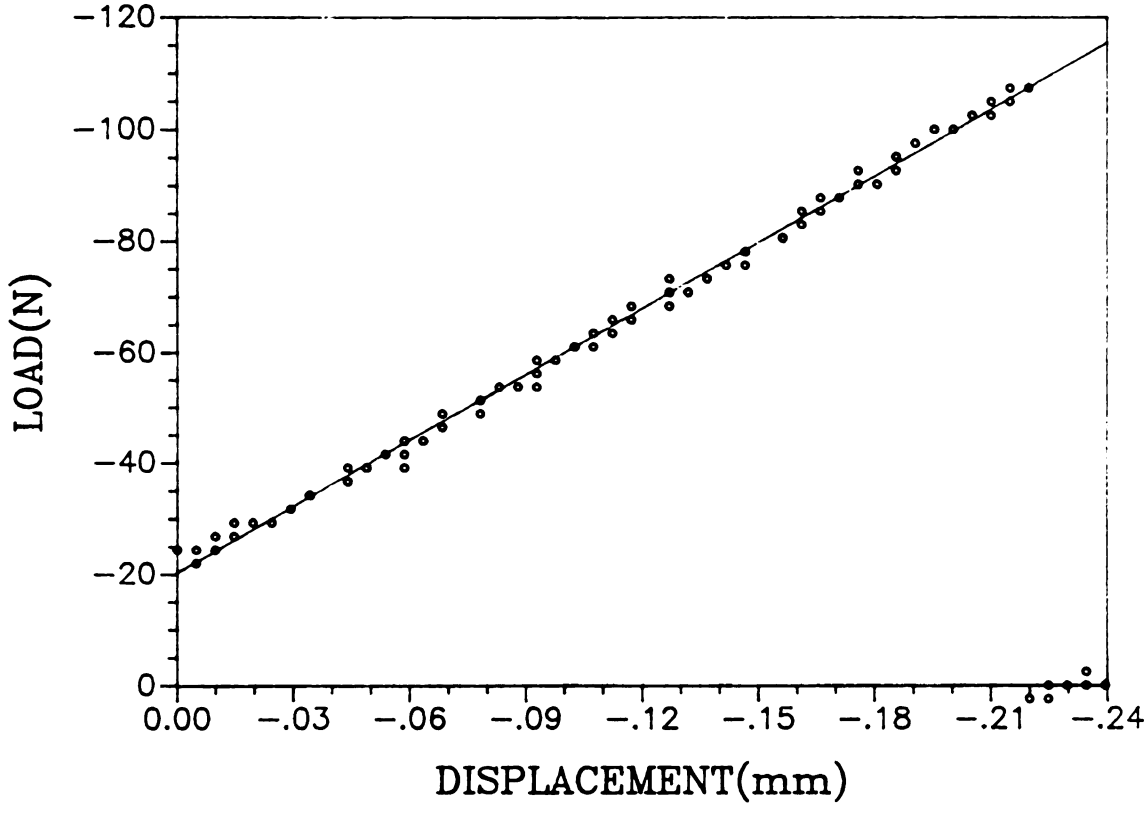

Figure 22. Load-displacement curve for Macor specimen

obtained as 57.12 GPa (equation 9). The dynamic Young's modulus of Macor measured by the sonic resonance method ranged from 61.6 to 63.4 GPa (Table 10), which was several percent higher in value than the static Young's modulus. Generally the modulus measured by dynamic method is reported to be higher by a few percent that the modulus measured by static method [147] (Appendix A).

3.1.2.4 Thermal Shock Fatigue of Macor Glass-Ceramic

For the Macor glass-ceramic specimens, decrement in Young's modulus and increment in internal friction upon thermal cycling were fit to the equations given in figure 23 and 24. E_o and Q_o^{-1} refer to the undamaged Young's modulus and internal friction, respectively. Thermal fatigue parameters A, α, B and β (table 10) were calculated from the Young's modulus and internal friction data using non-linear regression.

For a given ΔT, A and B represent the difference (for Young's modulus and internal friction, respectively) between the undamaged state and the steady state level of damage (damage saturation) (figure 3). A constant α measures the rate of decrease in Young's modulus and a constant β measures the rate of increase in internal friction.

The Young's modulus decrement as a function of cumulative thermal shock cycles reached a steady state value for specimens shocked at ΔT= 200, 300 and 350 °C. Specimens shocked at ΔT=400 and 450 °C showed a two-stage decrease after exhibiting an initial damage saturation at

Table 10. Thermal fatigue results for Macor glass-ceramics see figure 25. for schematic of the parameters relating to thermal fatigue damage

Specimen Label	MA-1	MA-2	MA-3	MA-4	MA-5	MA-6
$\Delta T(C)$	200	300	350	400	450	500
E_o (GPa)	61.7	63.3	63.4	62.4	62.2	61.6
A (GPa)	0.53	1.41	1.63	2.76	3.91	4.12
$A/E_o (x10^{-3})$	8.55	22.2	25.3	44.2	62.9	66.8
α	0.004	3.60	2.39	0.475	1.16	0.964
Q_o^{-1} $(x10^{-4})$	2.32	2.30	2.18	2.10	3.79	1.53
B $(x10^{-4})$	1.64	6.13	7.13	10.2	13.0	12.9
B/Q_o^{-1}	0.706	2.67	3.26	4.84	3.43	8.46
β	0.132	2.51	2.34	0.731	0.263	3.64

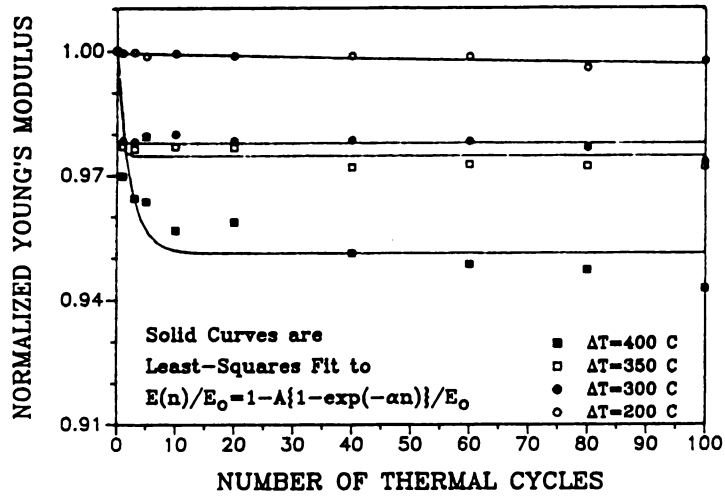

(a)

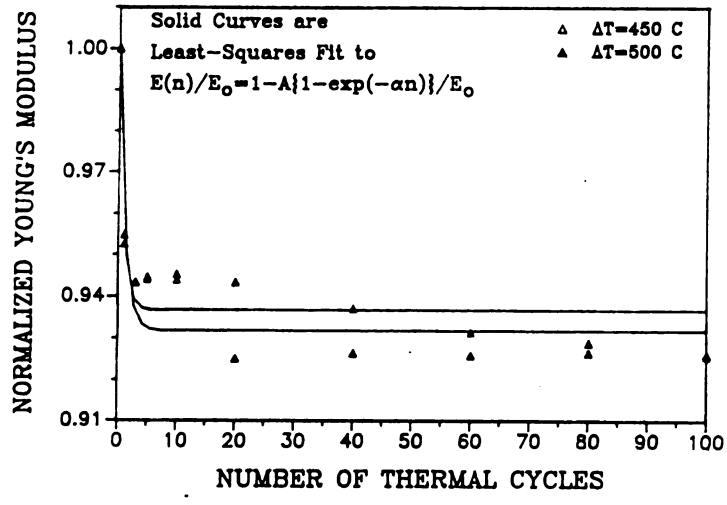

(b)

Figure 23. Young's modulus of Macor glass-ceramics as a function of the cumulative number of thermal shock cycles.
(a) ΔT=200, 300, 350 and 400 °C (b) ΔT=450 and 500 °C

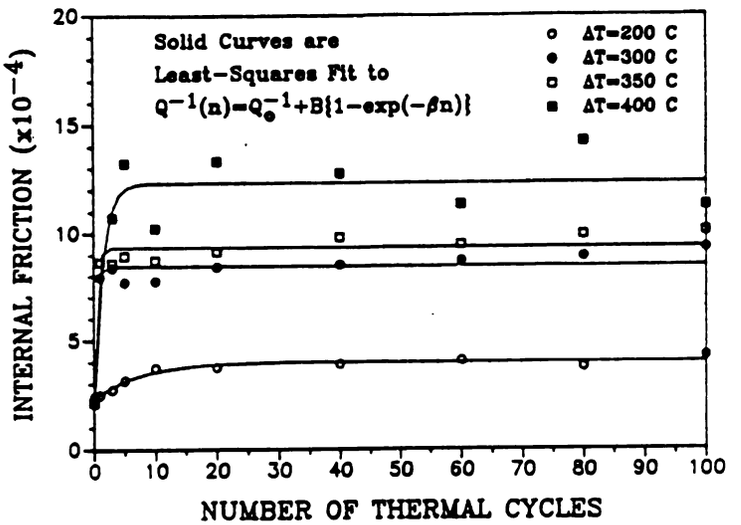

(a)

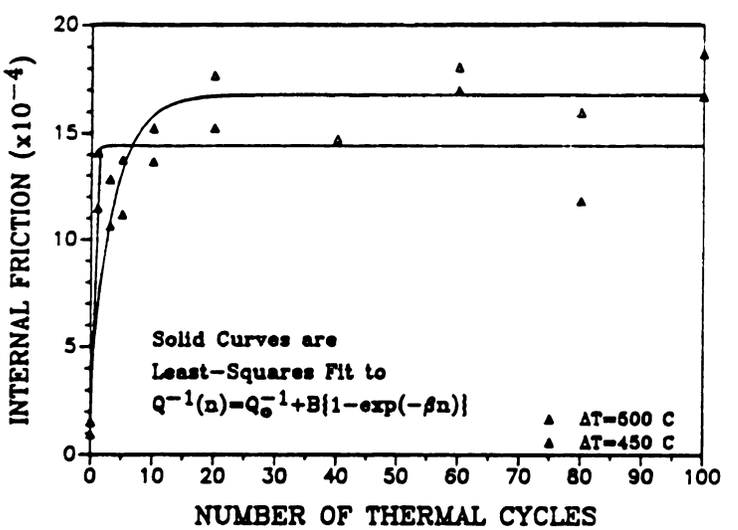

(b)

Figure 24. Internal friction of Macor glass-ceramics as a function of the cumulative number of thermal shock cycles. (a) ΔT=200, 300, 350 and 400 °C (b) ΔT=450 and 500 °C

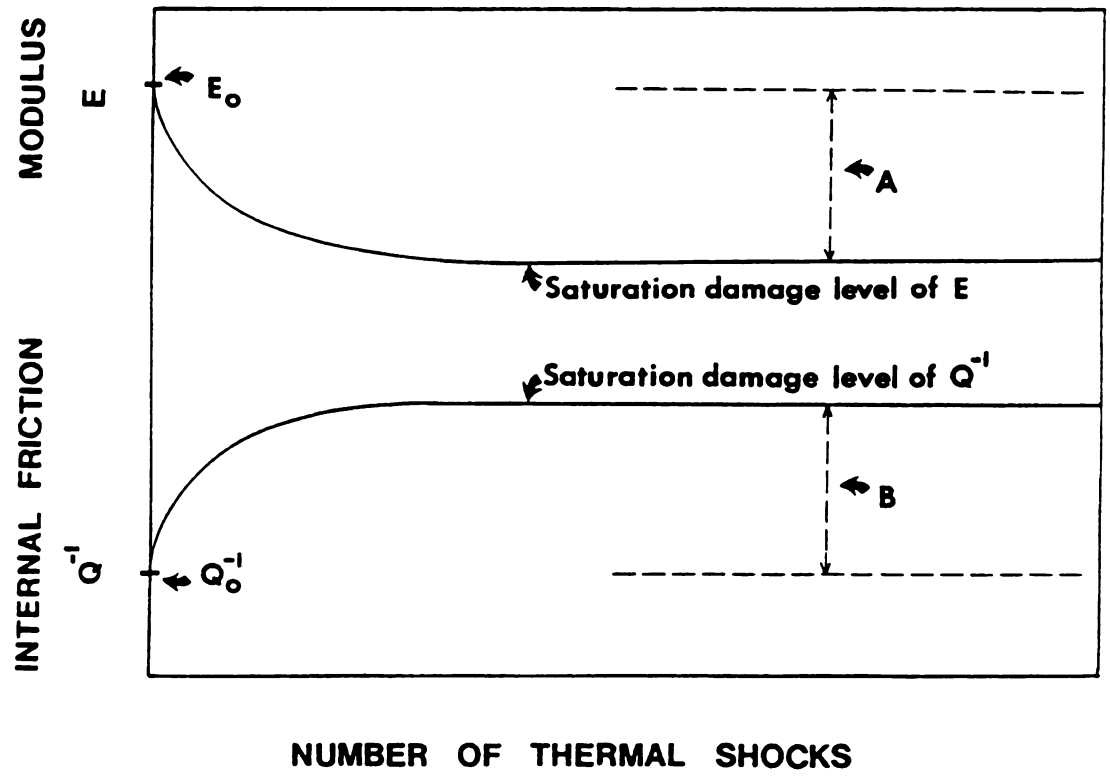

Figure 25. Schematic of Young's modulus decrease and internal friction increase with microcrack damage induced by thermal cycling.

twenty thermal shock cycles. For specimen shocked at ΔT=500 °C, a sharp decrease in Young's modulus was observed between the tenth and the twentieth shock, followed by another damage saturation regime.

This multi-stage thermal fatigue behavior may result from microcracking and microcrack coalescence resulting from the superposition of: (1) short range stress due to thermal expansion mismatch between the dispersed mica crystals and matrix phase and (2) the macroscopic thermal gradient stress induced by quenching in deionized water [137]. Damage saturation behaviors for ΔT=200, 300 and 350 °C may reflect microcrack arrest at interlocked micrometer scale mica flakes in the Macor. The multi-stage Young's modulus decrease for ΔT=400 and 450 °C specimens may indicate progressive crack extension over the mica flake crack arrester.

In this study, the Young's modulus for unshocked Macor specimens (table 10) was approximately 64 GPa [146] as measured by sonic resonance method and 57.5 GPa as measured quasistatically from beam deflection. Since static modulus determinations of Young's modulus are typically about 10 percent lower than dynamically determined moduli, the agreement between the static and dynamic determinations was acceptable.

3.1.2.5 Comparison of thermal fatigue damage in Macor glass-ceramics with SiC fiber/AS, SiC whisker/alumina and polycrystalline alumina

SiC fiber reinforced AS [22], SiC whisker reinforced alumina [24] and unreinforced polycrystalline alumina [25], showed a rapid change

in thermal shock damage as a function of an increasing number of thermal shock cycles. Changes in damage then leveled off, reaching a "saturation" as the cumulative number of thermal shock cycles increased (figure 25). The saturation value increased as thermal shock temperature difference increased.

For the SiC fiber/AS composite, the SiC whisker/alumina composite and alumina, the present authors have developed a power law relationship between the saturation damage level and thermal shock temperature difference which implies a fatigue-like power law relation in terms of thermal stress induced by repetative thermal shocking [22, 24, 25]. For Macor glass-ceramics, the SiC fiber/AS composite [22], the SiC whisker/alumina composite [24], and the polycrystalline alumina [25], log-log plots of the normalized saturation values (A/E_o and B/Q_o^{-1}) in figure 26 showed a power law relationship with nondimensional temperature difference, $\Delta T/T_r$ namely [22, 24, 25]

$$A/E_o = j1(\Delta T/T_r)^{p1} \tag{38}$$

$$B/Q_o^{-1} = j2(\Delta T/T_r)^{p2} \tag{39}$$

where T_r, is a reference temperature (293 K). ΔT, the temperature difference between the furnace temperature and the water bath temperature, was expressed in terms of degrees K (figure 26). Since ΔT is linearly related to the induced thermoelastic stress [1] for brittle materials, the power law relationship between the saturation

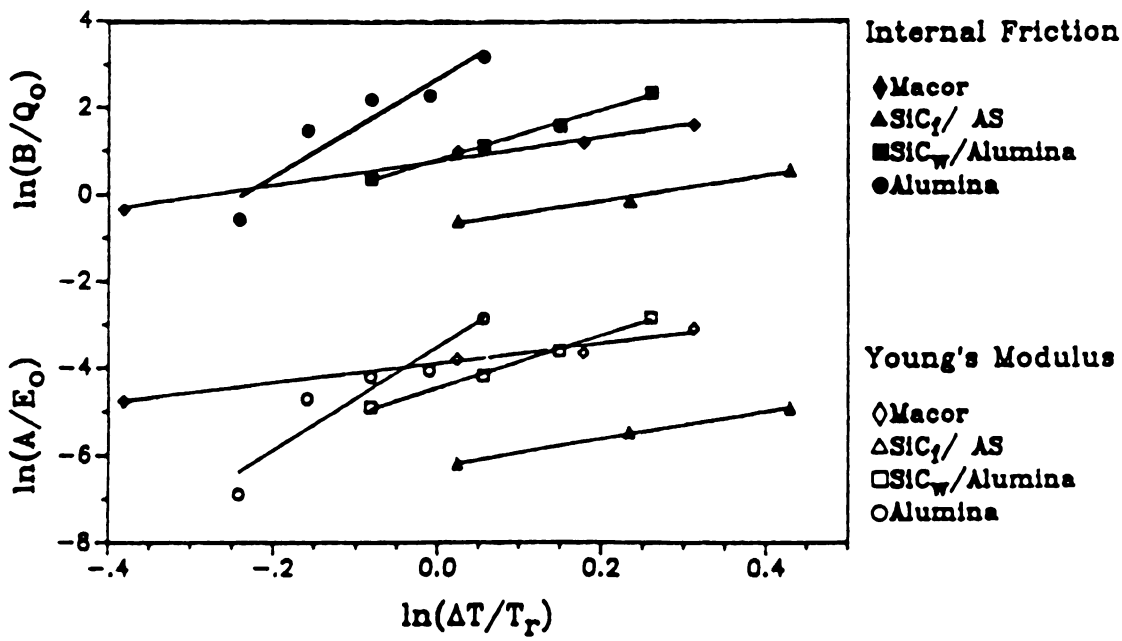

Figure 26. Logarithm of the normalized saturation damage parameters (A/E_0) and (B/Q_0^-) versus logarithm of the normalized temperature.

damage level and thermal shock difference implies a fatigue-like power law relation in stress. Recent work by other researchers [143, 144] has shown that crack extension due to repeated purely mechanical loading of ceramics can be described in terms of similar power law equation in stress.

In addition to the fatigue-like relations, the present authors have shown that changes in internal friction can be approximated by the linear equation, $\Delta Q^{-1} = D\epsilon$, where D is constant for low damage levels in polycrystalline alumina, SiC fiber/AS and SiC whisker/alumina composites (figure 27). For Macor glass-ceramics, the ΔQ^{-1} versus ϵ plot is also linear at lower damage levels. Scatter observed in the ΔQ^{-1} versus ϵ plot at higher damage levels may be due to extensive linkup of microcracks in the Macor specimens, as in the case of polycrystalline alumina [25].

3.1.2.6 Thermal fatigue results and their relation to thermal resistance parameters R''', R'''', and R_{st}

As material undergoes a rapid changes in temperature, sufficient stresses may develop for crack extension. Resistance to cracking is classically termed thermal shock resistance [2]. Thermoelastic analysis, which involves the initiation of cracks, yields thermal shock resistance parameters (R and R' [2]) which are not appropriate for thermal fatigue. However stored elastic energy analysis relates the stability of pre-existing cracks to Griffith's energy balance, where the thermal shock resistance parameters include R''', R'''' and

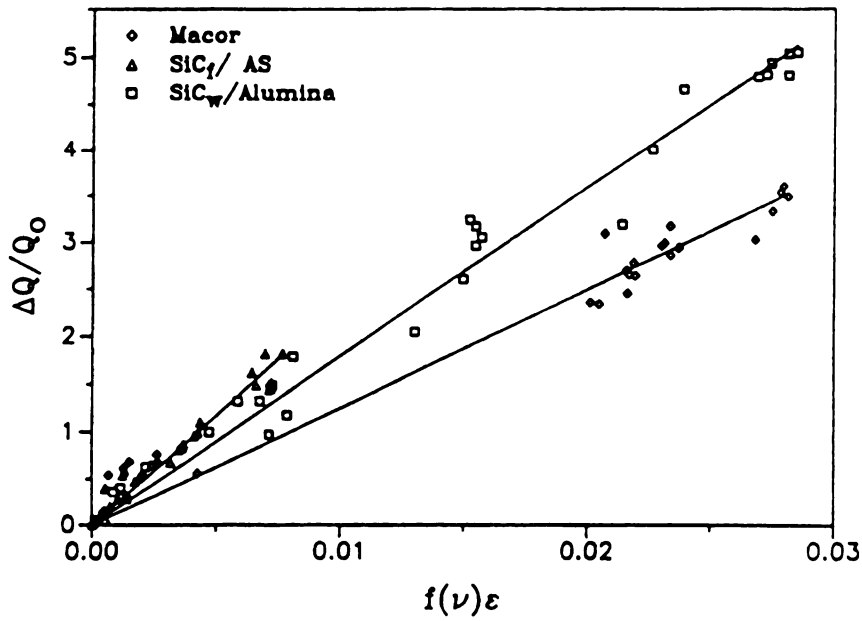

Figure 27. ΔQ^{-1} as a function of crack damage parameter for Macor glass-ceramics, SiC fiber/AS and SiC whisker/alumina composites.

R_{st}, which are

$$R''' = E/\sigma_f^2 (1-\nu) \tag{3}$$

$$R_{st} = K_{IC}(1-\nu^2)^{1/2}/E\theta \quad \text{(in plane stress)} \tag{40}$$

and $$R'''' = K_{IC}^2(1+\nu)/\sigma_f^2 \quad \text{(in plane stress)} \tag{41}$$

where σ_f = fracture strength

ν = Poisson's ratio

E = Young's modulus

θ = thermal expansion coefficient

K_{IC} = critical stress intensity factor

R_{st} measures the resistance of material to thermal shock damage by quasistatic crack growth. R''' (which does not contain a fracture energy term) and R'''' (which does), are measures of the resistance of material to thermal shock damage by kinetic crack growth. The thermal shock resistance parameters R''', R_{st}, and R'''', the empirical exponents p1 and p2 as well as material properties E, σ_f, θ, k, ν and K_{IC} are compared in table 11 for the four materials considered in this study.

An approximately hyperbolic relationship between p^1 and R'''' was observed (figure 28 and 29), such that

$$p^n_1 R'''' = C = \text{constant} \tag{42}$$

Table 11. Materials properties, thermal shock resistance parameters, and empirical exponent for the four materials included in this thermal fatigue study

Property+++	Alumina	SiC_w/Al_2O_3	SiC_f/AS	Macor
σ_f (MPa)	350* 320 [148]*	620 (148)*	800 (133)* 700 (149)**	90 * 103 (146)+
ν	0.23	0.22		0.26
θ ($\times 10^{-6}$ C)	8.2 (148)	7.35 (148)	2.2 (149)	11 (46)
E (GPa)	335	405	135	63
k (W/mK)	32.3 (148)	35.2 (148)	1.46 (149)	1.7 (152)
K_{IC}(MPa $m^{1/2}$)	2.75 ++ 2.5-5 (150)	6 ++ 5.6-8.7 (151)		2 ++ 1.6-1.8 (152)
$R'''(1-\nu)$	2.73	1.054	0.211	7.78
$R_{st}/(1-\nu^2)^{1/2}$	1	2	57	3
$R''''/(1+\nu)$	61.7 (μm)	93.6 (μm)	450 (μm)	490 (μm)
p1, p2	11.8, 11.3	6.0, 5.7	3.1, 2.8	2.7, 2.4
A/E_0(ΔT=300)	0.040	0.014	0.002	0.022
B/Q_0^{-1} (ΔT=300)	19.33	2.55	0.55	2.12

*** All the material properties without parenthesis were measured in this study. Thermal shock resistance parameters were calculated from the measured materials properties.

* Four point bend test.

** Three point bend test.

\+ Tensile strength.

++ K_{IC} was measured by indentation method.

+++ σ_f, ν, θ, E, K_{IC}, R''', R_{st}, and R'''' are defined in equations 3, 39, 40. p1, p2, A/E_0 and B/Q_0^{-1} are defined in equations 37 and 38, and k is thermal conductivity.

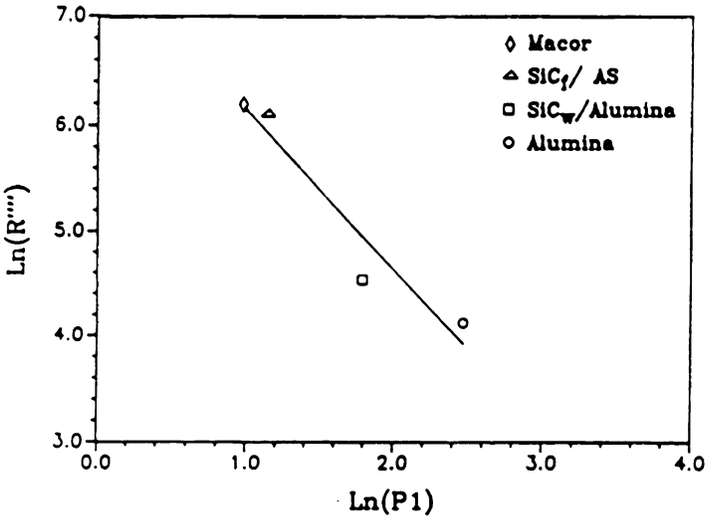

Figure 28. Logarithm of thermal shock damage parameter, R'''' versus Logarithm of thermal fatigue exponent, p1

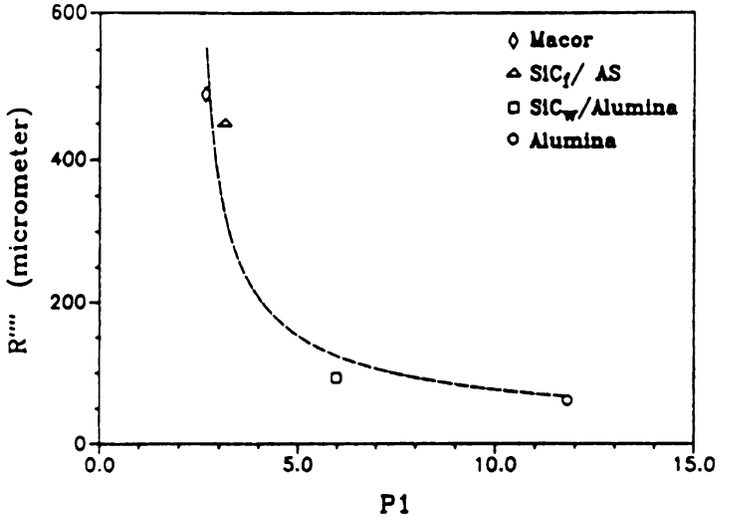

Figure 29. Thermal shock damage parameter, R'''' versus thermal fatigue exponent, p1

If R'''' is expressed in units of microns, a least square best fit gives n = 1.5 and C = 2090 microns with correlation coefficient 0.96. p1 was used to obtain a hyperbolic relationship between thermal fatigue exponent and R''''. Since p1 and p2 are approximately the same for each material tested (table 11), equation 42 would not change significantly if p2 were used in place of p1. Although this preliminary empirical p1-R'''' relationship requires further study, it suggests a useful guideline to compare these two parameters, where p1 and p2 arise out of recent thermal fatigue studies by the present authors [22, 24, 25] and the classical R'''' parameter was generated from "single quench and fracture" thermal shock testing protocols for ceramics [2]. In addition, since R'''' is a function of K_{IC} and σ_f, equation 42 indicates a link between the fatigue exponent p1 and p2 and material parameters such as fracture toughness.

3.1.2.7 Thermal Fatigue in Polycrystalline Titanium Diboride

Unshocked (annealed) Young's modulus values, E_0, (Table 12) measured in this study agree reasonably well with data of 497.3 to 504.8 GPa for 91.9 to 92.8 percent of theoretical density reported by Wiley et al. [199] using the same method as used in this study. But Young's modulus of TiB_2 of 240.2 GPa reported by Vahldiek [200] using the pulse-echo method were different significantly from the data obtained in this study. Internal friction data for unshocked specimens, Q_0^{-1}, were measured from 0.84×10^{-4} to 1.32×10^{-4}.

Table 12. Non-linear regression results of Young's modulus as a function of the number of thermal shock cycles.

Specimen	ΔT (°C)	E_0 (GPa)	A (GPa)	α	Correlation coefficient
T-200	200	547.18	0.74	0.065	0.706
T-250	250	552.48	2.21	0.012	0.928
T-300	300	561.11	20.28	0.164	0.979
T-400	400	534.11	21.22	0.267	0.867
T-500	500	586.76	33.85	0.245	0.949

For hot pressed titanium diboride, the Young's modulus, E, decreased monotonically with n, the cumulative number of thermal cycles (figure 30), as described by the equation 34.

Thermal fatigue parameters A and α (Table 12) were calculated on the E(n) data using non-linear regression. For a given ΔT, A represent a steady state level of damage (damage saturation) for a large number of cumulative thermal shock cycles, n.

The constant α measures the rate of decrease in Young's modulus. Young's modulus did not change significantly for the specimens with ΔT of 200 and 250 °C even after 100 cumulative thermal shock cycles. But Young's moduli of the specimens for ΔT of 300, 400, and 500 °C decreased monotonically (figure 30). The Young's moduli reached a saturation value although the values of Young's moduli showed fluctuations after 20 th thermal shock cycle.

Internal friction for the specimens with ΔT of 200 and 250 °C did not change significantly up to 100 cumulative cycles (figure 31). For the specimens of ΔT = 300, 400, and 500 C, internal friction increased after first shock but the values of internal friction showed fluctuations.

The thermogravic analysis of the TiB_2 suggests that the oxidation of TiB_2 specimens may be responsible for the fluctuations in internal friction and Young's modulus values (figure 32).

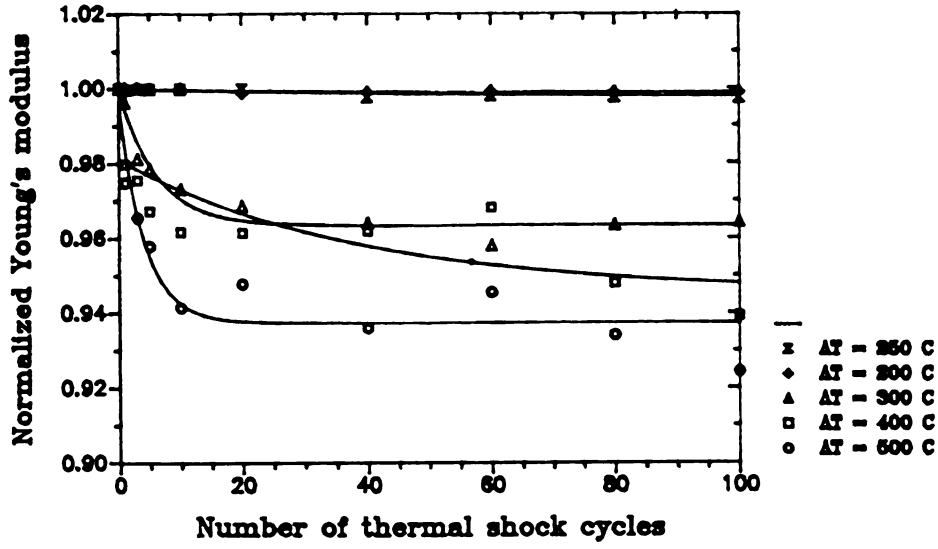

Figure 30. Young's modulus of polycrystalline titanium diboride as a function of the cumulative number of thermal shock cycles.

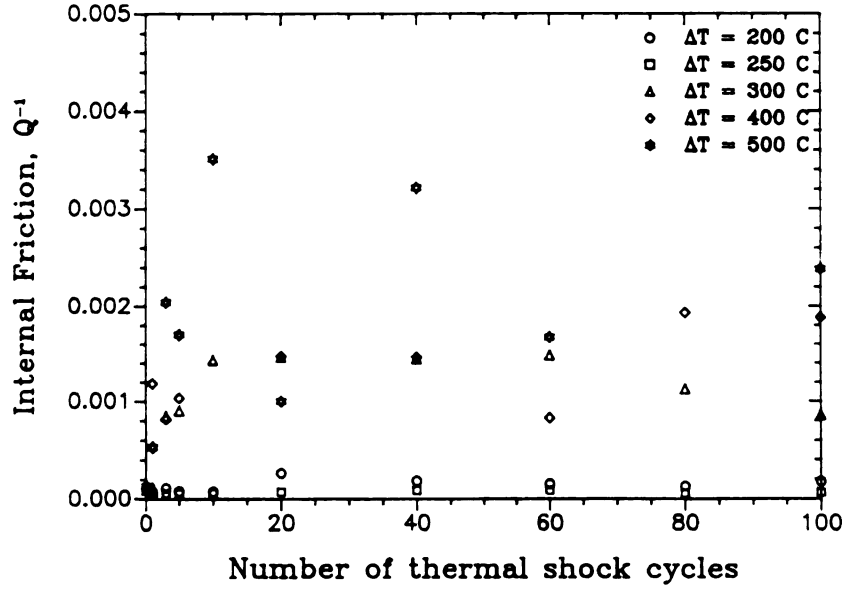

Figure 31. Internal Friction of polycrystalline titanium diboride as a function of the cumulative number of thermal shock cycles.

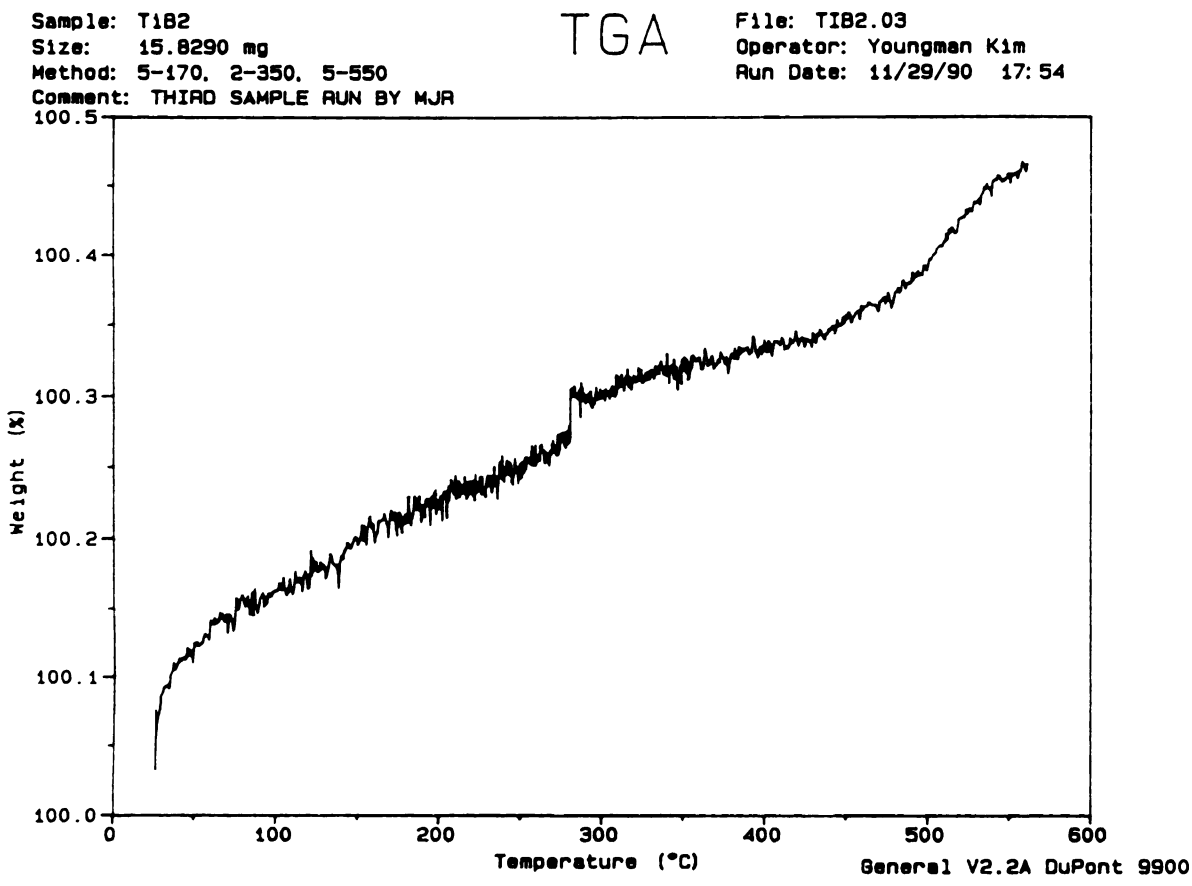

Figure 32. TGA Results for TiB_2 specimen.

3.1.2.8 The relation of A, B, α, and β to material properties

Previous thermal fatigue studies of Macor glass-ceramic [23], SiC whisker reinforced alumina [24], unreinforced polycrystalline alumina [25], and SiC fiber reinforced aluminosilicate [22], found the rate constants α and β, and the damage saturation (A/E_0 and B/Q_0^{-1}) increased as the thermal shock severity increased. Since for small values of n, the cumulative number of thermal shocks, $A\alpha$ (or $B\beta$) is the slope of the E (or Q^{-1}) versus n curve, the product $A\alpha$ is more meaningful than A or α itself. Since the normalized thermal shock damage saturation levels A and B are functions of ΔT (equations 38 and 39), and rate constants α and β are also functions of ΔT (Table 10), we selected a fixed ΔT of 300 C for the plots of $A\alpha$ and $B\beta$ versus strength and fracture toughness (figure 33). When $A\alpha = 0$ or $B\beta = 0$, then from the definitions of α, β, A and B, we would not expect damaged to be induced by repeated thermal cycling. Thus intercept values on the fracture toughness axes (figure 33) may represent a threshold fracture toughness level, above which the material would not suffer damage upon repeated thermal shock cycling at the corresponding ΔT. (Figure 33, as noted above, was constructed from the ΔT=300 °C data.) Thus, in addition to the fatigue exponent p1 and p2 (as discussed in the previous section), the thermal fatigue parameters $A\alpha$ and $B\beta$ are functions of the fracture toughness or strength of the material.

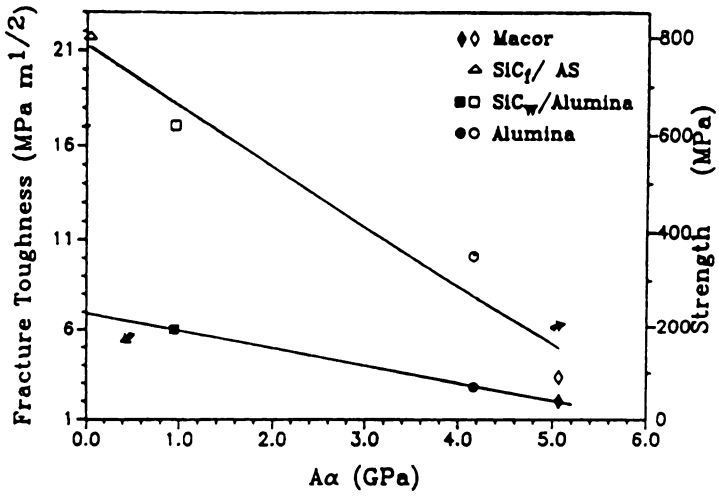

(a)

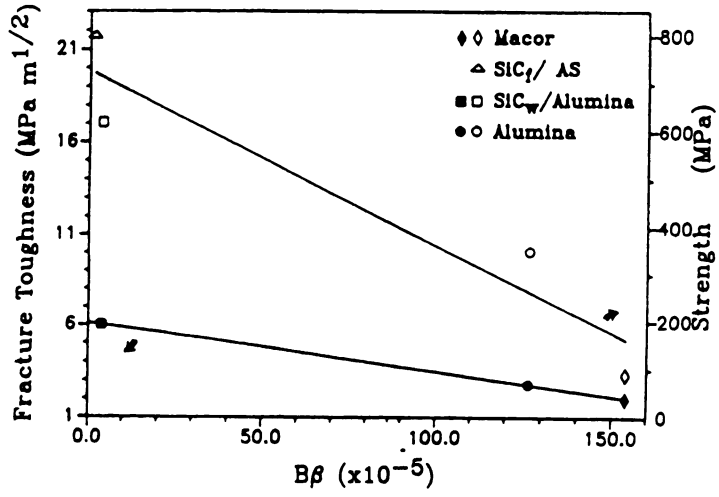

(b)

Figure 33. Fracture toughness and strength versus products thermal fatigue constants (a) $A\alpha$ and (b) $B\beta$

3.1.3 Elevated Temperature Elastic Modulus and Internal Friction Measurement

To calculate Young's modulus at an elevated temperature, a valid thermal expansion coefficient is required. The Young's modulus, shear modulus and thermal expansion coefficient of SiC fiber and LAS matrix were reported [140, 153] as E_f = 200 GPa, E_m = 88 GPa, G_f = 77 GPa, G_m = 36 GPa, $\alpha_f = 3.93 \times 10^{-6}$/°C, $\alpha_m = 1 \times 10^{-6}$/°C [153]. The value of α_m is based on a fully crystallized LAS matrix of β-spodumene. The value of α_m may be higher if the matrix contains a considerable amount of glassy phases and may be lower if the matrix forms β-spodumene-silica solid solution [153]. Poisson's ratio, ν, of a homogeneous isotropic material $\nu = E/2G - 1$. Using the known values for the Young's and shear moduli of the fiber and matrix, and assuming that the matrix and fiber materials are homogeneous and isotropic, Poisson's ratio of SiC fiber and LAS matrix were calculated as $\nu_f = 0.30$, $\nu_m = 0.22$.

Since the SiC fiber is aligned in the longitudinal direction (0^0), both the longitudinal and the transverse thermal expansion coefficients of the composite should be calculated. The longitudinal thermal expansion coefficient of fiber reinforce composites, α_ℓ, is given by [154],

$$\alpha_\ell = (E_m \alpha_m v_m + E_f \alpha_f v_f)/(E_m v_m + E_f v_f) \qquad (43)$$

where E_m, E_f = Young's modulus of matrix and fiber respectively

α_m, α_f = thermal expansion coefficient of matrix and fiber respectively

v_m, v_f = volume fraction of matrix and fiber respectively

The longitudinal thermal expansion coefficient was calculated to be 2.61×10^{-6}/C using equation 43 and the values of E_m, E_f, α_m, α_f, v_m=0.65, v_f=0.35 (The composite contains 35 volume percent of fiber). The calculated α_ℓ was put into equation 14 to obtain elevated temperature Youmg's modulus, E^T.

In addition, the transverse thermal expansion coefficient of uniaxially reinforced fiber composites, α_t, is given by [154]

$$\alpha_t = (1+\nu_m)\alpha_m v_m + (1+\nu_f)\alpha_m v_m - \alpha_\ell(\nu_m v_m + \nu_f v_m) \qquad (44)$$

where E_m, E_f= Young's modulus of matrix and fiber respectively

α_m, α_f= thermal expansion coefficient of matrix and fiber respectively

v_m, v_f= volume fraction of matrix and fiber respectively

ν_m, ν_f= Poisson's ratio of matrix and fiber respectively

α_ℓ = longitudinal thermal expansion coefficient of uniaxially reinforced fiber composite

For 35 volume percent SiC fiber/LAS composite, α_t is 1.93×10^{-6}.

The Young's modulus of SiC fiber/LAS composite RLA 5.23 decreased contiously with increasing temperature (figure 34), which is usual for ceramics. Young's modulus decreased relatively sharply between 550 °C and 750 °C followed by a slowered decrease up to 950 °C which was the highest temperature in this experiment. The amplitude of the flexural resonance signal was very weak in the temperature range 550 - 750 °C.

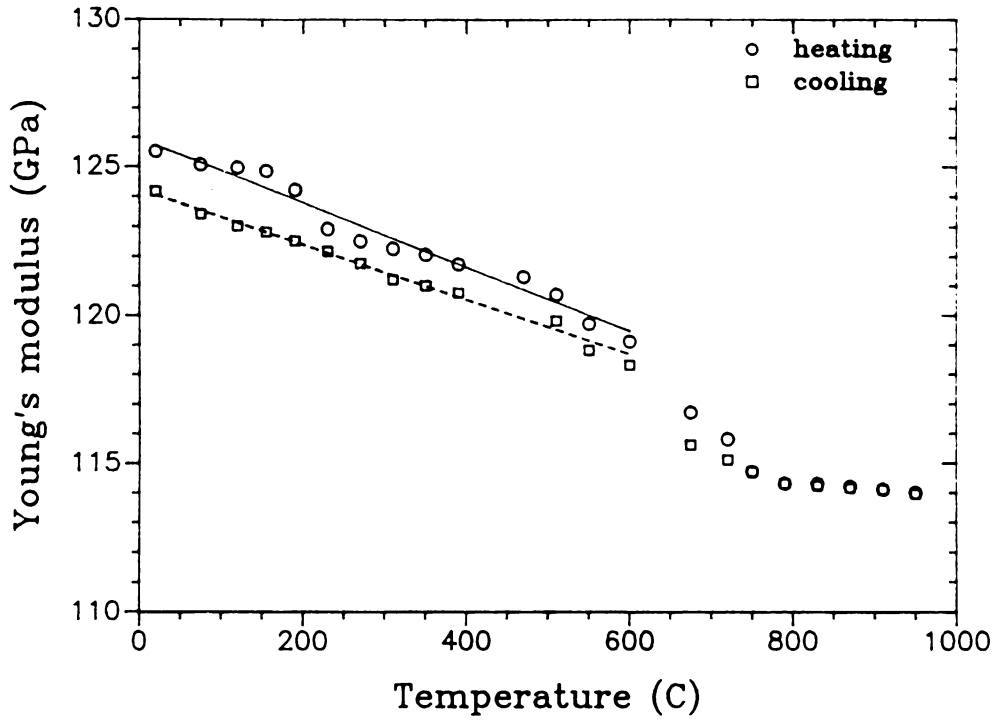

Figure 34. Young's modulus of SiC fiber-Aluminosilicate composite as a function of temperature.

The Young's modulus - temperature data pairs were analyzed using a linear regression to get an average Young's modulus changing rate with temperature between room temperature and 600 °C.

$$E = E(r.t.) + sT \tag{45}$$

where E(r.t.) = room temperature Young's modulus

s = slope of the modulus versus temperature

T = temperature Celcius degrees

The Young's modulus decreased with a average slope of 0.0108 GPa/°C on heating (with correlation coefficient of 0.961) and increased with a average slope of 0.0093 GPa/°C on cooling (with correlation coefficient of 0.994) within the range between room temperature and 600 °C. The normalized slope, S_n, which is a ratio of slope to room temperature Young's modulus was -8.606×10^{-5} /°C on heating and 7.491×10^{-5} /°C on cooling. The value of S_n obtained here appears to be reasonable by comparing the values of other researchers [35, 155, 156]. Generally Young's modulus measured is higher during cooling than during heating because of microcrack healing [35]. But the result from this study was the opposite. The room temperature modulus difference between heating up and after cooling down was 1.35 GPa which was 1.08 % of room temperature modulus.

The internal friction was also measured as a function of temperature during heating. The internal friction had increased

gradually from room temperature to 430 °C. At room temperature the internal friction was 22.67×10^{-5} and at 430 °C the internal friction was 37.19×10^{-5}. Between 430 °C and 750 °C no data could be recorded because of weak signal. However from 750 °C to 950 °C there was a gradual decrease in the internal friction from 32.87×10^{-5} to 28.20×10^{-5} (figure 35).

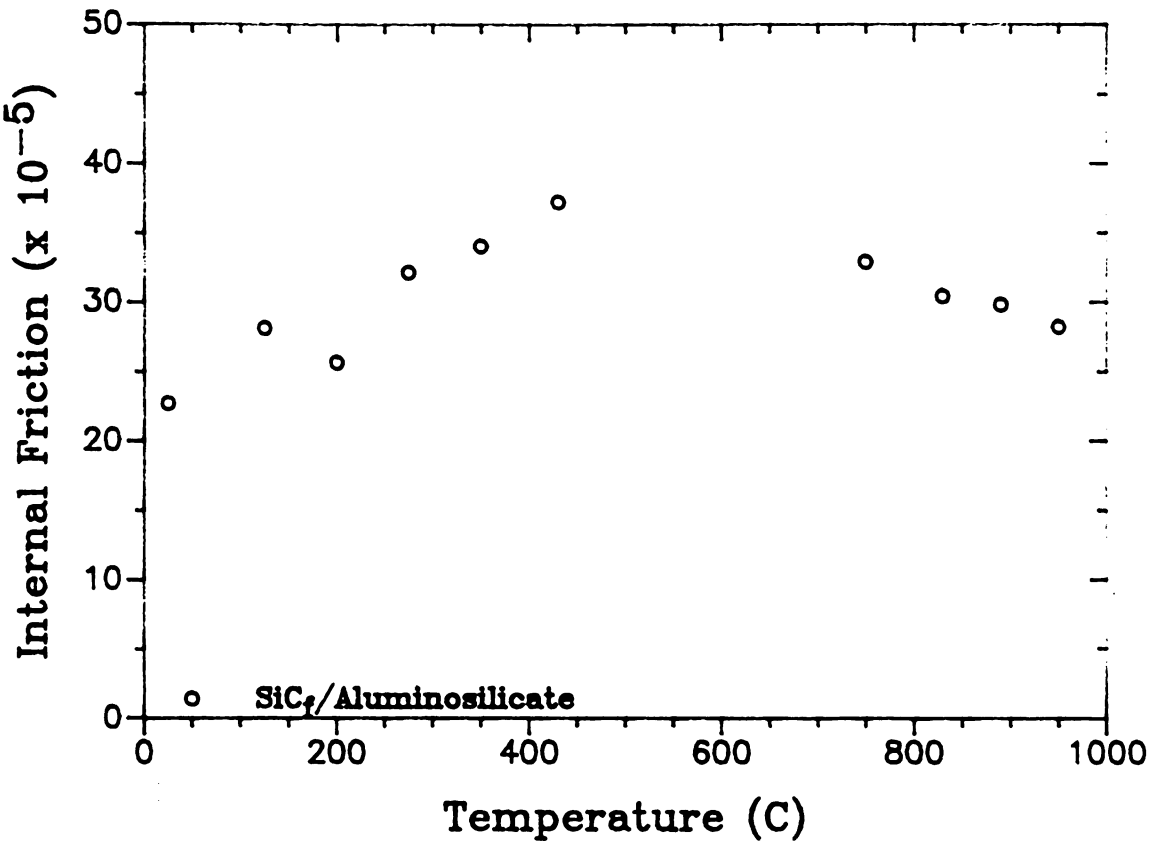

Figure 35. Internal friction of SiC fiber-Aluminosilicate composite as a function of temperature.

3.2. Time-dependent Elastic Modulus Recovery Measurement on Thermally Shocked SiC fiber/Aluminosilicate Composites, Machinable Glass Ceramics and Polycrystalline Alumina

3.2.1 Young's modulus recovery

The Young's modulus versus time data for the SiC fiber-AS composites (figure 36), Macor glass-ceramics (figure 37) and polycrystalline alumina (figure 38) were each fit to the following empirical equation using non-linear regression analysis [58].

$$E(t) = E_{t=o} + \Delta E \{1 - \exp(-\delta t)\} \qquad (46)$$

where E = Young's modulus at time t

$E_{t=o}$ = the Young's modulus at time t=0 (immediately following the thermal quench)

E_{sat} = E(t) for large time t (that is, the "saturated" value of E(t))

$\Delta E = E_{sat} - E_{t=o}$

δ = the modulus recovery time constant determined by non-linear regression on the modulus recovery data

t = time (in minutes) elapsed after the thermal shock

For each specimen of the three thermally shocked materials included in this study, linear regression on the Young's modulus

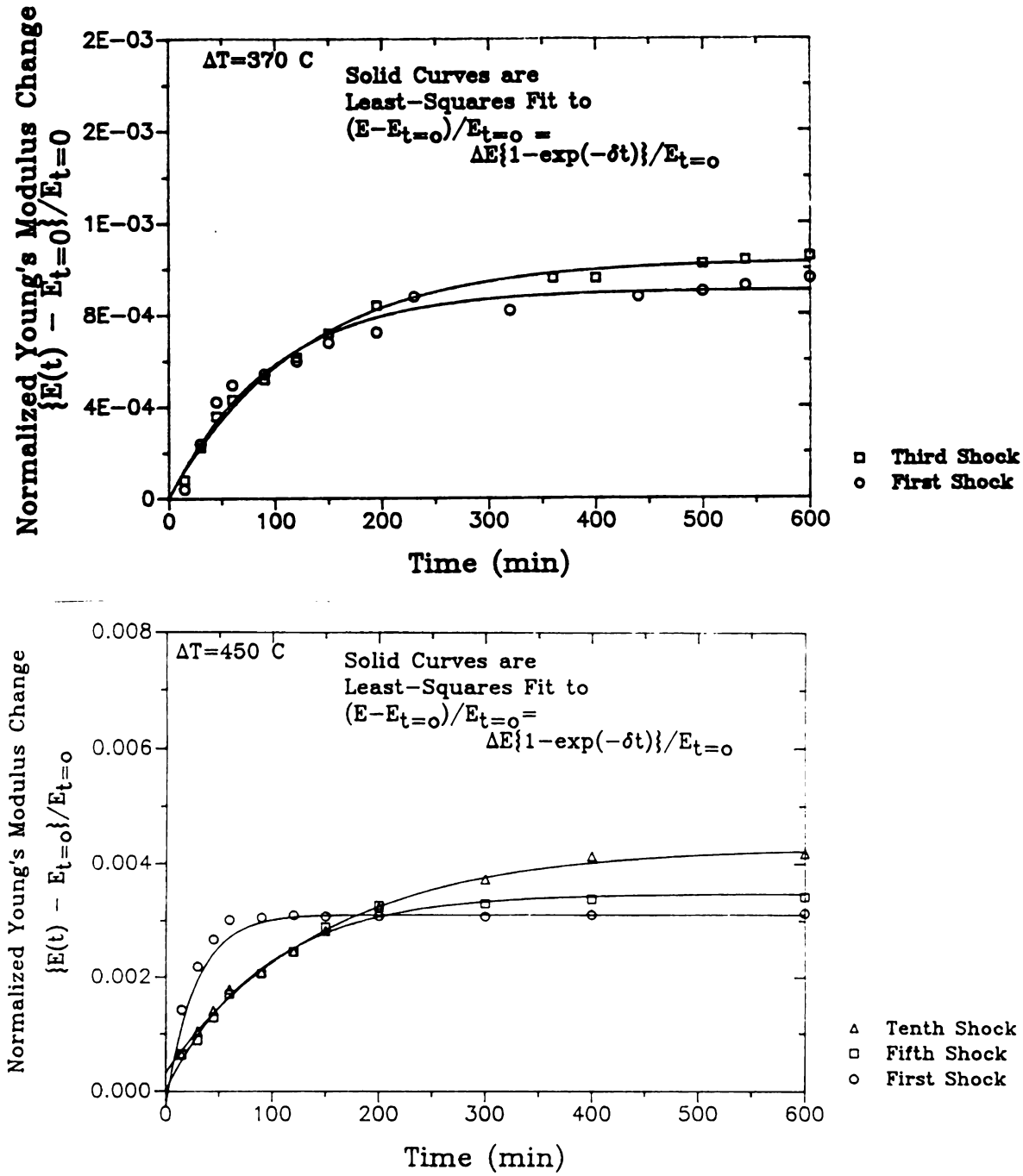

Figure 36. Normalized Young's modulus recoveries as a function of time for SiC fiber/Aluminosilicate specimen at (a) ΔT = 370 and (b) 450 °C.

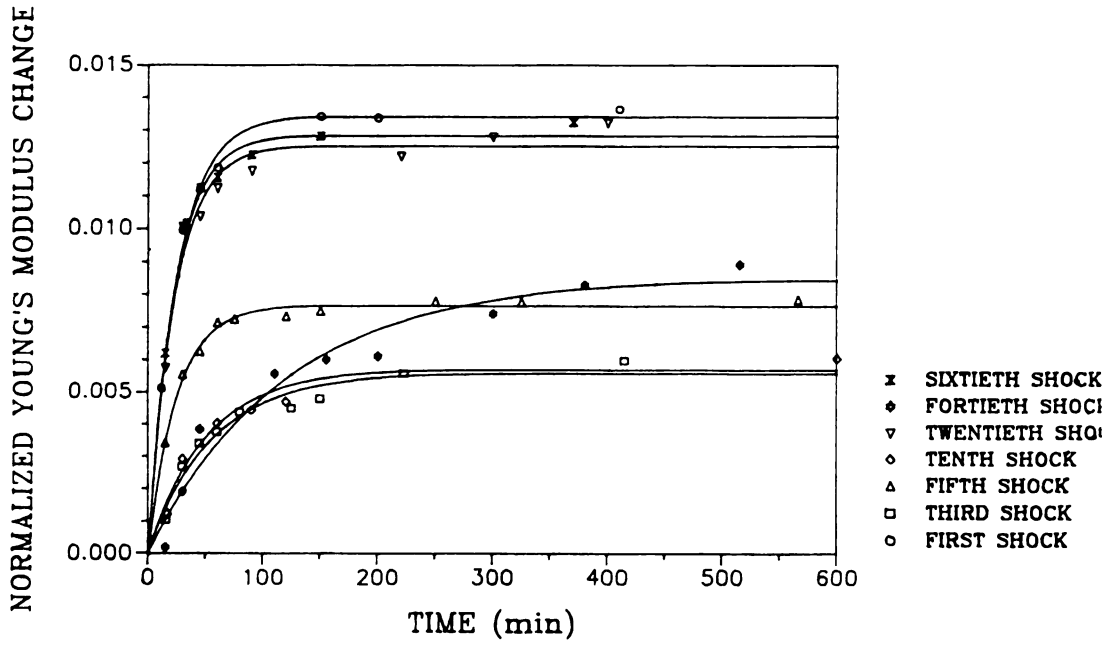

Figure 37. Normalized Young's modulus recoveries as a function of time for Macor glass-ceramic specimen at (a) ΔT = 300 °C.

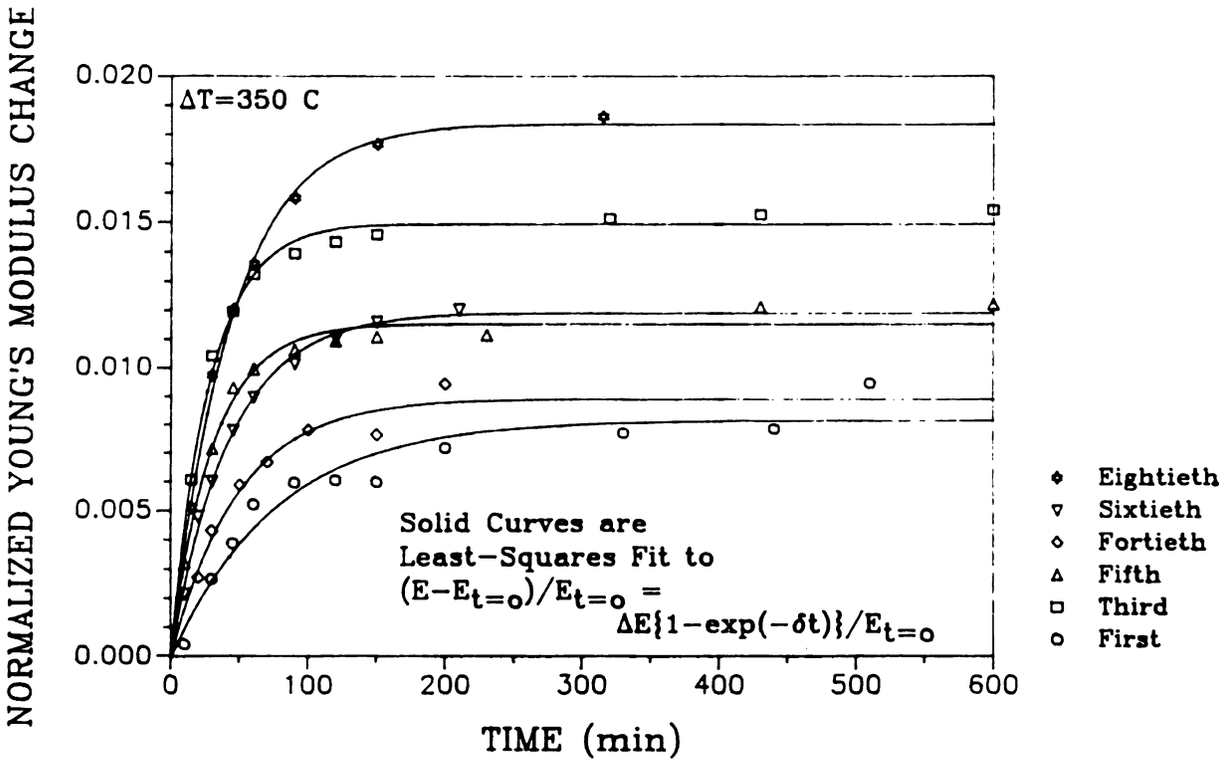

Figure 37. Normalized Young's modulus recoveries as a function of time for Macor glass-ceramic specimen at (b) ΔT = 350 °C.

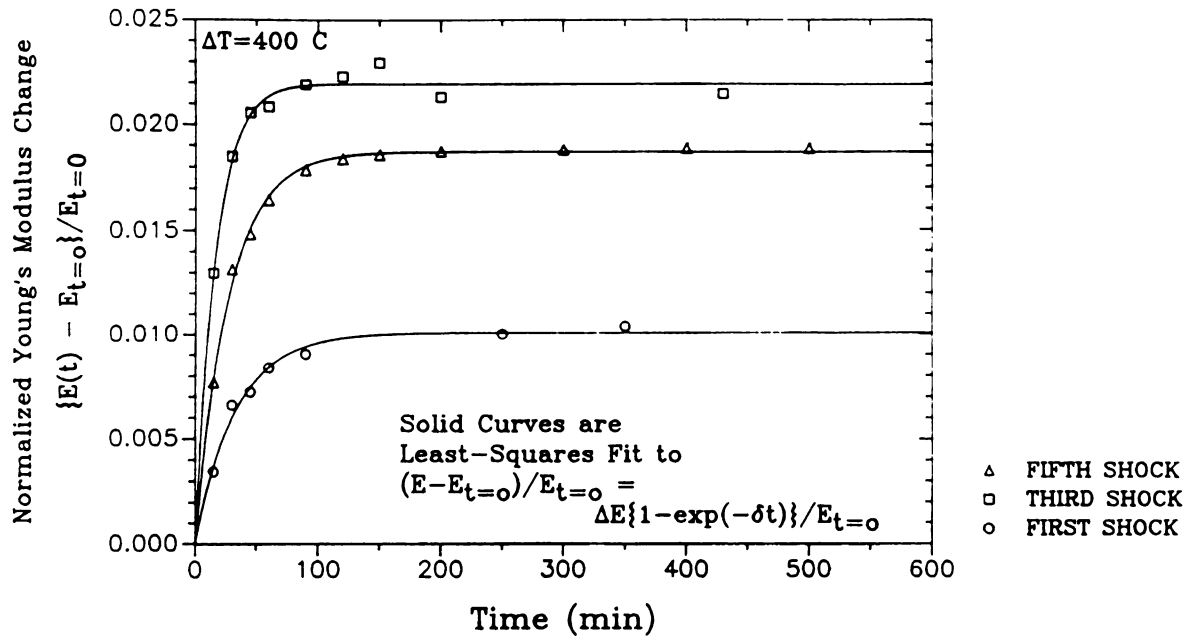

Figure 37. Normalized Young's modulus recoveries as a function of time for Macor glass-ceramic specimen at (c) ΔT = 400 °C.

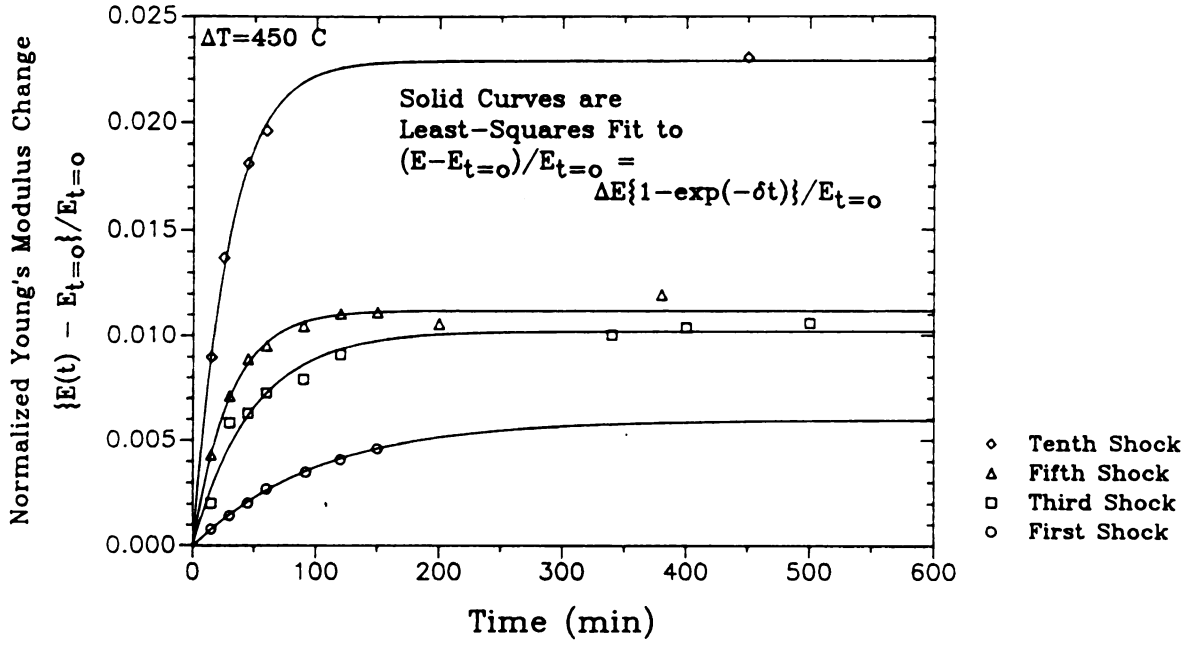

Figure 37. Normalized Young's modulus recoveries as a function of time for Macor glass-ceramic specimen at (d) ΔT = 450 °C.

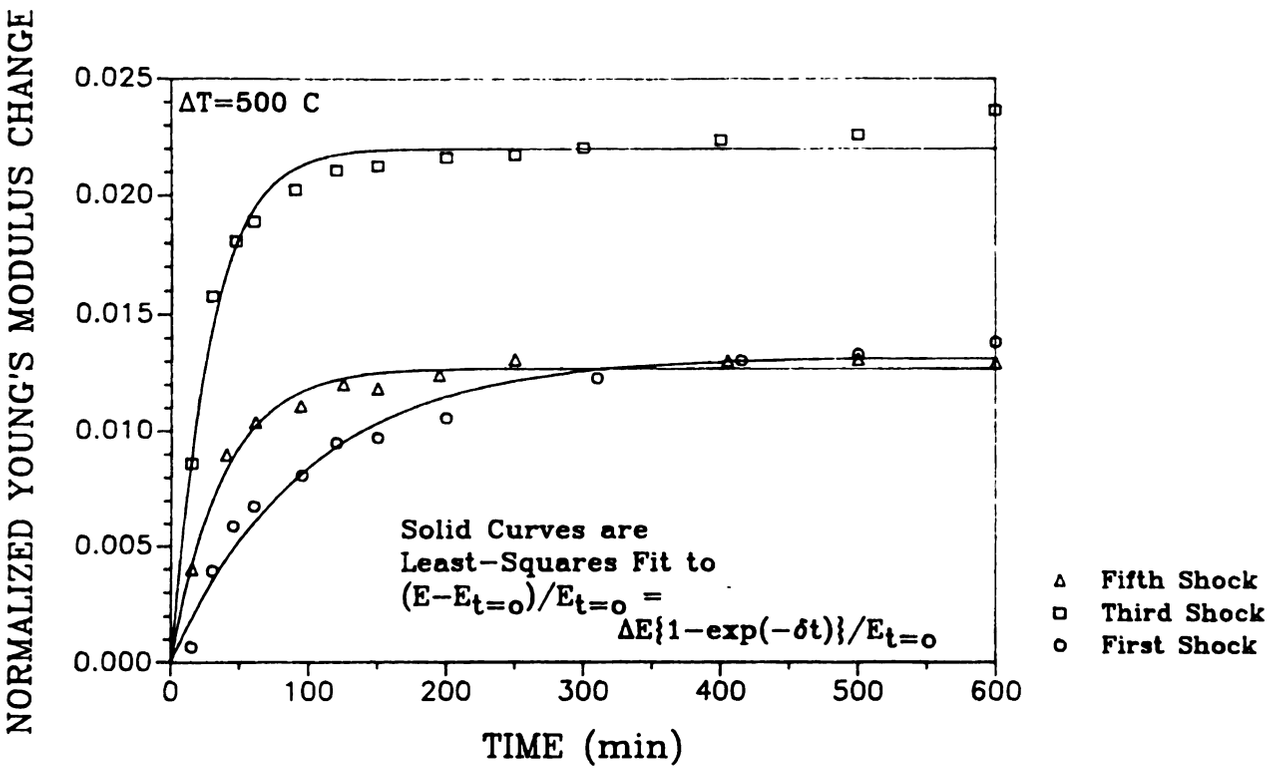

Figure 37. Normalized Young's modulus recoveries as a function of time for Macor glass-ceramic specimen at (e) ΔT = 500 °C.

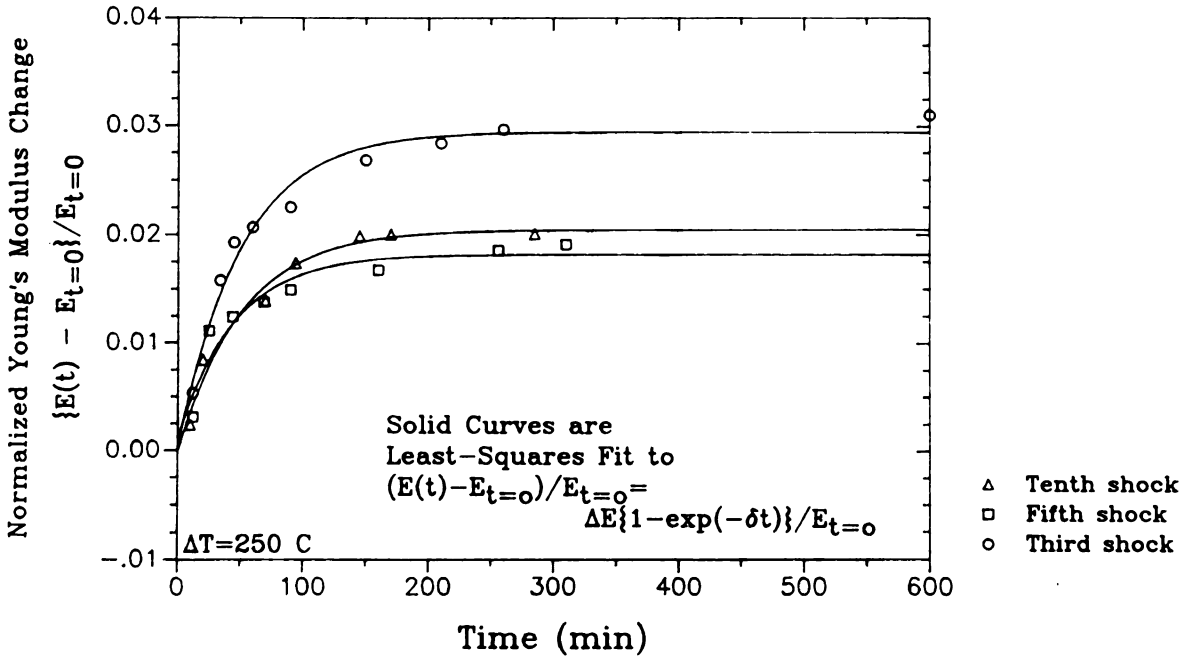

Figure 38. Normalized Young's modulus recoveries as a function of time for polycrystalline alumina specimen at ΔT = 250 °C.

recovery data showed that the modulus recovery with time was described well by equation 46 (with correlation coefficient higher than 0.949 for all the modulus versus time data). For each of the three materials, the Young's modulus recovery saturated (leveled off) for times approaching hundreds of minutes, and such saturation behavior is also in agreement with equation 46.

For the SiC fiber/AS composites, the modulus recovery time constant, δ and modulus $E_{t=o}$ decreased with an increasing the number of thermal shock cycles at a given ΔT (Table 13). The observed modulus recovery is very similar to that reported for modulus recovery in thermally shocked polycrystalline Yttrium Iron Garnet (YIG) [58]. However, for Macor (Table 14) and polycrystalline alumina (Table 15), the δ and $E_{t=o}$ values showed no consistent trend as a function of N, the number of thermal shock cycles.

It should be emphasized that for each of the thermal shock cycles for each of the specimens included in this study, the Young's modulus recovery was only partial. Never did the Young's modulus recover entirely to its pre-shocked value (Tables 12-15). In addition, E_{sat}, the value of E(t) for long times t (see equation 46 and Figures 36-38) decreased (on average) with an increase in the number of thermal shock cycles, N (Tables 13-15). Eventually, E_{sat} tended to a steady-state value as a function of N for each of the three materials included in this study (see Tables 13-15 and references 22, 23). The extent of the modulus recovery for a particular thermal shock cycle is shown in Tables 13-15 in terms of the ratio $\Delta E/(E_{un} - E_{t=o})$, where E_{un} refers

Table 13. The results of non-linear regression analysis of Young's modulus recovery versus time data for SiC fiber-AS composites

Specimen	Unshocked modulus E_{un}(GPa)	Number of thermal shocks, N	$E^{*}_{t=o}$(GPa)	E^{*}_{sat}(GPa)	$\Delta E/(E_{un}-E_{t=o})$	$\delta^{*}(min^{-1})$
RLA 5.14 (ΔT=450C)	132.72	1	132.05	132.51	68.7 %	0.0466
		5	131.70	132.16	45.1 %	0.0107
		10	131.35	131.87	38.0 %	0.0066
RLA 5.22 (ΔT=370C)	125.44	1	125.24	125.36	60.0 %	0.0061
		3	125.26	125.39	72.2 %	0.0058

* Refer equation 46.

Table 14. The results of non-linear regression analysis of Young's modulus recovery versus time data for Macor glass-ceramics

Specimen	Unshocked modulus E_{un}(GPa)	Number of thermal shocks, N	$E^{*}_{t=o}$(GPa)	E^{*}_{sat}(GPa)	$\Delta E/(E_{un}-E_{t=o})$	δ^{*}(min^{-1})
MA-2 (ΔT=300C)	63.31	1	61.59	62.42	48.3 %	0.0413
		3	62.03	62.37	26.6 %	0.0179
		5	61.96	62.44	35.6 %	0.0405
		10	62.46	62.81	41.2 %	0.0199
		20	61.64	62.41	46.1 %	0.0438
		40	62.06	62.58	41.6 %	0.0084
		60	61.79	62.58	52.0 %	0.0445
MA-3 (ΔT=350C)	63.35	1	61.63	62.14	29.7 %	0.0129
		3	61.43	62.35	47.9 %	0.0362
		5	61.77	62.48	44.9 %	0.0326
		40	61.43	61.98	28.6 %	0.0204
		60	61.52	62.26	40.4 %	0.0233
		80	60.92	62.04	46.1 %	0.0232
MA-4 (ΔT=400C)	62.43	1	60.65	61.26	34.3 %	0.0299
		3	59.72	61.03	48.3 %	0.0598
		5	59.99	61.11	45.9 %	0.0369
MA-5 (ΔT=450C)	62.18	1	59.01	59.37	11.4 %	0.0097
		3	58.11	58.70	14.5 %	0.0206
		5	58.12	58.77	16.0 %	0.0332
		10	57.44	58.76	27.8 %	0.0345
MA-6 (ΔT=500C)	62.14	1	58.45	59.22	20.9 %	0.0102
		3	57.45	58.71	26.9 %	0.0359
		5	57.94	58.67	17.4 %	0.0268

* Refer equation 46.

Table 15. The results of non-linear regression analysis of Young's modulus recovery versus time data for Alumina

Specimen	Unshocked modulus E_{un}(GPa)	Number of thermal shocks, N	$E^{*}_{t=o}$(GPa)	E^{*}_{sat}(GPa)	$\Delta E/(E_{un}-E_{t=o})$	δ^{*}(min^{-1})
Alumina (ΔT=250C)	293.95	1	285.0	288.45	41.3 %	0.0418
		3	278.0	286.14	51.0 %	0.0202
		5	280.3	285.57	38.6 %	0.0273
		10	270.6	276.17	23.9 %	0.0196

* Refer equation 46.

to the unshocked value of Young's modulus. A $\Delta E/(E_{un} - E_{t=o})$ equal to zero would indicate no recovery, while a value of 100 percent would indicate complete recovery. These ratios ranged from 38.0 to 72.2 percent for the SiC fiber/AS composites, from 11.4 to 52.0 for the Macor glass ceramics, and from 23.9 to 51.0 percent for the polycrystalline alumina (Tables 13-15).

3.2.2 Possible Modulus Recovery Mechanisms

3.2.2.1 Virtual mass changes due to moisture evaporation

Since the specimens in this study were thermally shocked into a room temperature water bath, one possible mechanism for the apparent partial modulus recovery might be a time-dependent evaporation of absorbed moisture from the quenched specimen. In order to check for the possibility of a moisture evaporation mechanism, we measured both the mass and the elastic modulus as a function of elapsed time (from the instant of quenching) for a series of thermally shocked Macor specimens. The observed mass of the Macor specimens was then compared to the calculated mass change that would be needed to produce the observed modulus change. Since the existence of such a mass change is in question, we shall refer to the change as a "virtual mass change." In order to calculate the virtual mass change, we began with the expression for the elastic modulus, E, of a prismatic bar-shaped

specimen that is appropriate to sonic resonance, our modulus measurement technique [101, 103]

$$E = \frac{0.94642\, L^4 f^2 \rho T}{b^2} \tag{12a}$$

$$= \frac{0.94642\, L^3 f^2 m\, T}{b^3 w} \tag{12b}$$

where L = specimen length

f = flexural resonant frequency

ρ = specimen density

b = specimen thickness

w = specimen width

m = specimen mass

T = shape factor for the prismatic specimen.

The shape factor T is the following function of the specimen dimensions and Poisson's ratio [102]

$$T = 1 + 6.585(1 + 0.0752\nu + 0.8109\nu^2)\,(b/L)^2 - 0.868(b/L)^4 - \frac{8.34(1 + 0.2023\nu + 2.173\nu^2)\,(b/L)^4}{1 + 6.338(1 + 0.14081\nu + 1.536\nu^2)\,(b/L)^2}$$

where ν = Poisson's ratio.

To determine the virtual mass that could potentially cause the observed modulus recovery, we first solve for the specimen mass, m, in equation 12b, such that

$$m = \frac{E_{t=o}\, t^3 w}{0.94642\, L^3 f^2 T} \qquad (47)$$

where $E_{t=o}$ refers to the modulus immediately following the thermal quench.

The virtual masses as a function of time were calculated by inserting the observed resonant frequency data into equation 47, which thus assumes that the observed resonant frequencies change only as a result of moisture evaporation from the quenched bar. Figure 39 shows the calculated virtual mass change (due to moisture evaporation) that would be required for the observed modulus changes for Macor specimens. The virtual mass values as a function of time were then fit to equation 48, where

$$m = m_{t=o} + \Delta m \{1 - \exp(-\zeta t)\} \qquad (48)$$

where m = mass of specimen at time t

$m_{t=o}$ = mass of specimen at time t=0 (immediately after the thermal quench)

Δm = saturated mass - $m_{t=o}$

ζ = a constant which is determined by non-linear regression

t = time (in minutes) elapsed after the thermal shock.

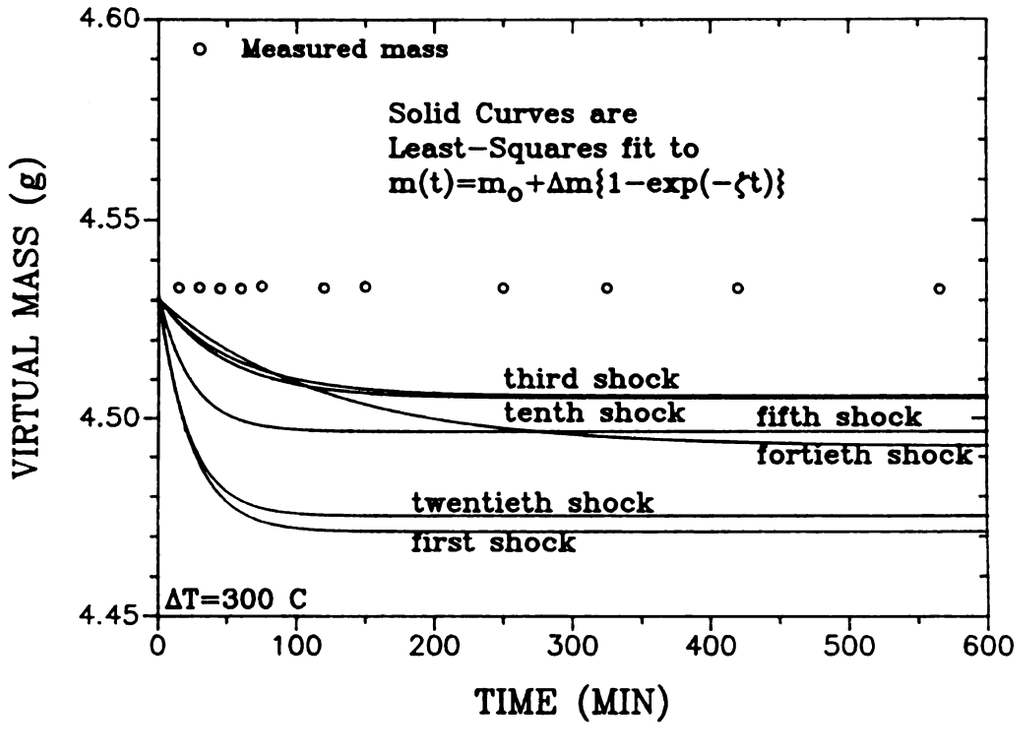

Figure 39. (a) Normalized virtual mass changes equivalent to Young's modulus recoveries for Macor glass-ceramic specimen (ΔT = 300 °C) under the assumption that the observed Young's modulus recoveries are due only to changes in the specimen mass.
The standard deviation of the measured mass at each point was smaller than the plotting symbol size used in this figure.

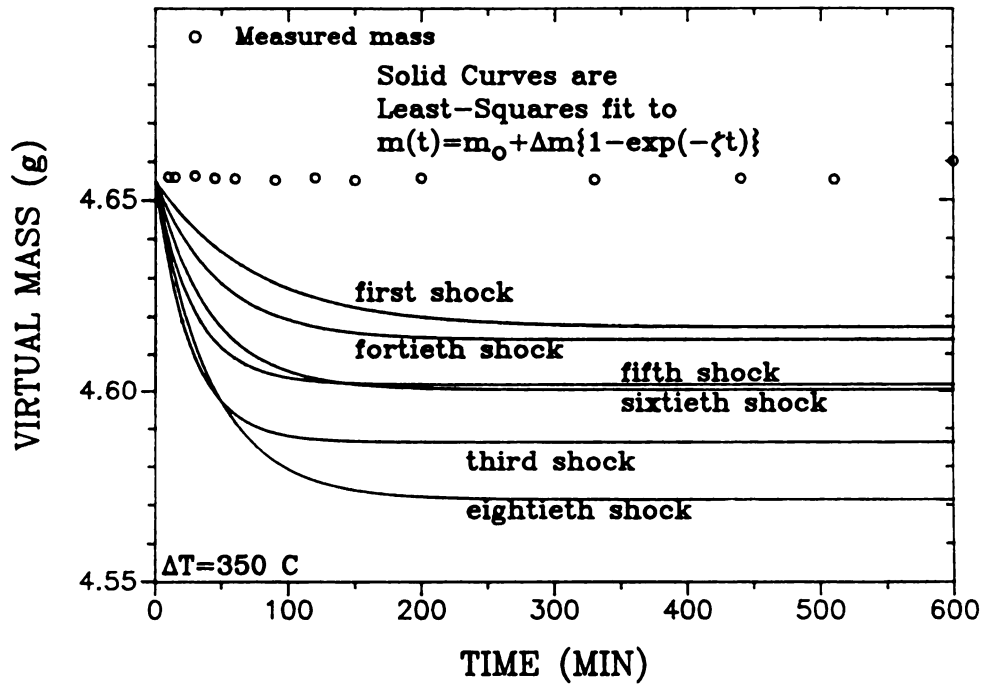

Figure 39. (b) Normalized virtual mass changes equivalent to Young's modulus recoveries for Macor glass-ceramic specimen (ΔT = 350 °C) under the assumption that the observed Young's modulus recoveries are due only to changes in the specimen mass.
The standard deviation of the measured mass at each point was smaller than the plotting symbol size used in this figure.

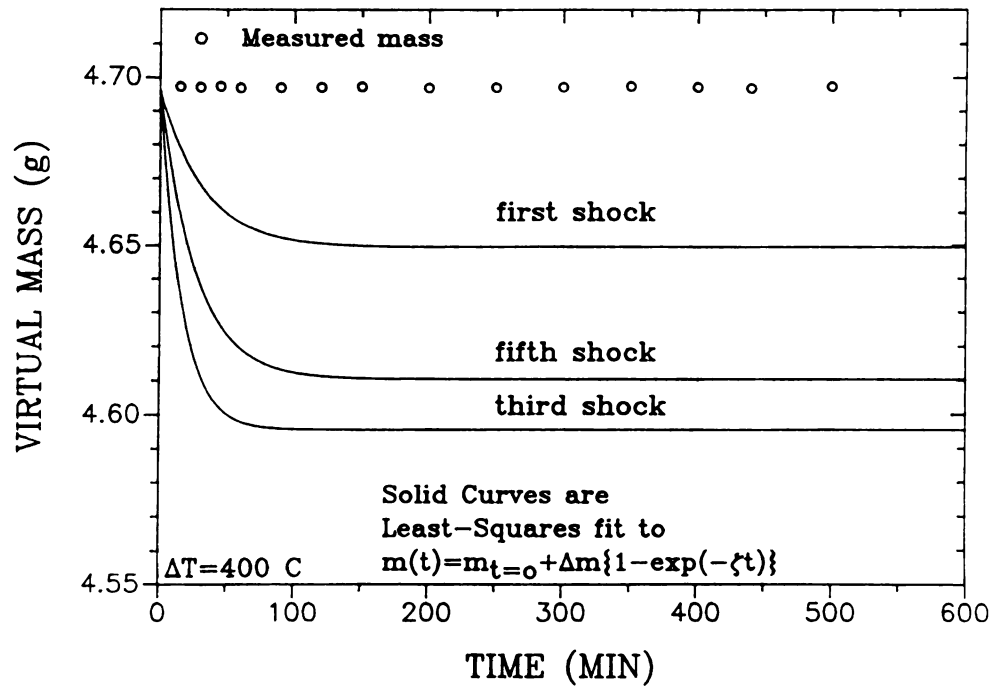

Figure 39. (c) Normalized virtual mass changes equivalent to Young's modulus recoveries for Macor glass-ceramic specimen (ΔT = 400 °C) under the assumption that the observed Young's modulus recoveries are due only to changes in the specimen mass.
The standard deviation of the measured mass at each point was smaller than the plotting symbol size used in this figure.

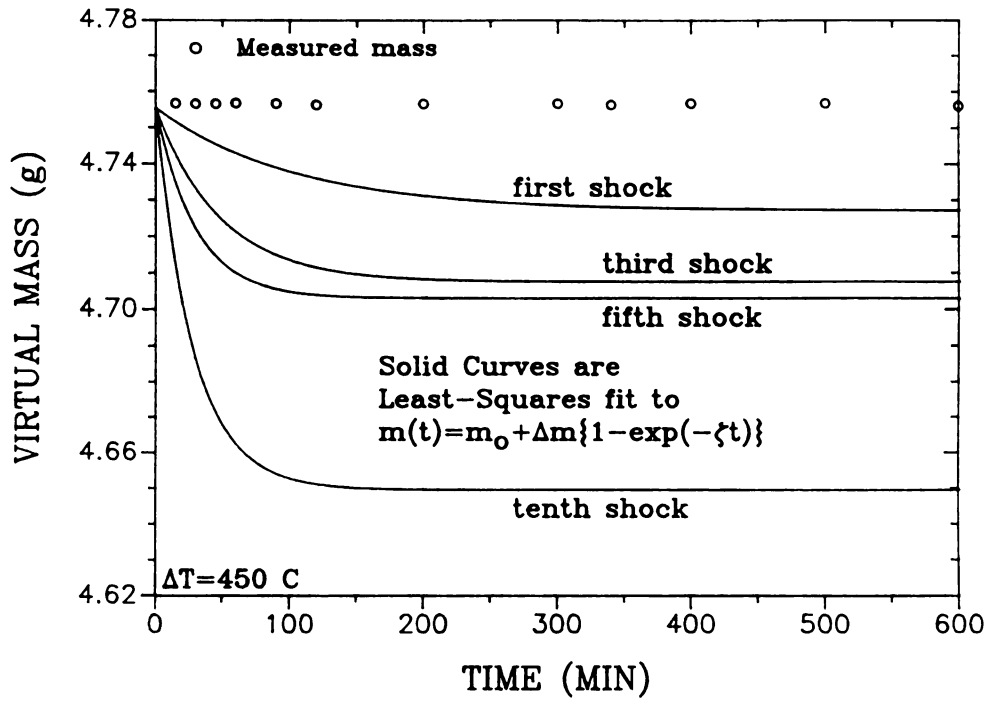

Figure 39. (d) Normalized virtual mass changes equivalent to Young's modulus recoveries for Macor glass-ceramic specimen (ΔT = 450 °C) under the assumption that the observed Young's modulus recoveries are due only to changes in the specimen mass.
The standard deviation of the measured mass at each point was smaller than the plotting symbol size used in this figure.

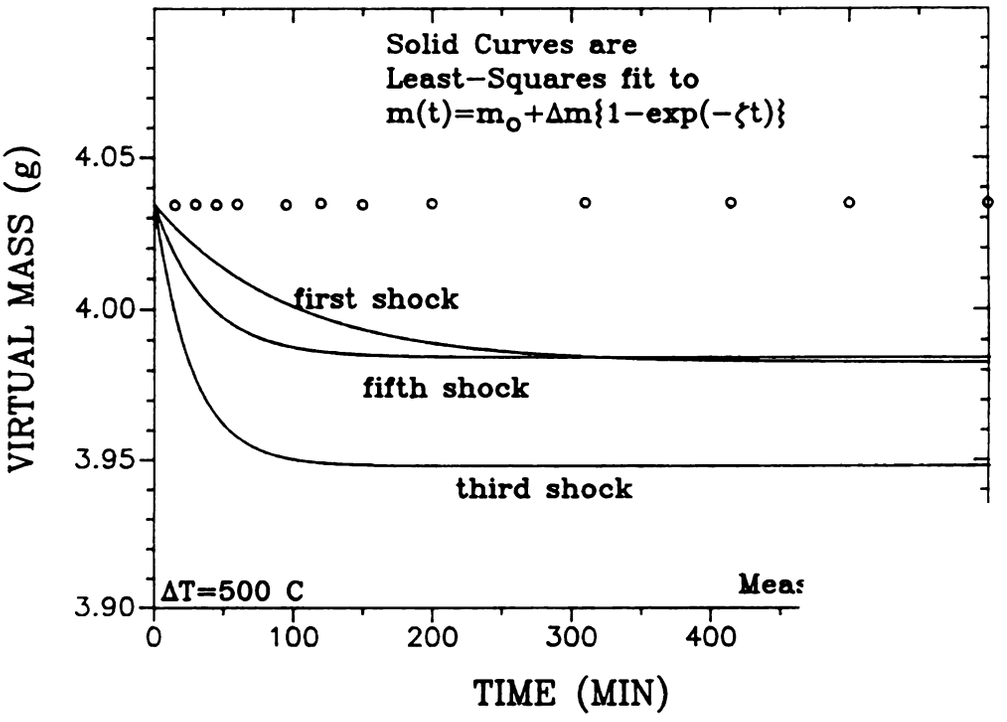

Figure 39. (e) Normalized virtual mass changes equivalent to Young's modulus recoveries for Macor glass-ceramic specimen (ΔT = 500 °C) under the assumption that the observed Young's modulus recoveries are due only to changes in the specimen mass.
The standard deviation of the measured mass at each point was smaller than the plotting symbol size used in this figure.

The virtual mass changes, Δm, predicted from equation 48 are two orders of magnitude larger than the measured mass changes for the thermally shocked Macor specimens (figure 39).

The mass change of the thermally shocked specimens was thus much too small to account for the observed modulus change, and in fact were smaller than the experimentally determined resolution limits of the electronic mass balance. The coefficient of variation for mass measurements on the control specimen ($= 8.0246 \times 10^{-5}$) was approximately the same as the coefficient of variation for the mass measurements on the thermally shocked specimens. Since the control specimens were not thermally shocked, variations in control specimen masses reflect the experimental scatter in the mass measurements themselves. The thermally shocked specimens' mass change thus was within the experimental scatter of the electronic balance's mass measurements.

3.2.2.2 Microcrack healing

To place our room-temperature crack-healing study in perspective, we shall briefly discuss other crack healing studies in ceramics. Then we shall compare the crack healing rates found in our study with the rates observed for other ceramic materials.

Mechanisms for microcrack healing can be classified in three different categories [35]: (1) healing by diffusion (thermal annealing), (2) healing by intermolear forces (adhesion), (3) healing by chemical reaction products. Crack healing by diffusion has

been reported for a variety of ceramics, including polycrystalline and single crystal alumina [36-41], magnesia [38, 42] and urania pellets [43-46]. However, the time-dependent modulus recovery observed in this study occurred at room temperature, so diffusive healing is likely to be insignificant for our specimens.

Crack healing by adhesion can occur at room temperature and has been reported for several materials. In mica, Bailey [49] found that 310 ergs/cm^2 was required to split mica initially, 190 ergs/cm^2 was regained on healing, and 250 ergs/cm^2 was required to resplit the mica. Using double cleavage drilled compression specimens of soda lime-silica glass and vitreous silica glasses, Michalske and Fuller [51] measured the strain energy release rate for crack closure and repropagation as a function of ambient relative humidity. Hydrogen-bonded linkage of surface adsorbed water molecules was proposed to account for the experimentally determined strain energy release rate of 0.15 J/m^2 to reopen healed cracks in humid environments [51]. The relatively high crack repropagation energies (1.7 $\pm$ 0.2 J/m^2) under the driest nitrogen atmosphere for soda-lime glass after healing of cracks was attributed to the formation of either cationic bridges or siloxane bonds between fracture surfaces [51]. Using chevron-notched short-bar specimens, Inagaki et al. [53] measured the work of fracture of soda-lime-silica glass as 5.5 J/m^2 in atmospheres of argon and of nitrogen. A work of fracture of 4.4 J/m^2 was found in air. The hysteresis observed in the load versus displacement curve upon loading and unloading the specimen was attributed to crack healing [53]. The

crack healing energy, measured from the area inside the load-displacement hysteresis loop, was 0.65 J/m^2 in the inert atmosphere and 0.21 J/m^2 in air [53]. Stavrinidis and Holloway [52] found that no crack closure occurred for soda-lime-silica glass immersed either in Dimethylsulphoxide or liquid paraffin, but found that crack closure did occur when specimens were immersed in distilled water. Thus for some ceramics, room-temperature crack healing can occur in humid air as well as in inert atmospheres.

Chemical reaction products can also heal cracks. Pulliam [54] observed crack healing for KCl and NaCl crystals in water and water vapor and attributed the healing to the precipitation of reaction products between crack surfaces. Roach and co-workers [55] found that interfacial layers deposited on crack surfaces in muscovite mica and silicate glass were corrosion products formed by environmental species interacting with the crack surface. For room-temperature testing in air of a heavy-metal fluoride glass, Lehman et al. [56] found that Vickers indentation-induced radial cracks decreased in length (apparently healed) as a function of time and relative humidity. The radial cracks from a 0.49 N Vickers indentation impression apparently closed after aging for 13 days at room temperature in an 85 percent relative humidity environment (figure 2 in [56]). Crack healing in the indented fluoride glass did occur at relative humidities that ranged from 0 to 85 percent, but as the relative humidity decreased, the observed crack healing rate decreased [56]. Viscous relaxation of the glass around the crack tip, and/or the generation and transport of

a fluoride gel phase to the crack aperture were proposed as possible low-temperature crack closure mechanisms [56]. In a crack healing study of soda-lime-silica float glass in humid environments, Holden and Frechette [57] proposed a crack healing mechanism that proceeded via formation of a moisture-induced gel layer, closure of the crack by stress relief, and gel drying in a controlled atmosphere. Thus, in room-temperature air environments and at a variety of relative humidities, reaction products also can induce crack healing in ceramics.

The time constants, δ, for Young's modulus recovery versus time that were obtained in this study were compared to the crack healing results of other researchers' (Table 16) [52, 54, 56, 58]. In order to uniformly and systematically compare our data to the data from other researchers, we used a regression equation of the form

$$MPP(t) = MPP_{t=o} + \Delta MPP \{1 - \exp(-\Gamma t)\} \qquad (49a)$$

where $MPP(t)$ = measured physical properties, such as crack length, strain energy release rate to repropagate a closed crack, and Young's modulus recovery

$MPP_{t=o}$ = measured physical properties at $t = 0$

$\Delta MPP = MPP_{sat} - MPP_{t=o}$

MPP_{sat} = MPP(t) for very large t (that is, the "saturated" value of MPP(t))

Γ = the physical property recovery time constant, as

determined by non-linear regression on the physical property recovery data

t = time (in minutes) elapsed after the beginning of the recovery measurement.

Note that equation 49a is identical to our equation 46 if the physical property measured (MPP) is the Young's modulus, as was the case in our experiment. If we express the equation 49a in terms of a normalized property change, then

$$\frac{MPP_{sat} - MPP(t)}{MPP_{sat} - MPP_{t=o}} = \exp(-\Gamma t) \qquad (49b)$$

Equation 49b emphasizes that the normalized property change is unitless and that Γ has units of inverse time. In table 16 (as was the case for our modulus recovery analysis), we used min^{-1} as the units for the physical property recovery time constant. In equation 49a, the term $MPP_{t=o}$ is the initial value (t = 0) for measured property MPP in the cracked specimen. $MPP_{t=o}$ is a measure of the extent to which property MPP is affected by the crack(s) in the specimen. Therefore, $MPP_{t=o}$ contains little, if any, information about the crack healing behavior during recovery. MPP_{sat} measures the "saturated value" of MPP (that is, the limit of MPP(t) for t large). Experimentally, MPP_{sat} can be difficult to determine accurately. For

Table 16. A comparison of the recovery time constants for the elasticity data obtained in this study and the calculated time constants for physical properties from other researchers

Material	Time constant (min^{-1})	Method of crack generation	Physical property measured	Reference
SiC/AS (ΔT=370 C)	0.006+	thermal shock	Young's modulus	this study
(ΔT=450 C)	0.047+	thermal shock	Young's modulus	this study
(ΔT=300 C)	0.041+	thermal shock	Young's modulus	this study
(ΔT=350 C)	0.013+	thermal shock	Young's modulus	this study
Macor (ΔT=400 C)	0.030+	thermal shock	Young's modulus	this study
(ΔT=450 C)	0.010+	thermal shock	Young's modulus	this study
(ΔT=500 C)	0.010+	thermal shock	Young's modulus	this study
Polycrystalline alumina (ΔT=250 C)	0.042+	thermal shock	Young's modulus	this study
Polycrystalline YIG (ΔT=165 C)	0.091++	thermal shock	Young's modulus	[58]
KCl*	0.028	cleavage	length of crack fill-up (crack angle = 2.6×10^{-3} rad)	[54]
NaCl*	0.023	cleavage	length of crack fill-up (crack angle = 7.5×10^{-4} rad)	[54]
Soda-lime-silica glass	2.333×10^{-4}	fine scratch and tapping	strain energy release rate (G)	[52]
Fluoride glass**	2.569×10^{-4}	Vickers indentation	modified radial crack size (2C - 2a)	[56]

\+ Recovery data for the first thermal shock cycle at given ΔT
++ Specimen edges unbeveled, the first thermal shock cycle
* Single crystal, saturated solutions of the crystals were fed into the induced cleavage crack
** ZBLANI (ZrF_4, BaF_2, LaF_3, AlF_3, NaF, InF_3) fluoride glass

example, it could be difficult to choose an appropriate time cutoff in evaluating MPP_{sat}. However, the recovery time constant, Γ, allows one to quantitatively compare the relative recovery rates of physical properties in terms of a modeled exponential-time dependence of the recovery. Regardless of the physical units of MPP(t), the time-dependence of MPP can be modeled (for equation 49b) in terms of a single number with reciprocal time units. This, of course, assumes that the property recovery can be described well with equations 49a or 49b.

The data from other researchers [52, 54, 56, 58] were taken directly from their published plots of property recovery. The recovery time constant Γ was calculated by a nonlinear regression fit of equation 49a to their data. A comparison of the recovery time constants for the elasticity data obtained in this study and the calculated Γ's from other researchers showed that the Γ's are generally in the same range for polycrystalline and single crystal specimens, while the Γ's for physical property recovery in cracked glass are much lower (Table 16).

The physical property recoveries summarized in Table 16 were determined for a variety of fracture conditions, including cleavage cracks [54], Vickers indentation cracks [56], scribing cracks [52], and cracks induced by thermal shock. However, except for this study and the study of cyclic thermal shock in polycrystalline YIG [58], the fracture conditions involved only a single load cycle (that is, a crack was induced in the specimen, and the crack subsequently healed)

without further reloading of the specimen. To express the comparisons in Table 16 in terms of similar loading histories, the recovery time constant data from this study (that is, the table's entries for SiC/AS, Macor, and polycrystalline alumina) represent the modulus recovery rates for the first loading cycle only.

3.3. The Measurement of the Surface Heat Transfer Coefficient for Ceramics Quenched into a Water Bath

3.3.1 Heat Transfer coefficient during thermal shock

3.3.1.1 Free Convection

For a vertical vertical plate of length L the average convection heat transfer coefficient, <h>, for free convection conditions can be calculated from [157],

$$\langle Nu_L \rangle = \langle h \rangle L/k \qquad (50)$$

where $\langle Nu_L \rangle$ = average Nusselt number

L = characteristic length

k = thermal conductivity of fluid

In this case, free convection means that the fluid moves as a results of the buoyancy force due to temperature variation generated density gradient within the fluid.

Churchill and Chu [158] suggest that the average Nusselt number, $\langle Nu_L \rangle$ is a function of the Rayleigh number, Ra_L and the Prandtl number Pr.

$$\langle Nu_L \rangle = [0.825 + 0.387\ Ra_L^{1/6} / \{1+(0.492/Pr)^{9/16}\}^{8/27}]^2 \quad (51)$$

Equation 51 may be applied over the entire range of the Rayleigh number, Ra_L. The transition from laminar to turbulent flow in a free convection boundary layer depends on the Rayleigh number, Ra_L which is the relative magnitude of the buoyancy and viscous forces in the fluid. The critical Rayleigh number for the vertical plate is

$$Ra_L = Gr_L \cdot Pr = \{g\beta(T_s - T_\infty)L^3\}/(\nu\alpha) \approx 10^9 \quad (52)$$

where Gr_L = Grashof number

g = gravitational acceleration

β = volumetric thermal expansion coefficient of the fluid

T_s = surface temperature of the plate

T_∞ = fluid temperature (free stream condition)

L = characteristic length

ν = kinematic viscosity which is given by the ratio, viscosity/density

α = thermal diffusivity of fluid

For the specimens quenched in this study, Ra_L was calculated from in equation 52 at the film temperature, $T_f=(T_s+T_\infty)/2$ [157, 159, 160]. Pr was obtained from the tables of thermophysical properties of water at the film temperature [160]. The calculated Ra_L and Pr obtained from the tables were inserted into equation 51 to obtain the average Nusselt number,$< Nu_L >$. The average convective heat transfer coefficient,<h> was calculated from equation 50 for each thermal shock of severity, $\Delta T = T_s - T_\infty$. Equation 52 relationships between heat transfer coefficient, temperature difference and quench water temperature are shown in figure 40.

3.3.1.2 Forced Convection

Forced convection means that the heat transfer flow is caused by some external means. The average heat transfer coefficient over the laminar and turbulent boundary layer over a flat plate is given as the following [157] for $Re_L > 2x10^5$. A transition from laminar to turbulent flow takes place in the range of Reynolds numbers from $2x10^5$ to $5x10^5$.

$$h = 0.036Pr^{0.43} \cdot (Re_L^{0.8} - 9200)(\mu_\infty/\mu_w)^{0.25} \cdot k/L \qquad (53)$$

where Re_L = Reynolds Number = $u_\infty L/\nu = (u_\infty^2/L)/(\nu u_\infty/L^2)$

which is the ratio, inertia force/viscous force

u_∞ = velocity of a fluid

ν = kinematic viscosity

Pr_L = Prandtl Number

L = characteristic length

k = thermal conductivity of fluid

μ_∞ = viscosity of fluid at free-stream temperature

μ_w = viscosity of fluid at wall temperature

The equation 53 correlates the experimental data of air, water, and oil covering the following ranges reasonably well [161, 162].

$$2\times10^5 < Re_L < 5.5\times10^6$$

$$0.7 < Pr < 380$$

$$0.26 < \mu_\infty/\mu_w < 3.5$$

The relationships given by equation 53 between the heat transfer coefficient, temperature difference and quench water temperature are shown in figure 41.

3.3.2 The Measurement of the Surface Heat Transfer Coefficient for Ceramics Quenched into a Water Bath

The thermocouple voltages versus cooling time are shown in figure 42 for the Macor specimens quenched at ΔT of 200, 280, 350, 400, 450 and 500 °C, for the alumina specimens quenched at ΔT of 250, 300, and 350 °C, for the titanium diboride specimens quenched at ΔT of 200, 300, 400, and 500 °C. The observed time-temperature behavior of the Macor, the alumina and the titanium diboride was similar. Following Beck's procedure (equation 18 - 21), $\hat{h}(T)$, the estimated surface heat

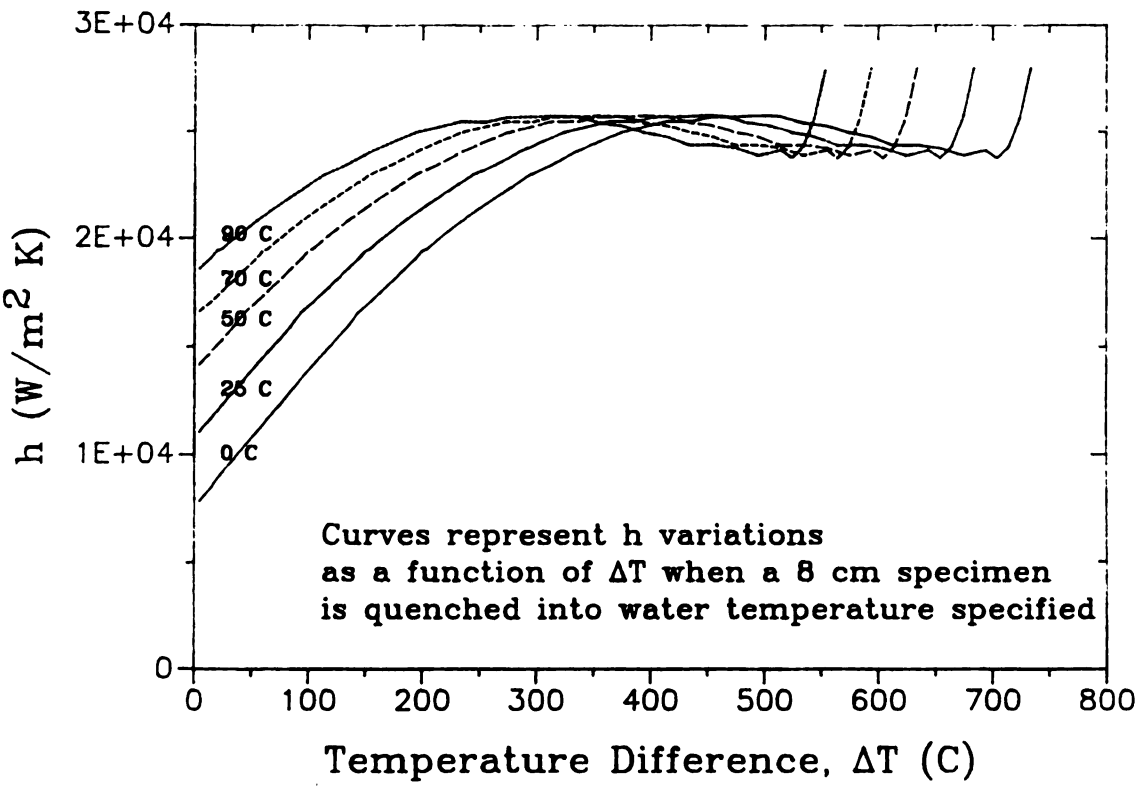

Figure 40. Calculated surface heat transfer coefficient for free convection water as a function of temperature.

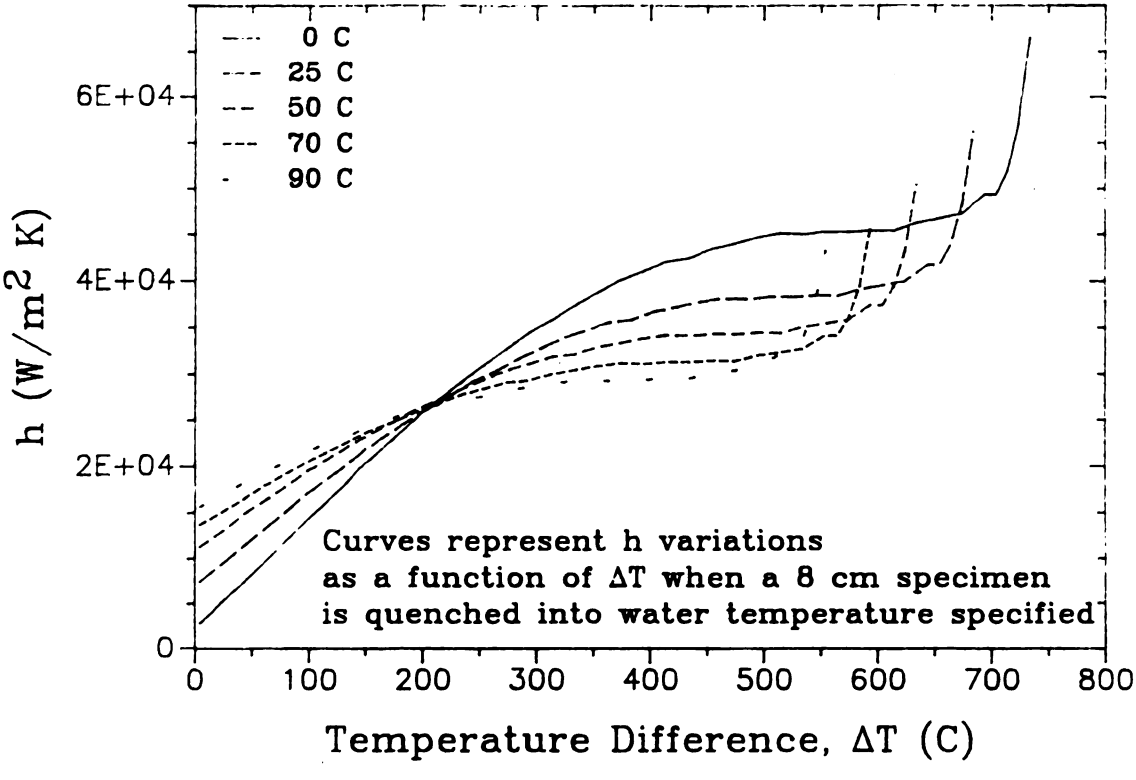

Figure 41. Calculated surface heat transfer coefficient for forced convection water as a function of temperature.

Figure 42(A). The experimentally obtained thermocouple voltage versus cooling time for the **Macor** at ΔT = (a) 200 °C, (b) 280 °C, (c) 350 °C, (d) 400 °C, (e) 450 °C and (f) 500 °C; each division on the x axis represents 6.25 msec, each division on the y axis represents 2 mv for ΔT = 200 °C and 5 mv for ΔT = 280, 350, 400, 450, 500 °C.

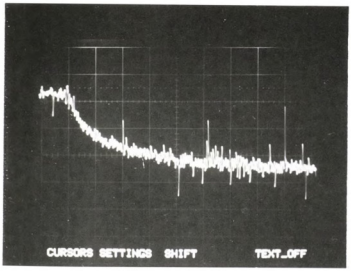
CURSORS SETTINGS SHIFT
TEXT_OFF

a

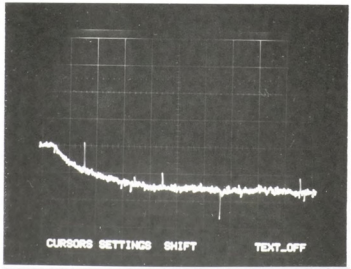
CURSORS SETTINGS SHIFT
TEXT_OFF

b

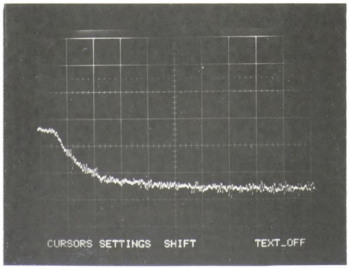
CURSORS SETTINGS SHIFT
TEXT_OFF

c

Figure 42(A). The experimentally obtained thermocouple voltage versus cooling time for the **Macor** at ΔT = (a) 200 °C, (b) 280 °C, (c) 350 °C, (d) 400 °C, (e) 450 °C and (f) 500 °C; each division on the x axis represents 6.25 msec, each division on the y axis represents 2 mv for ΔT = 200 °C and 5 mv for ΔT = 280, 350, 400, 450, 500 °C.

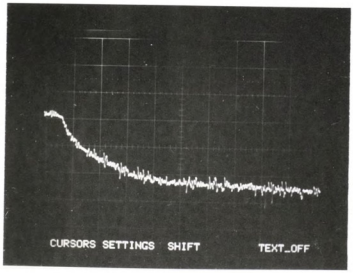
CURSORS SETTINGS SHIFT
TEXT_OFF

d

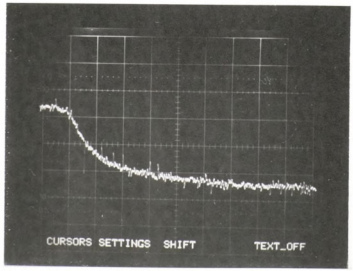
CURSORS SETTINGS SHIFT
TEXT_OFF

e

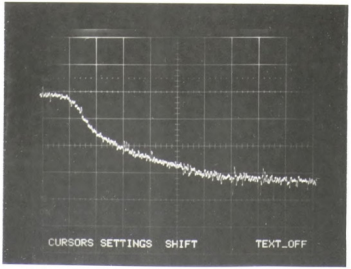
CURSORS SETTINGS SHIFT
TEXT_OFF

f

Figure 42(B). The experimentally obtained thermocouple voltage versus cooling time for the **alumina** at ΔT = (a) 250 °C, (b) 300 °C, and (c) 350 °C;
each division on the x axis represents 12.5 msec for ΔT = 250 °C, 25 msec for ΔT = 300 and 350 °C,
each division on the y axis represents 2 mv for ΔT = 250 °C 5 mv for ΔT = 300, 350 °C.

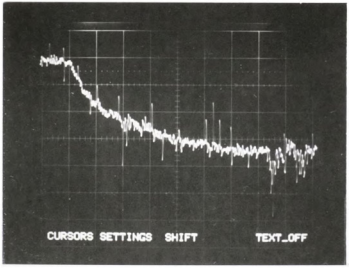
CURSORS SETTINGS SHIFT
TEXT_OFF

a

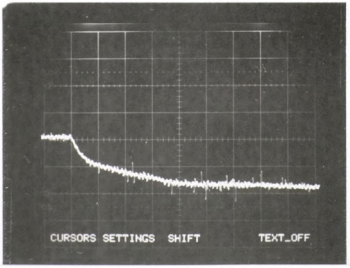
CURSORS SETTINGS SHIFT
TEXT_OFF

b

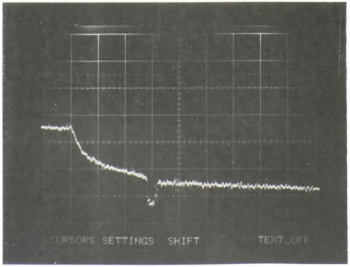
CURSORS SETTINGS SHIFT
TEXT_OFF

c

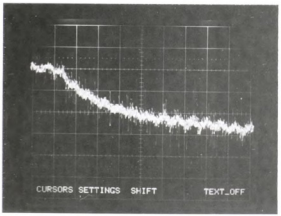

a

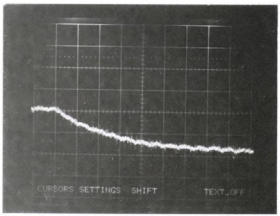

b

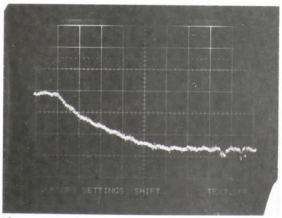

c

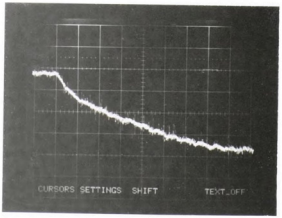

d

Figure 42(C). The experimentally obtained thermocouple voltage versus cooling time for the $\mathbf{TiB_2}$ at ΔT = (a) 200 °C, (b) 300 °C, (c) 400 °C, and (d) 500 °C;
each division on the x axis represents 25 msec,
each division on the y axis represents 2 mv for ΔT = 200 °C and 5 mv for ΔT = 300, 400, 500 °C.

transfer coefficients were obtained for Macor, alumina, and TiB_2 (figure 43).

The temperature dependent form of the specific heat for the three materials was obtained via a least-squares best fit (table 17) of available data [163-165]. Table 18 lists the numerical values of the polynomial coefficients β_i that were obtained from the regression of the time-temperature data (equations 20a and 20b).

The h values obtained in this study for alumina are in broad agreement with the h values calculated for alumina by Becher and co-workers [64, 65] and Hasselman and co-workers [66]. For the ceramic materials presented in this study, the results for h as a function of temperature (figure 43) show the same general trends observed by heat transfer researchers [166, 167] for the temperature dependence of h in metals and alloys.*

For a given material, the $\hat{h}(T)$ curves (figure 43) are similar to one another for the lower quench temperature differences (ΔT from approximately 200 °C to 350 °C). Above about 350 °C, the $\hat{h}(T)$ curves change as a function of the quench temperature difference, ΔT, which may reflect different physical mechanisms. As shown in the schematic plot of log h versus T (figure 44) [166-169] a local maximum in h may occur near the boundary of the boiling nucleation (regime N, figure 4) and the transition region (regime TR, figure 44).

---

* The authors were unable to find direct measurements of h as a function of quenching temperature for ceramic materials in the literature, although a number of researchers measured it for metals and alloys [166, 167].

Table 17. The specific heat, c_p, as a function of temperature.

c_p [J/(Kg °C)] = $c_1 + c_2 T + c_3 T^2 + c_4 T^3$ (unit of T = °C)

Material tested	c_1 [J/(Kg°C)]	c_2 [J/(Kg°C^2)]	c_3 [J/(Kg°C^3)]	c_4 [J/(Kg°C^4)]	Correlation coefficient
Macor[163]	709.3	1.917	-5.264×10^{-3}	5.631×10^{-6}	0.994
Al_2O_3[164]	791.4	1.407	-1.634×10^{-3}	7.029×10^{-7}	0.995
TiB_2 [165]	608.4	1.616	-2.007×10^{-3}	9.200×10^{-7}	0.996

Table 18. The polynomial series for measured temperature changes versus time.

$$\hat{T} = \beta_1 + \beta_2(t/\Delta t) + \beta_3(t/\Delta t)^2 + \beta_4(t/\Delta t)^3 + \beta_5(t/\Delta t)^4$$

Material	ΔT (°C)	β_1 (°C)	β_2 (°C)	β_3 (°C)	β_4 (°C)	β_5 (°C)	Correlation Coefficient
Macor (1.25+ msec)	200	228.373	-21.0781	1.70710	-0.064032	8.71108×10^{-4}	0.990
	280	300.675	-26.3890	1.66202	-0.052511	6.49613×10^{-4}	0.996
	350	386.063	-45.1718	3.06902	-0.093023	1.02663×10^{-3}	0.997
	400	444.360	-44.9530	3.57924	-0.159759	2.80356×10^{-3}	0.998
	450	494.987	-31.8487	0.17491	0.058024	-1.41338×10^{-5}	0.996
	500	549.354	-30.7892	0.92043	0.008522	-6.52572×10^{-4}	0.998
Alumina (2.5+ msec)	250	258.599	-18.8763	1.09412	-0.030958	3.23593×10^{-4}	0.997
	300	309.343	-21.9017	1.33047	-0.038322	3.91111×10^{-4}	0.994
	350	365.740	-28.3338	1.76099	-0.052364	5.52893×10^{-4}	0.994
TiB_2 (5.0+ msec)	200	223.069	-10.7032	0.38972	6.888×10^{-3}	4.36671×10^{-5}	0.996
	300	318.135	-18.1753	0.76477	-0.021633	2.90400×10^{-4}	0.996
	400	404.909	-30.1685	1.77243	-0.068937	1.08125×10^{-3}	0.999
	500	505.660	-31.3834	1.75078	-0.055859	6.40269×10^{-3}	0.998

+ The time specified in parenthesis represents the time step Δt (equations 20 -21).

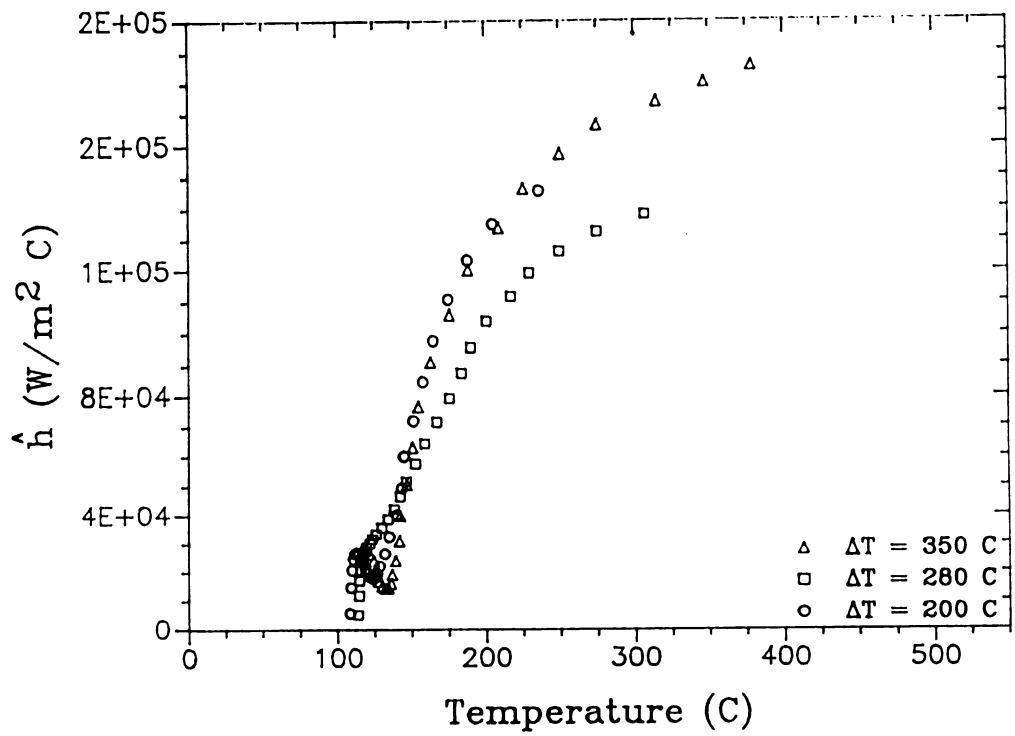

Figure 43. The estimated surface heat transfer coefficient versus temperature calculated from the experimentally obtained thermocouple voltage versus cooling time for a) Macor (ΔT = 200, 280, and 350 °C).

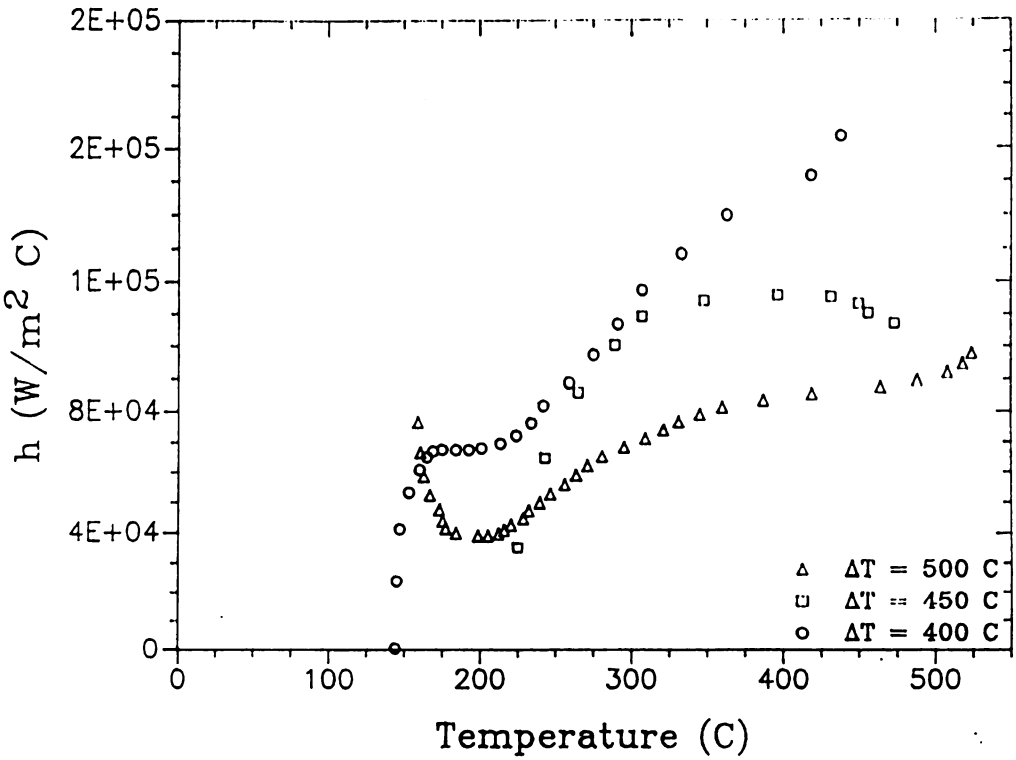

Figure 43. The estimated surface heat transfer coefficient versus temperature calculated from the experimentally obtained thermocouple voltage versus cooling time for b) Macor (ΔT = 400, 450, and 500 °C).

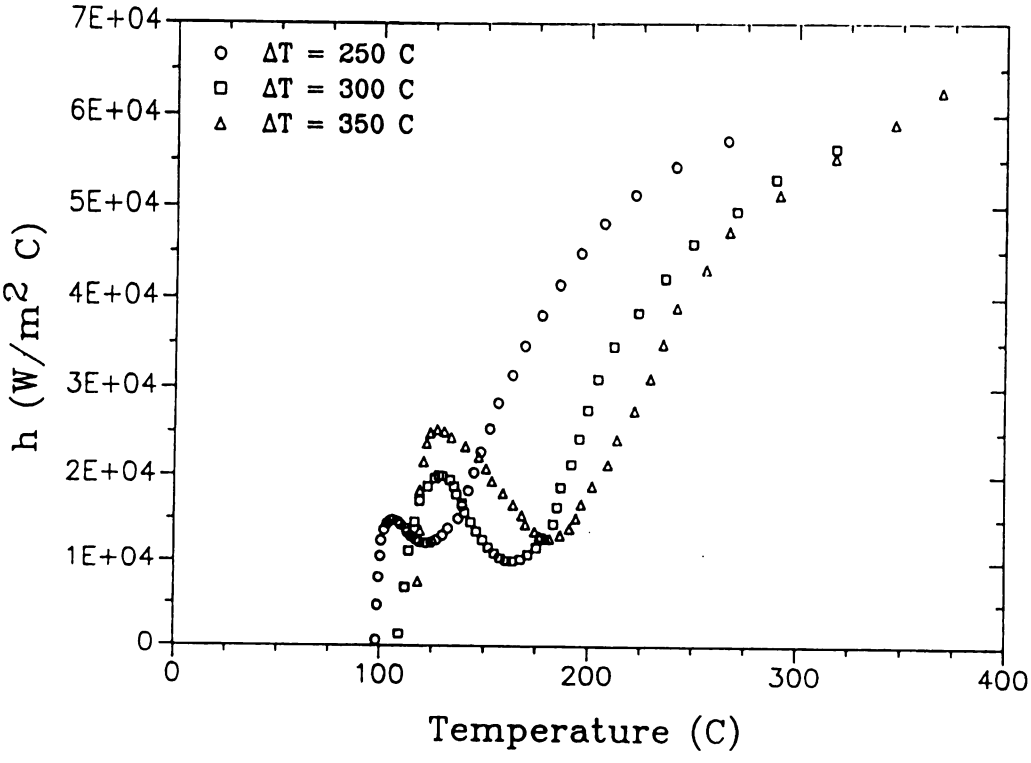

Figure 43. The estimated surface heat transfer coefficient versus temperature calculated from the experimentally obtained thermocouple voltage versus cooling time for c) alumina.

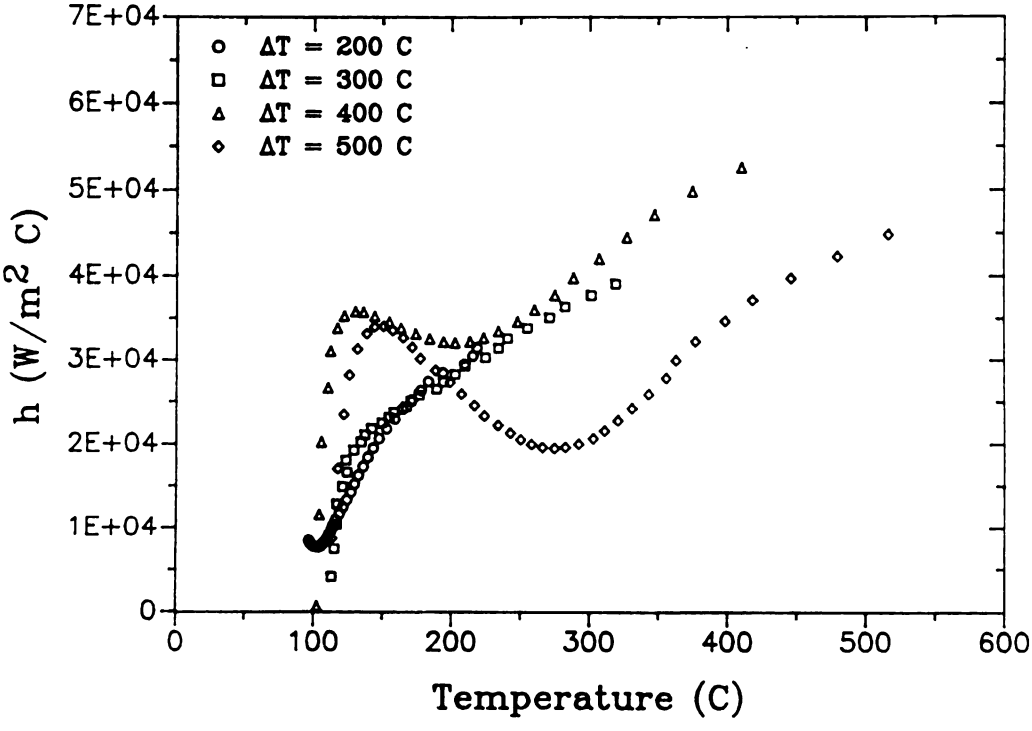

Figure 43. The estimated surface heat transfer coefficient versus temperature calculated from the experimentally obtained thermocouple voltage versus cooling time for d) TiB_2.

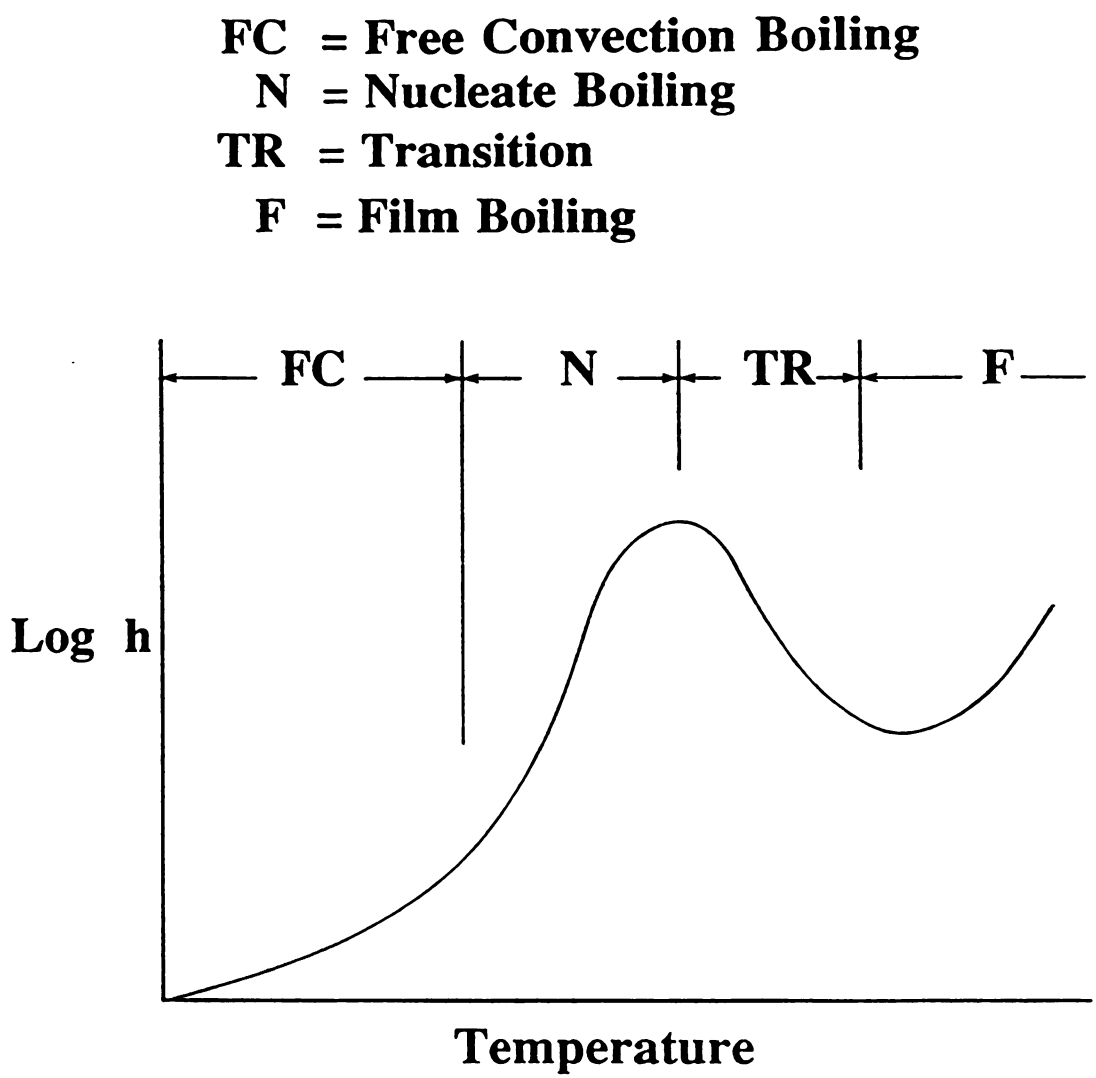

Figure 44. Schematic of log h versus Temperature (after [169]).

Physically, the boiling nucleation regime involves the formation and movement of bubbles on the specimen surface [67-69, 166-169]. The transition regime involves an unstable film which, as temperature rises, eventually stabilizes on the surface of the hot solid. The maximum in h corresponds to the rapid creation of bubbles and their departure from the heated solid [67-69, 166-169]. Heat transfer in the boiling nucleation and film formations regimes depend on such parameters as the latent heat of vaporization of liquid, the liquid viscosity, the surface tension of the liquid vapor interface, the number density of boiling nucleation sites on the solid's surface, and empirically determined constants depending on the particular solid-liquid interface [168, 169].

The transition among the various heat transfer mechanisms is embodied empirically in the temperature-time data. The derivative $d\hat{T}/dt$ is a monotonically increasing function whose initial value is a large negative number, and the factor $1/(T_\infty - \hat{T})$ is a monotonic increasing function whose initial value is a small negative number. Thus the product $1/(T_\infty - \hat{T}) \cdot d\hat{T}/dt$ goes through a maximum. To obtain h (equation 22), one must multiply $1/(T_\infty - \hat{T})$ by the $\rho V/A$ (which is essentially temperature independent, as discussed previously) and $c_p(T)$, where the experimental values of $c_p(T)$ are monotonically increasing functions of T [163-165]. Thus the values of h from equation 22 display a "waviness" as a function of T (figures 43a-43d), as do the h versus T plots obtained in the literature for non-ceramic materials [67-69, 166-169].

3.3.3 Maximum Surface Thermal Stress Calculation of TiB_2, Al_2O_3, and Macor glass-ceramic during quenching

The maximum surface thermal stress (equations 54 and 55) was calculated applying temperature dependent material properties, including Young's modulus, thermal expansion, Poisson's ratio, and thermal conductivity for titanium diboride, alumina and Macor glass-ceramic from measured surface heat transfer coefficient [170]. All material properties were fit to temperature functional form (Table 19) (figure 45).

$$\sigma_{max} = \frac{E \quad \alpha \, \Delta T}{(1 - \nu)} \cdot f(B) \qquad (54)$$

where, E = Young's modulus of the specimen

α = thermal expansion coefficient

ΔT = thermal shock severity

ν = Poisson's ratio

$f(B)$ = a function of the specimen's Biot modulus,

where [59]

$$f(B) = (1.5 + 3.25/B)^{-1} \qquad \text{when } 0<B<5 \qquad (55a)$$

$$f(B) = (1.0 + 3.25/B^{2/3})^{-1} \qquad \text{when } 5<B<20 \qquad (55b)$$

$$f(B) = (1.5 + 3.25/B - 0.5\, e^{-16/B})^{-1} \qquad \text{when } 0<B<20.^{*} \qquad (55c)$$

---

* Equation 55c may be in error by no more than 5 percent even for a B value as large as 200 [60].

Table 19. Material properties as a function of temperature, T (°C).

Material	Property	Functional form	Correlation Coefficient
TiB_2 [165]	E (N/m^2)	$4.967 \times 10^{11} - 3.844 \times 10^{7} T$	
	α (1/°C)	$4.101 \times 10^{-6} + 1.013 \times 10^{-8} T - 5.414 \times 10^{-12} T^2$	
	ν	$0.00987 + 1.1375 \times 10^{-5} T$	
	k (W/m °C)	$32.188 - 8.273 \times 10^{-4} T + 6.506 \times 10^{-6} T^2 - 8.783 \times 10^{-10} T^3$	
Al_2O_3 [164]	E (N/m^2)	$3.355 \times 10^{11} - 2.7 \times 10^{7} T$	
	α (1/°C)	$6.050 \times 10^{-6} + 1.9 \times 10^{-8} T - 1.9 \times 10^{-11} T^2$	
	ν	$0.233 - 1.49 \times 10^{-5} T$	
	k (W/m °C)	$20.5 - 3.19 \times 10^{-2} T + 1.9 \times 10^{-5} T^2$	
Macor [163]	E (N/m^2)	$6.569 \times 10^{10} - 1.318 \times 10^{7} T + 5.152 \times 10^{4} T^2 - 78.628 T^3$	
	α (1/°C)	$7.041 \times 10^{-6} + 1.1265 \times 10^{-8} T$	
	ν	$0.2714 - 1.881 \times 10^{-5} T + 5.308 \times 10^{-7} T^2 - 9.443 \times 10^{-9} T^3$	
	k (W/m °C)	$1.2884 + 2.420 \times 10^{-5} T + 5.853 \times 10^{-8} T^2 + 8.965 \times 10^{-10} T^3$	

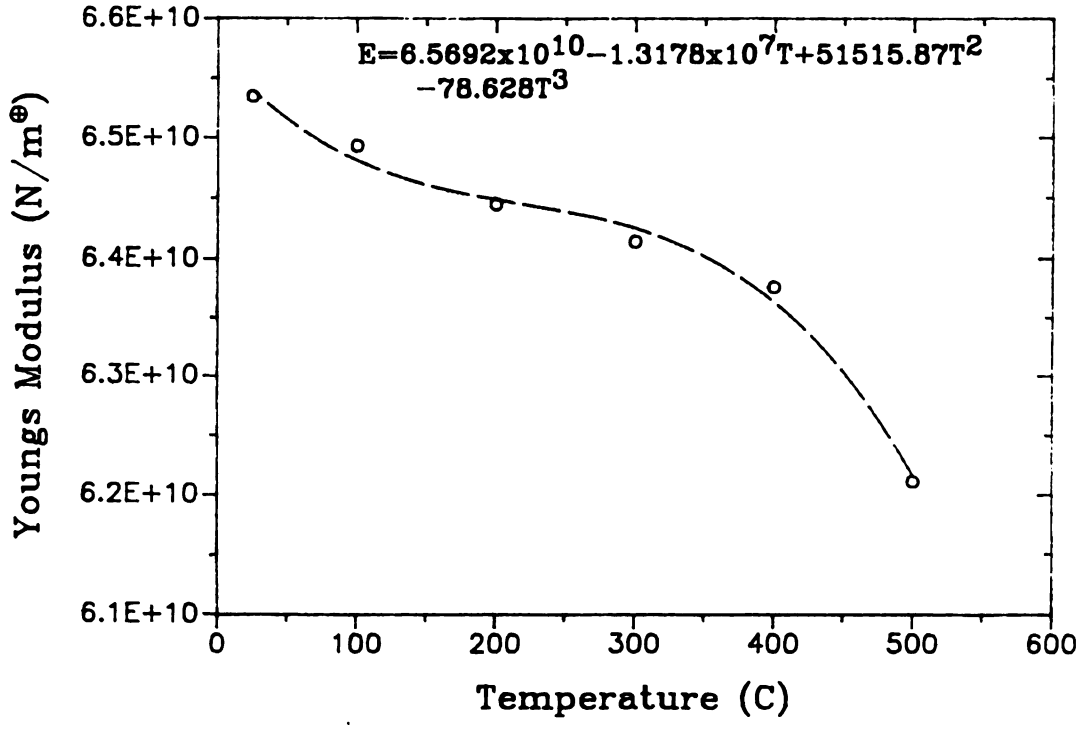

Figure 45(a). Young's modulus of Macor glass-ceramic as a function of temperature.

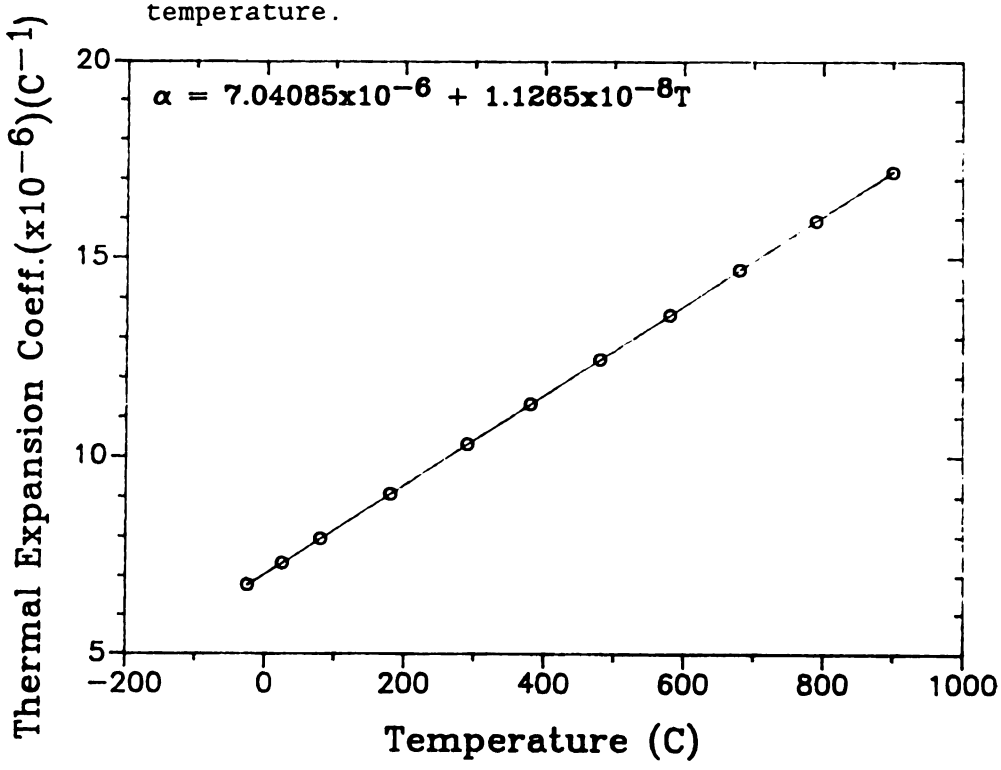

Figure 45(b). Thermal expansion coefficient of Macor glass-ceramic as a function of temperature.

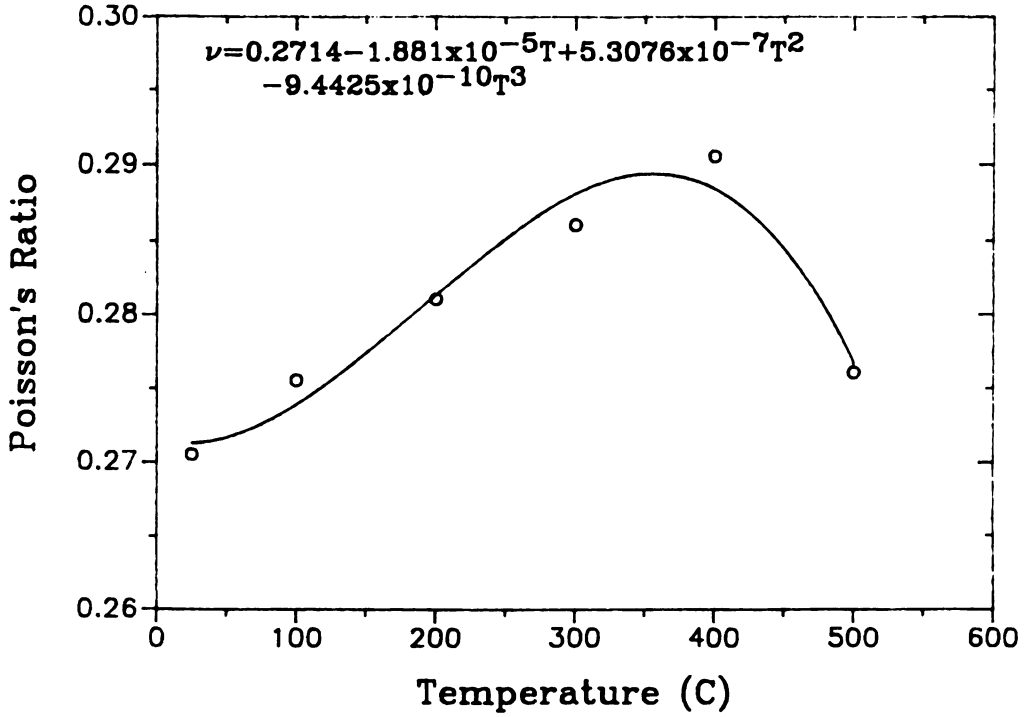

Figure 45(c). Poisson's ratio of Macor glass-ceramic as a function of temperature.

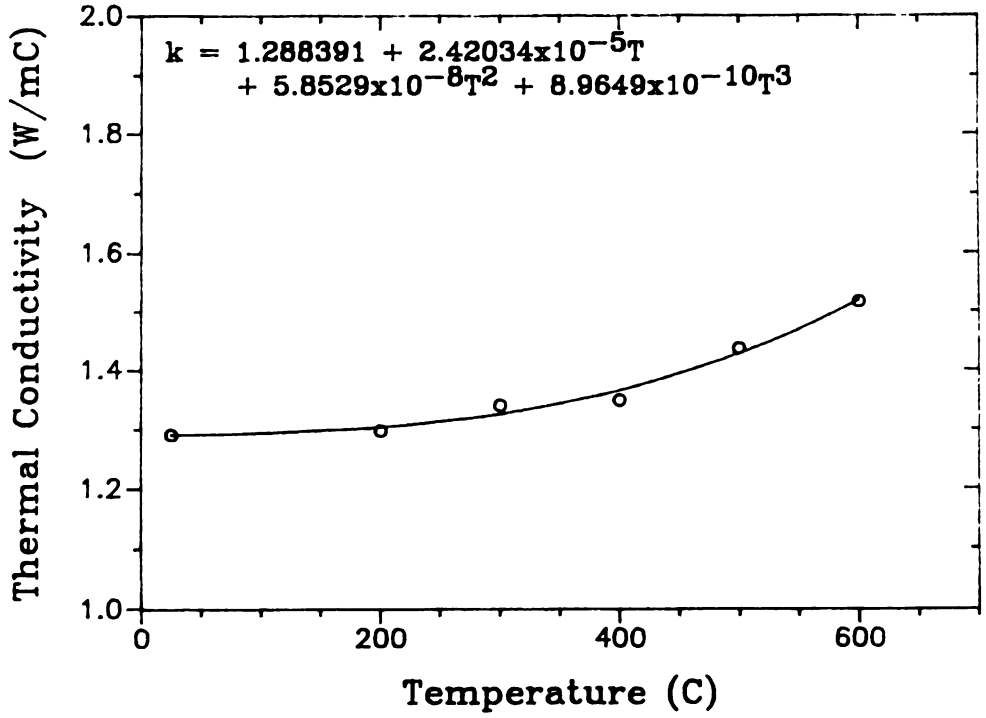

Figure 45(d). Thermal conductivity of Macor glass-ceramic as a function of temperature.

Figures 46 (a) - (c) show the maximum surface thermal stress developed during quenching for TiB_2 with 1.6 mm thickness, Al_2O_3 with 1 mm thickness, and Macor glass-ceramic with 1.785 mm thickness as a function of temperature. A fatigue-like power law relationship (equation 56) can be written in terms of the thermal stress, such that

$$A/E_0 = C\,(\sigma_{th}^{max}/\sigma_f)^q \qquad (56)$$

where σ_{th}^{max} = maximum value of maximum surface thermal stress at a given ΔT (figures 46 (a) - (c))

σ_f = fracture strength of material

C, q = thermal fatigue parameters

Fracture strength values of 308 MPa for TiB_2 [171], 350 MPa for alumina, and 100 MPa for Macor glass-ceramic [172] were used in the analysis. For the plot of $\ln(A/E_0)$ versus $\ln(\sigma_{th}^{max}/\sigma_f)$, the linear regression values of the slope q and intercept $\ln(\sigma_{th}^{max}/\sigma_f)$ are given in table 20 (figure 47).

Thus normalized Young's modulus saturation constants, A/E_0, were calculated as 0.0214 for TiB_2, 0.0085 for alumina, and 0.0026 for Macor glass-ceramic from the values of intercepts for three materials considered, which means that 2.14 percent decrease for TiB_2, 0.85 percent decrease for alumina, and 0.26 percent decrease for Macor glass-ceramic in Young's modulus when the materials reached a saturation damage level under maximum surface thermal stresses of fracture stresses.

Table 20. Linear regression results of $\ln(A/E_0)$ versus $\ln(\sigma_{th}^{max}/\sigma_f)$ (equation 56).

Material	q	intercept	correlation coefficient
TiB_2	2.70 ± 0.65	-3.85 ± 0.35	0.923
Al_2O_3	6.36 ± 1.27	-4.76 ± 0.25	0.945
Macor	2.19 ± 0.33	-5.93 ± 0.41	0.956

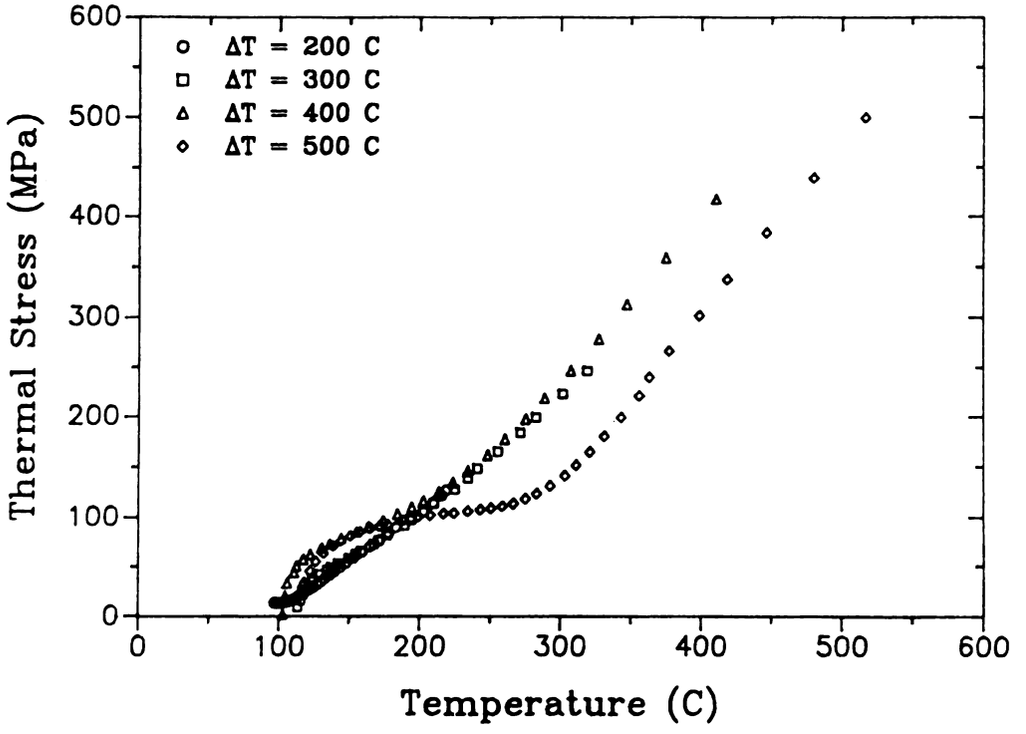

Figure 46(a). Maximum surface tensile stress calculated from measured surface heat transfer coefficient and temperature dependent parameters, E(T), α(T), ν(T) and k(T) for TiB_2 specimen.

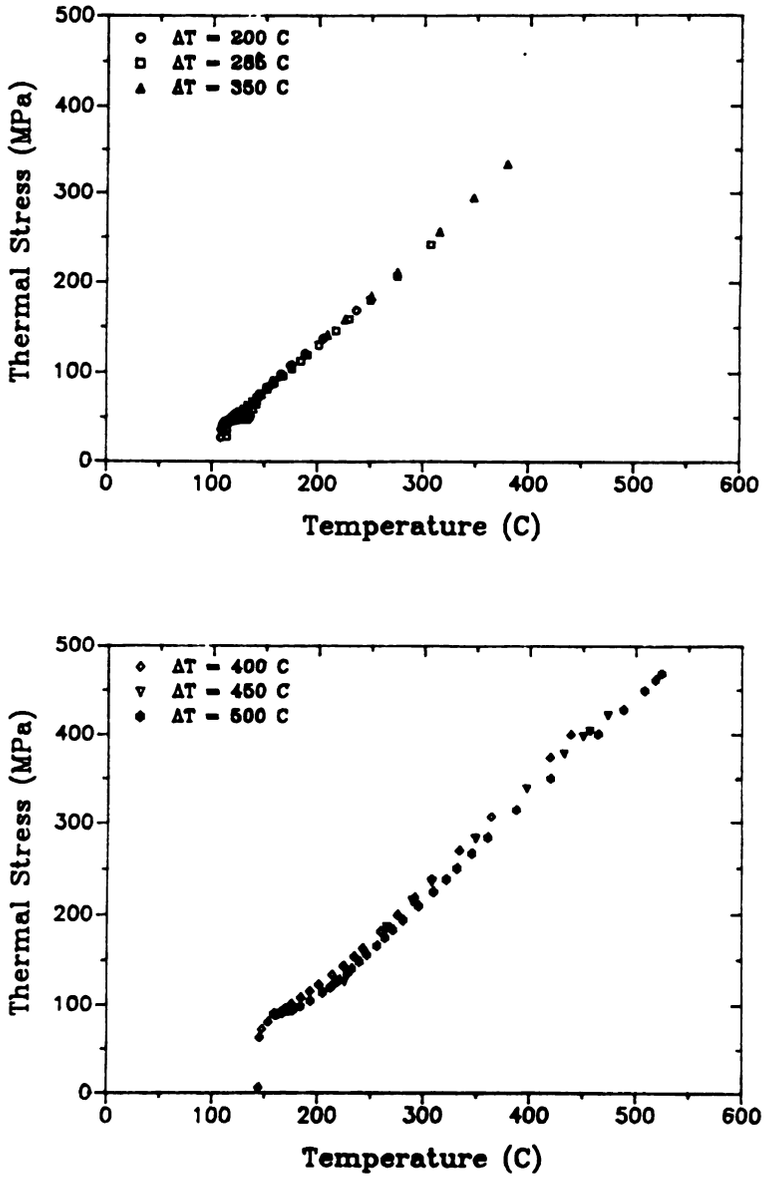

Figure 46(b). Maximum surface tensile stress calculated from measured surface heat transfer coefficient and temperature dependent parameters, E(T), α(T), ν(T) and k(T) for Macor specimen.

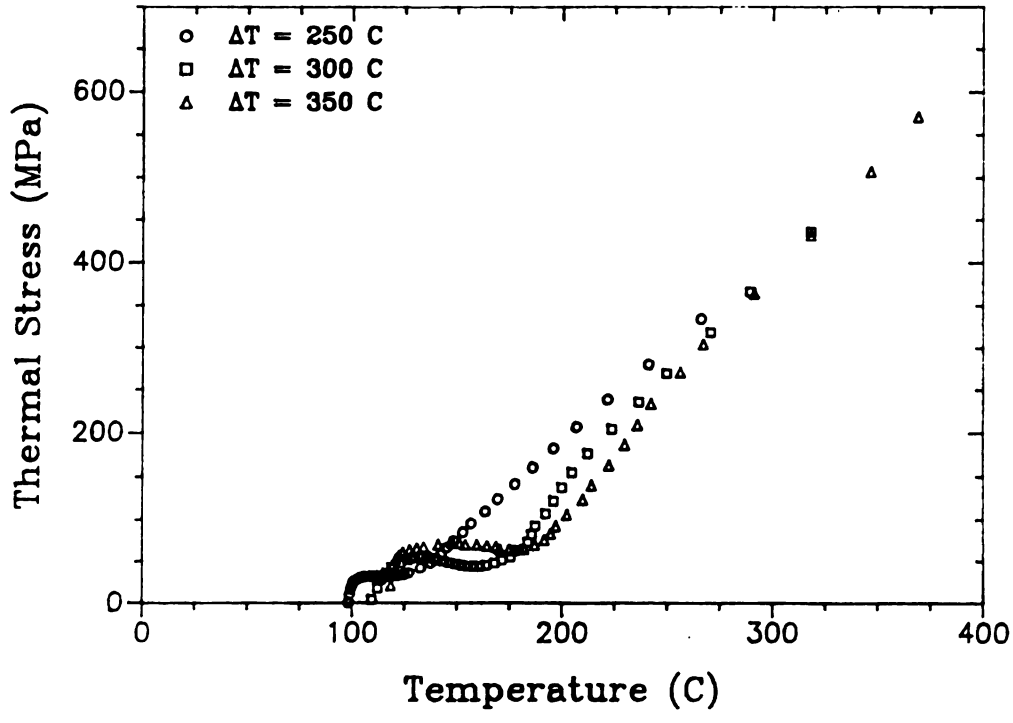

Figure 46(c). Maximum surface tensile stress calculated from measured surface heat transfer coefficient and temperature dependent parameters, E(T), α(T), ν(T) and k(T) for alumina specimen.

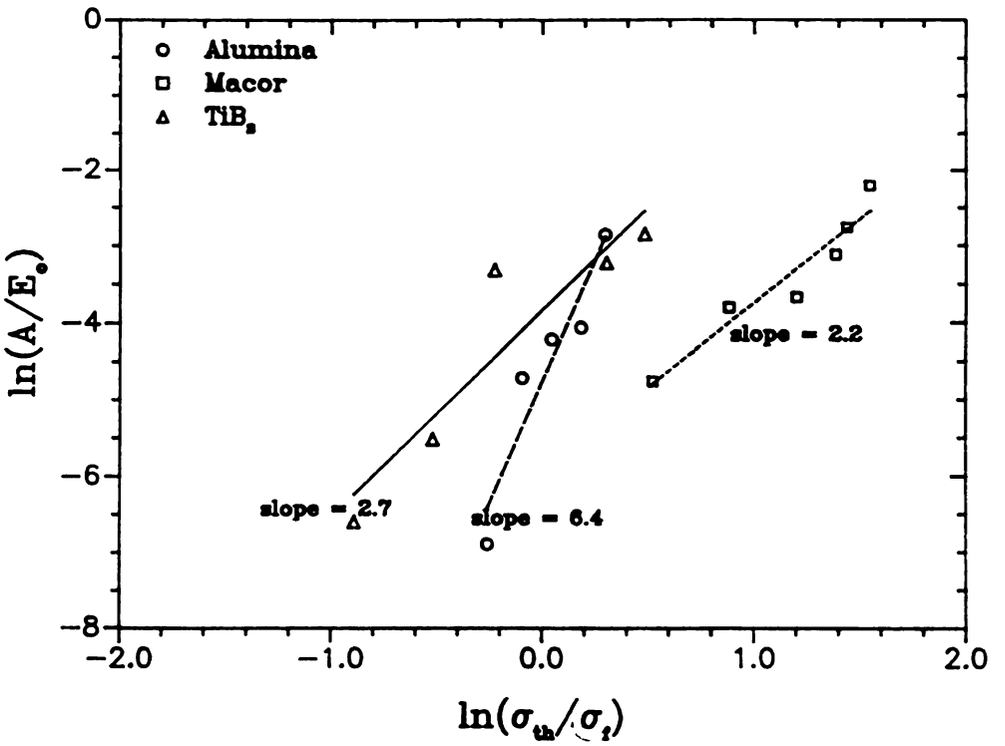

Figure 47. Logarithm of the normalized saturation damage parameter, A/E_0 versus logarithm of the normalized thermal stress.

3.3.4 A comparison of stress intensity factor among TiB_2, Al_2O_3, and Macor glass-ceramic induced by thermal stress

Consider a homogeneous flat plate with an edge crack initially at uniform temperature, T_0. If the plate is suddenly quenched into a medium at a lower temperature, T_∞ (figure 48), then the transient temperature distribution along the thickness direction of the plate may be obtained using the initial boundary conditions,

$$T = T_0 \qquad \text{at } t = 0 \qquad (57a)$$

$$\partial T/\partial x = -h_a(T-T_\infty)/k \qquad \text{on } x = L \qquad (57b)$$

$$\partial T/\partial x = h_a(T-T_\infty)/k \qquad \text{on } x = 0 \qquad (57c)$$

where h_a = surface heat transfer coefficient

k = thermal conductivity of the plate

L = thickness of the plate (figure 48)

The thermal stress in the quenched flat plate may be calculated from transient temperature distribution by applying boundary conditions on the flat plate and the crack surface (figure 48),

$$\sigma_{xx} = 0, \quad \sigma_{xy} = 0 \qquad \text{on } x = 0, L \qquad (58a)$$

$$\sigma_{yy} = 0, \quad \sigma_{xy} = 0 \qquad \text{for } b < x \leq L \text{ on } y = 0 \qquad (58b)$$

Noda et al. [173] formulated the nondimensional maximum transient stress intensity factor as a function of the Biot modulus, h_aL/k and

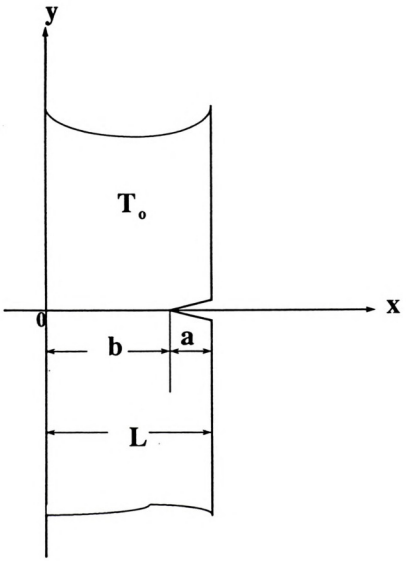

Figure 48. Cracked flat plate initially at temperature T_0 cooled by ambient temperature T_∞ at x = 0, x = L (after [173]).

the nondimensional crack length, a/L via fitting of numerical results [173], where L represents the plate thickness.

$$K_{Imax} = \frac{\alpha E(T_0 - T_a)\, a^{1/2}}{(1-\nu)} \left(\frac{3.04\, e^{3.6\gamma}}{B} + 0.76\, e^{3.7\gamma} - 0.21\, e^{-(15+10000\gamma)/B} \right.$$

where, B = Biot modulus (= hL/k)

γ = nondimensional crack length (= a/L)

α = thermal expansion coefficient

E = Young's modulus

a = crack length

T_0 = temperature of specimen before quenching

T_a = temperature of quenching medium

ν = Poisson's ratio.

In the present study Biot moduli for TiB_2, alumina, and Macor glass-ceramic were calculated from measured maximum surface heat transfer coefficient, h [170] at a given ΔT, specimen dimension, and thermal conductivity at the temperature of specimen before quenching, T_0 for a given ΔT. The maximum stress intensity factor, K_{Imax}, were calculated considering temperature dependent material properties at T_0 for a given ΔT, such as E, α and ν (equation 59).

K_{Imax} for TiB_2, alumina, and Macor glass-ceramic increased rapidly from zero, reached a peak value, and decreased as

nondimensional crack length increased (figures 49(a)-(c)). Pre-existing cracks on the specimen surface can propagate when the stress intensity factor at the crack tip induced by quenching exceeds material's fracture toughness (critical stress intensity factor). The crack propagates until the stress intensity factor at the crack tip is less than a certain stress intensity factor, which is not necessary to be critical stress intensity factor. Very shallow edge cracks do not propagate due to low stress intensity factor but deeper edge cracks with $K_I > K_{IC}$ will propagate (figures 49(a)-(c)).

For example, for Macor machinable glass ceramic (Corning code 9658) with strength of 100 MPa [172] and toughness of 1.7 MPa$\cdot m^{1/2}$ [152] a critical flaw size, a_{max}, of 74.5 μm may be calculated from

$$a_{max} = (K_{Ic}/(Y\ \sigma_f))^2 \qquad (60)$$

where K_{Ic} = critical stress intensity factor (fracture toughness)

Y = geometry factor of crack which is 1.97 for an edge crack loaded in four point loading configuration [174]

σ_f = fracture strength

Equation 60 assumes the specimen is loaded in uniform stress field.

For Macor specimen with ΔT of 200 °C, stress intensity factor did not reach the critical stress intensity factor of Macor 1.7 MPa $m^{1/2}$ up to the maximum strength controlling flaw size 74.5 μm, which is nondimensional crack length of 0.0417) (figure 49 (b)). The surface

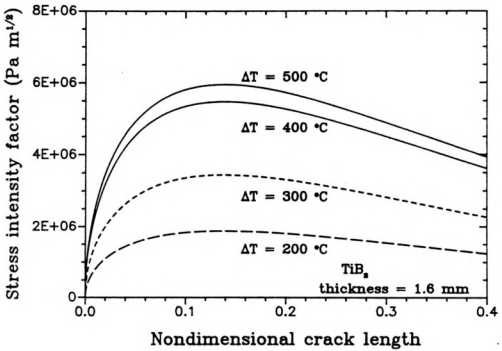

Figure 49(a). Calculated stress intensity factor as a function of nondimensional crack length for (a) TiB_2.

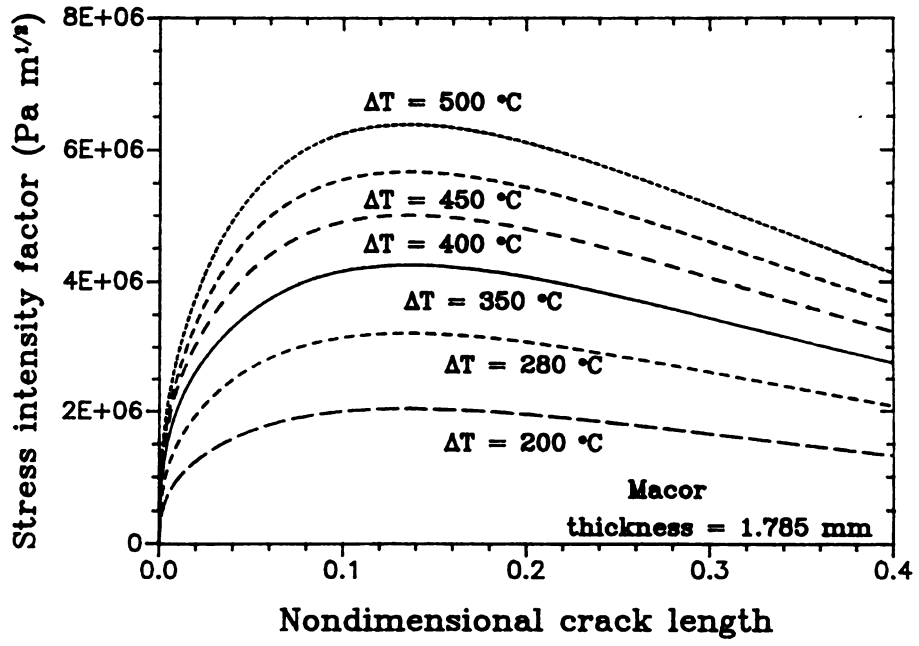

Figure 49(b). Calculated stress intensity factor as a function of nondimensional crack length for (b) Macor.

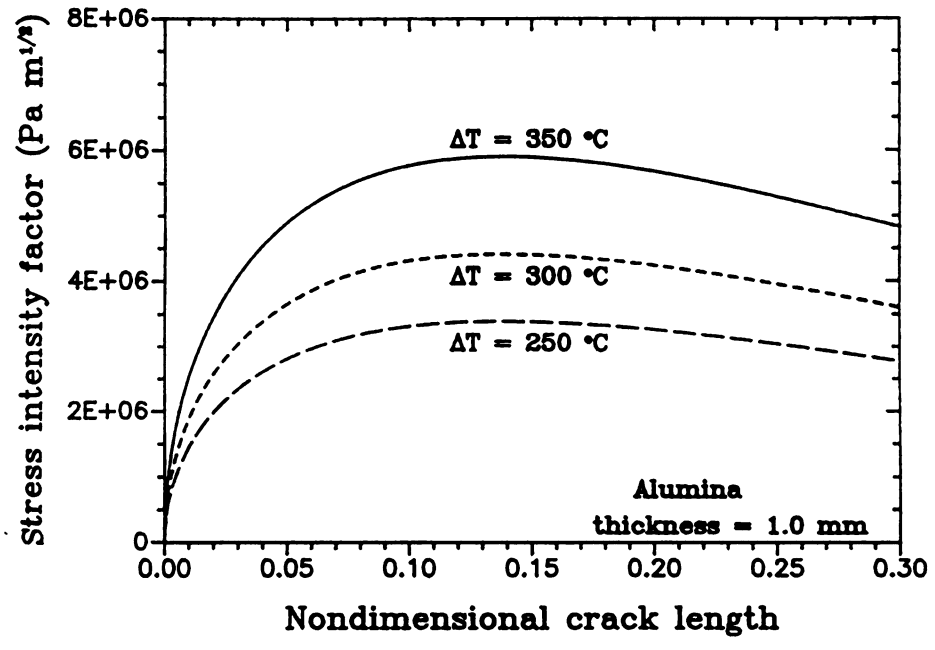

Figure 49(c). Calculated stress intensity factor as a function of nondimensional crack length for (c) alumina.

cracks in the specimen should not propagate and thus the Young's modulus of the specimen would not be reduced, which was experimentally verified [23].

The calculated stress intensity factor had higher value than the critical stress intensity factor of Macor, 1.7 MPa $m^{1/2}$ for crack length between approximately 24 μm (nondimensional crack length of 0.0134) and maximal flaw size, 74.5 μm (nondimensional crack length of 0.0417) for Macor specimen with ΔT of 280 °C (figure 49 (b)). Thus the cracks which have length between approximately 24 μm and maximal flaw size propagate. From figure 49(b) the range of crack length that may have higher stress intensity factor than K_{Ic} increases as ΔT increases. Thus statistically more cracks may involve to propagate for larger ΔT specimens. Also the cracks may propagate longer distance before they stop for larger ΔT specimens.

Effective Young's modulus of specimen having homogeneously distributed microcracks, E, was described in terms of crack size and geometry [76, 78, 97],

$$E = E_0 (1 - f(\nu_0) \epsilon) \qquad (61)$$

where E_0 = Young's modulus of crack-free specimen

$f(\nu_0)$ = a function of undamaged Poisson's ratio, ν_0

ϵ = crack damage parameter, $2N\langle A^2 \rangle/(\pi\langle P \rangle)$, where $\langle A \rangle$ is mean crack area, $\langle P \rangle$ is mean crack perimeter, N is volume number density of cracks.

We set the semiempirical equation for thermal fatigue (equation 34) and the effective Young's modulus equation (equation 61) be equal under the assumption that the modulus decrease in thermal fatigue is attributed to thermomechanical stress induced microcracking. For a large number of cumulative thermal shock cycles n, the normalized saturation parameter A/E_0 at a given ΔT (figure 25) is linearly related to crack damage parameter ϵ .

$$E_0 - A(1 - \exp(-\alpha n)) = E_0(1 - f(\nu_0)\epsilon)$$
$$A/E_0 = f(\nu_0)\epsilon \qquad (62)$$

When thermal stress induced crack shape is assumed as a penny, then the crack damage parameter ϵ increases as crack radius increases. Thus the normalized saturation parameter A/E_0 increases as ΔT increases. Also propagating cracks may stop before the stress transition point from tension to compression as cracks progressed from the surface to the middle (figures 1 and 48). The Young's modulus of thermally shocked Macor specimen may show a steady state value after a sufficient number of thermal shock cycles at a given ΔT.

For alumina specimens, maximal strength controlling flaw is obtained as 15.9 μm (equation 8) from geometry factor of 1.97 [174], fracture toughness of 2.75 MPa $m^{1/2}$, and strength of 350 MPa (Table 21). Even at maximal strength controlling flaw for ΔT = 250, 300 °C,

Table 21. The values of fracture toughness and strength for TiB_2, Al_2O_3 and Macor.

Material	Fracture toughness ($MPa \cdot m^{1/2}$)	Strength (MPa)
TiB_2 [175] (4.5 μm grain size)	5.75 (indentation)	425 (4 point bending)
TiB_2 [175] (40 μm grain size)	3.7 (indentation)	105 (4 point bending)
TiB_2 [176]	N.A.	429 ++
TiB_2 [171] (15 μm grain size)	N.A.+	308 (4 point bending)
Al_2O_3*	2.75+ (Indentation)	350+ (4 point bending)
Macor [152,172]*	1.7 (Double Torsion) 2.0+ (Indentation)	100 (4 point bending)

N.A. = Not Available.
* Materials compared in this study.
\+ Measured by authors.
++ Test method not specified.

figure 49 (c) shows that the stress intensity factor do not exceed the fracture toughness of alumina, 2.75 MPa $m^{1/2}$. But the previous thermal fatigue study [25] showed a decrease in Young's modulus of alumina at ΔT = 250 °C.

Since the strength was determined using four point bending fixture, the maximal strength controlling flaw size was calculated to be 47.2 to 320.0 μm from the geometry factor of 1.97 shown in reference [174] assuming pure bending case (Table 21). For ΔT = 400 and 500 °C, the calculated stress intensity factor for TiB_2 specimens exceed K_{Ic} (figure 49 (a)).

3.4. Effects of Surface Abrasion on the Thermal Fatigue of Ceramics

3.4.1 Thermal shock experiments on abraded and unabraded specimens

Prior to thermal shock testing, the Young's modulus of alumina and Macor specimens were measured before and after abrasion with 240 SiC grit (Table 6).

For the abraded and unabraded specimens of both the polycrystalline alumina and the machinable glass-ceramic, the Young's modulus, E, decreased monotonically with n, the cumulative number of thermal cycles (Figure 50), such that [22-25]

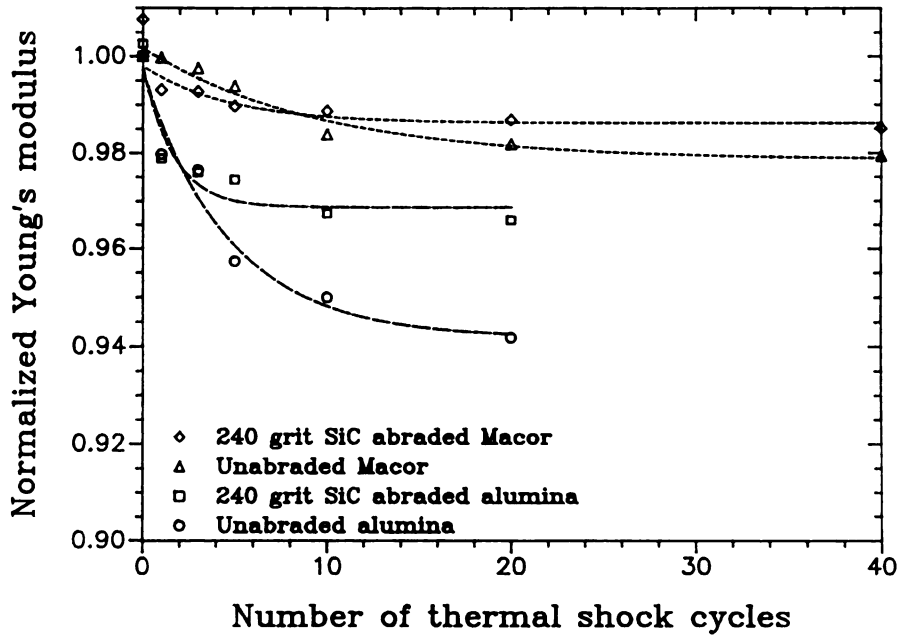

Figure 50. Effect of abrasion on the normalized Young's modulus versus the number of cumulative thermal shock cycles for Macor and alumina. All thermal shocking for each specimen was done from 270 °C into a room temperature deionized water bath.

$$E(n) = E_o - A\,(1 - \exp(-\alpha n)) \qquad (34)$$

where $E(n)$ = Young's modulus as a function of n, the cumulative number of thermal shock cycles

E_o = Young's modulus of unshocked specimen

A = damage saturation constant

α = rate of modulus decrement.

Parameters A and α (Table 22) were calculated via non-linear regression on the E(n) data for both the unabraded and the abraded specimens. Parameter A measures the difference between E_o and E(n) for a large number of cumulative thermal shock cycles, n (equation 34 and Figure 50). The constant α measures the rate of decrease in Young's modulus.

All specimens were quenched repeatedly from 270 °C into a room temperature water bath. The alumina specimens were subjected to a total of 20 quenches (thermal shocks) and the Macor specimens experienced a total of 40 quenches.

The unabraded specimens of polycrystalline alumina and glass-ceramic showed a larger drop in modulus and a smaller rate constant, α, than the abraded specimens (Table 22). In addition, the decrease in the normalized Young's modulus was larger for the alumina than for Macor (figure 50).

The observed changes in the normalized Young's modulus (figure 50) are indicative of thermal-shock induced crack damage [22-25]. The

Table 22. The results of non-linear regression of thermal fatigue data for abraded and unabraded specimens.

Material tested	Macor			Alumina		
	unabraded	abraded		unabraded	abraded	
		before*	after**		before*	after**
E_o (GPa)	59.97	63.35	62.77	293.03	353.31	352.20
A (GPa)	1.385	0.753		16.18	10.36	
α	0.104	0.257		0.216	0.982	
correlation coefficient	0.981	0.949		0.979	0.955	

* Unshocked Young's modulus before abrasion.
** Unshocked Young's modulus after abrasion.

experimental results (figure 50) indicate that for a given material quenched at a fixed quench temperature difference, the thermal shock damage accumulation can be different for abraded versus unabraded specimens.

In the next section, we estimate the net surface stresses for the abraded and the unabraded specimens, taking into account surface-abrasion-induced effects such as compressive surface stresses and changes in the surface heat transfer coefficient.

3.4.2 An estimate of the relative quenched-induced surface stresses for abraded and unabraded specimens

In general, σ_{max}, the maximum quench-induced tensile surface stress for a plate is given by [59]

$$\sigma_{max} = \frac{E \quad \alpha \, \Delta T}{(1 - \nu)} \cdot f(B)^{*} \qquad (54)$$

where E = Young's modulus of the specimen

α = thermal expansion coefficient

ΔT = thermal shock severity

ν = Poisson's ratio

$f(B)$ = a function of the specimen's Biot modulus, where [59]

$$f(B) = (1.5 + 3.25/B)^{-1} \qquad \text{when } 0<B<5 \qquad (55a)$$

$$f(B) = (1.0 + 3.25/B^{2/3})^{-1} \qquad \text{when } 5<B<20 \qquad (55b)$$

$$f(B) = (1.5 + 3.25/B - 0.5\, e^{-16/B})^{-1} \qquad \text{when } 0<B<20. \qquad (55c)$$

---

* Equation (54) assumes an infinite thin plate geometry, which is adequate for our specimens if we neglect edge effects.

The Biot modulus, B, is defined as

$$B = ha/k \tag{5}$$

where h = surface heat transfer coefficient

a = half thickness of the specimen

k = thermal conductivity of the specimen.

Surface abrasion can introduce surface compressive stresses, χ, and alter the surface heat transfer coefficient, h. In order to explore the connection between the various abrasion-induced property changes and thermal shock behavior, we estimated the net surface stresses for unabraded and abraded quenched specimens as

$$\sigma_{net}^{un} = \sigma_{max}^{un} = \frac{E^{un}\ \alpha^{un}\ \Delta T}{(1 - \nu^{un})} \cdot f(B^{un}) \tag{63}$$

and

$$\sigma_{net}^{ab} = |\sigma_{max}^{ab}| - |\chi| \tag{64}$$

where $\sigma_{max}^{ab} = \frac{E^{ab}\ \alpha^{ab}\ \Delta T}{(1 - \nu^{ab})} \cdot f(B^{ab})$

where the superscripts "ab" and "un" refer to the abraded and unabraded states of the parameters defined in equations 5, 54, 55. Estimates of the net surface stresses were made for alumina and Macor using equation 63 and 64 (figure 51 and 52) with a ΔT of 250 °C, which corresponds to the quench from 270 °C to room temperature water that was employed in the experimental phase of this study. Temperature dependent values for all parameters were available for the unabraded states of alumina and Macor [170]. Assumptions involving the magnitude of physical property changes induced by abrasion are discussed below.

Surface abrasion of materials can dramatically increase h for a given material/fluid bath combination. As the surface roughness increases, the number density of boiling nucleation sites increases, thus increasing the surface heat transfer, h, for the boiling nucleation regime (see figure 53 and [75, 177, 178]). For example, in the boiling nucleation regime of n-pentane at atmospheric pressure, the h of a copper plate with a mirror finish increased by up to a factor of 6 as the surface was abraded [75]. Similar trends were observed for nickel and Inconel plates [75]. For 304 stainless steel and Zircalloy-2 tubes cooled by water flow, surface roughness increased h by up to 100 percent [177, 178].[+] In the absence of data on the effects of abrasion on h for ceramics, we assumed that the

---

+ The peak heat flux in the boiling nucleation regime (Figure 53) increased by 100 percent. According to the relation q (heat flux) = h ΔT, h also increased by 100 percent.

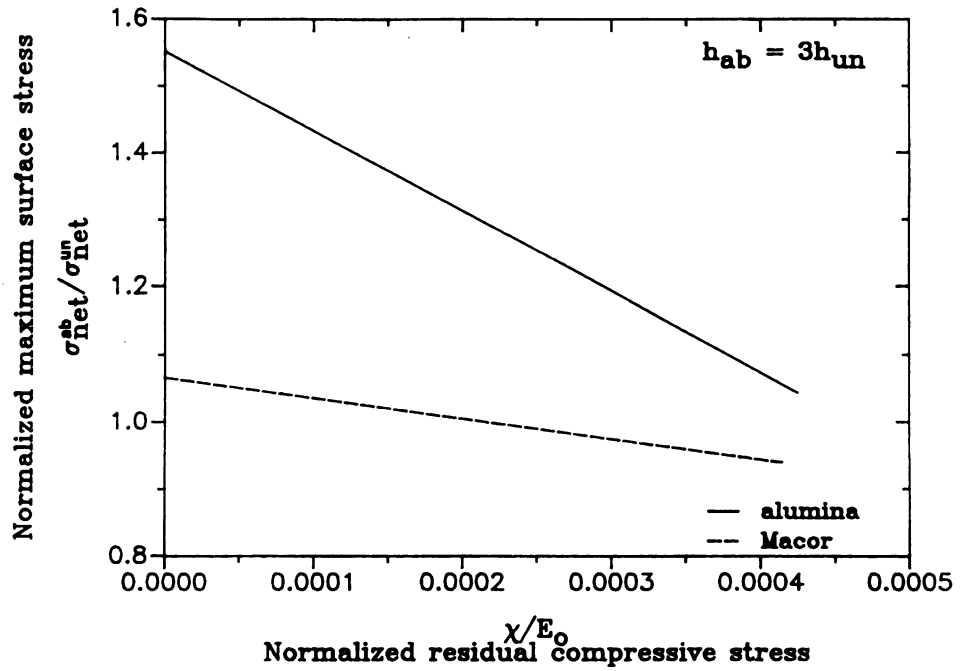

Figure 51. The surface stress ratio, $\sigma^{ab}_{max}/\sigma^{un}_{max}$, versus the ratio of pre-existing compressive surface stress to the unshocked Young's modulus, χ/E_o where $h_{ab} = 3h_{un}$.

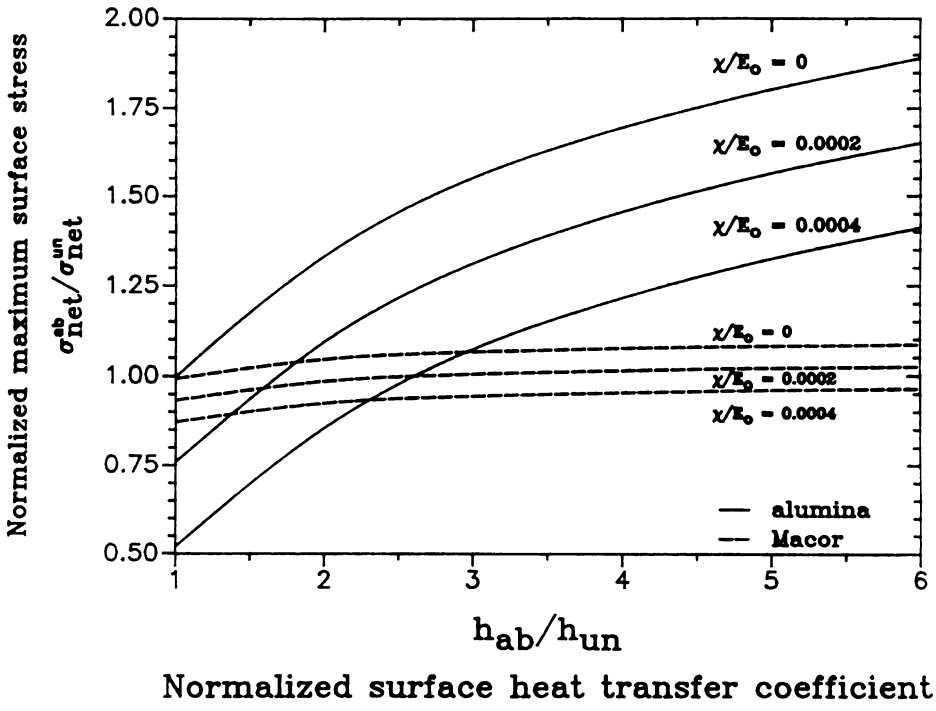

Figure 52. The surface stress ratio, $\sigma^{ab}_{max}/\sigma^{un}_{max}$, versus the relative heat transfer coefficient, h_{ab}/h_{un} at χ/E_o = 0, 0.0002, and 0.0004 for both alumina and Macor.

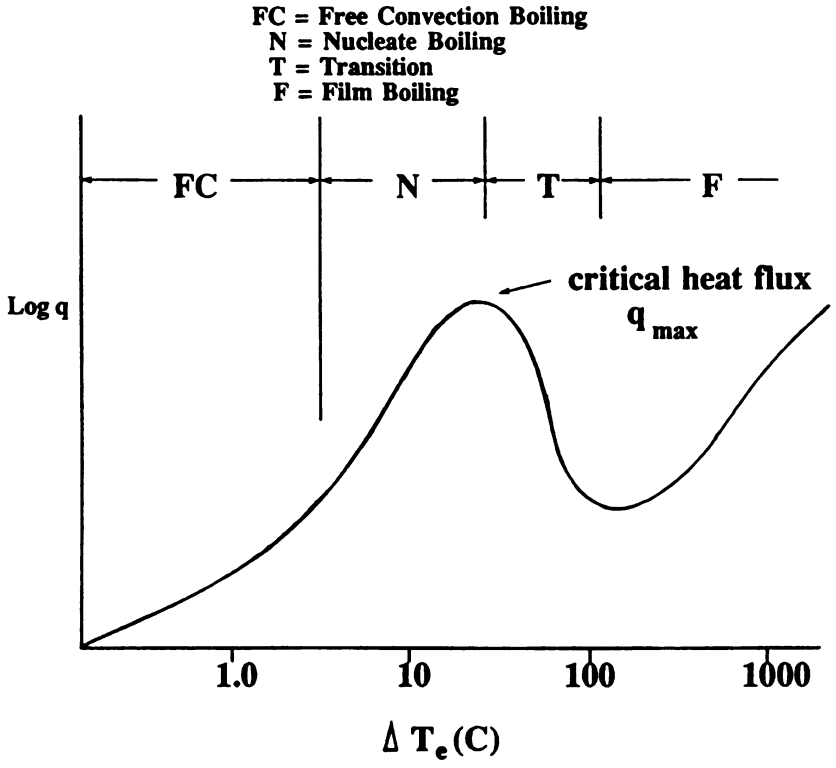

Figure 53. Idealized schematic showing the heat transfer regimes in water [67], where $\Delta T_e = T_s - T_{sat}$, T_s = temperature of specimen surface, T_{sat} = 100 °C for water. For example, if ΔT, the quench temperature difference is 250 °C, ΔT_e is 170 °C .

ratio of h^{ab}/h^{un} ranges from about 1 to 6, in agreement with the data discussed here for other materials [75, 177, 178].

Surface-abrasion-induced residual compressive surface stresses, χ, have been documented for Pyroceram C9606 glass ceramic [71], where a 46 percent abrasion-induced increase in bend strength was found, and for polycrystalline alumina [72], where x-ray diffraction measurements on surface abraded alumina gave χ values as high as 170 MPa [72]. (Our study included polycrystalline alumina and Macor glass ceramics, thus we sought literature on χ for materials similar to those encompassed by our experiments.) In this study, we evaluate equation 6 for a physically reasonable range of χ,

such that $0 < \chi < \chi_{max}$. To estimate χ_{max} (Macor), the upper limit of χ for Macor, we set

$$\frac{\chi_{max}(\text{Macor})}{E_o(\text{Macor})} = \frac{\chi_{max}(\text{alumina})}{E_o(\text{alumina})} \qquad (65)$$

where E_o - the measured Young's modulus for undamaged (neither shocked or abraded) specimens [72, this study]

χ_{max}(alumina) - 170 MPa, the upper limit of the magnitude of χ, as in Lange et al.'s experiment on abraded alumina [72].

Thus, for this study we used the range $0 < \chi/E_o < 0.0004$ for both Macor and alumina. Since the measured E_o for undamaged Macor specimens was about 62.7 GPa, this corresponded to an assumed χ_{max}(Macor) of about 25 MPa (equation 64).+

In this study, the measured surface-abrasion induced changes in the effective elastic moduli were small (Table 22). Thus we used the measured (macroscopic) modulus for the abraded specimens as E^{ab}, and the measured macroscopic modulus of the unabraded specimens as E^{un}. Modulus changes in the specimens' abrasion-effected outer layers were probably larger than the changes indicated by our choice of E^{ab} [97, 179], but since the relative changes in modulus were small, this approximation likely is adequate. In addition, we assumed that Poisson's ratio, thermal conductivity, and thermal expansion are not functions of the abrasion treatment. Actually, microcracks introduced by abrasion may decrease the thermal conductivity of the abraded surfaces, but since abrasion induced microcracks are likely oriented approximately normal to the specimen surface, the changes in thermal conductivity should be small for this case, where the predominant heat flow is also normal to the specimen surface [180].

Equation 64 predicts that for a fixed value of h^{ab}, the surface stress ratio $\sigma^{ab}_{net} / \sigma^{un}_{net}$ decreases as the normalized residual stress

---

+ We did not consider χ_{max} as the maximum attainable value of χ for a given specimen. Instead, we took χ_{max} as a high, but experimentally realizable value of compressive surface stress that corresponds to a high degree of abrasion-induced surface damage.

χ/E_o increases, although the slopes of $\sigma_{net}^{ab} / \sigma_{net}^{un}$ versus χ/E_o differ greatly for alumina and Macor (see figure 3, where h^{ab}/h^{un} is fixed at 3 and a quench from 270 °C into a room temperature water bath is assumed). Although Biot modulus B (equation 5) is a linear function of h, equations 3a - 3c show that the form of f(B) in surface stress equations (equations 55, 63, and 64) depends on the magnitude of B itself. For both Macor and alumina, calculations of B based on direct experimental measurements of h^{un} as a function of temperature [170] and literature values of thermal conductivity k as a function of temperature [163, 164] gave maximum B values as 2.1 and 100 for alumina and Macor, respectively. For large B values, the factor f(B) approaches 1.0. Thus $\sigma_{net}^{ab} / \sigma_{net}^{un}$ becomes insensitive to B (and insensitive to h) for values of B greater than about 10 to 15.

For a thermally shocked plate-shaped specimen of a given material, a large Biot modulus (as was the case for our Macor specimens, as shown in Figure 51) resulted in a net surface stress that changed relatively little with abrasion-induced changes in h. Equations 63 and 64 predict that specimens with a Biot modulus of about 5.0 or less show appreciable changes in the net surface stress as the specimen surface is abraded (as was the case for the alumina specimens in figure 51). Since Biot modulus is a function of specimen geometry, the sensitivity to surface abrasion will be a predictable function of specimen geometry[+], assuming the model represented in

---

+ In equation 4, the Biot modulus is a linear function of plate thickness. For specimen geometries other than plates, B is still a function of a characteristic specimen dimension(s).

equation 63 and 64 gives a reasonable approximation of the net surface stress state.

For alumina specimens (low Biot modulus), the value of σ_{net}^{ab} / σ_{net}^{un} can vary by more than a factor of two as h^{ab}/h^{un} ranges from 1 to 6 and χ/E_o ranges from zero to 0.0004 (figure 52).++ For example, at an intermediate χ/E_o value of 0.0002, σ_{net}^{ab} / σ_{net}^{un} increases from about 0.75 to about 1.65 as h^{ab}/h^{un} increases from 1 to 6. Thus, σ_{net}^{ab} can be either greater than or less than σ_{net}^{un}, depending on the values of the nondimensional parameters χ/E_o and h^{ab}/h^{un}. Of course, the condition $\sigma_{net}^{ab} = \sigma_{net}^{un}$ represents the physical situation in which the net surface stresses in the surface-abraded specimen equals the net surface stresses in the unabraded specimen (which occurs along the line $\sigma_{net}^{ab} / \sigma_{net}^{un} = 1$ in figure 52). As was the case in figure 51, the changes in $\sigma_{net}^{ab} / \sigma_{net}^{un}$ for Macor (with its relatively large Biot modulus) are predicted to be much less than for alumina.

3.4.3 Estimating the surface flaw extension

Abrasion induced changes in the flaw population may be related to the net surface stresses through the stress intensity factor, K. Thermal shock loads are transient in nature, and thermoelastic stresses are a strong function of position within the specimen [60].

++ In figure 52, the specimen dimensions were assumed to be the same as for the alumina and Macor specimens included in this study (Table 6). Specimen dimensions are of interest since B is a function of plate thickness (equation 5).

(For example, if we consider an axis z oriented normal to a free surface of a plate-shaped specimen where z = 0 is at the plate surface, then the thermal quench stresses can decrease rapidly as one proceeds from z = 0 toward the mid-plane of the plate [60].) Moreover, the crack growth may be dynamic in the rapid transient overstress that thermal quench loading can represent. A dynamic stress intensity factor, K_{ID}, for dynamic crack extension, for example, may be written as [95, 181]

$$K_{ID} = K_{IS} \; g(\Delta a) \; f(\dot{a}) \tag{66}$$

where $g(\Delta a)$ is the Eshelby crack advance integral, $f(\dot{a})$ is a function of crack velocity, and K_{IS} is the static form of the stress intensity factor [95]. For crack velocities that are small with respect to the Rayleigh velocity, $f(\dot{a})$ is approximately unity. In addition, $g(\Delta a)$ is a well behaved function of the relative crack advance [95] so that the relative trends in the behaviors of abraded versus unabraded specimens likely may be outlined at least roughly by considering the ratio of the static stress intensities, K_{IS}, such that

$$\frac{K_{IS}^{ab}}{K_{IS}^{un}} = \frac{Y^{ab} \, \sigma_{net}^{ab} \, (c^{ab})^{1/2}}{Y^{un} \, \sigma_{net}^{un} \, (c^{un})^{1/2}} \tag{67}$$

where Y and c refer to the crack geometry factor and flaw length, respectively. As before the superscript "ab" refers to the abraded specimen properties and "un" refers to the unabraded specimen properties.

If we approximate $Y^{ab} = Y^{un}$, then the relative static stress intensity factor $K_{IS}^{ab} / K_{IS}^{un}$ is just the product of square root of the crack length ratio c^{ab}/c^{un} and the stress ratio $\sigma_{net}^{ab} / \sigma_{net}^{un}$ plotted in figures 51 and 52. Thus, the square root of the relative crack lengths and the relative surface stresses $\sigma_{net}^{ab} / \sigma_{net}^{un}$ should be considered in terms of crack propagation. As discussed above, surface abrasion not only changes the flaw population, it also can induce surface compressive stresses and changes in h that in turn modify the net surface stresses. Although it has not been treated here, crack propagation during cyclic thermal quenching will release and redistribute the residual stresses, χ, such that χ itself is likely a function of the evolving thermal shock damage.

Upon thermal quenching from 270 °C into a room temperature water bath, the experimentally observed elastic modulus decrement for unabraded polycrystalline alumina is much more than for polycrystalline alumina abraded by 240 grit SiC. Thus, although surface abrasion with 240 SiC grit almost certainly means that the mean flaw size for the abraded specimens was greater than the mean flaw size of the unabraded specimens, the net effect of surface abrasion (in this study) was that the unabraded specimens suffered greater damage upon thermal cycling than did the abraded specimen.

This apparently contradictory result may be understood in terms of figures 51 and 52 and the discussion above.

The interplay among the the abrasion-induced effects such as compressive surface stresses, changes in h (and other physical properties), and changes in the flaw population are complex and merit further study. In lieu of the stress intensity factor approach, one might consider using Hasselman's thermal shock theory involving elastic strain energy and thermal shock induced crack propagation [6]. However, Hasselman's thermal shock theory does not consider the effects of surface abrasion, including the modified surface-layer modulus, residual compressive stresses, and abrasion-induced changes in the heat transfer coefficient.

3.5 The Effect of Surface Limited Microcracks on the Effective Young's Modulus of Ceramics

3.5.1 Analysis

3.5.1.1 Layer Composite Model

Surface-limited microcrack distributions are distributions such that the microcracks tend to occur at or near the specimen surface, rather than in the specimen bulk. In this study, such distributions are modeled in terms of a layered composite, where a reduced-modulus microcracked outer layer is "bonded" to an undamaged substrate (figure 54). In order to discuss a specific geometry, we shall consider bar-

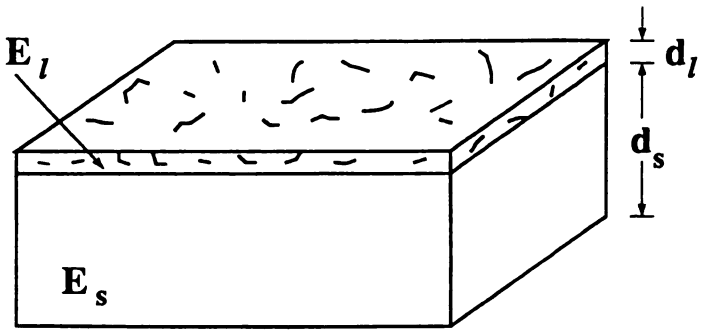

Two layer composite model

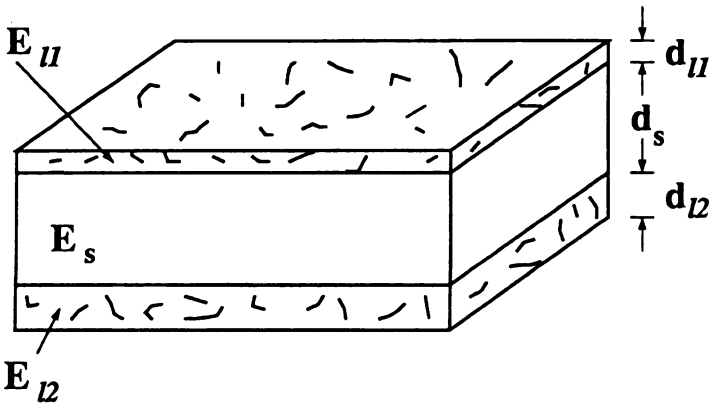

Three layer composite model

Figure 54. Schematic of (a) two and (b) three layer composite model.

shaped specimens. Specimens having microcracks on both long transverse surfaces (figure 2), for example, may be considered as a three layer composite composed of reduced Young's modulus microcracked layers on the top and bottom surfaces and an undamaged layer between top and bottom surfaces (figure 54).

Microcracking in each damaged layer can be expressed in terms of

$$\frac{(E_0 - E)}{E_0} = \frac{2}{\pi} f\, G'\, N_v = f\, G\, N_v \qquad (68)$$

where f is a function of the spatial orientation of the microcracks [76, 78]. The microcrack geometry factor, G, is given by $2G'/\pi$, where $G' = \langle A^2 \rangle / \langle P \rangle$. $\langle A \rangle$ and $\langle P \rangle$ are the mean microcrack area and the mean microcrack perimeter, respectively. N_v is the crack number density per unit volume of the microcracked material. The form of equation 68 emphasizes the functional relationships for crack orientation, crack geometry, and crack number density which we shall explore in this paper.

3.5.1.1.1 Rule of Mixtures Model

The overall Young's modulus of surface microcracked specimens can be modeled using the rule of mixtures assuming a two layer composite for microcracks on a single surface, while a three layer composite may be used for specimens microcracked on both surfaces (figure 54). The

rule of mixtures expression for $\bar{E}_{2_{ROM}}$, the overall modulus of a two layer composite is

$$\bar{E}_{2_{ROM}} = E_{\ell} v_{\ell} + E_s v_s \tag{69}$$

where the subscripts ℓ and s refer to damaged layer and undamaged substrate layer respectively for the moduli E and volume fraction v.

The rule of mixtures expression for $\bar{E}_{3_{ROM}}$, the overall modulus of a three layer composite is

$$\bar{E}_{3_{ROM}} = E_{\ell 1} v_{\ell 1} + E_s v_s + E_{\ell 2} v_{\ell 2} \tag{70}$$

where the subscripts $\ell 1$, $\ell 2$, and s refer to damaged layer 1, damaged layer 2, and undamaged substrate layer for the moduli E and volume fraction v, respectively (Appendix B).

The layer modulus for each of the two microcrack damaged layers can expressed as [76-78]

$$E_{\ell 1} = E_s (1 - f_1 G_{\ell 1} N_{\ell 1}) \tag{71a}$$

$$E_{\ell 2} = E_s (1 - f_2 G_{\ell 2} N_{\ell 2}) \tag{71b}$$

Thus, $\bar{E}_{3_{ROM}}$ may be expressed as

$$\bar{E}_{3_{ROM}} = E_s(1 - f_1 G_{\ell 1} N_{\ell 1}) v_{\ell 1} + E_s(1 - v_{\ell 1} - v_{\ell 2}) + E_s(1 - f_2 G_{\ell 2} N_{\ell 2}) v_{\ell 2} \quad \text{or,}$$

$$\frac{\bar{E}_{3ROM}}{E_s} = (1 - f_1 G_{\ell 1} N_{\ell 1}) v_{\ell 1} + (1 - v_{\ell 1} - v_{\ell 2}) + (1 - f_2 G_{\ell 2} N_{\ell 2}) v_{\ell 2} \quad (72)$$

where $N_{\ell 1}$, $N_{\ell 2}$ = number density of cracks in microcracked layer 1 and 2 respectively

$N_{\ell 1} v_{\ell 1} = N_{v1} = n_{\ell 1}/V_{specimen}$

$N_{\ell 2} v_{\ell 2} = N_{v2} = n_{\ell 2}/V_{specimen}$

$n_{\ell 1}$ = number of cracks in microcracked layer 1

$n_{\ell 2}$ = number of cracks in microcracked layer 2.

Therefore,

$$\frac{(E_s - \bar{E}_{3ROM})}{E_s} = f_1 G_{\ell 1} N_{\ell 1} v_{\ell 1} + f_2 G_{\ell 2} N_{\ell 2} v_{\ell 2}$$

$$= f_1 G_{\ell 1} N_{v1} + f_2 G_{\ell 2} N_{v2} \quad (73)$$

If the geometry (shape and size) and crack alignment are the same for layers $\ell 1$ and $\ell 2$, then

$f_1 = f_2 = f$ alignment

$G_{\ell 1} = G_{\ell 2} = G_{\ell}$ geometry

and

$$\frac{(E_s - \bar{E}_{s_{ROM}})}{E_s} = f\, G_\ell [N_{\ell 1} v_{\ell 1} + N_{\ell 2} v_{\ell 2}] = f\, G_\ell [\, N_{v1} + N_{v2}\,] = f\, G_\ell N_v \quad (74)$$

where, $N_{v1} + N_{v2} = (n_{\ell 1} + n_{\ell 2})/V_{specimen} = n_{total}\ /V_{specimen} = N_v$

For the two-layer case (one microcracked layer and one undamaged layer), the equation for the relative Young's modulus change becomes

$$\frac{(E_s - \bar{E}_{2_{ROM}})}{E_s} = v_\ell\ f\ G_\ell\ N_\ell = f\ G_\ell\ N_v. \quad (75)$$

Thus, for the ROM model, the normalized Young's modulus change induced by microcracking, $(E_s - E)/E_s$ can be expressed as a linear function of the volume microcrack number density and the crack geometry parameter (figure 55). The form of equations 74 and 75 show that the ROM models for the specimens having one or two microcracked layers can be written in terms of N_v, the crack number density per unit volume. (In order to obtain equation 74, we considered the special case where the alignment factor f and the geometry factor G where identical for the two microcracked layers). Thus, Rule of Mixtures model for surface limited crack distributions can be written in the same functional form as that for equation 68, which describes a microcracked body having homogeneously distributed microcracks. Therefore, in the ROM model we can imagine the modulus under tensile loading as being equivalent for the (1) the layer model, where microcracks are confined within a designated surface layer or (2) a

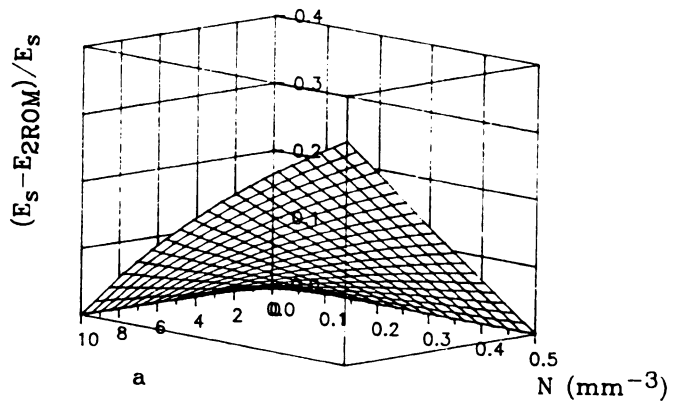

Figure 55(a). The relationship between a, the volume number density of cracks in layer, and the normalized Young's modulus change for (a) two layer composite based on rule of mixtures model (when fG = 0.1).

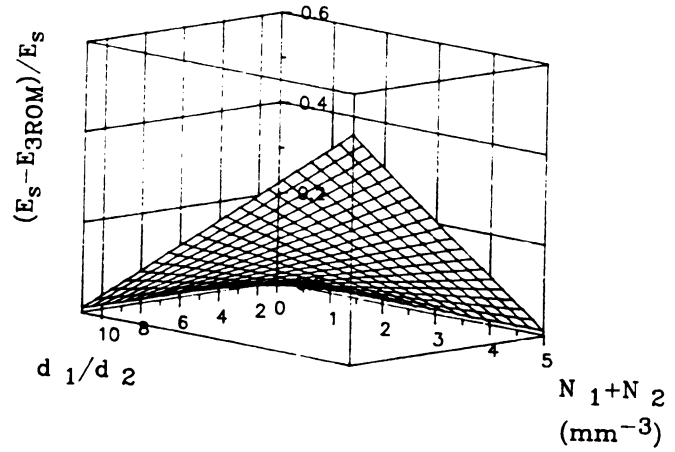

Figure 55(b). The relationship between $d_{\ell 1}/d_{\ell 2}$, the volume number density of cracks in layers, and the normalized Young's modulus change for (b) three layer composite based on rule of mixtures model (when fG = 0.1, $d_{\ell 2}$ = 0.1 x bar thickness).

homogeneous model, where the layer constraint are relaxed and the microcracks are distributed over the entire specimen volume.

If we label layer thicknesses as

$d_{\ell 1}$ = thickness of microcracked layer 1

$d_{\ell 2}$ = thickness of microcracked layer 2

d_s = thickness of the undamaged layer,

and the relative layer thickness as $R_1 = d_{\ell 1}/d_s$, $R_2 = d_{\ell 2}/d_s$, then $\bar{E}_{3_{ROM}}$ can be expressed as

$$\begin{aligned}\bar{E}_{3_{ROM}} &= (E_{\ell 1}d_{\ell 1} + E_s d_s + E_{\ell 2}d_{\ell 2})/(d_{\ell 1} + d_s + d_{\ell 2}) \\ &= (E_{\ell 1}R_1 + E_s + E_{\ell 2}R_2)/(R_1 + 1 + R_2) \\ &= E_s(1 - f_1 G_{\ell 1} N_{\ell 1})R_1/(R_1 + 1 + R_2) + E_s/(R_1 + 1 + R_2) \\ &\quad + E_s(1 - f_2 G_{\ell 2} N_{\ell 2})R_2/(R_1 + 1 + R_2) \qquad (76)\end{aligned}$$

Rearranging equation 76 gives,

$$\frac{(E_s - \bar{E}_{3_{ROM}})}{E_s} = \frac{f_1 G_{\ell 1} N_{\ell 1}R_1 + f_2 G_{\ell 2} N_{\ell 2}R_2}{R_1 + 1 + R_2} \qquad (77)$$

If the geometry (shape and size) and crack alignment (randomly oriented or aligned) are the same for layers 1 and 2, then

$$\frac{(E_s - \bar{E}_{3_{ROM}})}{E_s} = f G_{\ell} \frac{(N_{\ell 1}R_1 + N_{\ell 2}R_2)}{R_1 + 1 + R_2} \qquad (78)$$

For the two-layer case (one microcracked layer and one undamaged layer), the equation for the relative Young's modulus change becomes

$$\frac{(E_s - \dot{E}_{2ROM})}{E_s} = \frac{a}{a+1} \cdot f\, G_\ell\, N_\ell \qquad (79)$$

where a is d_ℓ/d_s (figure 56).

3.5.1.1.2 Dynamic Beam Vibration Model

The overall Young's modulus of surface microcracked specimens can be modeled using a dynamic beam vibration theory assuming a two layer composite for specimens microcracked on single surface (figure 54) [Appendix C].

$$\dot{E}_{2DYN} = E_\ell \frac{I_\ell}{(I_\ell + I_s)} + E_s \frac{I_s}{(I_\ell + I_s)} \quad \text{(figure 57)} \qquad (80)$$

$$I_s = (d_s^3/3 - d_s^2 d + d_s d^2)w \qquad (81)$$

$$I_\ell = (d_\ell^3/3 + d_\ell^2 d + d_\ell d^2)w \qquad (82)$$

$$d = \frac{(E_s d_s^2 - E_\ell d_\ell^2)}{(2E_s d_s + 2E_\ell d_\ell)} \qquad (83)$$

where, d = distance between neutral plane and the interface of microcracked layer and undamaged layer (figure 54)

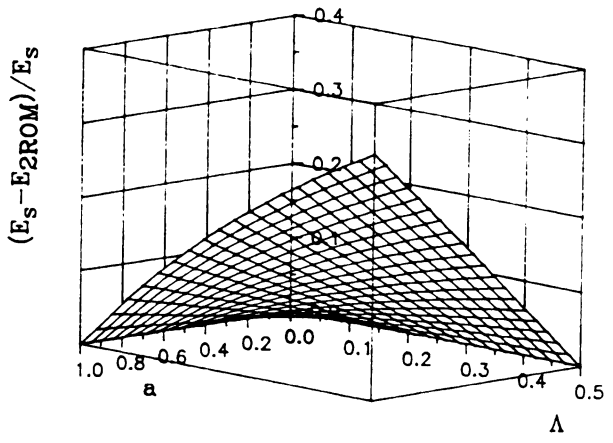

Figure 56(a). The relationship between a, Λ (= $fG_\ell N_\ell$) and the normalized Young's modulus change for (a) two layer composite based on rule of mixtures model.

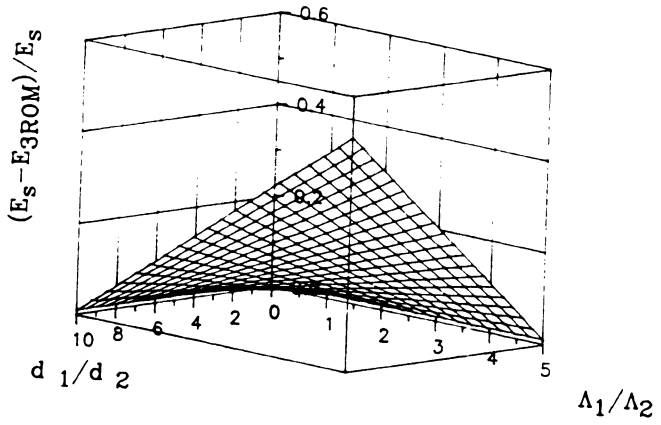

Figure 56(b). The relationship between $d_{\ell 1}/d_{\ell 2}$, Λ_1/Λ_2(= $f_1G_{\ell 1}N_{\ell 1}/f_1G_{\ell 1}N_{\ell 1}$), and the normalized Young's modulus change for (a) three layer composite based on rule of mixtures model (when Λ_2 = 0.1, $d_{\ell 2}$ = 0.1 x bar thickness).

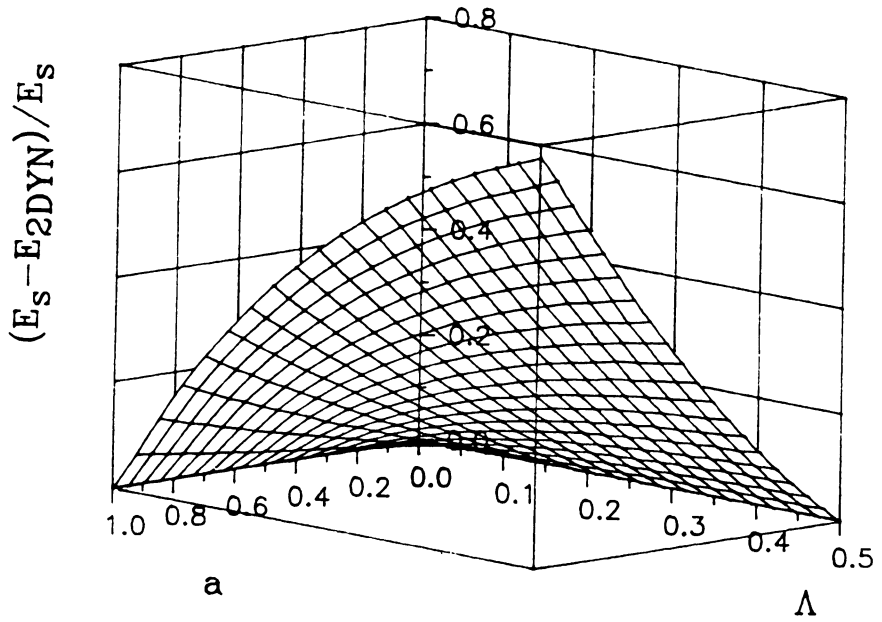

Figure 57. The relationship between a, Λ (= $fG_\ell N_\ell$) and the normalized Young's modulus change for (a) two layer composite based on dynamic beam vibration model.

w = width of the specimen

d_ℓ = thickness of layer

d_s = thickness of substrate

E_ℓ = layer modulus

E_s = substrate modulus

For two layer composite model, the Young's modulus of layer can be related with that of substrate in terms of a function of undamaged Poisson's ratio, f, crack damage parameter, ϵ [76-78].

$$E_\ell = E_s (1 - f \epsilon_\ell) \tag{84}$$

where, $\epsilon_\ell = \frac{2N_\ell}{\pi} \cdot \frac{\langle A^2 \rangle}{\langle P \rangle}$

N_ℓ = number of cracks / volume of layer

A = area of crack

P = perimeter of crack

Inserting equation 84 into 83 gives

$$d = \frac{(d_s^2 - d_\ell^2 + d_\ell^2 f \epsilon_\ell)}{2(d_s + d_\ell - d_\ell f \epsilon_\ell)} \tag{83a}$$

$$= \frac{(d_s^2 - d_\ell^2 + d_\ell C_1)}{2(d_s + d_\ell - C_1)} \tag{83b}$$

where, $C_1 = d_\ell \; f \; \epsilon_\ell = f \; \epsilon_A$ (85)

$$\epsilon_A = \frac{2N_A}{\pi} \cdot \frac{\langle A^2 \rangle}{\langle P \rangle}$$

N_A = number density of cracks per area

$d_\ell + d_s = t$ (= thickness) for two layer composite model

$$d_s^2 - d_\ell^2 = (d_s+d_\ell)(d_s-d_\ell) = td_s - td_\ell,$$

Thus equation 83b becomes

$$d = \frac{(td_s - td_\ell + d_\ell C_1)}{2(t - C_1)} \qquad (83c)$$

$$= \frac{d_s}{2(1-C_2)} - \frac{d_\ell}{2} \qquad (83d)$$

where, $C_2 = C_1/t = d_\ell \; f \; \epsilon_\ell/t = f \; \epsilon_A/t = f \; \epsilon_V$ (86)

$$\epsilon_V = \frac{2N_V}{\pi} \cdot \frac{\langle A^2 \rangle}{\langle P \rangle}$$

N_V = number density of cracks per whole specimen

For the simplicity of further calculation, let's define $\beta = 1/(1-C_2)$. Then equation 83d becomes

$$d = (\beta d_s - d_\ell)/2 \qquad (83f)$$

Inserting equation 83f into equation 81 and defining $a = d_\ell/d_s$ gives

$$I_s = \frac{[\, d_s^3\, ((4 - 6\beta + 3\beta^2) + 6(1-\beta)a + 3a^2)]\, w}{12} \qquad (81a)$$

When C_2 is small, $\beta = 1/(1 - C_2) \approx 1 + C_2$, $C_2^2 \approx 0$. Then equation 81a becomes

$$I_s = \frac{d_s^3\, (1 + 3a^2 - 6aC_2)\, w}{12} \qquad (81b)$$

Inserting equation 83f into equation 82 and defining $a = d_\ell/d_s$ give

$$I_\ell = \frac{d_s^3\, (a^3 + 3a + 6aC_2)\, w}{12} \qquad (82a)$$

Then

$$I_s + I_\ell = \frac{d_s^3\, (1 + a)^3\, w}{12} \qquad (87)$$

Inserting equations 81b, 82a, 84 and 87 into equation 80 gives

$$\tilde{E}_{2_{DYN}} = \frac{E_\ell\, (a^3 + 3a + 6aC_2)}{(1 + a)^3} + \frac{E_s\, (3a^2 + 1 - 6aC_2)}{(1 + a)^3}$$

$$= \frac{E_s (1 - f \epsilon_\ell)(a^3 + 3a + 6aC_2)}{(1 + a)^3} + \frac{E_s (3a^2 + 1 - 6aC_2)}{(1 + a)^3}$$

$$= \frac{E_s \{(1 + a)^3 - (a^3 + a^2 + 3a + 3)C_2 - 6(1 + a)C_2^2\}}{(1 + a)^3} \qquad (80a)$$

When C_2 is small, C_2^2 approaches 0, thus $\bar{E}_{2DYN}$ becomes

$$\bar{E}_{2DYN} = E_s \cdot \left[1 - \frac{(a^3 + a^2 + 3a + 3)C_2}{(1 + a)^3} \right] \qquad (80b)$$

$$= E_s \cdot \left[1 - \frac{(a^2 + 3)}{(1 + a)^2} C_2 \right] \qquad (80c)$$

where, $a = d_\ell / d_s$

$C_2 = C_1/t = d_\ell \, f \, \epsilon_\ell / t$

As a approaches zero, d_ℓ approaches zero, which in turn means that C_2 approaches zero. When C_2 approaches zero, $\bar{E}_{2DYN}$ approaches the undamaged modulus, E_s. When a approaches infinity, $\bar{E}_{2DYN}$ becomes $E_s(1 - f \epsilon_V)$ (figure 58).

For specimens microcracked on both surfaces (figure 54), the overall Young's modulus of three layer composites, $\bar{E}_{3DYN}$, can be expressed in terms of dynamic beam vibration theory [Appendix C]

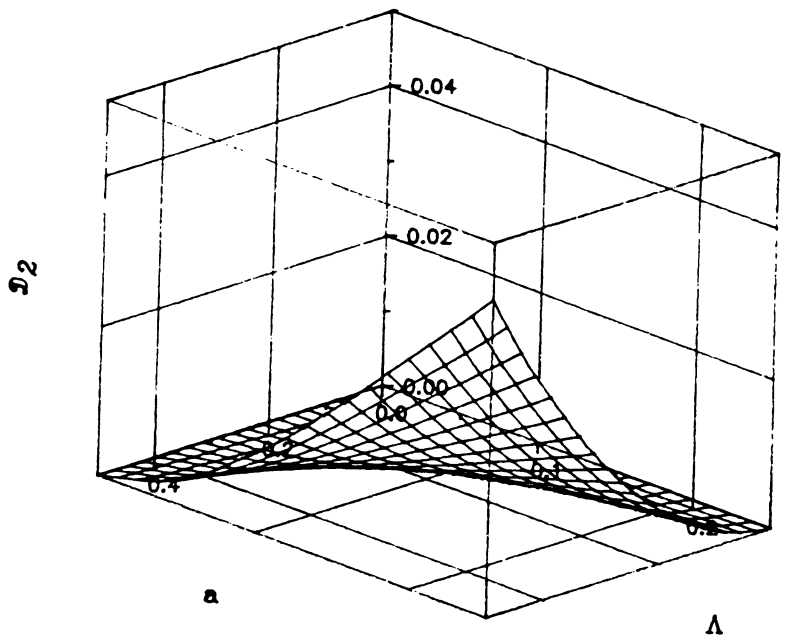

Figure 58. The relationship between a, Λ, and the difference between full (equation 80) and approximation (equation 80c) in normalized Young's modulus change of two layer composite.

$$\bar{E}_{3DYN} = E_{\ell 1}\frac{I_{\ell 1}}{(I_{\ell 1} + I_s + I_{\ell 2})} + E_s\frac{I_s}{(I_{\ell 1} + I_s + I_{\ell 2})} + E_{\ell 2}\frac{I_{\ell 2}}{(I_{\ell 1} + I_s + I_{\ell 2})} \quad \text{(figure 59)} \qquad (88)$$

$$I_{\ell 1} = \left[(d_s - d)^2 d_{\ell 1} + (d_s - d)d_{\ell 1}^2 + \frac{d_{\ell 1}^3}{3}\right] w \qquad (89)$$

$$I_s = \left[\frac{d_s^3}{3} - d_s^2 d + d_s d^2\right] w \qquad (90)$$

$$I_{\ell 2} = \left[\frac{d_{\ell 2}^3}{3} + d_{\ell 2}^2 d + d_{\ell 2} d^2\right] w \qquad (91)$$

where, $$d = \frac{(E_{\ell 1} d_{\ell 1}^2 + 2E_{\ell 1} d_{\ell 1} d_s + E_s d_s^2 - E_{\ell 2} d_{\ell 2}^2)}{(2E_{\ell 1} d_{\ell 1} + 2E_s d_s + 2E_{\ell 2} d_{\ell 2})} \qquad (92)$$

w = width of the specimen

$E_{\ell 1}, E_{\ell 2}$ = modulus of layer 1 and layer 2, respectively

$d_{\ell 1}, d_{\ell 2}$ = thickness of layer 1 and layer 2, respectively.

For three layer composite model, the Young's modulus of layer 1 and layer 2 can be related with that of substrate in terms of a function of undamaged Poisson's ratio, f, crack damage parameter, ϵ. Inserting equations 71a and 71b into equation 92

$$d = \frac{t(d_{\ell 1} + d_s - d_{\ell 2}) - C_{a1}(d_{\ell 1} + 2d_s) + C_{a2} d_{\ell 2}}{2(t - C_{a1} - C_{a2})} \qquad (92a)$$

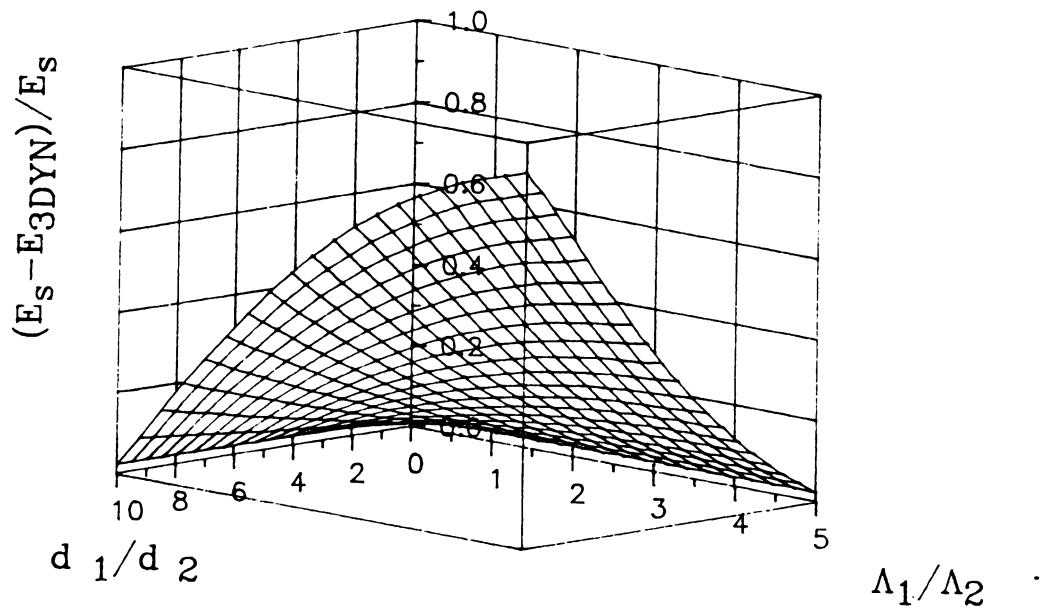

Figure 59. The relationship between $d_{\ell 1}/d_{\ell 2}$, Λ_1/Λ_2, and the normalized Young's modulus change for (a) three layer composite based on dynamic beam vibration model. (when Λ_2 = 0.1, $d_{\ell 2}$ = 0.1 x bar thickness)

$$= \frac{(d_{\ell 1} + d_s - d_{\ell 2}) - C_{b1}(d_{\ell 1} + 2d_s) + C_{b2}d_{\ell 2}}{2(1 - C_{b1} - C_{b2})} \qquad (92b)$$

$$= \frac{(1 - C_{b1})d_{\ell 1} + (1 - 2C_{b1})d_s - (1 - C_{b2})d_{\ell 2}}{2(1 - C_c)} \qquad (92c)$$

where $t = d_{\ell 1} + d_s + d_{\ell 2}$

$C_{a1} = f_1 \epsilon_{\ell 1} d_{\ell 1}$

$C_{a2} = f_2 \epsilon_{\ell 2} d_{\ell 2}$

$C_{b1} = f_1 \epsilon_{\ell 1} d_{\ell 1}/t$

$C_{b2} = f_2 \epsilon_{\ell 2} d_{\ell 2}/t$

$C_c = C_{b1} + C_{b2}$

For small C_c, $1/(1 - C_c) \approx 1 + C_c$.

$$d = \{ (1 - C_{b1})d_{\ell 1} + (1 - 2C_{b1})d_s - (1 - C_{b2})d_{\ell 2}\}(1 + C_c)/2 \qquad (92d)$$

Dropping second order terms in C gives

$$d = \{1 + R_1 - R_2 - C_{b1}(1+R_2) + C_{b2}(1+R_1)\}d_s/2 = C\, d_s \qquad (92e)$$

where $R_1 = d_{\ell 1}/d_s$, $R_2 = d_{\ell 2}/d_s$

$$C = \{1 + R_1 - R_2 - C_{b1}(1+R_2) + C_{b2}(1+R_1)\}/2 . \qquad (93)$$

Thus moments of inertia, $I_{\ell 1}$, I_s, and $I_{\ell 2}$ can be expressed in terms of R_1, R_2, d_s, and C;

$$I_{\ell 1} = w d_s^3 \{R_1^3/3 + (1-C)R_1^2 + (1-2C+C^2)R_1\} \qquad (89a)$$

$$I_s = wd_s^3(1/3 - C + C^2) \tag{90a}$$

$$I_{\ell 2} = wd_s^3(R_2^3/3 + CR_2^2 + C^2R_2) \tag{91a}$$

$$I_{\ell 1} + I_s + I_{\ell 2} = wd_s^3(R_1+R_2+1)[\{(R_1+1)^2-(R_1+1)R_2+R_2^2\} + 3C(R_2-R_1-1) + 3C^2]$$

$$= wd_s^2t\,[\{(R_1+1)^2-(R_1+1)R_2+R_2^2\} + 3C(R_2-R_1-1) + 3C^2]/3 \tag{94}$$

For small C_{b1} and C_{b2}, $C_{b1}^2 = C_{b2}^2 = C_{b1}C_{b2} \approx 0$ and thus

$$C^2 \approx (1 + R_1 - R_2)\{(1 + R_1 - R_2) - 2C_{b1}(1+R_2) + 2C_{b2}(1+R_1)/4 \tag{95}$$

Inserting equation 93 and 95 into equation 94 gives

$$I_{\ell 1} + I_s + I_{\ell 2} = \frac{wd_s^2t}{12}(R_1 + R_2 + 1)^2 \tag{94a}$$

The product of modulus and moments of inertia for each layer was expressed in terms of R_1, R_2, d_s, C_{b1}, C_{b2}, C, and E_s

$$E_{\ell 1}I_{\ell 1} = E_swd_s^3(1 - f_1\,\epsilon_{\ell 1})\,\{R_1^3/3 + (1-C)R_1^2 + (1-2C+C^2)R_1\}$$

$$= \frac{E_swd_s^3}{3}\left[\{3(1-C)^2R_1 + 3(1-C)R_1^2 + R_1^3\} - \frac{tC_{b1}}{d_s}\{3(1-C)^2 + 3(1-C)R_1 + R_1^2\}\right. \tag{96}$$

where, $f_1\,\epsilon_{\ell 1} = tC_{b1}/d_{\ell 1} = tC_{b1}/(d_sR_1)$

$$E_sI_s = E_swd_s^3(1 - 3C + 3C^2)/3 \tag{97}$$

$$E_{\ell 2}I_{\ell 2} = E_s w d_s^3 (1 - f_2\,\epsilon_{\ell 2})(R_2^3/3 + CR_2^2 + C^2 R_2)$$

$$= -\frac{E_s w d_s^3}{3}\left[(3C^2 R_2 + 3CR_2^2 + R_2^3) - \frac{tC_{b2}}{d_s}(3C^2 + 3CR_2 + R_2^2)\right] \qquad (98)$$

where, $f_2\,\epsilon_{\ell 2} = tC_{b2}/d_{\ell 2} = tC_{b2}/(d_s R_2)$

Inserting equations 93 and 95 into equations 96, 97 and 98 gives

$$E_{\ell 1}I_{\ell 1}+E_s I_s+E_{\ell 2}I_{\ell 2} = \frac{wd_s^2 t}{12}\left[(R_1+R_2+1)^2 - \{R_1^2+3(R_2+1)^2\}C_{b1} - \{R_2^2 + 3(R_1+1)^2\}C_{b2}\right] \qquad (99)$$

After a bit of algebra, one obtains

$$\bar{E}_{3DYN} = \frac{(E_{\ell 1}I_{\ell 1} + E_s I_s + E_{\ell 2}I_{\ell 2})}{(I_{\ell 1} + I_s + I_{\ell 2})} \qquad (88a)$$

$$= E_s \cdot \left[1 - \frac{\{R_1^2+3(R_2+1)^2\}C_{b1} + \{R_2^2 + 3(R_1+1)^2\}C_{b2}}{(R_1 + R_2 + 1)^2}\right] \qquad (88b)$$

where $R_1 = d_{\ell 1}/d_s$, $R_2 = d_{\ell 2}/d_s$

$C_{b1} = d_{\ell 1} f_1 \epsilon_{\ell 1}/t$

$C_{b2} = d_{\ell 2} f_2 \epsilon_{\ell 2}/t$ (figure 60)

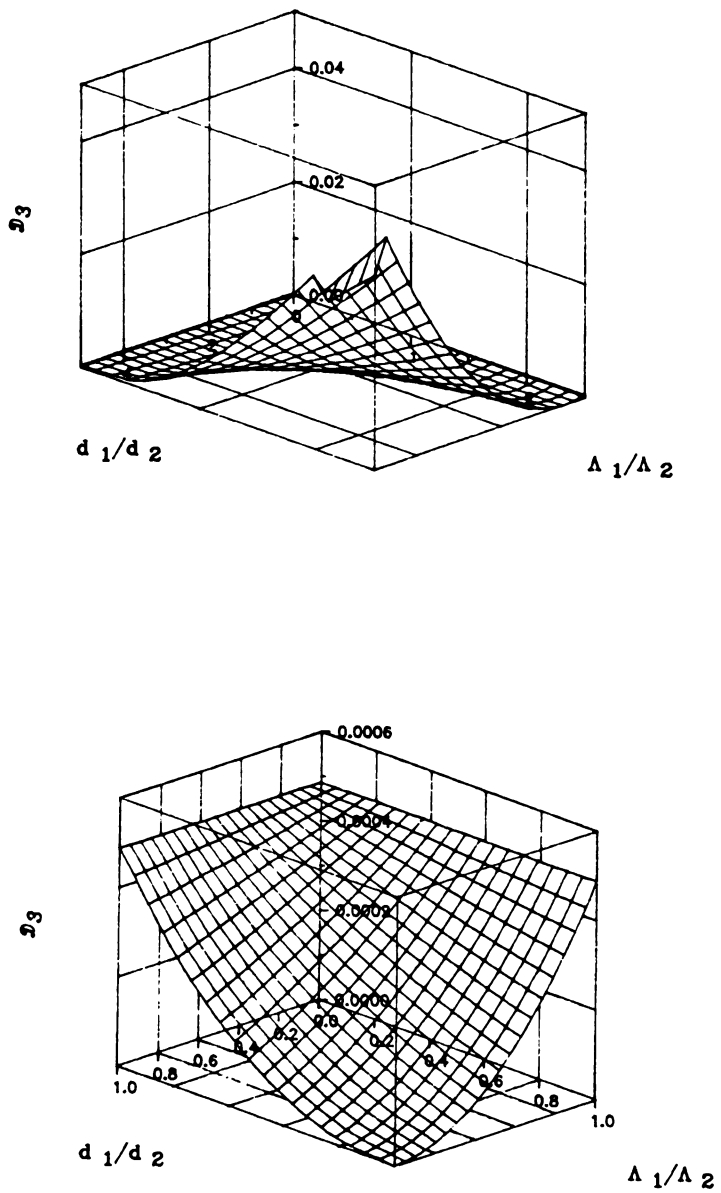

Figure 60. The relationship between $d_{\ell 1}/d_{\ell 2}$, Λ_1/Λ_2, and the difference between full (equation 88) and approximation (equation 88b) in normalized Young's modulus change of three layer composite.

As both R_1 and R_2 approach zero (or $d_{\ell 1}$ and $d_{\ell 2}$ approach zero), both C_{b1} and C_{b2} approach zero. When C_{b1} and C_{b2} approach zero then $\bar{E}_{3DYN}$ approachs E_s. As R_1 approaches zero, $\bar{E}_{3DYN}$ approaches $E_s\{1 - R_2(R_2^2 + 3)\, f_2 G_{\ell 2} N_{\ell 2}/(R_2 + 1)^3\}$. As R_2 approaches zero, $\bar{E}_{3DYN}$ approaches $E_s\{1 - R_1(R_1^2 + 3)\, f_1 G_{\ell 1} N_{\ell 1}/(R_1 + 1)^3\}$, which is the same result as the two layer composite case (equation 80c). As $R_1 \rightarrow 0$ and $R_2 \rightarrow \infty$, $\bar{E}_{3DYN}$ approaches $E_s(1 - f_2 G_{\ell 2} N_{\ell 2})$. As $R_2 \rightarrow 0$ and $R_1 \rightarrow \infty$, $\bar{E}_{3DYN}$ approaches $E_s(1 - f_1 G_{\ell 1} N_{\ell 1})$. As both R_1 and R_2 approach an infinity ($d_s \rightarrow 0$) (figure 61), $\bar{E}_{3DYN}$ approaches $E_s[1 - \{\lambda(f_1 G_{\ell 1} N_{\ell 1} - f_2 G_{\ell 2} N_{\ell 2}) + f_2 G_{\ell 2} N_{\ell 2}\}]$ where $\lambda = 4\{d_{\ell 1}/(d_{\ell 1}+d_{\ell 2})\}^3 - 6\{d_{\ell 1}/(d_{\ell 1}+d_{\ell 2})\}^2 + 3\{d_{\ell 1}/(d_{\ell 1}+d_{\ell 2})\}$ (Appendix G).

3.5.1.2 Comparison of ROM and dynamic modulus calculations

When layer thickness d_ℓ approaches zero for two layer composite ($a \rightarrow 0$), the ratio of normalized Young's modulus change (dynamic beam vibration theory) (equation 80c) to normalized Young's modulus change (rule of mixtures) (equation 79) approaches 3 (Appendix D). When layer thickness d_ℓ approaches the bar thickness for two layer composite ($a \rightarrow \infty$), the ratio of normalized Young's modulus change (dynamic beam vibration theory) (equation 80c) to normalized Young's modulus change (rule of mixtures) (equation 79) approaches 1 (Appendix D)

For three layer composite when both layer thickness $d_{\ell 1}$ and $d_{\ell 2}$ approach zero (R_1 and $R_2 \rightarrow 0$), the ratio of normalized Young's

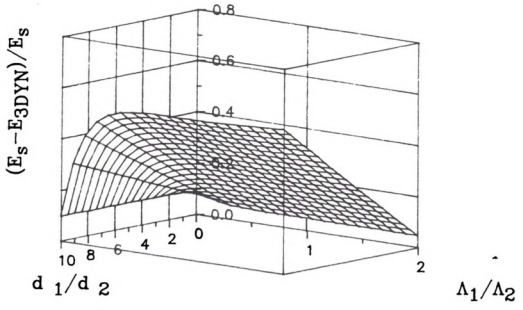

Figure 61. The relationship between $d_{\ell 1}/d_{\ell 2}$, Λ_1/Λ_2, and the limit of normalized Young's modulus change when both R1 and R2 goes to infinity for three layer
(when $d_{\ell 2}$ = 0.1 x bar thickness, Λ_2 = 0.1).

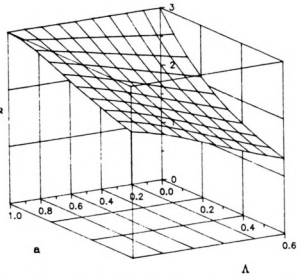

Figure 62(a). The relationship between a, Λ, and the ratio of normalized Young's modulus change (dynamic) to normalized Young's modulus change (ROM) for two layer composite.

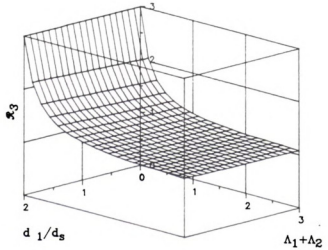

Figure 62(b). The relationship between $d_{\ell 1}/d_s$, $\Lambda_1 + \Lambda_2$, and the ratio of normalized Young's modulus change (dynamic) to normalized Young's modulus change (ROM) for two layer composite (when $d_{\ell 1} = d_{\ell 2}$, $\Lambda_1 = \Lambda_2$).

modulus change (dynamic beam vibration theory) (equation 88b) to normalized Young's modulus change (rule of mixtures) (equation 77) approaches 3 (Appendix D).

3.5.2 Crack Geometry Modification to conform Indentation Crack Shape

3.5.2.1 Generalized Models for Surface-Limited Microcrack Damage

For convenience, the authors' previous expressions for surface-limited microcracking [97] are summarized below.

ROM model

Two layer case (one microcracked surface layer, an undamaged substrate layer)

$$\frac{(E_s - \bar{E}_{2_{ROM}})}{E_s} = v_\ell \; f \; G_\ell \; N_\ell \qquad (75)$$

where v_ℓ = volume fraction of layer

f = crack orientation function

G_ℓ = crack geometry factor ($= 2\langle A^2 \rangle / (\pi \langle P \rangle)$, where $\langle A \rangle$ and $\langle P \rangle$ represent the mean area and the mean perimeter of microcracks in microcracked layer, respectively

N_ℓ = number density of microcracks in layer.

Three layer case (two microcracked surface layers, an undamaged substrate layer)

$$\frac{(E_s - \bar{E}_{3_{ROM}})}{E_s} = v_{\ell 1} f_1 G_{\ell 1} N_{\ell 1} + v_{\ell 2} f_2 G_{\ell 2} N_{\ell 2} \qquad (73)$$

where $v_{\ell 1}$, $v_{\ell 2}$ = volume fraction of layer 1 and layer 2, respectively

f_1, f_2 = crack orientation function for the cracks in layer 1 and layer 2, respectively

$G_{\ell 1}$, $G_{\ell 2}$ = crack geometry factor ($= 2\langle A^2 \rangle / (\pi \langle P \rangle)$) for the cracks in layer 1 and layer 2, respectively

$N_{\ell 1}$, $N_{\ell 2}$ = number density of microcracks in layer 1 and layer 2, respectively.

Dynamic modulus model

Two layer case (one microcracked surface layer, an undamaged substrate layer)

$$\frac{(E_s - \bar{E}_{2_{DYN}})}{E_s} = \frac{(a^2 + 3)}{(1 + a)^2} C_b - \frac{a(a^2 + 3)}{(1 + a)^3} f G_\ell N_\ell \qquad (80c)$$

where, $a = d_\ell / d_s$

$C_b = d_\ell \, f G_\ell N_\ell \, / t$

Three layer case (two microcracked surface layers with the same thickness, an undamaged substrate layer)

$$\frac{(E_s - \tilde{E}_{3DYN})}{E_s} = \frac{\{R_1^2 + 3(R_2 + 1)^2\}C_{b1} + \{R_2^2 + 3(R_1 + 1)^2\}C_{b2}}{(R_1 + R_2 + 1)^2}$$

$$= \frac{R_1\{R_1^2+3(R_2+1)^2\}f_1G_{\ell 1}N_{\ell 1} + R_2\{R_2^2 + 3(R_1+1)^2\}f_2G_{\ell 2}N_{\ell 2}}{(R_1 + R_2 + 1)^3} \quad (88b)$$

where $R_1 = d_{\ell 1}/d_s$, $R_2 = d_{\ell 2}/d_s$

$C_{b1} = d_{\ell 1}f_1G_{\ell 1}N_{\ell 1}/t$

$C_{b2} = d_{\ell 2}f_2G_{\ell 2}N_{\ell 2}/t$

As expressed above, the ROM and dynamic modulus expressions can be expressed in terms of any one of a number of microcracking theories [76-78]. Budiansky and O'Connell [76], Salganik [141], Hoenig [77], and Laws and Brockenbrough [78] each express the effective Young's modulus, E, of the microcracked body with Poisson's ratio ν as [76-78, 183],

$$E = E_0\{1 - f(\nu, \nu_0)\epsilon\} \quad (61)$$

where the subscript "$_0$" refers to the non-microcracked state of each parameter. The function $f(\nu, \nu_0)$ depends on the spatial orientation

of the microcracks (Table 23). The crack damage parameter, ϵ, is defined [76-78] by

$$\epsilon = \frac{2}{\pi} \frac{\langle A^2 \rangle}{\langle P \rangle} N_V \qquad (100)$$

where, N_V = volume number density of microcracks

$\langle A \rangle$ = mean crack area

$\langle P \rangle$ = mean crack perimeter

Thus the crack damage parameter, ϵ, is a function of the microcrack volume number density N_V, the crack geometry, and the crack dimensions.

In the summary above and in this section, we treat microcracking in terms of the crack orientation function (f), and the crack damage parameter (expressed here as the product of microcrack geometry G and the crack number density N_V). In this way, we seek to emphasize the functional relationships between microcrack geometry and crack number density.

Differences between the four "linear" microcracking theories include the treatment of spatial alignment of microcracks. Budiansky and O'Connell [76] and Salganik [141] deal with randomly oriented microcrack populations only, Hoenig [77] treats aligned microcracks, and Laws and Brockenbrough [78] treat both randomly oriented and

Table 23 Microcracking-modulus relations for three-dimensional crack distributions

Crack geometry	$f(\nu_0)$	G	ϵ	Orientation
penny	$\frac{16(1-\nu_0^2)}{3}$	$\pi a/2$	$N\langle a^3\rangle$	aligned
	$\frac{16(1-\nu_0^2)(10-3\nu_0)}{45(2-\nu_0)}$			random
half penny	$\frac{16(1-\nu_0^2)}{3}$	$\pi a/4$	$0.5\ N\langle a^3\rangle$	aligned
	$\frac{16(1-\nu_0^2)(10-3\nu_0)}{45(2-\nu_0)}$			random
slit	$\frac{\pi^2(1-\nu_0)}{2}$	$2c^2\ell^2/(c+\ell)$	$4N\langle c^2\ell^2\rangle/\pi(c+\ell)$	aligned
	$\frac{\pi^2(1+\nu_0)(5-4\nu_0)}{30}$			random
ellipse	$\frac{16(1-\nu_0^2)}{3}$	$\pi^2 bd^2/4E(k)$	$N\pi\langle bd^2\rangle/2E(k)$	aligned
	$\frac{16(1-\nu_0^2)(10-3\nu_0)}{45(2-\nu_0)}$			random
half ellipse	$\frac{16(1-\nu_0^2)}{3}$	$\pi^2 bd^2/8E(k)$	$N\pi\langle bd^2\rangle/4E(k)$	aligned
	$\frac{16(1-\nu_0^2)(10-3\nu_0)}{45(2-\nu_0)}$			random

ν_0 = undamaged Poisson's ratio
$\langle a\rangle$ = average radius of crack for penny and half penny cracks
c = half of average crack size for slit cracks
ℓ = depth of slit cracks
b = half of the major axis for elliptical and half elliptical cracks
d = half of the minor axis for elliptical and half elliptical cracks
E(k)= complete elliptical integral of the second kind

$k = (b^2-d^2)^{1/2} / b$

aligned microcrack populations. While in each of the four theories the alignment function f is expressed as a function of Poisson's ratio, Budiansky and O'Connell [76] express f as function of both ν (Poisson's ratio of the microcracked state) and ν_0 (Poisson's ratio of the nonmicrocracked state). Salganik [141] and Laws and Brockenbrough [78] express f in terms of ν_0 only. Despite these apparent differences in the form of f, the values of f differ little from one another for realistic ranges of ν and ν_0 [183].

Thus, the linear microcracking theories are quite similar. In order to treat particular microcrack geometries, we choose to describe the layer modulus in terms of Laws and Brockenbrough [78]. Table 23 summarizes Laws and Brockenbrough [78] microcracking relations, which include "standard" crack geometries of circular, elliptical, and slot type crack geometries.

3.5.2.2 Relative Crack Size Versus Layer Depth Considerations

The nature of the microcracked surface layer(s) for particular microcracked bodies can be classified in terms of the mean microcrack size <c> and the depth of the microcrack damage layer, d_ℓ. In this paper, we shall consider two limits of relative crack/layer depth.

If $\langle c \rangle \ll d_\ell$, then the microcracked layer itself can be considered to be a three-dimensional body. Within the microcracked layer, the implicit assumption [78, 182, 183] that the microcracks are distributed homogeneously in space (over size scales large compared to

<c>, the mean crack dimension) may or may not be valid*. If the assumption of spatial homogeneity of microcrack distribution is reasonable and if the crack alignment, crack geometry, and crack number density in the layer(s) can be determined or estimated, then the effective modulus of the microcracked layer can be calculated based on modulus-microcracking relationships introduced by Budiansky and O'Connell [76], Salganik [141], and others [77, 78, 182]. The effective elastic modulus of the entire specimen can then be calculated based on a Rule of Mixtures or a dynamic modulus model developed by the authors (equations 73, 75, 80c, 88b). The case that $\langle c \rangle \ll d_\ell$ could correspond physically, for example, to a microcracked specimen in which the microcrack damaged surface layer(s) resulted from a diffusively-induced phase martensitic-type phase transformation. Alternatively, the case that $\langle c \rangle \ll d_\ell$ might correspond to a layered composite specimen in which the layers where microcracked.*

If $\langle c \rangle = d_\ell$, then the crack layer depth is defined by the penetration of the cracks in the microcracked layer (assumed perpendicular cracks). This case might correspond to, for example, a surface crack array formed via surface grinding [83] or thermal shock of a brittle material. Alternatively, $\langle c \rangle = d_\ell$ would correspond to the model crack field formed by an array of indentation cracks on one or more surfaces of a specimen.

* Homogeneous distribution in space refers here to the location of, for example, the centroids of the crack surfaces. Homogeneous spatial distribution makes no assumptions about the mutual orientation of the crack faces.

Although indentation cracks have been used as model cracks in a number of studies, the detail indentation crack morphology is not included in the standards considered crack geometries (circular, elliptical and slot, as listed in table 23).

3.5.2.3 Indentation Cracks as an Example of a Model Crack System

Sharp indenters (such as Vickers or Knoop) may produce an "ideal" distribution of surface microcracks, in which the number, size, and spatial location of the microcracks can be controlled. However, to model an array of indentation cracks, we should consider in some detail the morphology of individual indentation cracks, since the modulus-microcracking relations (equation 61 and Table 23) are posed in terms of $\langle A^2 \rangle$, the mean of the square of the crack size, and $\langle P \rangle$, the mean crack perimeter (equation 100).

For Vickers indentation cracks, two idealized crack morphologies are typically cited [184, 185] : (1) half penny or semicircular radial-median crack system, and (2) Palmqvist cracks, consisting of a system of separate semi-elliptical cracks (see figure 63 for schematics of each idealized crack system). Vickers indentation induced Palmqvist cracks have been observed in ceramics, glass ceramics, and cermets [186-191]. Some researchers have argued that the Palmqvist-type crack morphology occurs at low indent loads (for a c/a ratio less than about 3, where the crack length c and indent diagonal length a are defined in figure 63). At higher indentation

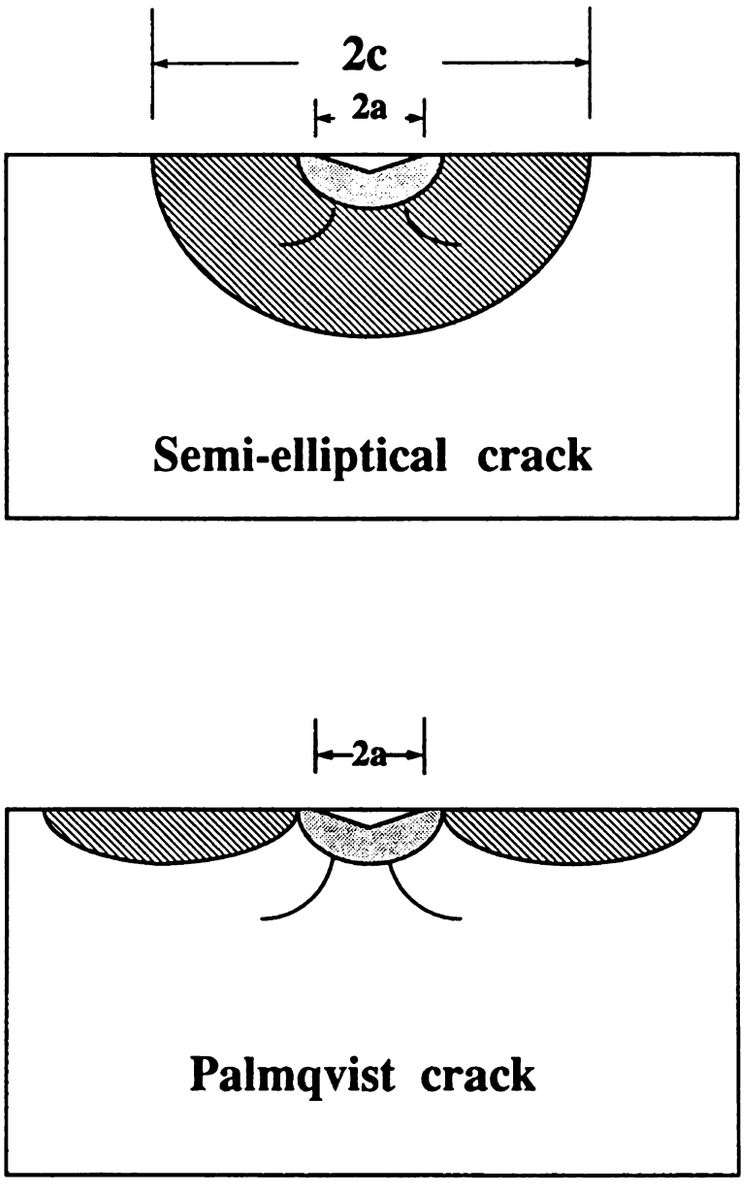

igure 63. Schematics of (a) indentation half ellipse crack
(b) Palmqvist crack.

loads the crack morphology switches to the half-penny type [186-189].

However, Palmqvist cracks are not necessarily limited to low load regimes, and Palmqvist crack morphologies are not always limited to an idealized system of four semi-elliptical cracks per Vickers indent. By serial polishing, Shetty et al. observed non-ideal Palmqvist cracks generated by Vickers indentation at loads from 50 N to 200 N in Corning Pyroceram 9606 glass ceramics and at loads up to 500 N in WC-Co cermets [190-191]. Thus, even at relatively high loads, a well developed radial-median crack system (a half-penny crack) was not observed for the Pyroceram and WC-Co cermets [190, 191].

In addition to Palmqvist cracks, the "half-penny" or semicircular crack is the second idealized form of Vickers indentation cracks [91, 192]. As noted above, ceramics that exhibit Palmqvist crack morphologies at low loads may develop half penny cracks at higher loads. Thus the half penny crack morphology has been termed a "fully-developed radial-median crack system." The ideal half-penny morphology also may be disrupted by microstructural features. If a polycrystalline specimen's grain size approaches the indent impression size, then Vickers indent cracks can exhibit a number of complicated systems of multiple cracks in which the cracks tend to follow grain boundaries [193].

To accurately model a system of indentation cracks, we thus must determine the particular crack morphology, which can in fact depend on the indentation load, the specimen's microstructure, the relative load range, and a number of other factors. It is only when our assumed (or

measured) crack geometry is realistic that we can utilize the flexibility of the indentation-generated cracks to test surface microcracking-modulus theories.

For both Vickers and Knoop indentations, a plastically deformed zone, commonly taken to be hemispherical in shape, is formed directly below the indent impression (figure 63). In order to test "microcrack alignment" relations, one needs a system in which the cracks are well defined. A "model" crack system, such as that provided by indentation cracks, can serve that purpose.

From an experimental standpoint, indentation cracks are quite convenient for a study of surface-limited microcrack damage. Via indentation, a controlled array of cracks can be introduced into the specimen surface(s), where the indentation crack size, crack orientation, and crack location can be controlled by the experimenter.

For a microcrack field produced by indentation at a fixed load, the layer thickness of the microcracked surface layer will be identical to the mean depth of the indentation cracks (figure 64), thus the theories assuming a three-dimensional crack array may not be adequate to describe the modulus of the damaged layers. In addition, the indentation crack geometry does not coincide with the standard crack geometries listed in table 23. Finally, there is a residual stress field associated with indentation-induced microcracks that may alter the measured elastic modulus.

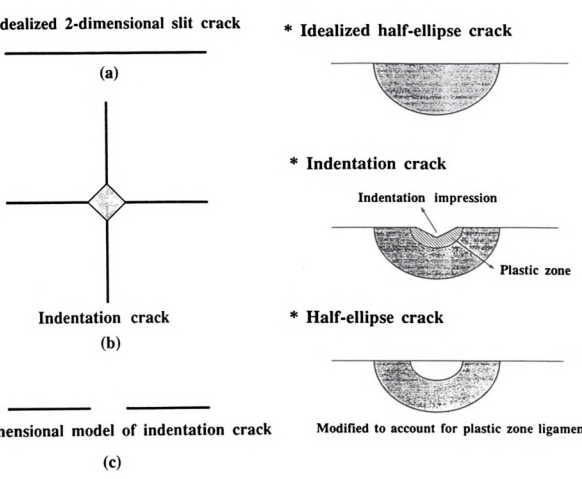

igure 64. Modification of crack geometry to account for plastic zone ligament of Vickers indentation induced crack.

To treat the case that <c> = d_ℓ, we shall consider both two dimensional and three dimensional microcracks models.

The geometry of even fully-developed indentation cracks differs from the idealized crack geometries listed in Table 23. In addition to a semicircular or semielliptical shape (rather than a circular or elliptical shape), the faces of the indentation cracks are joined by a plastic zone ligament that joins the crack surfaces (figure 64).

For three-dimensional microcrack distributions, we can still represent the crack geometry in terms of the generalized geometry parameter $G = \langle A^2 \rangle / \langle P \rangle$, where we compute the mean crack area <A> and crack perimeter <P> as they are modified by the presence of the plastically deformed zone "ligament."

For example, for an unmodified semi-elliptical crack, the mean crack area is given by $\pi bd/2$, where b and d are the semimajor and semiminor axes of the ellipse, respectively. To account for the crack face area reduction due to the plastic zone ligament, we subtract $\pi h^2/2$, where h is the radius of the ligament (plastic zone) in the plane of the semi-elliptical crack.

Table 24 compares the expressions for unmodified slit and semi-elliptical cracks and modified expressions.

Alternatively, the indentation crack surface-damaged layer can be modeled as a two dimensional crack distribution in which an array of through-plate cracks are, for example, oriented normal to the plane of the plate (Appendix F). This provides a model microcracked layer with

e 24. Crack geometry modifications

k geometry	$f(\nu_0)$	Area	Perimeter++
lit, unmodified	$\pi^2(1-\nu_0)/2$	$2c\ell$	$2c+2\ell$
fied 3D slit	$\pi^2(1-\nu_0)/2$	$2c\ell-\pi h^2/2$	$2c+2\ell+\pi h$
ified 3D slit iptical- ent bottom	$\pi^2(1-\nu_0)/2$	$2c\ell-\pi h^2 k'/2$	$2(c+\ell+hE(k))$
f ellipse odified	$16(1-\nu_0^2)/3$	$\pi bd/2$	$2bE(k)$
dified lf ellipse	$16(1-\nu_0^2)/3$	$\pi(bd-h^2)/2$	$2bE(k)+\pi h$
dified lf ellipse liptical- dent bottom	$16(1-\nu_0^2)/3$	$\pi(bd-h^2K')/2$	$2E(k)(b+h)$
lmqvist	$16(1-\nu_0^2)/3$	$\pi bd/4-hd$	$bE(k)+d-h$

ν_0 = undamaged Poisson's ratio
c = half of average crack size for slit cracks
ℓ = depth of slit cracks
b = half of the major axis for elliptical and half elliptical cracks
d = half of the minor axis for elliptical and half elliptical cracks
h = half of indentation impression diagonal size
E(k)= complete elliptical integral of the second kind

$k = (b^2-d^2)^{1/2} / b$

$k' = (1 - k^2)^{1/2}$

+ Perimeter does not include free surface.

cks oriented normal to the specimen surface and having a crack th equal to the damaged-layer depth, as is the case for entation-induced cracks. However, the subsurface geometry of the entation crack (semicircular or semielliptical, for example) can be represented in terms of a two-dimensional model. (The three-ensional analogue of the two dimensional slit crack distribution is three dimensional through-plate crack.)

Appendix E compares models for aligned slit cracks in three-mensional bodies (the third entry in Table 23) with two dimensional dels of aligned slit cracks in plates (Appendix F). In the limit at the crack layer depth approaches the specimen thickness, the ree-dimensional slot crack expression approximates the two-mensional crack expression (Appendix E).

spite the similarity of the three-dimensional slot expression and e two-dimensional crack model, however, the basic slot geometry can ot entirely describe the geometry of an indentation crack.

The two dimensional crack models can be modified to treat the lastic zone (ligament) of the indentation crack. As seen on the urface, if the length of the indentation crack is 2c, then this value ncludes 2h, where 2h is the diameter of the indentation-induced lastic zone. Thus one can model a single indentation crack of length c as two separate indentation cracks, each of length c - h.

It has been observed experimentally that the overall modulus of pecimens subjected to indentation-crack damage can be described well

rms of three dimensional crack models that have been modified to
nt for the plastic zone ligament.

Model Experiment

.1 Measurements on Undamaged Specimens

Room temperature values of Young's modulus, Poisson's ratio,
ure toughness, and hardness were measured in order to: (1)
lish the "zero damage" values for the elastic moduli and (2)
de a check of consistency on the physical property measurements
lus, fracture toughness) with the literature.

For the undamaged polycrystalline alumina specimens, the measured
's modulus was approximately 320 - 340 GPa, with a shear modulus
out 138 to 132 GPa and a Poisson's ratio between 0.20 and 0.22.
bserved range of undamaged elastic modulus values can be
ined in terms of well-known modulus versus porosity relations
ndix H).

The hardness and toughness of the alumina specimens determined by
ntation were 12.9 GPa and 3.1 MPa $m^{1/2}$, respectively. The
ture toughness and hardness measured for alumina specimen in this
agrees reasonably well with the toughness values of 2.9 and 4.6
$m^{1/2}$ and hardness values of 13.1 to 20.1 GPa reported by Marshall
ycrystal, DCB method) (Table I in reference [90]), toughness
es of 2.5-5 MPa $m^{1/2}$ reported by Becher and coworkers [194] and

the toughness value of 2.1 MPa $m^{1/2}$ and hardness value of 23 GPa reported by Evans and Charles (sapphire, Double Torsion method) [109].

3.5.3.2 Characterization of the Indentation Cracks

A composite layer damage model developed by two of the authors [97] was used to evaluate the indentation data. Initially, the undamaged polycrystalline specimen is characterized by a single, uniform elastic modulus. As indentation damage is introduced into the specimen surface, the surface damaged regions are modeled as layers of reduced modulus that are "perfectly" bonded to an undamaged substrate (figure 65). Specimens indented on a single long transverse surface were thus modeled as a two layer composite composed of an indentation-damaged layer perfectly bonded to an underlying undamaged layer. Specimens indented on the two long transverse surfaces were modeled as a three layer composite, with an undamaged middle layer sandwiched between indented top and bottom layers [97] (figure 65).

In this study, the microcrack number density was obtained directly from the number of indentations and specimen dimensions. The surface trace of the indentation cracks was measured by optical microscopy directly from the radial crack length. From the total of 1546 indentation cracks generated in the experiment, the mean radial crack length was computed on the basis of optical measurements from 298 of the indents, or about one-fifth of the total number of indents generated in the study (Table 25). The mean radial crack length,

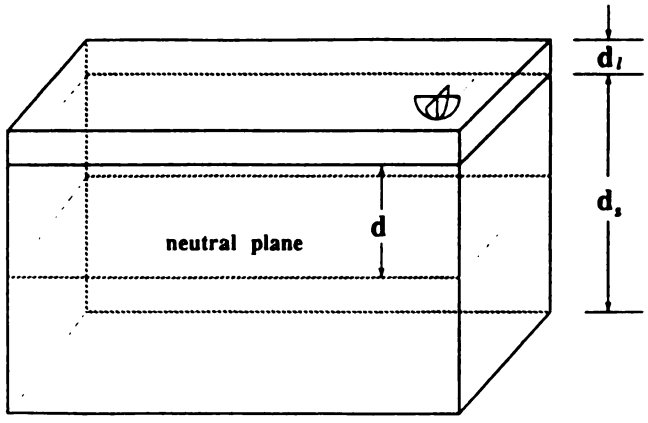

two layer composite model

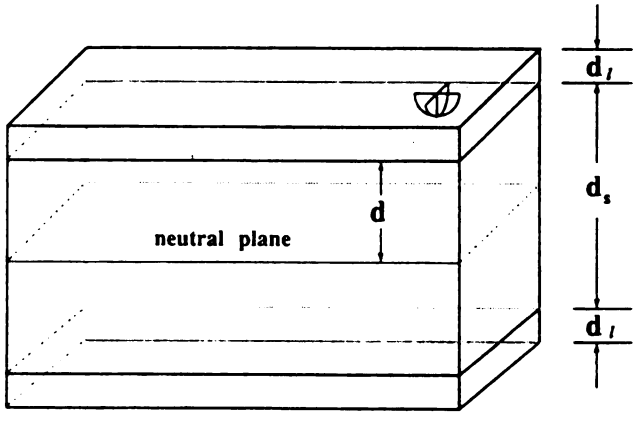

three layer composite model

Figure 65. Schematics of (a) two layer and (b) three layer composites when indentation damage is introduced into specimen surface.

determined optically using the Vickers microindenter agreed to within approximately 15 to 20 percent with the fractographic measurements of the major axis length of the indent cracks (figure 66).

The shape and depth of the indentation cracks were determined fractographically, since these parameters were not accessible directly from the surface of the indented alumina bars. For each of the three indentation loads used in this study, the indentation-induced cracks were elliptical (figure 66), with the major axis oriented along the specimen surface and the minor axis perpendicular to the specimen surface. The crack "depth" thus corresponds to the minor axis of the indentation cracks. Five crack depth measurements were made for the indentation loads of 49 N and 98 N, while three crack depth measurements were made for indentation load of 196 N.

The optically determined mean radial crack lengths were determined for up to a hundred or more indentations at a given load (Table 2), while the fractographic measurements of crack depth were determined for relatively few cracks. Thus, the statistics of the radial crack lengths were very much better than the statistics for the crack depth measurements.

In order to take advantage of the good radial crack length statistics, an "effective crack depth" was determined in the following way. The ratio of crack depth to radial crack length was assumed to be constant at each load. The "effective crack depth" was computed by multiplying the mean radial crack length (Table 25) by the radial

Figure 66. Micrographs of compression side fracture surface showing the shape and size of median crack for (a) 49 N, (b) 98 N, (c) 196 N load indentations.

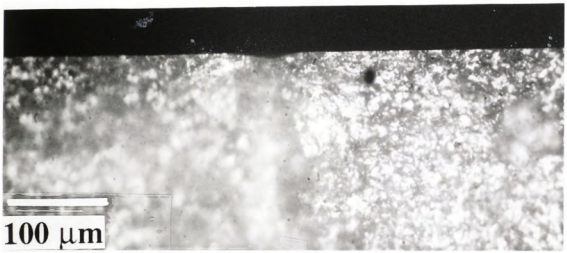

a

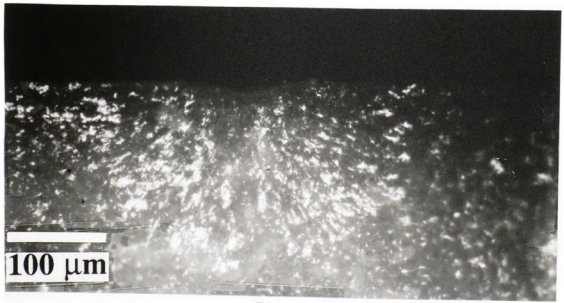

b

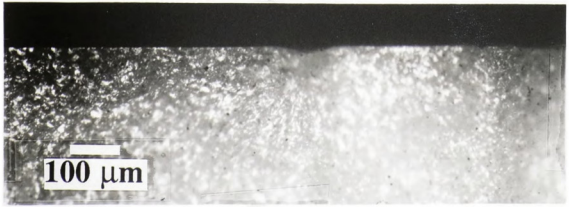

c

crack length/crack depth ratio measured from the micrographs. Effective depths were calculated to be 0.100 mm, 0.144 mm, and 0.239 mm for the 49 N, 96 N, and 196 N, respectively, according to the procedure described above. For each of the three loads, the measured mean crack depth and the computed effective crack depth agreed to within 17.7 percent (Table 26).

3.5.3.3 Modulus Decrement as a Function of Vickers Indentation Damage

In this study, the Young's moduli were determined using the fundamental flexural resonance frequencies of prismatic bar shaped specimens, thus the measured moduli represent the in-plane modulus along the length direction of the specimen [101]. Therefore, we assume that only the cracks that are aligned normal to the specimen length contribute to the Young's modulus change.

The normalized Young's modulus change, $(E_0-E)/E_0$, increased linearly as number density of indentations increased (Tables 27 and Figure 67). The slopes presented in Table 27 were obtained by least-squares fitting of the $(E_0- E)/E_0$ versus N data. The uncertainties in slope were calculated from a commercial linear regression and plotting package (PLOTIT, Scientific Programming Enterprises, Haslett, MI). The correlation coefficient was greater than 0.993 for each of the six specimens, except for the specimen indented on both surfaces at a 49 N load, where the correlation coefficient was 0.989.

Table 25. Mean radial crack lengths as a function of indent load, as measured optically for the indicated number of indentation sites.

Load (N)	Radial crack length (mm)	Number of radial crack lengths measured	Total number of indents per specimen
49	0.2276 ± 0.0203	128	280 (S*), 260 (B*)
98	0.3701 ± 0.0351	132	238 (S), 552 (B)
196	0.6448 ± 0.0319	38	150 (S), 66 (B)

* S indicates that only single long transverse faces of the specimen was indented, while B indicates that both long transverse faces of the specimen was indented.

Table 26. Indentation crack depth as a function of indent load, as measured from micrographs of fracture surface.

Load (N)	Crack depth (mm)	Ratio of crack depth to radial crack length	Effective crack depth (mm)
49	0.110 ± 0.010	0.44	0.100
98	0.175 ± 0.023	0.39	0.144
196	0.250	0.37	0.239

Table 27. Experimentally determined slope S, of the $(E_0 - E)/E_0$ versus $N\ (mm^{-2})$ data, where $(E_0 - E)/E_0$ is the normalized value of the modulus change due to a surface crack number density N of microcracks in the polycrystalline alumina specimens.

Load (N)	Slope, single surface indented	Slope, both surfaces indented
49	$0.539 \times 10^{-2} \pm 0.16 \times 10^{-3}$	$0.475 \times 10^{-2} \pm 0.42 \times 10^{-3}$
98	$1.162 \times 10^{-2} \pm 0.27 \times 10^{-3}$	$1.159 \times 10^{-2} \pm 0.27 \times 10^{-3}$
196	$6.749 \times 10^{-2} \pm 0.49 \times 10^{-3}$	$7.422 \times 10^{-2} \pm 0.61 \times 10^{-3}$

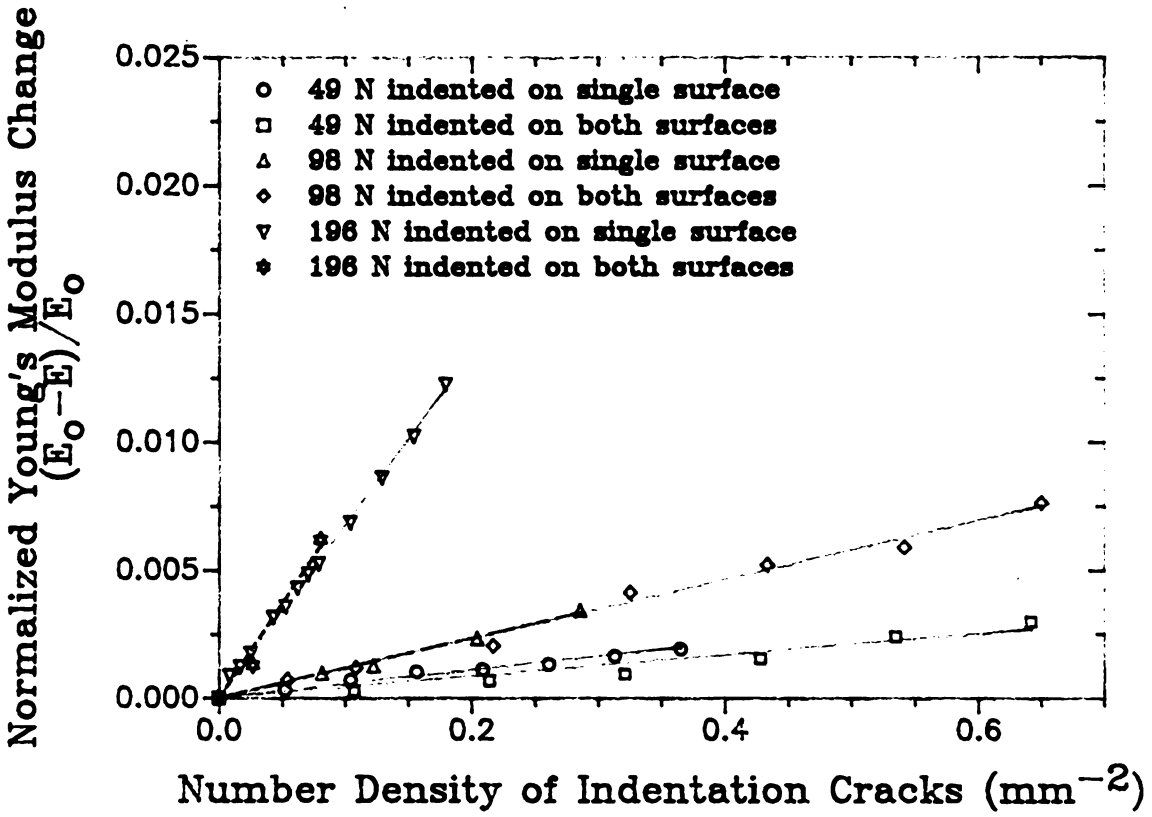

Figure 67. Experimental results of the $(E_o-E)/E_o$ versus N (mm^{-2}) where $(E_o-E)/E_o$ is the normalized value of the modulus change due to a surface crack number density N of microcracks.

The lack of significant differences between the $(E_o - E)/E_o$ versus N slopes for specimens indented on a single long transverse face and those specimens indented on both long transverse faces has a important implication for compressive stress effects (Table 27). Residual stress fields are known to accompany Vicker's indentation [195, 196]. As the number of indentations increase, a developing layer of compressive stress from the indentation crack field might perturb the modulus measurements. While compressive stresses on a single specimen face might slightly perturb the measured modulus, equivalent compressive stresses on two opposing long transverse faces of the specimen should have a zero net effect [197] on the modulus measured by the sonic resonance technique, as was the case in this study. Compressive stresses thus might slightly perturb the modulus measured for specimens indented on a single specimen face, but such perturbations should be absent for specimens indented on two faces. The equivalence of the $(E_o - E)/E_o$ versus N slopes for specimens indented on a single face and specimens indented on two faces implies that compressive-stress-induced perturbations of the measured modulus change data are not significant, at least given the level of experimental uncertainty involved in this study (Table 27).

Tables 28 and 29 compare the slopes of experimental values of $(E_0-E)/E_0$ versus N (mm^{-3}) with that of theory predictions from each of eight different crack geometries [198] (figures 68 and 69). The crack number density for the three - dimensional crack distributions were calculated from the volume of the "damaged layer", and the number of

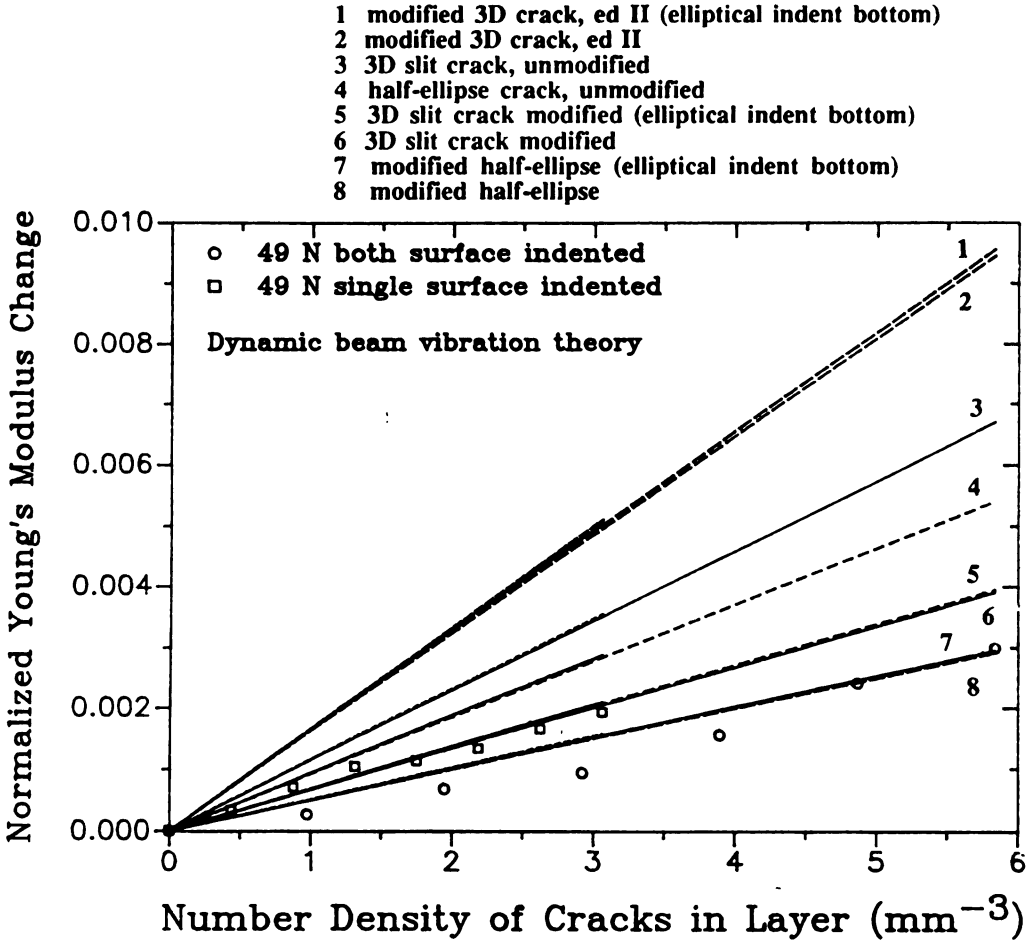

Figure 68(a). The comparison of experimental value of $(E_0-E)/E_0$ versus N (mm^{-3}) with dynamic beam vibration theory predictions from each of eight different crack geometries for (a) 49 N indentation load.

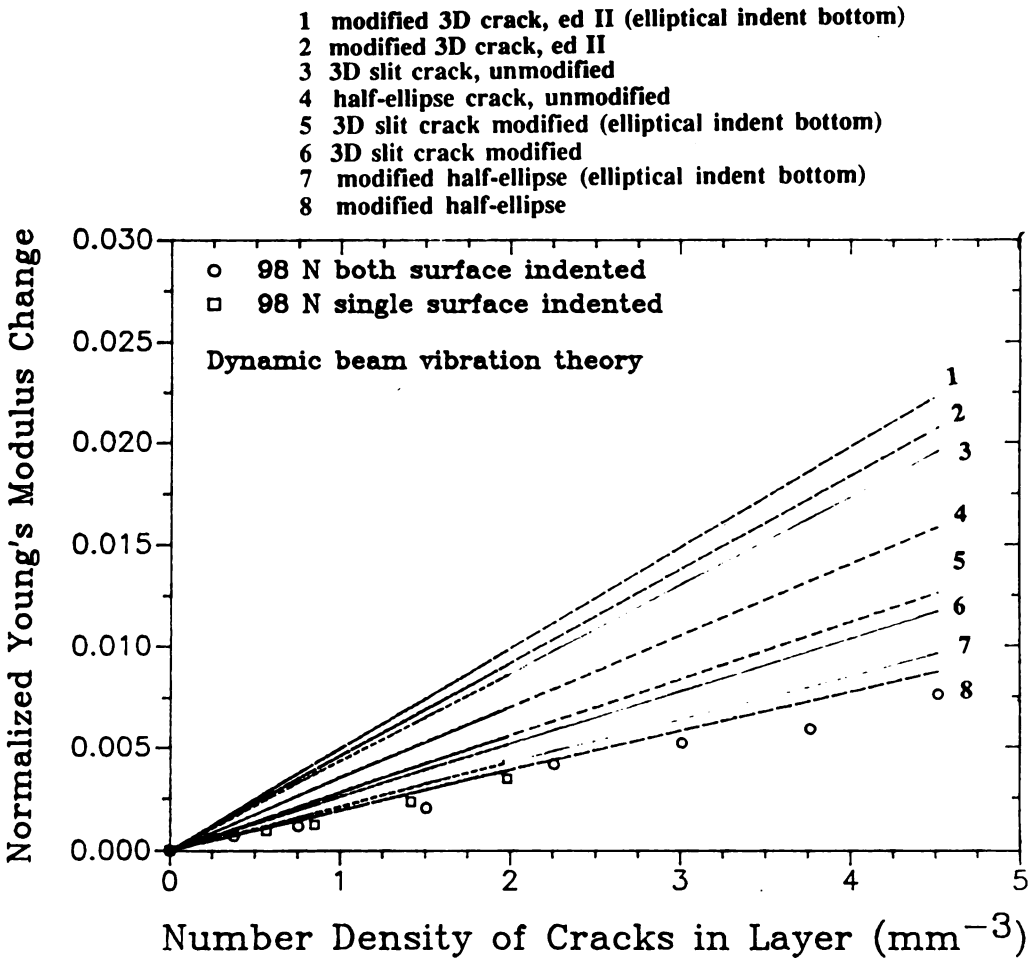

Figure 68(b). The comparison of experimental value of $(E_0-E)/E_0$ versus N (mm^{-3}) with dynamic beam vibration theory predictions from each of eight different crack geometries for (b) 98 N indentation load.

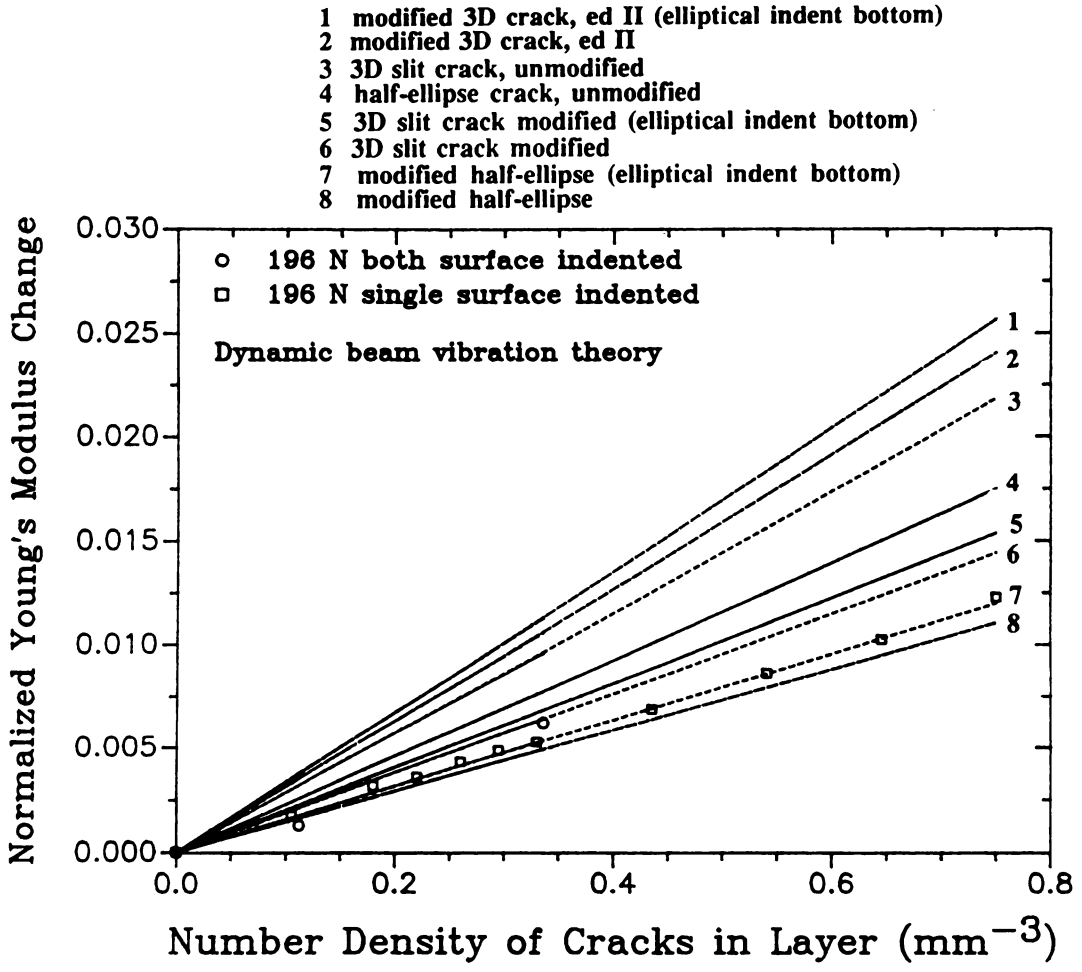

Figure 68(c). The comparison of experimental value of $(E_0-E)/E_0$ versus N (mm^{-3}) with dynamic beam vibration theory predictions from each of eight different crack geometries for (c) 196 N indentation load.

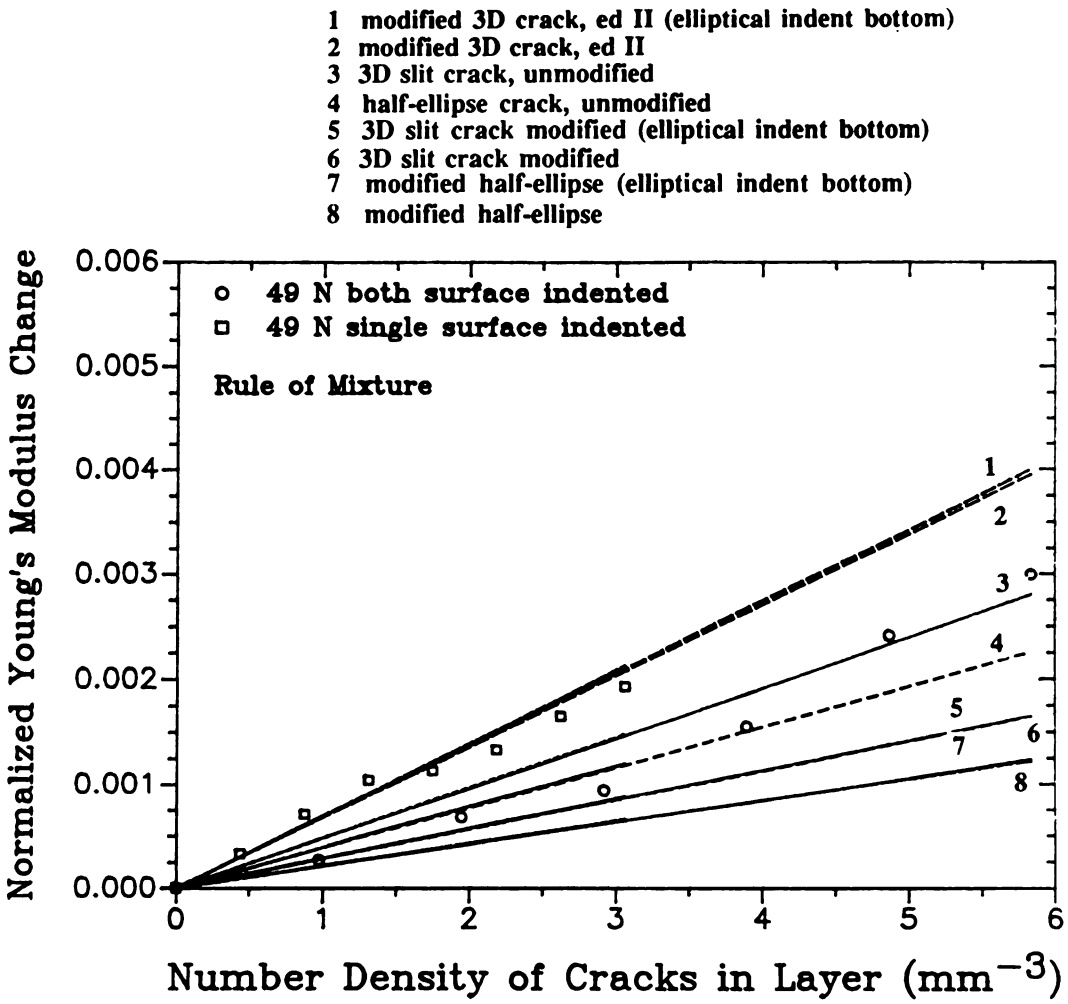

Figure 69(a). The comparison of experimental value of $(E_0-E)/E_0$ versus N (mm^{-3}) with rule of mixtures predictions from each of eight different crack geometries for (a) 49 N indentation load.

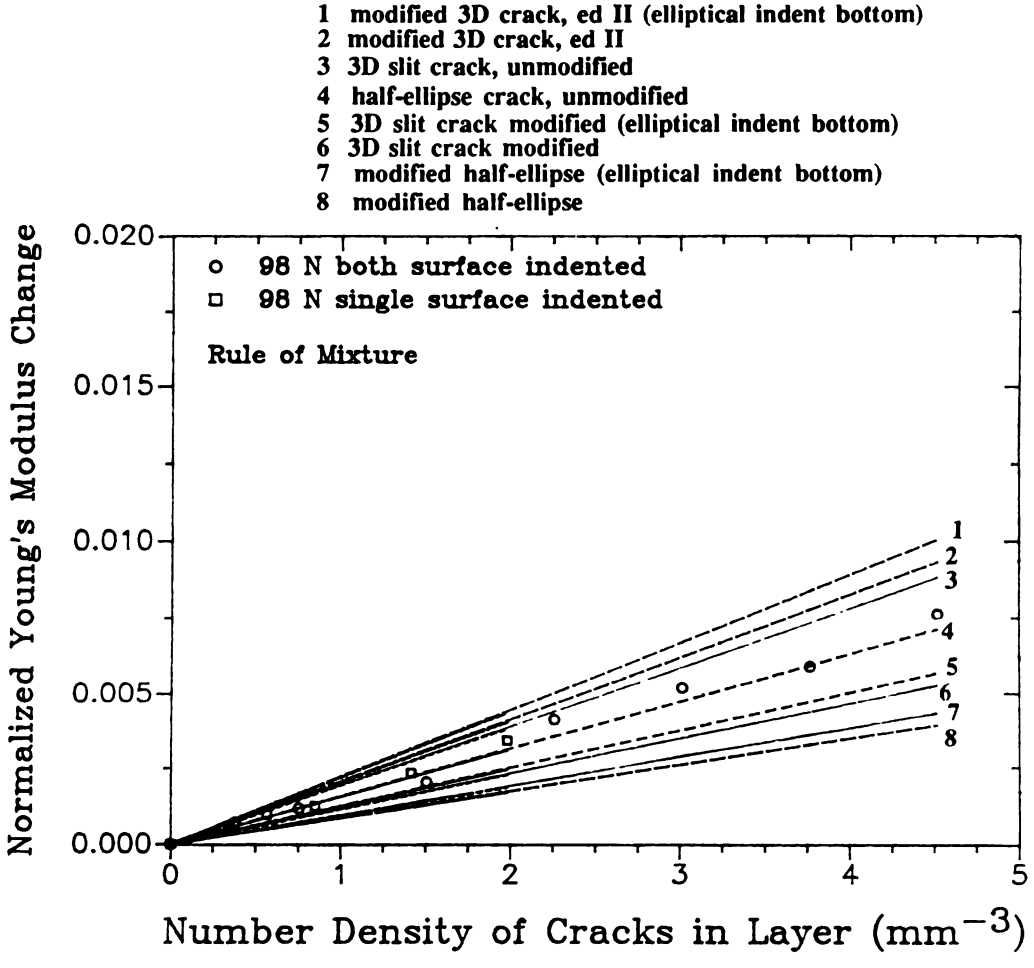

Figure 69(b). The comparison of experimental value of $(E_0-E)/E_0$ versus N (mm^{-3}) with rule of mixtures predictions from each of eight different crack geometries for (b) 98 N indentation load.

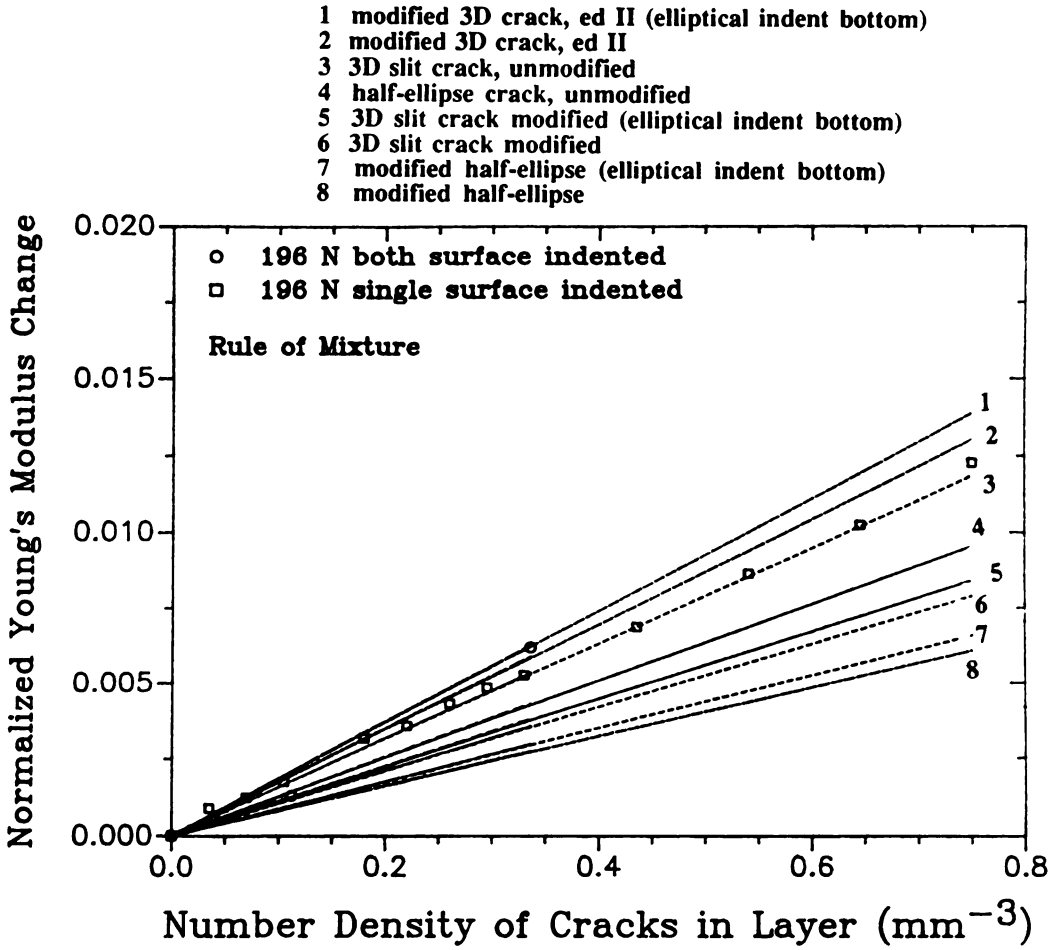

Figure 69(c). The comparison of experimental value of $(E_0-E)/E_0$ versus N (mm^{-3}) with rule of mixtures predictions from each of eight different crack geometries for (c) 196 N indentation load.

Table 28. The comparisons of the slopes in the $(E_0-E)/E_0$ versus N (mm^{-3}) plot of experimental results with those of theoretical prediction (Dynamic beam vibration theory) assuming various crack geometries, where N (mm^{-3}) was calculated considering only layer volume.

		49 N indented	98 N indented	196 N indented
Experiment	Both*	0.459×10^{-3}	1.659×10^{-3}	1.773×10^{-2}
	Single*	0.644×10^{-3}	1.673×10^{-3}	1.613×10^{-2}
Modified slit				
	Both	0.669×10^{-3}	2.595×10^{-3}	1.906×10^{-2}
	Single	0.679×10^{-3}	2.579×10^{-3}	1.914×10^{-2}
Modified half ellipse				
	Both	0.500×10^{-3}	1.941×10^{-3}	1.465×10^{-2}
	Single	0.507×10^{-3}	1.929×10^{-3}	1.470×10^{-2}
Half ellipse				
	Both	0.927×10^{-3}	3.509×10^{-3}	2.304×10^{-2}
	Single	0.941×10^{-3}	3.489×10^{-3}	2.321×10^{-2}
Slit				
	Both	1.147×10^{-3}	4.333×10^{-3}	2.855×10^{-2}
	Single	1.159×10^{-3}	4.318×10^{-3}	2.893×10^{-2}
Modified 3D cracks edition II				
	Both	1.620×10^{-3}	4.589×10^{-3}	3.150×10^{-2}
	Single	1.647×10^{-3}	4.574×10^{-3}	3.188×10^{-2}
Modified slit elliptical indent bottom				
	Both	0.678×10^{-3}	2.796×10^{-3}	2.031×10^{-2}
	Single	0.686×10^{-3}	2.781×10^{-3}	2.042×10^{-2}
Modified half ellipse elliptical indent bottom				
	Both	0.507×10^{-3}	2.135×10^{-3}	1.590×10^{-2}
	Single	0.513×10^{-3}	2.120×10^{-3}	1.594×10^{-2}
Modified 3D cracks, ed. II elliptical indent bottom				
	Both	1.640×10^{-3}	4.947×10^{-3}	3.356×10^{-2}
	Single	1.666×10^{-3}	4.932×10^{-3}	3.401×10^{-2}

* Both = indented on both surfaces, Single = indented on a single surface.

Table 29. The comparisons of the slopes in the $(E_0-E)/E_0$ versus N (mm^{-3}) plot of experimental results with those of theoretical prediction (Rule of Mixtures) assuming various crack geometries, where N (mm^{-3}) was calculated considering only layer volume.

		49 N indented	98 N indented	196 N indented
Experiment	Both*	0.459×10^{-3}	1.659×10^{-3}	1.773×10^{-2}
	Single*	0.644×10^{-3}	1.673×10^{-3}	1.613×10^{-2}
Modified slit				
	Both	0.282×10^{-3}	1.169×10^{-3}	1.060×10^{-2}
	Single	0.284×10^{-3}	1.153×10^{-3}	1.052×10^{-2}
Modified half ellipse				
	Both	0.209×10^{-3}	0.874×10^{-3}	0.815×10^{-2}
	Single	0.212×10^{-3}	0.861×10^{-3}	0.810×10^{-2}
Half ellipse				
	Both	0.387×10^{-3}	1.580×10^{-3}	1.283×10^{-2}
	Single	0.393×10^{-3}	1.559×10^{-3}	1.272×10^{-2}
Slit				
	Both	0.479×10^{-3}	1.952×10^{-3}	1.590×10^{-2}
	Single	0.484×10^{-3}	1.926×10^{-3}	1.581×10^{-2}
Modified 3D cracks edition II				
	Both	0.677×10^{-3}	2.067×10^{-3}	1.753×10^{-2}
	Single	0.686×10^{-3}	2.038×10^{-3}	1.738×10^{-2}
Modified slit elliptical indent bottom				
	Both	0.283×10^{-3}	1.259×10^{-3}	1.131×10^{-2}
	Single	0.287×10^{-3}	1.241×10^{-3}	1.121×10^{-2}
Modified half ellipse elliptical indent bottom				
	Both	0.212×10^{-3}	0.962×10^{-3}	0.884×10^{-2}
	Single	0.215×10^{-3}	0.948×10^{-3}	0.877×10^{-2}
Modified 3D cracks, ed. II elliptical indent bottom				
	Both	0.685×10^{-3}	2.228×10^{-3}	1.866×10^{-2}
	Single	0.695×10^{-3}	2.198×10^{-3}	1.853×10^{-2}

* Both = indented on both surfaces, Single = indented on a single surface.

indents in a given surface, such that N = number of indentations / (depth of layer x specimen width x specimen length). The best correlation between dynamic beam vibration theory and experimental data was obtained for "modified" half-ellipse cracks and "modified" half ellipse cracks with elliptical indent bottom for all the loads used in this study, where "modified" refers to modifications in the crack area and crack perimeter to account for the geometry of the indentation crack. The best correlation between rule of mixtures theory and experimental data was obtained for half-ellipse cracks for 98 N indentations and 3D slit cracks for 196 N indentations.

Tables 30 and 31 compare the slopes of experimental values of $(E_0-E)/E_0$ versus N (mm^{-2}) with that of theory predictions from each of three different crack geometries [198] (figures 70 and 71). The crack number density for the two - dimensional crack distributions were calculated from the relation that N = number of indentations / (specimen width x specimen length). The correlation between dynamic beam vibration theory and experimental data was not so good for any models of cracks. The best correlation between rule of mixtures theory and experimental data was obtained for "modified" 2D slit cracks. Figures 72-74 show the best correlation plots between theory predictions and experimental data for all the loads used for indentations.

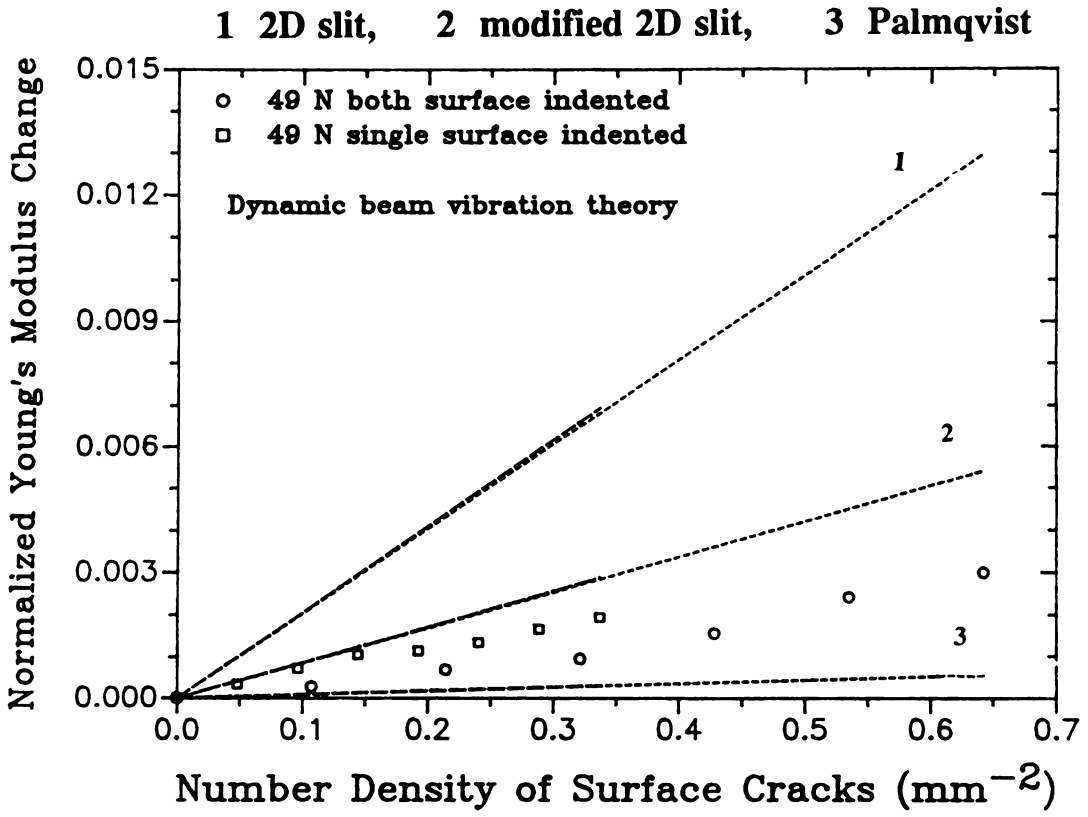

Figure 70(a). The comparison of experimental value of $(E_0-E)/E_0$ versus N (mm^{-2}) with dynamic beam vibration theory predictions from each of three different crack geometries for (a) 49 N indentation load.

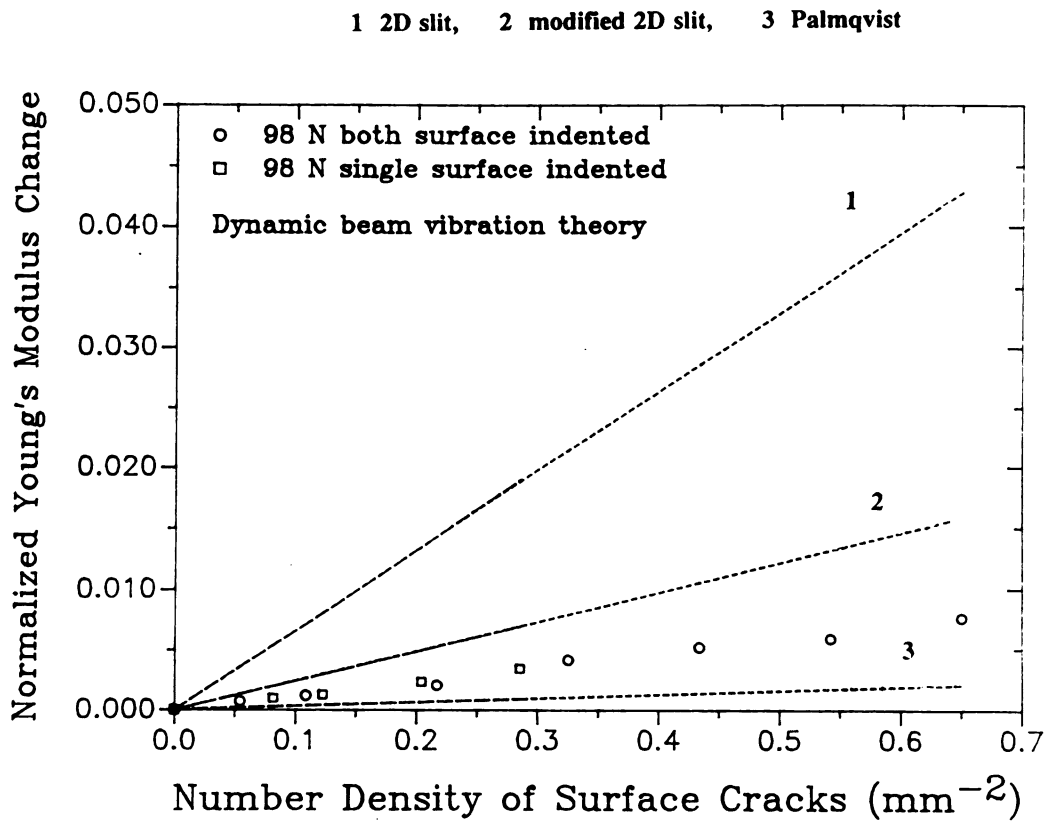

Figure 70(b). The comparison of experimental value of $(E_0-E)/E_0$ versus N (mm^{-2}) with dynamic beam vibration theory predictions from each of three different crack geometries for (b) 98 N indentation load.

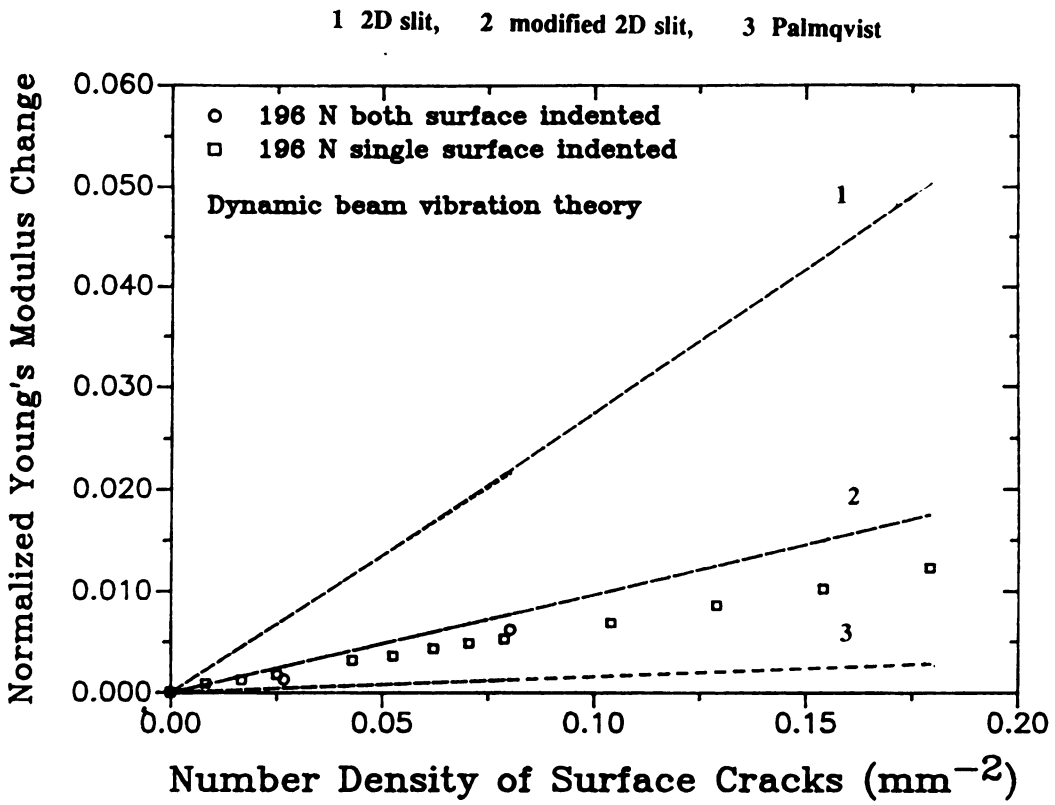

Figure 70(c). The comparison of experimental value of $(E_0-E)/E_0$ versus N (mm^{-2}) with dynamic beam vibration theory predictions from each of three different crack geometries for (c) 196 N indentation load.

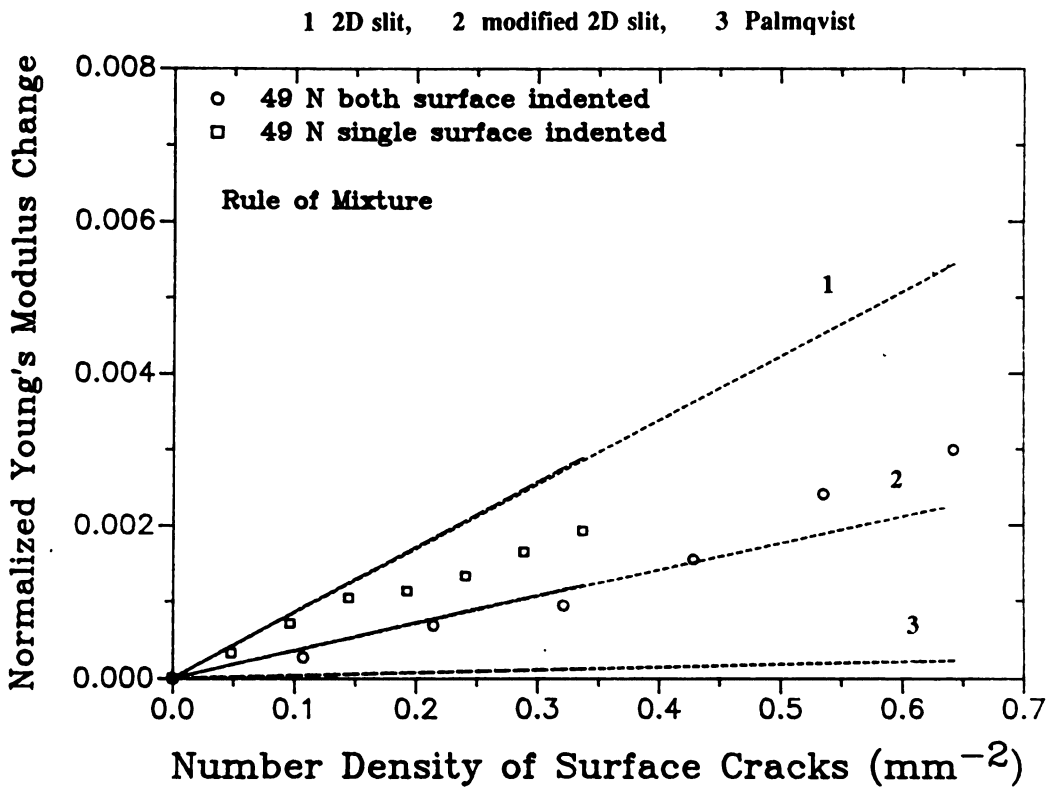

Figure 71(a). The comparison of experimental value of $(E_0-E)/E_0$ versus N (mm^{-2}) with rule of mixtures predictions from each of three different crack geometries for (a) 49 N indentation load.

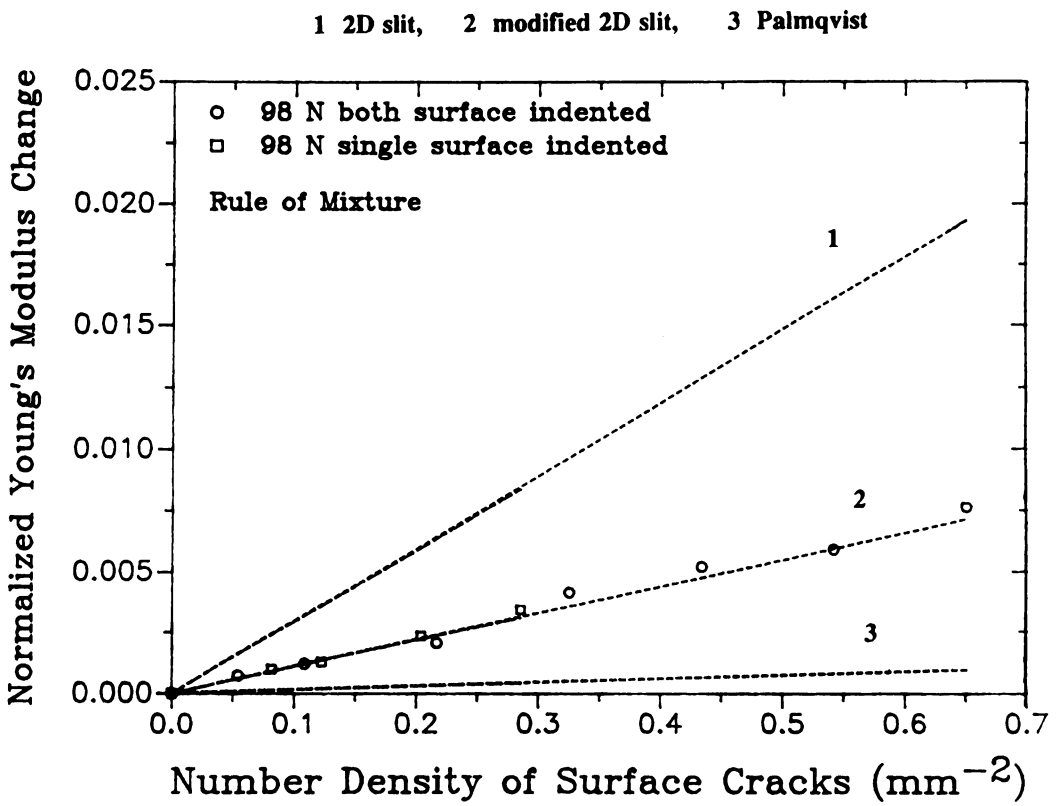

Figure 71(b). The comparison of experimental value of $(E_0-E)/E_0$ versus N (mm^{-2}) with rule of mixtures predictions from each of three different crack geometries for (b) 98 N indentation load.

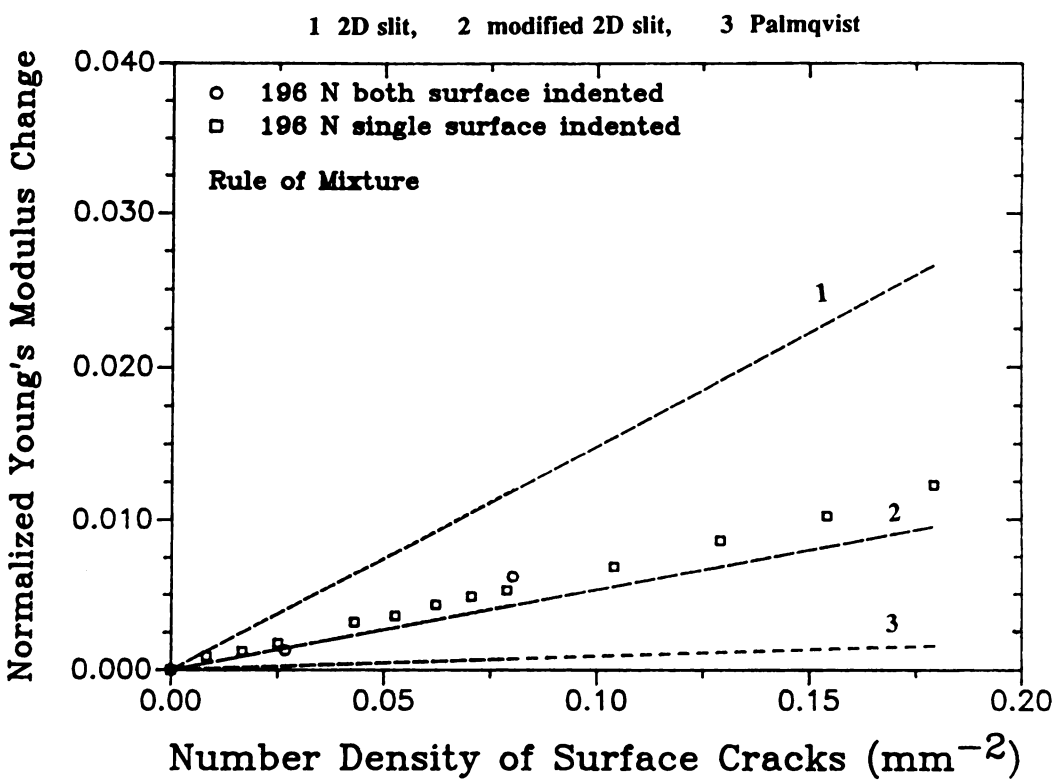

Figure 71(c). The comparison of experimental value of $(E_0-E)/E_0$ versus N (mm^{-2}) with rule of mixtures predictions from each of three different crack geometries for (c) 196 N indentation load.

Table 30. The comparisons of the slopes in the $(E_0-E)/E_0$ versus N (mm^{-2}) plot of experimental results with those of theoretical prediction (Dynamic Beam Vibration Theory) assuming various crack geometries, where N (mm^{-2}) is a surface number density of cracks.

		49 N indented	98 N indented	196 N indented
Experiment	Both*	0.475×10^{-2}	1.159×10^{-2}	7.422×10^{-2}
	Single*	0.539×10^{-2}	1.162×10^{-2}	6.749×10^{-2}
2D Slit				
	Both	2.020×10^{-2}	6.589×10^{-2}	0.2688
	Single	2.055×10^{-2}	6.611×10^{-2}	0.2770
Modified 2D slit				
	Both	0.843×10^{-2}	2.437×10^{-2}	9.640×10^{-2}
	Single	0.855×10^{-2}	2.423×10^{-2}	9.713×10^{-2}
Palmqvist				
	Both	0.859×10^{-3}	3.209×10^{-3}	1.595×10^{-2}
	Single	0.869×10^{-3}	3.186×10^{-3}	1.588×10^{-2}

Table 31. The comparisons of the slopes in the $(E_0-E)/E_0$ versus N (mm^{-2}) plot of experimental results with those of theoretical prediction (Rule of Mixtures) assuming various crack geometries, where N (mm^{-2}) is a surface number density of cracks.

		49 N indented	98 N indented	196 N indented
Experiment	Both*	0.475×10^{-2}	1.159×10^{-2}	7.422×10^{-2}
	Single*	0.539×10^{-2}	1.162×10^{-2}	6.749×10^{-2}
2D Slit				
	Both	0.844×10^{-2}	2.967×10^{-2}	0.1493
	Single	0.856×10^{-2}	2.926×10^{-2}	0.1482
Modified 2D slit				
	Both	0.352×10^{-2}	1.097×10^{-2}	5.369×10^{-2}
	Single	0.357×10^{-2}	1.082×10^{-2}	5.324×10^{-2}
Palmqvist				
	Both	0.358×10^{-3}	1.444×10^{-3}	8.855×10^{-3}
	Single	0.368×10^{-3}	1.428×10^{-3}	8.821×10^{-3}

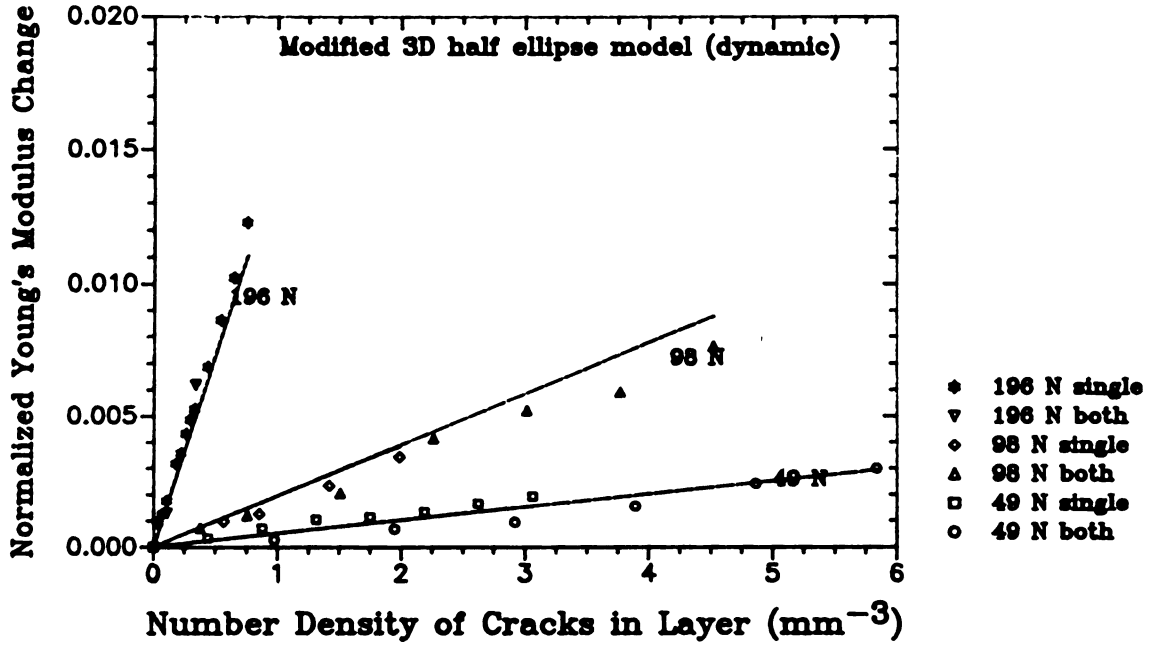

Figure 72. $(E_0\text{-}E)/E_0$ versus N plots between theory predictions and experimental data for modified half ellipse model-dynamic beam vibration theory.

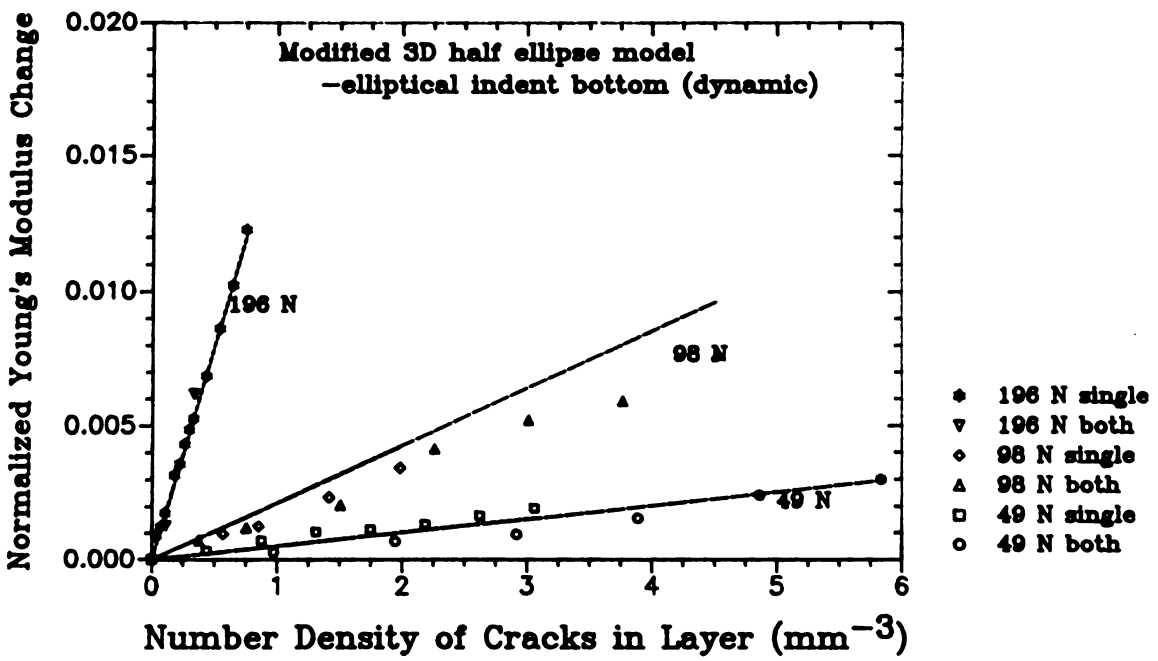

Figure 73. $(E_0-E)/E_0$ versus N plots between theory predictions and experimental data for modified half ellipse model with elliptical indent bottom - dynamic beam vibration theory.

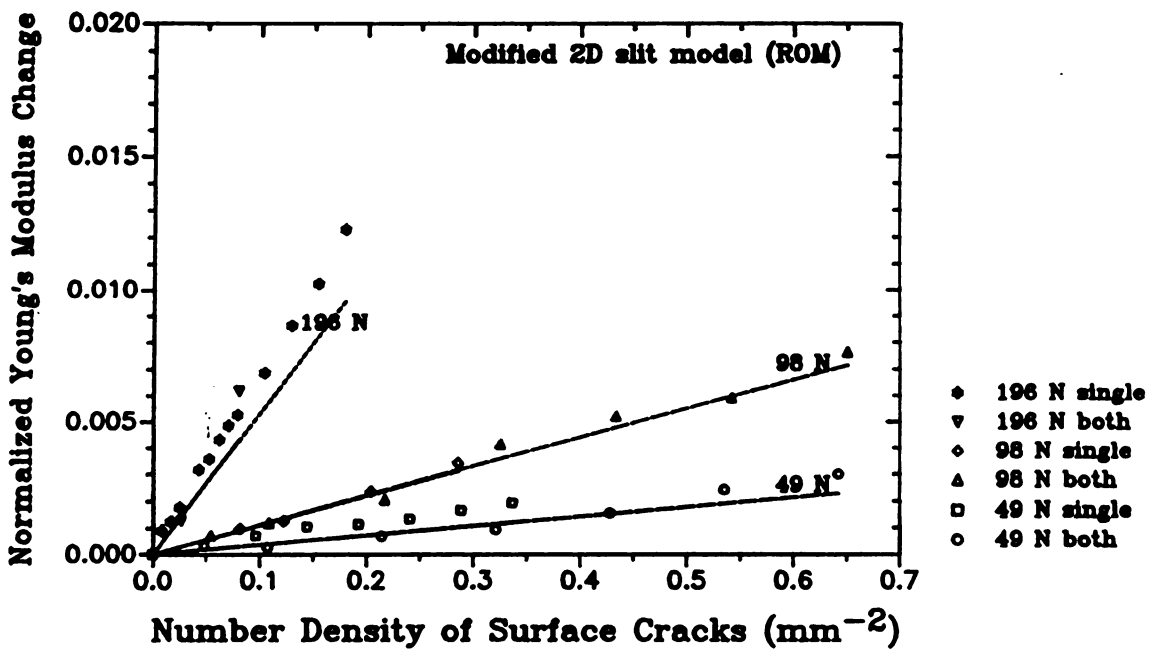

Figure 74. $(E_0-E)/E_0$ versus N plots between theory predictions and experimental data for modified 2D slit crack model - rule of mixtures.

4. Conclusions

4.1 Thermal Fatigue

Thermal shock damage for SiC fiber/Aluminosilicate composites, Macor glass-ceramics, and polycrystalline titanium diboride was monitored by Young's modulus and internal friction changes. For the Macor glass-ceramics and SiC fiber/Aluminosilicate composites studied, the ΔQ^{-1} versus ϵ plots were linear for low level of damage, corresponding to $\Delta Q^{-1} = D\epsilon$.

The fatigue-like power law relation between the damage saturation level and ΔT, the quench temperature difference, observed for Macor glass-ceramics, SiC fiber/Aluminosilicate composites, and polycrystalline titanium diboride was identical in form to the power law fatigue relation observed in previous studies of SiC whisker/alumina composites [24] and unreinforced alumina [25]. Exponents p1 and p2 in the power law fatigue relations (equations 1 and 2) are functions of thermal shock resistance parameters such as R'''' and hence p1 and p2 are likely also functions of materials parameters such as fracture toughness. In addition, the thermal fatigue parameters $A\alpha$ and $B\beta$ are apparently functions of fracture toughness.

The results of this study suggest the existence of threshold fracture toughness (or strength) above which thermal shock damage will not accumulate for a given ΔT (figure 33).

4.2 Time-Dependent Elastic Modulus Recovery Measurement on Thermally Shocked SiC fiber/Aluminosilicate Composites, Machinable Glass Ceramics and Polycrystalline Alumina

Time-dependent partial recoveries in Young's modulus were observed for thermally shocked SiC fiber/AS composites, Macor glass-ceramics and polycrystalline alumina specimens. The observed mass changes for specimens undergoing Young's modulus recovery were found to be two orders of magnitude smaller than the mass changes that would be necessary to account for the observed modulus recovery. Thus mass changes arising from the evaporation of water absorbed during the cyclic thermal quenching of the specimens could not account for the Young's modulus recovery.

The observed Young's modulus recovery in the three ceramic materials is likely due to room-temperature microcrack healing. Numerical estimates of property recovery rates were obtained from a regression analysis of available data on room-temperature crack healing in ceramics. The calculated recovery time constants for cleavage cracks in single crystals and for thermal shock cracks in polycrystalline YIG agreed relatively well the time constants for modulus recovery determined in the present study (Table 16). However, the recovery time constants for soda-lime-silica and fluoride glasses were approximately a factor of 10^{-2} smaller that single crystal and polycrystalline time constants.

Although the particular microcrack healing mechanism has not been documented in this study, it is assumed that water or water vapor in

the quench medium or in the ambient atmosphere (laboratory air) interacted with the fresh surfaces of cracks induced by cyclic thermal shock. For the materials included in this study further work is needed to determine whether chemically reactive fresh crack surfaces may promote crack healing via mechanisms such as adhesion or by the build-up of reaction products.

4.3 The Measurement of the Surface Heat Transfer Coefficient for Ceramics Quenched into a Water Bath

A technique for measuring the surface heat transfer coefficient, h, is developed for ceramics quenched into a water bath that combines a parameter estimation method with a fast-response capability of recently developed thin-film thermocouples. The surface heat transfer coefficient values were measured for three ceramic materials: alumina, Macor glass-ceramic and hot-pressed titanium diboride.

The maximum surface tensile stress developing during quenching was calculated from the measured surface heat transfer coefficient as a function of temperature using temperature dependent parameters, Young's modulus, the coefficient of thermal expansion, Poisson's ratio, and thermal shock severity.

4.4 Effects of Surface Abrasion on the Thermal Fatigue of Ceramics

In addition to modifying the surface flaw population, surface abrasion of ceramics can reduce the elastic modulus of the surface layer of the ceramic [97, 179], introduce surface compressive residual stresses [71, 72], and increase the surface heat transfer coefficient, h [75, 177, 178]. The reduction in the surface layer modulus and the surface compressive stresses act to reduce the surface tensile stresses that drive microcracks and macrocracks during thermal cycling. However, the increase in h (and the subsequent increase in B) acts to increase the surface tensile stresses, so that the effect of surface abrasion has components that act in a competing manner. The net surface tensile stress induced during quenching must then be considered together with the increases in flaw size due to abrasion in order to estimate the level of thermal shock damage for abraded ceramics.

4.5 The Effect of Surface Limited Microcracks on the Effective Young's Modulus of Ceramics

A modulus-microcracking model was presented for surface limited microcrack distributions based on the concept that a specimen containing a surface-limited population of microcracks could be viewed as a composite, with the microcrack damaged regions as layers of reduced modulus, ideally bonded to an undamaged substrate.

The modulus of the individual damaged layers was modeled in terms of the crack damage parameters, $\Lambda = fGN$, which account for the spatial

orientation of the cracks, the crack geometry, and the number density of the microcracks. The moduli of the damaged layers were employed in a Rule of Mixtures model and a dynamic modulus model developed by the authors in the present study.

For the particular case of model indentation crack distributions, corrections were made to the crack perimeter and area calculations to account for the ligament bridging the two crack faces in an indentation crack.

The dimensions and geometry of indentation-induced cracks for the three different indentation loads (49 N, 98 N and 196 N) were observed fractographically (figure 66). The radial crack sizes for the loads were measured with optical microscope.

For the Vickers induced indentation cracks, the measured normalized Young's modulus changes, $(E_0-E)/E_0$, increased linearly with increasing microcrack number density N. The observed crack induced modulus changes were compared to a number of microcracking models.

Dynamic beam vibration theory prediction under the crack shape assumption of "modified" half-ellipse cracks and "modified" half ellipse cracks with elliptical indent bottom (3D models) best fit the experimental data for all the loads used in this study. In the 3D models [4], the crack number density was calculated in terms of the "damaged layer".

The best correlation between rule of mixtures theory and experimental data (2D models) was obtained for "modified" 2D slit cracks.

5. Summary

Thermal fatigue damage for SiC fiber/Aluminosilicate composites, Macor glass-ceramics, and polycrystalline titanium diboride was non-destructively monitored as a function of the cumulative number of thermal shock cycles via Young's modulus and internal friction measurements using the sonic resonance method. A fatigue-like power law relation between the damage saturation level and ΔT, the quench temperature difference, was observed. The results also suggest the existence of a fracture toughness (or strength) threshold above which thermal shock damage will not accumulate for a given ΔT.

Partial time-dependent recoveries in Young's modulus were observed for thermally shocked SiC fiber/AS composites, Macor glass-ceramics and polycrystalline alumina specimens. The observed Young's modulus recovery in the three ceramic materials is likely due to room-temperature microcrack healing. Further work is needed to determine whether chemically reactive fresh crack surfaces in these materials may promote crack healing via mechanisms such as adhesion or by the build-up of reaction products.

A measurement technique for the surface heat transfer coefficient was developed combining the inverse parameter estimation method with the fast response capability of thin film thermocouples. The maximum surface tensile stress developed during quenching was calculated from the measured surface heat transfer coefficient as a function of temperature. An empirically-based fatigue-like power law relation was

observed between the damage saturation level, A/E_0, and the maximum surface tensile stress developed during quenching.

Effects of surface abrasion on the thermal fatigue of ceramics was investigated via the reduction in the elastic modulus of the surface layer, surface compressive residual stresses, and the increase in the surface heat transfer coefficient, h during quenching. The increase in h (and the subsequent increase in Biot modulus) increases the surface tensile stresses, so that surface abrasion has components that act in a competing manner. The net surface tensile stress induced during quenching must then be considered together with the increases in flaw size due to abrasion in order to estimate the level of thermal shock damage for abraded ceramics.

Modulus-microcracking models based on a Rule of Mixtures model and a dynamic modulus model were presented for surface limited microcrack distributions based on the concept that a specimen containing a surface-limited population of microcracks could be viewed as a composite. The microcrack damaged regions act as layers of reduced modulus, ideally bonded to an undamaged substrate.

The modulus of the individual damaged layers was modeled in terms of the damage parameter, $\Lambda = fGN$, which accounts for the spatial orientation of the cracks, the crack geometry, and the number density of the microcracks. For the particular case of model indentation crack distributions, corrections were made to the crack perimeter and area expressions to account for the bridge formed by the

hemispherically deformed zone between the two crack faces in an indentation crack.

For the Vickers induced indentation cracks, the experimental values of the measured normalized Young's modulus change, $(E_0-E)/E_0$, increased linearly with increasing microcrack number density N. The observed crack-induced modulus changes were compared to a number of microcracking models. The surface-limited damage model based on the dynamic beam vibration theory and on a modified half-ellipse crack shape fit the experimental data well.

APPENDIX A Dynamic and Static Elastic Constants

Adiabatic and Isothermal Elastic Constants

When elastic constants are measured statically, the specimen is deformed very slowly and the resultant deformation is measured. The specimen deformation occurs slowly compared to the rate of heat flow in the specimen. In addition, the specimen is in contact with a mechanical testing machine which functions as a heat sink, thus Static elastic constant measurements are isothermal processes.

Conversely, the velocity of an acoustic wave through a region of sample is very rapid compared to the rate of heat flow in the specimen. For Dynamic elastic constant measurements (for example, the sonic resonance method), there is no thermal energy transfer between the region of sample where work is being done and its surroundings. Dynamic elastic constant measurements are thus adiabatic processes. The adiabatic process (dynamic method) yields different values for elastic constants compared to those measured by isothermal process (static method).

For static (isothermal) measurements part of the energy is converted to heat which is subsequently isothermally removed by the surroundings. The remaining energy is stored as isothermal elastic deformation strain, ϵ_i. For adiabatic measurements, the heat raises the local specimen temperature. A local thermal expansion is induced by the local temperature increase. The expansion resists the dimensional change produced by stress. The adiabatic deformation

strain, ϵ_a therefore is less than the isothermal strain, ϵ_i for the same amount of applied stress. Thus the material behaves more stiffly under adiabatic conditions than isothermal [a1, a2].

Adiabatic elastic constants are defined by,

$$c^S_{mn} = (\partial\sigma_m / \partial\epsilon_n)_S , \qquad s^S_{mn} = (\partial\epsilon_m / \partial\sigma_n)_S \tag{A1}$$

Isothermal elastic constants are defined by,

$$c^T_{mn} = (\partial\sigma_m / \partial\epsilon_n)_T , \qquad s^T_{mn} = (\partial\epsilon_m / \partial\sigma_n)_T \tag{A2}$$

The combined first and second law of thermodynamics is

$$\begin{aligned} dQ = TdS &= dU + dW \\ &= dU - \sigma_m d\epsilon_m \end{aligned} \tag{A3}$$

where dQ = the heat entering into the system

dU = the change in internal energy of the system

dW = PdV, the work done by the system

Hence $dU = TdS + \sigma_m d\epsilon_m$ (A4)

$dA = d(U - TS) = -SdT + \sigma_m d\epsilon_m$ (A5)

$dG = d(U - TS + PV) = -SdT + \epsilon_m d\sigma_m$ (A6)

Since dA and dG are total differentials, then

$$dA = (\partial A/\partial \epsilon_m)_T \, d\epsilon_m + (\partial A/\partial T)_\epsilon \, dT$$

$$dG = (\partial G/\partial \sigma_m)_T \, d\sigma_m + (\partial G/\partial T)_\sigma \, dT$$

From equations (A5) and (A6), we obtain

$$\sigma_m = (\partial A/\partial \epsilon_m)_T, \qquad S = -(\partial A/\partial T)_\epsilon \tag{A5'}$$

$$\epsilon_m = -(\partial G/\partial \sigma_m)_T, \qquad S = -(\partial G/\partial T)_\sigma \tag{A6'}$$

From the Maxwell relationships for the total differentials dA and dG

$$-(\partial \sigma_m/\partial T)_\epsilon = (\partial S/\partial \epsilon_m)_T = F_m \tag{A5''}$$

$$(\partial \epsilon_m/\partial T)_\sigma = (\partial S/\partial \sigma_m)_T = \alpha_m \tag{A6''}$$

where F_m = inelastic stress

α_m = thermal expansion coefficient

Here σ_m and ϵ_m refer to all the stress and strain components respectively. α_m are the components of the thermal expansion tensor. From the total differential of $d\sigma_m$ and dS

$$\begin{aligned} d\sigma_m &= (\partial \sigma_m/\partial \epsilon_m)_T \, d\epsilon_m + (\partial \sigma_m/\partial T)_\epsilon \, dT \\ &= c^T_{mn} \, d\epsilon_m - F_m \, dT \end{aligned} \tag{A7}$$

$$\begin{aligned} dS &= (\partial S/\partial \epsilon_m)_T \, d\epsilon_m + (\partial S/\partial T)_\epsilon \, dT \\ &= F_m \, d\epsilon_m + (\partial S/\partial T)_\epsilon \, dT \\ &= F_m \, d\epsilon_m + (C_\epsilon/T) \, dT \end{aligned} \tag{A8}$$

where $C_\epsilon = T(\partial S/\partial T)_\epsilon$ the specific heat at constant strain per unit volume

Similarly, from total differential of $d\epsilon_m$ and dS taking σ_m and T as independent variables,

$$d\epsilon_m = (\partial \epsilon_m/\partial \sigma_m)_T \, d\sigma_m + (\partial \epsilon_m/\partial T)_\sigma \, dT$$
$$= s^T_{mn} \, d\sigma_m + \alpha_m \, dT \qquad \text{(A9)}$$
$$dS = (\partial S/\partial \sigma_m)_T \, d\sigma_m + (\partial S/\partial T)_\sigma \, dT$$
$$= \alpha_m \, d\sigma_m + (\partial S/\partial T)_\sigma \, dT$$
$$= \alpha_m \, d\sigma_m + (C_\sigma/T) \, dT \qquad \text{(A10)}$$

where $C_\sigma = T(\partial S/\partial T)_\sigma$ the specific heat at constant stress per unit volume

Under constant stress conditions ($d\sigma_m = 0$), one can divide equation 7 by dT to obtain

$$F_m = c^T_{mn} \, \alpha_n \qquad \text{(A11)}$$

Similarly from equation (9),

$$\alpha_m = s^T_{mn} \, F_n \qquad \text{(A12)}$$

Under adiabatic conditions the entropy S is constant and thus dS = 0. Equations (A7) and (A8) become

$$d\sigma_m = c^T_{mn}\, d\epsilon_n + (T/C_\epsilon)\, F_m F_n\, d\epsilon_n = c^S_{mn}\, d\epsilon_n \tag{A13}$$

$$c^S_{mn} - c^T_{mn} = (T/C_\epsilon)\, F_m F_n \tag{A14}$$

after dT is eliminated.

Similarly from equation (A9) and (A10),

$$s^S_{mn} - s^T_{mn} = -\alpha_m \alpha_n T/C_\sigma \tag{A15}$$

By eliminating $d\sigma_n$ between equations (A7) and (A10), using equation (A11) and the definition of the specific heat at constant strain, we obtain

$$C_\sigma - C_\epsilon = T\, \alpha_n F_n = T\, \alpha_m \alpha_n c^T_{mn} \tag{A16}$$

Appendix A. References

a1. A. B. Bhatia, Ultrasonic Absorption, Chap. 3, Oxford University Press, Oxford, 1967.

a2. A. S. Nowick and B. S. Berry, Anelastic Relaxation in Crystalline Solids, Chap. 6, Academic Press, New York, 1972.

APPENDIX B. A Rule of Mixtures Model for Two-Layer and Three-Layer Composite Models of Surface-Microcracked Specimens

For two layer composite (figure B1(a)),

$$e_{layer} = e_{undamaged} = e_{overall} \tag{B1}$$

where e_{layer} = strain in microcracked layer

$e_{undamaged}$ = strain in undamaged layer

$e_{overall}$ = overall strain

Then

$$\sigma_\ell = E_\ell \, e_\ell \tag{B2a}$$

$$\sigma_s = E_s \, e_s \tag{B2b}$$

For microcracked layer cross-sectional area, A_ℓ and undamaged layer cross-sectional area, A_s, then load (force) P_ℓ in the microcracked layer and the load P_s in the undamaged layer are given by

$$P_\ell = \sigma_\ell A_\ell = E_\ell e_\ell A_\ell \tag{B3a}$$

$$P_s = \sigma_s A_s = E_s e_s A_s \tag{B3b}$$

where $P_{overall} = P_s + P_\ell = \sigma_{overall} \, A_{total} = \sigma_\ell A_\ell + \sigma_s A_s$, such that

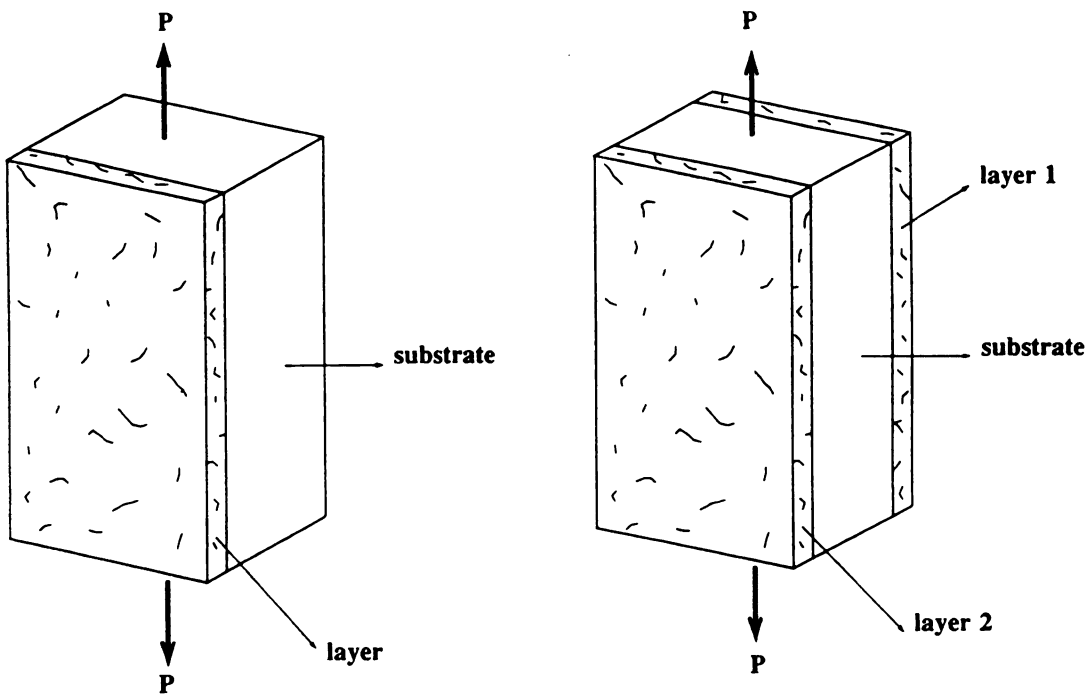

Figure B1. Schematic of uniaxial tensile loading for (a) two layer composite and (b) three layer composite model.

$$\sigma_{overall} = \sigma_{\ell} A_{\ell}/A_{total} + \sigma_s A_s/A_{total} = \sigma_{\ell} v_{\ell} + \sigma_s v_s \quad (B4)$$

If equation B4 is differentiated with respect to strain, then

$$d\sigma_{overall}/de = (d\sigma_{\ell}/de)v_{\ell} + (d\sigma_s/de)v_s \quad (B5)$$

If $d\sigma_{\ell}/de$ and $d\sigma_s/de$ are linear, then

$$\bar{E}_{2_{ROM}} = E_{\ell} v_{\ell} + E_s v_s \quad (B6)$$

For a three layer composite (figure B1(b)),

strain in microcracked layer 1 = strain in microcracked layer 2 = strain in undamaged layer = overall strain

$$e_{layer\ 1} = e_{layer\ 2} = e_{undamaged} = e_{overall} \quad (B7)$$

For the three layer modulus (two microcracked layers and an undamaged layer), a similar procedure leads to

$$d\sigma_{overall}/de = (d\sigma_{\ell 1}/de)v_{\ell 1} + (d\sigma_s/de)v_s + (d\sigma_{\ell 2}/de)v_{\ell 2} \quad (B8)$$

If $(d\sigma_{\ell 1}/de)$ and $(d\sigma_{\ell 2}/de)$ are linear, then

$$\bar{E}_{3_{ROM}} = E_{\ell 1} v_{\ell 1} + E_s v_s + E_{\ell 2} v_{\ell 2} \quad (B9)$$

If the stress-strain behavior for the non-microcracked ceramic is linear (which is typically true, except at very high temperatures), then $d\sigma_s/de$ should be linear, since it refers to the non-microcracked stress-strain behavior. A key assumption for the ROM model is then the linearity of $d\sigma_\ell/de$, which refers to the stress-strain behavior of the microcracked layer(s).

APPENDIX C. Layer composite model approach for Young's modulus change using dynamic beam vibration theory

The free, undamped vibration of a monolithic bar can be described approximately by the Bernoulli-Euler beam equation [c1, c2].

$$EI \frac{\partial^4 W(x,t)}{\partial x^4} + \frac{a\rho}{g} \frac{\partial^2 W(x,t)}{\partial t^2} = 0 \qquad (C1)$$

where, E = Young's modulus (Kgf/m^2)

I = the second moment of inertia of the cross section of the bar with respect to the neutral axis

W = transverse deflection of the bar, which is a function of position along longitudinal axis, x, and time, t

a = cross sectional area of the bar

ρ = density of the bar

g = acceleration due to gravity

Assuming perfect interfacial bonding between the microcracked layer and undamaged layer, for a single microcracked layer (figure C1), equation C1 becomes

$$(E_s I_s + E_\ell I_\ell) \frac{\partial^4 W(x,t)}{\partial x^4} + \frac{(a_\ell \rho_\ell + a_s \rho_s)}{g} \frac{\partial^2 W(x,t)}{\partial t^2} = 0 \qquad \text{(B2)}$$

Subscripts, ℓ and s represents properties associated with the microcracked layer and undamaged substrate layer respectively. Since the density change after microcracking typically is negligible and the sum of microcracked layer cross sectional area and the undamaged layer area is total cross sectional area of the beam, $\{(a_\ell \rho_\ell + a_s \rho_s)/g\}$ in equation C2 should be $a\rho/g$.

The transverse vibration of a bar for free-free suspension requires that the bending moments and the shearing forces must be zero at both ends of the bar.

$$\frac{\partial^2 W(0,t)}{\partial x^2} = 0 \; ; \; \frac{\partial^3 W(0,t)}{\partial x^3} = 0 \qquad \text{for } t \geq 0 \qquad \text{(C3a)}$$

$$\frac{\partial^2 W(L,t)}{\partial x^2} = 0 \; ; \; \frac{\partial^3 W(L,t)}{\partial x^3} = 0 \qquad \text{for } t \geq 0 \qquad \text{(C3b)}$$

where, L = length of the specimen

The solution of equation B2 under the boundary conditions given in equations C3a and C3b gives [c1, c2]

$$W_n(x,t) = \{C_1\cos(\omega_n t)+C_2\sin(\omega_n t)\}\cdot$$

$$\left[\cos(k_n x)+\cosh(k_n x) - \{\cos(k_n L)-\cosh(k_n L)\}\cdot\frac{\{\sin(k_n x)+\sinh(k_n x)\}}{\{\sin(k_n L)-\sinh(k_n L)\}}\right] \quad (C4)$$

$$\text{where} \quad \omega_n = k_n^2\left[\frac{\{(E_s I_s+E_\ell I_\ell)g}{a\rho}\right]^{1/2}$$

C_1, C_2 = integer constants

n = nth mode of vibration.

Each W_n represents a harmonic transverse vibration with frequency, $F = \omega_n/2\pi$. These boundary conditions lead to the following frequency equation

$$\cos(k_n L)\cosh(k_n L) = 1 \quad (C5)$$

The first root, $k_1 L$ of equation B5 is 4.730048 [c1, c2]. The fundamental transverse (flexural) vibration frequency, n = 1, of the composite is

$$F = \frac{k_1^2}{2\pi}\left[\frac{\{(E_s I_s+E_\ell I_\ell)g}{a\rho}\right]^{1/2}$$

$$= \frac{11.1528}{L^2}\left[\frac{\{(E_s I_s+E_\ell I_\ell)g}{a\rho}\right]^{1/2} \quad (C6)$$

The moments of inertia I_s and I_ℓ (figure C1) were calculated from

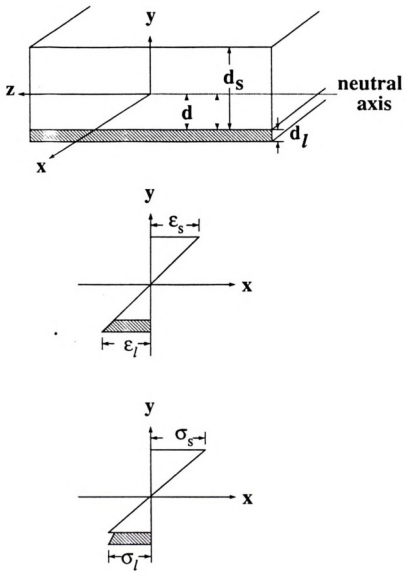

Figure C1. Schematic of two layer model composite beam, strain and stress distribution.

$$I_s = \int_{-d}^{d_s-d} y^2 da = \left(\frac{d_s^3}{3} - d_s^2 d + d_s d^2 \right) w \qquad \text{(C7a)}$$

$$I_\ell = \int_{-d-d_\ell}^{-d} y^2 da = \left(\frac{d_\ell^3}{3} + d_\ell^2 d + d_\ell d^2 \right) w \qquad \text{(C7b)}$$

where, w = width of the specimen

d_ℓ = thickness of layer

d_s = thickness of substrate

When the two layer composite beam (figure C1) experiences pure bending, the neutral axis of the beam shifts from the centroid of cross section of the composite beam to a stiffer side. The distance from the neutral axis to the indented layer interface, d, can be calculated using the equilibrium of the axial forces during pure bending [c3] (figure C1).

$$\int_{-d}^{d_s-d} \sigma_s \, da + \int_{-d-d_\ell}^{-d} \sigma_\ell \, da = 0 \qquad \text{(C8)}$$

where, σ_ℓ = normal stress of microcracked layer (= $E_\ell y/r$) (C9a)

σ_s = normal stress of undamaged layer (= $E_s y/r$) (C9b)

r = radius of curvature of the neutral axis

Stresses σ_ℓ and σ_s can be expressed in terms of E_ℓ, E_s, d_ℓ and d_s such that using equations (C9a) and (C9b), the following expression for d may be obtained from equation C8.

$$d = \frac{(E_s d_s^2 - E_\ell d_\ell^2)}{(2E_s d_s + 2E_\ell d_\ell)} \qquad (C10)$$

Substituting equations C8-C10 into C7 gives the calculated fundamental transverse frequencies for two layer composite beam.

$$F = \frac{6.4391}{L^2} \cdot \left\{ \frac{\{(E_s d_s^3 + E_\ell d_\ell^3) - 3(E_s d_s^2 - E_\ell d_\ell^2)/4(E_s d_s + E_\ell d_\ell)\}}{(d_s + d_\ell)\rho} \right\}^{1/2} \qquad (C11)$$

The overall Young's modulus, $\bar{E}_{2_{DYN}}$, for two layer composite model is thus given by,

$$\bar{E}_{2_{DYN}} = \frac{(E_\ell I_\ell + E_s I_s)}{(I_\ell + I_s)} \qquad (C12)$$

For specimens microcracked on both surfaces, a three layer composite model which is composed of microcracked layer 1, microcracked layer 2 and noncracked layer in between should be considered (figure C2). The thickness of layers may be assumed to be the same when the specimen is loaded with a given stress profile on both surfaces. But layer 1 and layer 2 can have different values of Young's moduli depending on how many microcracks appear on each

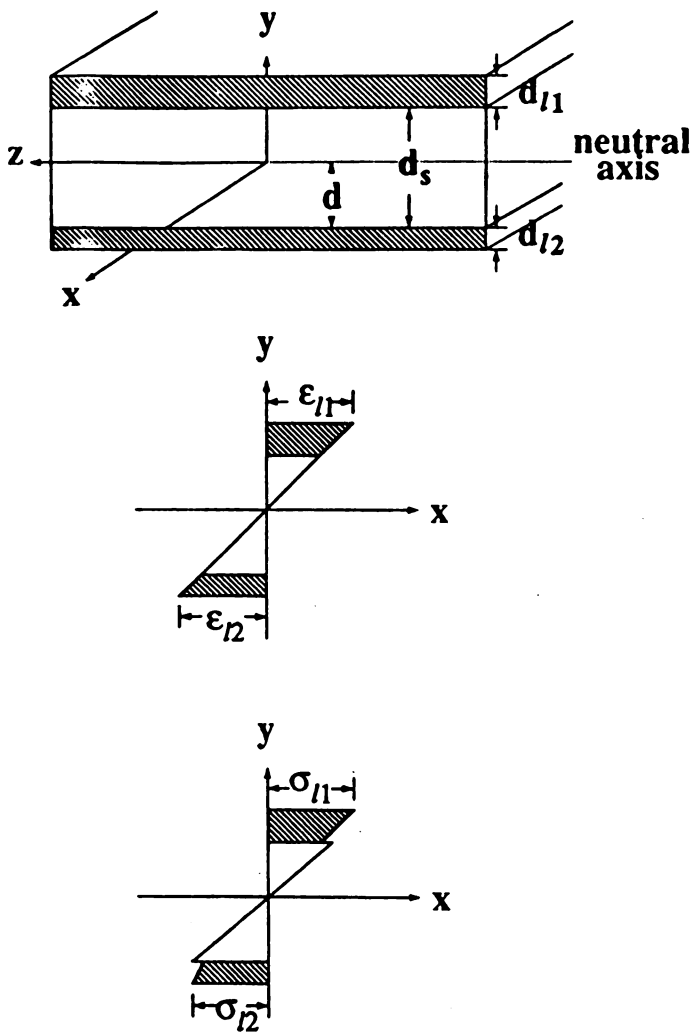

Figure C2. Schematic of three layer model composite beam, strain and stress distribution.

surface. Equation C2 becomes

$$(E_{\ell 1}I_{\ell 1}+E_sI_s+E_{\ell 2}I_{\ell 2}) \cdot \frac{\partial^4 W(x,t)}{\partial x^4} + \frac{a\rho}{g} \cdot \frac{\partial^2 W(x,t)}{\partial t^2} = 0 \qquad \text{(C13)}$$

where, $E_{\ell 1}$ = Young's modulus of layer 1

$E_{\ell 2}$ = Young's modulus of layer 2

Applying the free-free end boundary conditions (equation C4) and using equation C5 and C6 give the fundamental transverse vibration frequency for three layer composite (figure C2).

$$F = \frac{11.1528}{L^2} \cdot \left[\frac{(E_{\ell 1}I_{\ell 1} + E_sI_s + E_{\ell 2}I_{\ell 2})}{a\rho} \right]^{1/2} \qquad \text{(C14)}$$

$$I_{\ell 1} = \int_{d_s-d}^{d_s+d_{\ell 1}-d} y^2 da = \left[(d_s-d)^2 d_{\ell 1} + (d_s-d)d_{\ell 1}^2 + \frac{d_{\ell 1}^3}{3} \right] w \qquad \text{(C15a)}$$

$$I_s = \int_{-d}^{d_s-d} y^2 da = \left[\frac{d_s^3}{3} - d_s^2 d + d_s d^2 \right] w \qquad \text{(C15b)}$$

$$I_{\ell 2} = \int_{-d-d_{\ell 2}}^{-d} y^2 da = \left[\frac{d_{\ell 2}^3}{3} + d_{\ell 2}^2 d + d_{\ell 2} d^2 \right] w \qquad \text{(C15c)}$$

where, $d_{\ell 1}$, $d_{\ell 2}$ = thickness of layer 1 and layer 2, respectively

d_s = thickness of undamaged layer

w = width of the specimen

From the equilibrium of the axial forces (figure C2),

$$\int_{d_s-d}^{d_s+d_{\ell 1}-d} \sigma_{\ell 1}\, da + \int_{-d}^{d_s-d} \sigma_s\, da + \int_{-d-d_{\ell 2}}^{-d} \sigma_{\ell 2}\, da = 0 \qquad \text{(C16)}$$

where, $\sigma_{\ell 1}$ = normal stress of top indented layer (= $E_{\ell 1} y/r$) (C17a)

σ_s = normal stress of substrate layer (= $E_s y/r$) (C17b)

$\sigma_{\ell 2}$ = normal stress of bottom indented layer (= $E_{\ell 2} y/r$) (C17c)

r = radius of curvature of the neutral axis

The distance from the neutral axis to the interface of microcracked layer 2, d, is calculated in terms of known values,

$$d = \frac{(E_{\ell 1} d_{\ell 1}^2 + 2E_{\ell 1} d_{\ell 1} d_s + E_s d_s^2 - E_{\ell 2} d_{\ell 2}^2)}{(2E_{\ell 1} d_{\ell 1} + 2E_s d_s + 2E_{\ell 2} d_{\ell 2})} \qquad \text{(C18)}$$

Substituting equations C15 and C18 into C14 allows one to calculate the fundamental transverse vibration frequency.

The overall Young's modulus, $\bar{E}_{3_{DYN}}$, of three layer composite model is

$$\bar{E}_{3_{DYN}} = \frac{(E_{\ell 1} I_{\ell 1} + E_s I_s + E_{\ell 2} I_{\ell 2})}{(I_{\ell 1} + I_s + I_{\ell 2})} \qquad \text{(C19)}$$

Appendix C References

c1. E. Volterra and E. C. Zachmanoglou, pp 321-322, Dynamics of Vibrations, Charles E. Merril Books, Inc., Columbus, OH, 1965.

c2. S. K. Clark, pp 75-87, Dynamics of Continuous Elements, Prentice Hall, Inc., Englewood Cliffs, NJ, 1972.

c3. S. P. Timoshenko and D. H. Young, pp 113-115, Strength of Materials, fourth ed., Van Nostrand Reinhold Co., Princeton, NY, 1962.

APPENDIX D The ratio of normalized Young's modulus change (dynamic) to normalized Young's modulus change (ROM) when $a(d_\ell/d_s)$ approaches zero.

For two layer composite model, the moment of inertia of layer (equation 82 in the text) can be written as the following when $a \to 0$ ($d_\ell \to 0$),

$$I_\ell \approx d_\ell d^2 w \tag{D1}$$

When $d_\ell \to 0$, $d_s \approx 2d$ (figure C1). The moment of inertia of substrate (equation 81 in text) can be expressed as,

$$I_s \approx 2d^3 w/3 \tag{D2}$$

d is in turn one half of specimen thickness, t, when $d_\ell \to 0$. Thus equations D1 and D2 become,

$$I_\ell = d_\ell t^2 w/4 \tag{D3}$$

$$I_s = t^3 w/12 \tag{D4}$$

$$I_s + I_\ell = \frac{wt^3}{12}\left[1 + 3\left[\frac{d_\ell}{t}\right]\right]$$

$$= I_s\left[1 + 3\left[\frac{d_\ell}{t}\right]\right] \tag{D5}$$

The overall Young's modulus for two layer (dynamic), $\bar{E}_{2DYN}$ is written as

$$\bar{E}_{2DYN} = \frac{(E_\ell I_\ell + E_s I_s)}{(I_\ell + I_s)} = \frac{3(d_\ell/t) I_s E_\ell + E_s I_s}{I_s\{1 + 3(d_\ell/t)\}} = \frac{3(d_\ell/t)E_\ell + E_s}{1 + 3(d_\ell/t)} \tag{D6}$$

$$E_s - \bar{E}_{2DYN} = \frac{3(d_\ell/t)(E_s - E_\ell)}{1 + 3(d_\ell/t)} \approx 3(d_\ell/t)(E_s - E_\ell) \tag{D7}$$

$$\bar{E}_{2ROM} = E_s v_s + E_\ell v_\ell = E_s\{1 - (d_\ell/t)\} + E_\ell(d_\ell/t) \tag{D8}$$

$$E_s - \bar{E}_{2ROM} = E_s - [E_s\{1 - (d_\ell/t)\} + E_\ell(d_\ell/t)] = (d_\ell/t)(E_s - E_\ell) \tag{D9}$$

$$\lim_{(d_\ell/t) \to 0} \left[\frac{E_s - \bar{E}_{2DYN}}{E_s - \bar{E}_{2ROM}}\right] = \lim_{(d_\ell/t) \to 0} \left[\frac{E_s - \bar{E}_{2DYN}}{E_s} \cdot \frac{E_s}{E_s - \bar{E}_{2ROM}}\right]$$

$$= \lim_{(d_\ell/t) \to 0} \left[\frac{3(d_\ell/t)(E_s - E_\ell)}{(d_\ell/t)(E_s - E_\ell)}\right] = 3 \tag{D10}$$

For three layer composite model, when $d_{\ell 1} \to 0$ and $d_{\ell 2} \to 0$ then the moments of inertia (equations 89 - 91 in the text) becomes upon dropping second and third order terms in $d_{\ell 1}$ and $d_{\ell 2}$,

$$I_{\ell 1} = (d_s - d)^2 d_{\ell 1} w \tag{D11}$$

$$I_s = (d_s^3/3 - d_s^2 d + d_s d^2) w \tag{D12}$$

$$I_{\ell 2} = d_{\ell 2}\, d^2\, w \tag{D13}$$

$d_s \approx t \approx 2d$ when $d_{\ell 1} \to 0$ and $d_{\ell 2} \to 0$. Thus equations D11 - D13 become,

$$I_{\ell 1} = t^2 d_{\ell 1}\, w/4 = 3\, I_s d_{\ell 1}/t \tag{D14}$$

$$I_s = t^3\, w/12 \tag{D15}$$

$$I_{\ell 2} = t^2 d_{\ell 2}\, w/4 = 3\, I_s d_{\ell 2}/t \tag{D16}$$

$$I_{\ell 1}+I_s+I_{\ell 2} = I_s\{3(d_{\ell 1}/t) + 1 + 3(d_{\ell 2}/t)\} \tag{D17}$$

$$\bar{E}_{3DYN} = \frac{E_{\ell 1}I_{\ell 1} + E_s I_s + E_{\ell 2}I_{\ell 2}}{I_{\ell 1} + I_s + I_{\ell 2}}$$

$$= \frac{3(d_{\ell 1}/t)E_{\ell 1} + E_s + 3(d_{\ell 2}/t)E_{\ell 2}}{3(d_{\ell 1}/t) + 1 + 3(d_{\ell 2}/t)} \tag{D18}$$

$$E_s - \bar{E}_{3DYN} = \frac{-3(d_{\ell 1}/t)E_{\ell 1} + 3(d_{\ell 1}/t)E_s + 3(d_{\ell 2}/t)E_s - 3(d_{\ell 2}/t)E_{\ell 2}}{3(d_{\ell 1}/t) + 1 + 3(d_{\ell 2}/t)}$$

$$\approx -3(d_{\ell 1}/t)E_{\ell 1} + 3(d_{\ell 1}/t)E_s + 3(d_{\ell 2}/t)E_s - 3(d_{\ell 2}/t)E_{\ell 2} \tag{D19}$$

$$\bar{E}_{3ROM} = E_{\ell 1}v_{\ell 1} + E_s v_s + E_{\ell 2}v_{\ell 2}$$

$$= (d_{\ell 1}/t)E_{\ell 1} + E_s\{1 - (d_{\ell 1}/t) - (d_{\ell 2}/t)\} + (d_{\ell 2}/t)E_{\ell 2} \tag{D20}$$

$$E_s - \bar{E}_{3ROM} = -(d_{\ell 1}/t)E_{\ell 1} + (d_{\ell 1}/t)E_s + (d_{\ell 2}/t)E_s - (d_{\ell 2}/t)E_{\ell 2} \tag{D21}$$

$$\lim_{(d_\ell/t) \to 0} \left(\frac{E_s - \bar{E}_{3DYN}}{E_s - \bar{E}_{3ROM}} \right) = \lim_{(d_\ell/t) \to 0} \left(\frac{E_s - \bar{E}_{3DYN}}{E_s} \cdot \frac{E_s}{E_s - \bar{E}_{3ROM}} \right)$$

$$= \lim_{(d_\ell/t) \to 0} \left(\frac{3\{-(d_{\ell 1}/t)E_{\ell 1} + (d_{\ell 1}/t)E_s + (d_{\ell 2}/t)E_s - (d_{\ell 2}/t)E_{\ell 2}\}}{-(d_{\ell 1}/t)E_{\ell 1} + (d_{\ell 1}/t)E_s + (d_{\ell 2}/t)E_s - (d_{\ell 2}/t)E_{\ell 2}} \right) = 3 \tag{D22}$$

The normalized overall Young's modulus change (dynamic beam vibration theory) is three times larger than the normalized overall Young's modulus change (Rule of mixtures) when layer thickness is very thin compared with substrate thickness ($d_{\ell 1} \to 0$ and $d_{\ell 2} \to 0$).

APPENDIX E. A Relation Between Expressions for 2-Dimensional Through Plate Slit Cracks in Plates and 3-Dimensional Slot Cracks in Surface Damaged Bars

For aligned slit cracks in three dimensions, the Young's modulus normal to slits, E, is [Table 23, e1]

$$E/E_0 = 1 - 2\pi(1-\nu_0^2)GN \qquad (E1)$$

For slit cracks of length 2a and depth ℓ, G becomes $\{4a^2\ell^2/2(a+\ell)\}$, which gives

$$E/E_0 = 1- 2\pi(1-\nu_0^2)\{a^2\ell^2/(a+\ell)\}N \qquad (E2)$$

For a plate of surface area A and thickness t, the volumetric crack number density, N, equals n/At where n is the number of cracks in the specimen, and At is the specimen volume. If we express t in terms of a constant multiple k of the crack depth ℓ, then $t = k\ell$ and equation E2 becomes

$$E/E_0 = 1- 2\pi(1-\nu_0^2)\{a^2\ell/(a+\ell)\}n/Ak \qquad (E3)$$

As the crack depth ℓ approaches the plate thickness (that is, $k \to 1$), the crack becomes a through slot type crack with length 2a and depth ℓ.

$$\lim_{k\to 1} \frac{E}{E_0} = 1 - 2\pi(1-\nu_0^2) \frac{a^2 \ell}{(a+\ell)} \cdot \frac{n}{A} \qquad \text{(E4)}$$

In general, if $\ell = ra$, then we can rewrite equation E4 as

$$E/E_0 = 1 - 2\pi(1-\nu_0^2)N_a \{r/(1+r)\}\{a^2\} \qquad \text{(E5)}$$

If $\ell >> a$ (the crack depth is large compared to the crack length), then r is large and equation E5 becomes

$$E/E_0 = 1 - 2\pi(1-\nu_0^2) \{a^2\} N_a \qquad \text{(E6)}$$

where N_a is the crack number density per unit surface area. If the field is sufficiently dilute that the factor $2\pi(1 - \nu_0^2)$ is small compared to one, then using the geometric series expansion and retaining only the terms of order $O(N_a)$, equation E6 can be rewritten as

$$E/E_0 \approx [1 + 2\pi N_a(1-\nu_0^2)\{a^2\}]^{-1} \qquad \text{(E7)}$$

which is identical to the expression obtained by Hasselman for dilute 2-dimensional aligned crack distributions.

When $a = \ell$ (that is, $r = 1$), then equation E5 becomes

$$E/E_0 = 1 - \pi(1-\nu_0^2)\{a^2\}N_a \qquad (E8)$$

Analogous to equation E6, equation E8 may be rewritten as

$$E/E_0 \approx [1 + \pi N_a(1-\nu_0^2)\{a^2\}]^{-1} \qquad (E9)$$

for the dilute crack case.

Appendix E References

e1. N. Laws and J. R. Brockenbrough, "The Effect of Micro-crack System on the Loss of Stiffness of Brittle Solids", Int. J. Solids. Structures, 23[9]: 1247-1268, 1987.

e2. D. P. H. Hasselman and J. P. Singh, "Analysis of Thermal Stress Resistance of Microcracked Brittle Ceramics", Am. Ceram. Soc. Bull., 58[9]: 856-860, 1979.

APPENDIX F. Two-Dimensional Models of Aligned, Through-Plate Cracks Aligned two-dimensional crack models

Two dimensional microcrack-modulus models typically treat an array of through-plate cracks oriented normal to the plane of the plate [f1-f3].

Based on Yokobori and Ichikawa's expression for the strain energy of coplanar rows of cracks (plane strain) [f1], Hasselman [f2] expressed for the effective Young's modulus of the plate normal to the plane as (figure F1)

$$E = E_0 \left[1 - \{16 N_a h^2 (1-\nu_0^2) \ln(\cos(\pi a/2h))\}/\pi\right]^{-1} \quad \text{(F1)}$$

where E_0, ν_0 = undamaged Young's modulus and Poisson's ratio respectively

N_a = number density of cracks per unit area

a = half-length of the crack

h = half of transverse intercrack spacing

For a very dilute crack number density (when $N \to 0$, $h \to \infty$), $\ln(\cos(\pi a/2h))$ may be approximated as [f4]

$$\ln\left[\cos\left[\frac{\pi a}{2h}\right]\right] = \frac{(\pi a/2h)^2}{2} - \frac{(\pi a/2h)^4}{12} - \frac{(\pi a/2h)^6}{45} - \frac{17(\pi a/2h)^8}{2520} - \cdots \quad \text{(F2)}$$

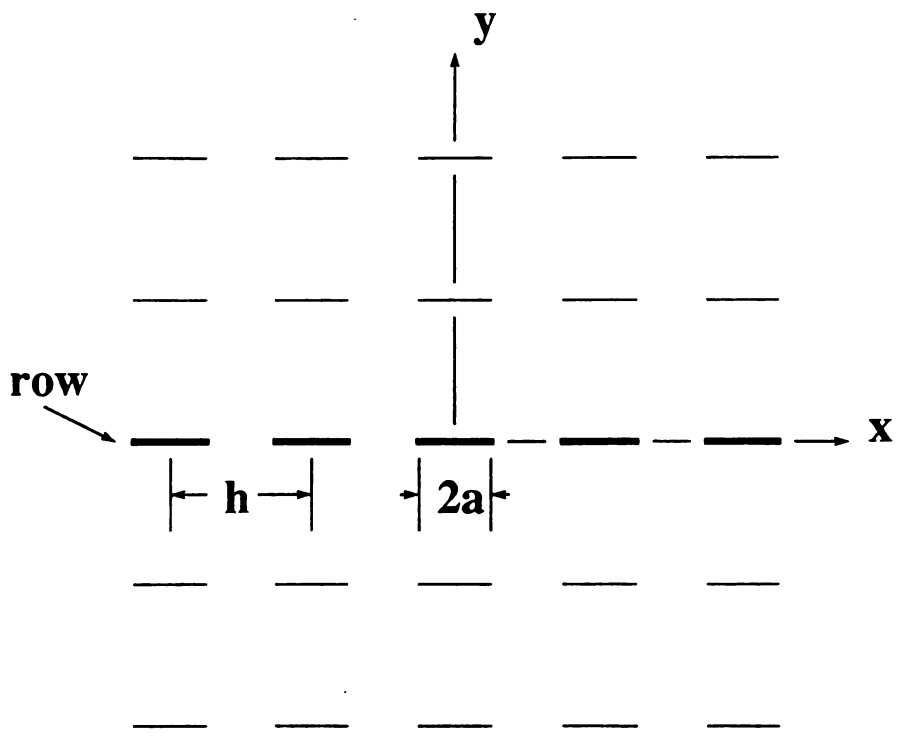

Figure F1. Schematic of plate with rectangular array of cracks, which considers interaction between rows of cracks.

In the dilute crack number density approximation where h>a, only the first term of equation B2 is retained, so that equation F1 becomes

$$E = E_0 \left[1 + 2\pi N_a (1-\nu_0^2) a^2\right]^{-1} \qquad \text{(F3)}$$

where all parameters are as defined in equation B1.

Delameter, Herrmann and Barnett [f3] derived the effective Young's modulus, E, for a sheet containing a rectangular array normal to the plane of cracks, (plane stress) (figure F2)

$$E = E_0 \left[1 + \left[\frac{2\pi a^2 B_1^I}{bd}\right]\right]^{-1} \qquad \text{(F4)}$$

where E_0 = undamaged Young's modulus

a = half-length of the crack

d = transverse intercrack spacing

$B_1^I = 2(d/\pi a)^2 \ln(\sec(\pi a/d))$.

When d>>a, B_1^I approaches unity. Also 1/bd is equivalent to the crack number density of cracks per unit area.

$$E = E_0 \left[1 + (2\pi a^2 N_a)\right]^{-1} \qquad \text{(F5)}$$

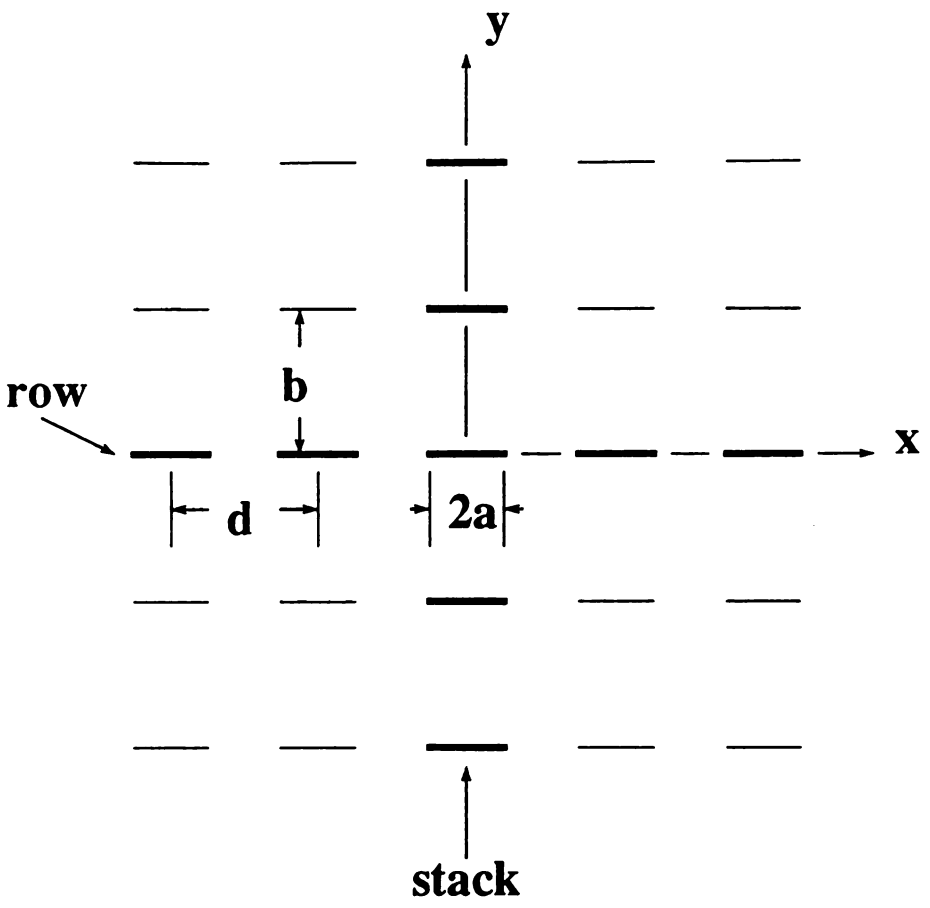

Figure F2. Flat plate with a doubly periodic rectangular array of cracks, which considers interactions of row and stack of cracks on effective elastic constants (after [f3]).

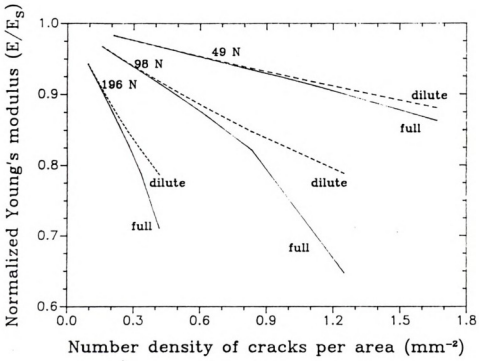

Figure F3. Normalized Young's modulus change as a function of surface number density of cracks for full (equation f4) and dilute (equation f1).

Appendix F References

f1. T. Yokobori and M. Ichikawa, "Elastic Solid with an Infinite Row of Collinear Cracks and the Fracture Criterion", J. Phy. Soc. Jpn., 19: 2341-2342, 1964.

f2. D. P. H. Hasselman and J. P. Singh, "Analysis of Thermal Stress Resistance of Microcracked Brittle Ceramics", Am. Ceram. Soc. Bull., 58[9]: 856-860, 1979.

f3. W. R. Delameter, G. Hermann and D. M. Barnett, "Weakening of an Elastic Solid by a Rectangular Array of Cracks", 43[3]: 74-80, J. Appl. Mech., Trans. ASME, 1975.

f4. I. S. Gradshteyn and I. M. Ryzhik, p 46, Table of Integrals, Series, and Products, Academic Press, 1980.

APPENDIX G Limiting value of $(E_s - E_{s_{DYN}})/E_s$ for $R_1 \to \infty$, $R_2 \to \infty$ $(d_s \to 0)$.

Form equation 88b in the text,

$$\frac{E_s - E_{s_{DYN}}}{E_s} = \frac{R_1\{R_1^2 + 3(R_2 + 1)^2\}\Lambda_1 + R_2\{R_2^2 + 3(R_1 + 1)^2\}\Lambda_2}{(R_1 + R_2 + 1)^3}$$

$$- \frac{(d_{\ell 1}/d_s)[(d_{\ell 1}/d_s)^2 + 3\{(d_{\ell 2}+d_s)/d_s\}^2]\Lambda_1 + (d_{\ell 2}/d_s)[(d_{\ell 2}/d_s)^2 + 3\{(d_{\ell 1}+d_s)/d_s\}^2]\Lambda_2}{(t/d_s)^3}$$

$$- \frac{d_{\ell 1}[d_{\ell 1}^2 + 3(d_{\ell 2} + d_s)^2]\Lambda_1 + d_{\ell 2}[d_{\ell 2}^2 + 3(d_{\ell 1}+d_s)^2]\Lambda_2}{t^3}$$

where $d_{\ell 1}$ = thickness of microcracked layer 1

$d_{\ell 2}$ = thickness of microcracked layer 2

d_s = thickness of undamaged layer

$t = d_{\ell 1} + d_s + d_{\ell 2}$, specimen thickness

$R_1 = d_{\ell 1}/d_s$, $R_2 = d_{\ell 2}/d_s$

$\Lambda_1 = f_1 G_{\ell 1} N_{\ell 1}$

$\Lambda_2 = f_2 G_{\ell 2} N_{\ell 2}$

For $R_1 \to \infty$, and $R_2 \to \infty$,

$$\lim_{d_s \to 0} \left(\frac{E_s - E_{3DYN}}{E_s} \right) = \frac{d_{\ell 1}(d_{\ell 1}^2 + 3d_{\ell 2}^2)\,\Lambda_1 + d_{\ell 2}(d_{\ell 2}^2 + 3d_{\ell 1}^2)\,\Lambda_2}{t^3}$$

$$= \left[\left(\frac{d_{\ell 1}}{t} \right)^3 + 3 \left(\frac{d_{\ell 2}^2\, d_{\ell 1}}{t^3} \right) \right] \Lambda_1 + \left[\left(\frac{d_{\ell 2}}{t} \right)^3 + 3 \left(\frac{d_{\ell 1}^2\, d_{\ell 2}}{t^3} \right) \right] \Lambda_2$$

$$= (v_1^3 + 3v_2^3 v_1)\,\Lambda_1 + (v_2^3 + 3v_1^3 v_2)\,\Lambda_2$$

where v_1 = volume fraction of microcracked layer 1

v_2 = volume fraction of microcracked layer 2

For $d_s \to 0$, $v_1 + v_2 = 1$ or $v_2 = 1 - v_1$, thus

$$\lim_{d_s \to 0} \left(\frac{E_s - E_{3DYN}}{E_s} \right) = (4v_1^3 - 6v_1^2 + 3v_1)\,\Lambda_1 + (-4v_1^3 + 6v_1^2 - 3v_1 + 1)\,\Lambda_2$$

$$= \lambda(\Lambda_1 - \Lambda_2) + \Lambda_2 \qquad \text{(figure G1)}$$

where $\lambda = 4v_1^3 - 6v_1^2 + 3v_1$

If $d_{\ell 1} = d_{\ell 2}$, then $v_1 = 0.5$. For $v_1 = 0.5$, $\lambda = 0.5$,

$$\lim_{d_s \to 0} \left(\frac{E_s - E_{3DYN}}{E_s} \right) = (\Lambda_1 + \Lambda_2)/2$$

For rule of mixtures

$$\frac{E_s - E_{3_{ROM}}}{E_s} = \frac{R_1 \Lambda_1}{R_1 + 1 + R_2} + \frac{R_2 \Lambda_2}{R_1 + 1 + R_2}$$

$$= v_1(\Lambda_1 - \Lambda_2) + \Lambda_2$$

$$\lim_{d_s \to 0} \left(\frac{E_s - E_{3_{DYN}}}{E_s - E_{3_{ROM}}} \right) = \frac{\lambda(\Lambda_1 - \Lambda_2) + \Lambda_2}{v_1(\Lambda_1 - \Lambda_2) + \Lambda_2}$$

If $\Lambda_1 = \Lambda_2$, then in general,

$$\lim_{d_s \to 0} \left(\frac{E_s - E_{3_{DYN}}}{E_s - E_{3_{ROM}}} \right) = 1$$

If $v_1 = 1$ or $v_2 = 1$, then again the ratio is 1.

If $v_1 = 0.5$ ($d_{\ell 1} = d_{\ell 2}$) then

$$\lim_{d_s \to 0} \left(\frac{E_s - E_{3_{ROM}}}{E_s} \right) = (\Lambda_1 + \Lambda_2)/2$$

Thus the ratio is 1 for $v_1 = v_2 = 0.5$.

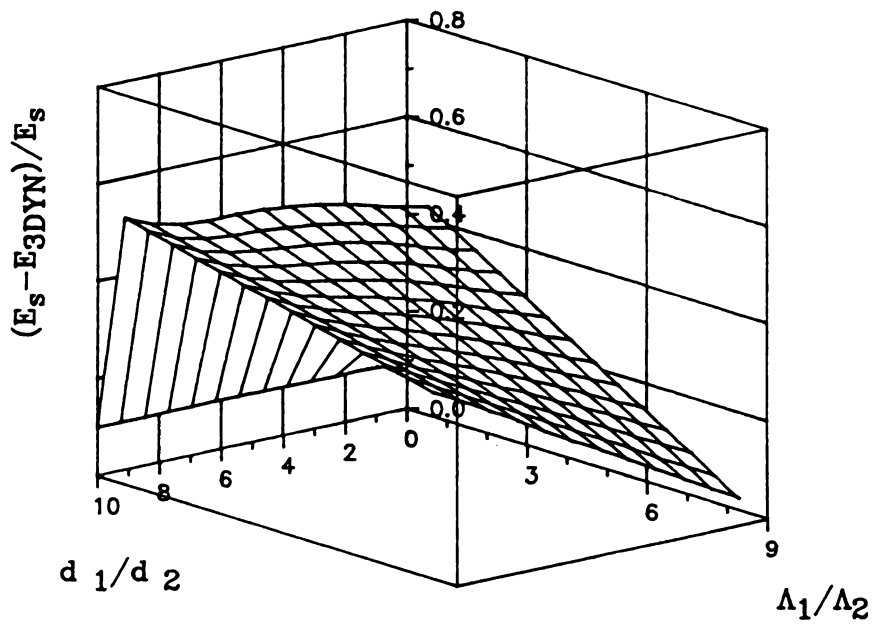

Figure G1. The relationship between $d_{\ell 1}/d_{\ell 2}$, Λ_1/Λ_2, and the limit of normalized Young's modulus change when both R1 and R2 goes to an infinity for three layer (when $d_{\ell 2}$ = 0.1 x bar thickness, Λ_2 = 0.1).

APPENDIX H: Porosity Dependence of Young's Modulus in Unindented (Polished) Alumina Specimens

The Young's moduli of unindented (polished) alumina specimens decrease as the porosity increases. In this study, the volume fraction porosity of the specimens ranged from about 0.060 to 0.075, based on a theoretical density of 3.98 g/cm^3 for alumina. In this appendix, we show that moduli measured for the undamaged alumina specimens are reasonable in terms of known modulus-porosity relations.

Two commonly used Young's modulus - porosity relations are [h1],

$$E = E_0 e^{-kP} \tag{H1}$$

$$E = E_0(1-mP) \tag{H2}$$

where, E = Young's modulus at porosity volume fraction, P

E_0 = Young's modulus at zero porosity volume fraction ($P = 0$)

P = volume fraction porosity

k, m = empirical constants

Phani [h2] and Phani and Niyogi [h3] suggested that the Young's modulus-porosity relationship may be expressed as

$$E = E_0(1-P)^n \tag{H3}$$

where n is an empirical constant.

Bounds for E_o, the theoretically dense value for the Young's modulus of polycrystalline alumina, can be estimated from single crystal modulus data. The Voigt (upper bound) and Reuss (lower bound) for polycrystalline alumina are 408.5 GPa and 398.3 GPa, respectively [h4]. In equations H1 - H3, E_o was taken as 403.4 GPa, which is the arithmetic mean of the Voigt and Reuss bounds. Values of k = 3.2, m = 2.9, and n = 3.1 were determined via a least-square fit of the modulus-porosity data to equations H1, H2, and H3, respectively. The correlation coefficients of 0.935, 0.934, and 0.934 were obtained for the least-squares fit to equations H1, H2, and H3, respectively.

References

h1. J. C. Wang, "Young's Modulus of Porous Materials, Part 2: Young's Modulus of Porous Material with Changing Pore Structure", J. Mat. Sci., 19[3]: 809-814, 1984.

h2. K. K. Phani, "Elastic Constant-Porosity Relations for Polycrystalline Thoria", J. Mat. Sci. Lett., 15[7]: 747-750, 1986.

h3. K. K. Phani and S. K. Niyogi, "Porosity Dependence of Ultrasonic Velocity and Elastic Modulus in Sintered Uranium Dioxide - A Discussion", J. Mat. Sci. Lett., 5[4]: 427-430, 1986.

h4. G. Simmons and H. Wang, Single Crystal Elastic Constants and Calculated Aggregate Properties: A Handbook, The M. I. T. press, Cambridge, MA, 1971.

Computer programs for elastic modulus, internal friction, surface heat transfer, and for surface stress calculations are listed in an Appendix of W. J. Lee's Ph.D. Dissertation, Michigan State University, 1991. The modulus program calculates the Young's modulus and the shear modulus of primatic-bar shaped specimens from the fundamental flexural resonance frequency and torsional frequency [102, 103]. Poisson's ratio was calculated from the Young's modulus and shear modulus assuming the materials to be macroscopically isotropic.

The internal friction program computes the measured internal friction which is in turn composed of the specimen internal friction and the apparatus internal friction.

The surface heat transfer coefficient program calculates the experimental surface heat transfer coefficient using the temperature dependent functional forms of specific heat and the measured specimen surface temperature.

The maximum surface tensile stress program calculates maximal tensile stress developed during quenching using the temperature depenent functions of Young's modulus, thermal expansion coefficient, quench temperature difference, Poisson's ratio and Biot modulus.

A commercial software, PlotIT (Scientific Programming Enterprises, Haslett, MI) was used to plot the graphs in this study and to analyze experimental data statistically, such as regression and correlation coefficients.

APPENDIX I. Normalized Young's modulus change calculation for eleven different crack geometry models based on dynamic beam vibration theory.

This program calculates the nomalized Young's modulus change as a function of crack number density and crack geometry models based on dynamic beam vibration theory composite layer model.

```
10 REM ** calculation of OVERALL MODULUS assuming 2-D limiting form of
     (Slit) cracks-Hasselmann, THREE LAYER COMPOSITE MODEL **
20 CLS:KEY OFF
25 PRI = 0 : LIG = 1  : LPRI = 1 : DPRI = 0
27 ROM$ = "RULE OF MIXTURES CALCULATION"
30 DIM EE(15), DIFF(15)
40 REM EE is the vector containing the experimental modulus data
42 FOR U = 1 TO 11
45 GOSUB 9500 : REM Initialize avemin vector
50 FOR HHH = 1 TO 1
60 READ SETS  : REM Sets is the number of data sets
70 FOR GG = 1 TO SETS
80    READ NDATA, MODEL,LD,LABEL$, HD : REM hd is the half-diagonal indent
            length at load
100   READ WID,LENGTH,THICKNESS,DL,DS,RADIUS,POISSON,ES
110   GOSUB 1500  : REM Dl, Ds modification
120   GOSUB 14000 : REM EVALUTATE ELLIPTIC INTEGRALS, ECCENTRICITY
160   IF MODEL = 2 THEN GOSUB 10000 : REM Two layer model
180   IF MODEL = 2 THEN GOTO 870
200   FOR KK = 1 TO NDATA
205      GOSUB 9000 : REM Initialize for sums, get constants
210      GOSUB 1000 : REM Calculation of layer modulus (TOP and BOTTOM)
280      GOSUB 4500 : REM Calculation of NORMALIZED YOUNG'S MODULUS CHANGE
320      GOSUB 4700 : REM Conversion of units for elastic modulus
360      GOSUB 4800 : REM Calculation of Experimental value of Normalized of
                        Normalized Young's modulus
500      IF PRI = 1 THEN GOSUB 5000 : REM PRINT RESULTS TO CRT
700   NEXT KK
800   IF PRI = 1 THEN GOSUB 8000 : REM Print summary results to CRT for data set
820 REM STOP
870 NEXT GG
900 RESTORE : REM Reset data pointer so that data can be reevaluated for
              different values of dl,ds
950 GOSUB 9700 : REM print out avemin vector to the crt
960 GOSUB 15500 : REM Print results to disk file
980 NEXT HHH
985 NEXT U
990 END
1000 REM **Calculation of layer modulus (TOP and BOTTOM) under 2-D Rectangular
       (slit) crack model **
1005 READ TIND,BIND,EE(KK)
1007 IF LIG = 1 THEN GOSUB 7000 : REM model as two cracks, omitted central "liga
ment where the
1008 REM                  indent impression appears
1010 REM WID = Width of the specimen in [m] **
1020 REM LENGTH = Length of the specimen in [m] **
1025 REM THICKNESS = thickness of the specimen in [m] **
1030 REM DL = Depth of the layer in [m] for the Vickers indentation**
1040 REM RADIUS =  Radius means Half of slit crack size in [m], which is half of
                   measured radial crack size, 2c **
1050 REM POISSON = undamaged Poisson's ratio of the specimen*
1060 NUMDTLAYER = TIND/(WID*LENGTH) :REM  **NUMDTLAYER stands for NUMBER density
     of top layer(mm-2), TIND represents number of indents on top surface
1065 NVTLAYER = TIND/(WID*LENGTH*DL) :REM
1070 NUMDBLAYER = BIND/(WID*LENGTH) :REM**NUMDBLAYER and BIND are NUMBER density
     of bottom layer(mm-2) and Number of indentations on the bottom
1075 NVBLAYER = BIND/(WID*LENGTH*DL) :REM
1080 NDSURFACE = NUMDTLAYER + NUMDBLAYER : REM **NDSURFACE represents total(T+B)
                                 number density of cracks (mm-2)**
1100 NDVOLUME = (TIND+BIND)/(WID*LENGTH*THICKNESS) : REM **NDVOLUME is
                            number density of cracks in whole specimen**
1120 REM ES = THE SUBTRRATE MODULUS IN [N/M2] **
1200 IF VOL = 0 THEN ET = FNLAY(NUMDTLAYER) : REM Not volume based model
1220 IF VOL = 0 THEN EB = FNLAY(NUMDBLAYER)
1230 REM IF KK < 3 THEN PRINT "NTL  = ";NUMDTLAYER;"  NBL = ";NUMDBLAYER :STOP
1240 IF VOL = 1 THEN ET = FNLAY(NVTLAYER)
```

```
1200 IF VOL = 0 THEN ET = FNLAY(NUMDTLAYER) : REM Not volume based model
1220 IF VOL = 0 THEN EB = FNLAY(NUMDBLAYER)
1240 IF VOL = 1 THEN ET = FNLAY(NVTLAYER)
1260 IF VOL = 1 THEN EB = FNLAY(NVBLAYER)
1400 RETURN
1500 REM Ds, Dl
1510 DL = DL - (DL/100)*(HHH - 1)
1520 IF MODEL = 2 THEN DS = THICKNESS - DL
1540 IF MODEL = 3 THEN DS = THICKNESS - (2!*DL)
1900 RETURN
1990 RETURN
2000 REM **calculation of the distance from the neutral axis to the bottom layer
2020 REM DS = Sustrate thickness in [m] **
2030 DISTANCE = (ET*DL*DL + 2*ET*DL*DS + ES*DS*DS - EB*DL*DL)/(2*ET*DL + 2*ES*DS
 + 2*EB*DL)
2100 RETURN
3000 REM **Calculation of the second moment of inertia of TOP, SUBSTRATE and
         BOTTOM layer**
3005 INET =((DS-DISTANCE)*(DS-DISTANCE)*DL + (DS-DISTANCE)*DL*DL + (DL^3)/3)*WID
3010 INS =((DS^3)/3 - (DS*DS*DISTANCE) + (DS*DISTANCE*DISTANCE))*WID
3020 INB =((DL^3)/3 + (DL*DL*DISTANCE) + (DL*DISTANCE*DISTANCE))*WID
3100 RETURN
4500 REM **calculation of NORMALIZED YOUNG'S MODULUS CHANGE **
4510 EOVERALL = (ET*INET+ES*INS+EB*INB)/(INET+INS+INB)
4530 NYMC = (ES-EOVERALL)/ES
4590 RETURN
4700 REM Conversion of units for elastic modulus
4710 CONV = 1000000000#
4720 NDVV = NDVOLUME/CONV  : REM ** 1000000000 [mm3] = 1 [m3] **
4740 NDSS = NDSURFACE /1000000!  : REM ** 1000000 [mm2] = 1 [m2] **
4760 ESS = ES/CONV : EBB = EB/CONV : EEOVER = EOVERALL/CONV  : REM ** 1000000000
                              [N/m2] = 1 [GPa] **
4780 IF MODEL = 3 THEN ETT = ET/CONV
4790 IF MODEL = 2 THEN ELAYER = EL/CONV
4795 RETURN
4800 REM  Calculation of Experimental value of Normalized Young's modulus
4830 ENYMC = (ESS - EE(KK))/ESS
4840 IF ENYMC < > 0! THEN DD = (ENYMC - NYMC)/ENYMC : REM For the initial,
                         damaged value, enymc is zero
4860 DIFF(KK) = (EEOVER - EE(KK))/EE(KK) : DIFF(KK) = DIFF(KK)*DIFF(KK)
4870 REM IF KK = NDATA THEN PRINT DIFF(KK) : STOP
4880 SUM = SUM + DIFF(KK)
4885 IF KK = NDATA THEN AVE(GG) = SQR(SUM/(NDATA - 1!))
4900 IF KK = NDATA THEN GOSUB 5400 : REM Bookeeping on min sums
4990 RETURN
5000 REM Print results to crt
5100 A$ = " ###.####  ###.####   ###.####  ###.####  #.#####  #.#####  ##.######"
5105 IF KK = 1 THEN PRINT " " : PRINT " "
5107 IF KK = 1 THEN PRINT LABEL$ : PRINT " "
5110 IF KK = 1 THEN PRINT" Et (GPa)  Eb (GPa)   Eov(GPa)  E exp      nymc     en
ymc      dd   "
5130 PRINT USING A$;ETT,EBB,EEOVER,EE(KK),NYMC,ENYMC,DD
5200 RETURN
5400 REM Bookeeping on min sums
5405 IF AVE(GG) > AVEMIN(GG,1) THEN RETURN
5420 AVEMIN(GG,1) = AVE(GG)
5440 AVEMIN(GG,2) = DL
5460 AVEMIN(GG,3) = LD
5480 AVEMIN(GG,4) = MODEL
5490 IF VOL = 0 THEN SLOPE = SLOPE*1000000!: REM 2D crack densities
5495 IF VOL = 1 THEN SLOPE = SLOPE*1E+09   : REM 3D crack densities
5500 AVEMIN(GG,5) = SLOPE
5520 AVEMIN(GG,6) = HD
5800 RETURN
7000 REM calculation, on two cracks, neglecting central ligament
7100 TIND = TIND*2! : BIND = BIND * 2! : LNIND = LNIND * 2!
```

```
7130 REM
7140 IF KK > 1 THEN RETURN
7150 RADIUS = (RADIUS - HD)/2! : REM hd = the half indent inpression (in meters
7200 RETURN
8000 REM Print summary results to CRT for data set
8010 TT = 0! :  REM TT is the thickness, computed from layer(s) + substrate
8020 PRINT " "
8030 PRINT "dl = ";DL;"   ds = ";DS;"
8040 IF MODEL = 2 THEN TT = DL + DS : PRINT "thick = ";TT;THICKNESS
8050 IF MODEL = 3 THEN TT = 2!*DL + DS : PRINT "thick = ";TT;THICKNESS
8070 PRINT "average sum = ";AVE(GG)
8190 RETURN
8200 REM 2D slit crack
8210 DEF FNLAY(X) = ES*(1 - (2! * PI* (1-POISSON^2) * X * RADIUS^2)) :VOL = 0
8212 SLOPE =  (2! * PI* (1-POISSON^2) * RADIUS^2)
8215 CR$ = "2D slit crack"
8220 RETURN
8250 REM DEF modified 2D slit cracks
8255 CR$ = "modified 2D slit cracks"
8260 DEF FNLAY(X) = ES*(1 - (2!*FACTOR * PI* (1-POISSON^2) * X * RADIUS^2))
8265 SLOPE = (2!*FACTOR * PI* (1-POISSON^2) * RADIUS^2)
8270 VOL = 0
8290 RETURN
8295 REM
8296 REM
8297 REM
8300 REM MODIFIED for 3D slit cracks
8305 CR$ = " 3D slit cracks, MODIFIED"
8310 FC1 = .5*(PI*PI)*(1! - POISSON*POISSON):REM Fac1 is the prefactor, aligned
                                              slit cracks
8320 FC2 = (2!/PI) : REM Fac2 is a multiplicative factor associated with epsilon
8330 PER = (2!*RADIUS + 2*DL) + (PI*HD): REM Per is the perimeter of
                          the slit crack, ignoring the free surface
8340 S1 =  (2!*RADIUS*DL) - (.5*PI*HD*HD):  REM s is the area of the slit crack
8350 SSQ = S1*S1 : REM Ssq is the square of the crack area (slit crack)
8360 REM With lig = 1 , factor of 2.8 gives reasonable fit DEF FNLAY(X) = ES*(1
- (2.8*X*FC1*FC2*SSQ)/PER): VOL = 1 : REM 3D modified slit
8370 DEF FNLAY(X) = ES*(1 - (X*FC1*FC2*SSQ)/PER): VOL = 1 : REM 3D modified slit
8380 SLOPE =  (FC1*FC2*SSQ)/PER: VOL = 1 : REM 3D modified slit
8390 RETURN
8396 REM
8397 REM
8400 REM Calculate for MODIFIED half ellipse cracks
8405 CR$ = "MODIFIED half ellipse cracks"
8407 REM Much better fit if lig = 0 rather than lig = 1
8410 FAC1 = (16!/3!)*(1! -POISSON*POISSON):  REM Fac1 is the prefactor, aligned
                                              elliptical cracks
8420 FAC2 = (2!/PI) : REM Fac2 is a multiplicative factor associated with
                           epsilon
8430 PERIM = (2!*RADIUS*ELL) + (PI*HD): REM Perim is the perimeter of        a
half-ellipse ignoring the free surface, but including indent ligament
8435 RP = 1!/PERIM
8440 REM PERIM = (2!*radius*ell) + 2!*(radius -(2!*hd) + PI*hd): REM Perim is th
perimeter of a half-ellipse ignoring the free surface, but including indent liga
ment
8450 A11  = ((PI/2!)*RADIUS*DL) - (.5*PI*HD*HD):  REM A11 is the area of a half-
ellipse, corrected for indent ligament
8460 ASQ = A11*A11 : REM Asq is the square of the crack area (half-ellipse)
8470 DEF FNLAY(X) = ES*(1! - X*FAC1*FAC2*ASQ*RP) : VOL = 1 : REM modified HALF-E
LLIPSE cracks
8480 SLOPE = FAC1*FAC2*ASQ*RP : REM modified HALF-ELLIPSE cracks
8490 RETURN
8496 REM
8497 REM
8500 REM HALF ELLIPSE CRACKS, UNMODIFIED
8505 CR$ = " HALF ELLIPSE CRACKS, UNMODIFIED "
```

```
8507 REM For lig = 0, -1.4 < dd < .5, for lig = 1 reasonable fit except for
         3-layer, 98 N load
8510 FAC1 = (16!/3!)*(1! - POISSON*POISSON):  REM Fac1 is the prefactor, aligned
                                                  elliptical cracks
8520 FAC2 = (2!/PI):REM Fac2 is a multiplicative factor associated with
                    epsilon
8530 PERIM = 2!*RADIUS*ELL : REM Perim is the perimeter of a half-ellipse
                                 ignoring the free surface
8540 REM PERIM = 2!*radius : REM Perim is the perimeter of a half-ellipse
                                 ignoring the free surface
8545 RP = 1!/PERIM
8550 AA =  (PI/2!)*RADIUS*DL :  REM AA is the area of a half-ellipse
8560 ASQ = AA*AA : REM Asq is the square of the crack area (half-ellipse)
8570 DEF FNLAY(X) =ES*(1 - (X*FAC1*FAC2*ASQ*RP)): VOL = 1:REM HALF-ELLIPSE crack
8580 SLOPE  =FAC1*FAC2*ASQ*RP :REM HALF-ELLIPSE crack
8590 RETURN
8596 REM
8597 REM
8600 REM  3D  SLIT CRACKS, UNMODIFIED
8605 CR$ = " 3D  SLIT CRACKS, UNMODIFIED "
8610 FC1 = .5*(PI*PI)*(1! - POISSON*POISSION): REM Fac1 is the prefactor, aligne
                                                  slit cracks
8620 FC2 = (2!/PI) : REM Fac2 is a multiplicative factor associated with
                     epsilon
8625 PER = 2*RADIUS + 2*DL : REM Per is the perimeter of the slit crack
8630 REM PER = 2!*(DL + 2!*RADIUS) : REM Per is the perimeter of the slit crack,
                                       inclduing the free surface
8635 RP = 1!/PER
8640 SS =  2!*RADIUS*DL :  REM s is the area of the slit crack
8650 SSQ = SS*SS : REM SSQ is the square of the crack area (slit crack)
8660 DEF FNLAY(X) = ES*(1! - (X*FC1*FC2*SSQ*RP)) : VOL = 1 : REM 3D SLIT CRACKS
8680 SLOPE = FC1*FC2*SSQ*RP : REM 3D SLIT CRACKS
8690 RETURN
8696 REM
8697 REM
8700 REM SHETTY CRACKS
8705 CR$ = " SHETTY CRACKS "
8707 REM For lig = 1, fitting is very poor (one - two orders of magnitude errors
         in terms of nymc
8710 FAC1 = (16!/3!)*(1! - POISSON*POISSON):  REM Fac1 is the prefactor, aligne
              elliptical cracks
8720 FAC2 = (2!/PI) : REM Fac2 is a multiplicative factor associated with
                      epsilon
8730 PERIM= (RADIUS *ELL) + DL - HD : REM Perim is the perimeter of half-ellipse
 ignoring the free surface, but including indent ligament
8735 RP = 1!/PERIM
8740 AREA = ((PI/4!)*RADIUS*DL - (HD*DL)): REM AREA area of a half-ellipse, corr
ected for indent ligament
8750 ASQ = AREA*AREA : REM Asq is the square of the crack area (half-ellipse)
8760 DEF FNLAY(X) = ES*(1! - (X*FAC1*FAC2*ASQ*RP)) : VOL = 1 :REM sketty cracks
8780 SLOPE = FAC1*FAC2*ASQ*RP :REM sketty cracks
8790 RETURN
8796 REM
8797 REM
8800 REM modified 3D cracks, edition II
8810 CR$ = "modified 3D cracks, edition II "
8820 FC1 = .5*(PI*PI)*(1! - POISSON*POISSON) :  REM Fac1 is the prefactor, align
ed                                                slit cracks
8830 FC2 = (2!/PI) : REM Fac2 is a multiplicative factor associated with
                     epsilon
8835 PER = (2!*RADIUS + 2!*DL + PI*HD)
8840 RP = 1!/PER
8850 SA =  (2!*RADIUS*DL) - (.5*PI*HD*HD) :  REM s is the area
                          of the slit crack
8860 SSQ = SA*SA : REM Ssq is the square of the crack area (slit crack)
8865 GOSUB 14000 : REM Elliptic integral subroutine
```

```
8870 DEF FNLAY(X) = ES*(1! - (X*VV*FC1*FC2*SSQ*RP)) : VOL = 1 : REM  SLIT cracks
8880 SLOPE = VV*FC1*FC2*SSQ*RP : REM Slope is the slope of the            delta
E/Eo versus N data for SLIT cracks
8890 RETURN
8896 REM
8897 REM
8996 REM
8997 REM
9000 REM Initialize for sums, get constants
9050 SUM = 0! : REM Sum is the sum of the residuals (difference between
                    and modeled values are the residuals).
9060 DD = 0! : TT = 0! :  REM Initialize dd value
9120 REM Crack functions
9240 IF U = 1 THEN  GOSUB 8200 : REM 2D slit crack
9260 IF U = 2 THEN  GOSUB 8250 : REM modified 2D slit cracks
9280 IF U = 3 THEN  GOSUB 8300 : REM 3D SLIT CRACK, MODIFIED
9300 IF U = 4 THEN  GOSUB 8400 : REM 3D MODIFIED half ellipse cracks
9320 IF U = 5 THEN  GOSUB 8500 : REM 3D HALF ELLIPSE CRACKS, UNMODIFIED
9330 IF U = 6 THEN  GOSUB 8600 : REM 3D SLIT CRACKS, UNMODIFIED
9340 IF U = 7 THEN  GOSUB 8700 : REM SHETTY cracks
9360 IF U = 8 THEN  GOSUB 8800 : REM modified 3D cracks, edition II
9365 REM Elliptical shaped indent cross-section
9370 IF U = 9 THEN  GOSUB 13500 : REM modified 3D slit, ellip hd
9380 IF U =10 THEN  GOSUB 13630 :  REM modified 3D half-ellipse, ellip hd
9390 IF U =11 THEN  GOSUB 13770 : REM modified 3D cracks, edition II
9400 RETURN
9490 RETURN
9500 REM Initialize avemin vector
9520 FOR WQ = 1 TO 6
9600   AVEMIN(WQ,1) = 99999.9 : AVEMIN(WQ,2) = 0!
9610 NEXT WQ
9690 RETURN
9700 REM
9705 IF LIG = 1 THEN L$ = "  with ligament (radius and ndensity revised)
9707 IF LIG = 0 THEN L$ = "  without ligament correction "
9720 AV$ =" ####     ##     ##.####^^^^        ##.###^^^^    ##.###^^^^
^^"
9730 PRINT " " : PRINT " "
9732 IF LPRI = 1 THEN LPRINT " " : LPRINT " "
9735 PRINT CR$;L$
9736 PRINT ROM$
9737 IF LPRI = 1 THEN LPRINT CR$;L$
9738 IF LPRI = 1 THEN LPRINT ROM$
9740 PRINT"Load(N)  Layers   Min Ave Sum        Dl           Slope    hd "
9742 IF LPRI = 1 THEN LPRINT"Load(N)  Layers   Min Ave Sum        Dl           S
lope    hd "
9760 IF LPRI = 1 THEN LPRINT " "
9820 FOR A = 1 TO SETS
9840   PRINT USING AV$;AVEMIN(A,3);AVEMIN(A,4);AVEMIN(A,1);AVEMIN(A,2),AVEMIN(A,
5),AVEMIN(A,6)
9842  IF LPRI = 1 THEN LPRINT USING AV$;AVEMIN(A,3);AVEMIN(A,4);AVEMIN(A,1);AVEM
IN(A,2),AVEMIN(A,5), AVEMIN(A,6)
9860 NEXT A
9990 RETURN
10000 REM Two layer model
10040 GOSUB 14000 : REM Compute elliptic integrals
10060 FOR KK = 1 TO NDATA
10070     GOSUB 9000 : REM Initialize for sums, get constants
10080     GOSUB 11000 : REM Calculation of layer modulus
10100     GOSUB 12000 : REM CALCULATION OF THE DISTANCE BETWEEN THE NEUTRAL AXIS
                            AND THE THE INTERFACE BETWEEN THE LAYER AND SUBSTRATE
10120     GOSUB 12200 : REM CALCULATION OF THE SECOND MOMENT OF INERTIA OF
                            SUBSTRATE AND LAYER
10140     GOSUB 12400 : REM calculation of NORMALIZED YOUNG'S MODULUS CHANGE
10180     GOSUB 4700  : REM Conversion of units for elastic modulus
10220     GOSUB 4800  : REM Calculation of Experimental value of Normalized of
```

```
                                Normalized Young's modulus
10260     IF PRI = 1 THEN GOSUB 12440 : REM PRINT RESULTS TO CRT
10300 NEXT KK
10390 IF PRI = 1 THEN GOSUB 8000 : REM Print summary results to CRT for data set
10400 REM STOP
10500 RETURN
11000 REM **Calculation of layer modulus under 2-D Rectangular(slit) crack model
11005 READ LNIND, EE(KK)
11007 IF LIG = 1 THEN GOSUB 7000 : REM model as two cracks, omitted central "lig
ament where the
11008 REM                  indent impression appears
11010 REM WID = Width of the specimen in [m] **
11020 REM LENGTH =  Length of the specimen in [m] **
11025 REM THICKNESS = thickness of the specimen in [m] **
11030 REM DL =  Depth of the layer in [m] for indentation**
11040 REM RADIUS is Half of slit crack size in[m], which is half of measured
                 radial crack size, 2c **
11050 REM POISSON = undamaged Poisson's ratio of the specimen*
11060 NUMDLAYER = LNIND/(WID*LENGTH) :REM  **NUMDLAYER stands for NUMBER
                                        density of layer(mm-2) **
11100 NDVOLUME = (LNIND)/(WID*LENGTH*THICKNESS) : REM **NDVOLUME is
                                        number density of cracks in whole specimen
11105 NVLAYER = (LNIND)/(WID*LENGTH*DL): REM
11120 REM ES  is substrate modulus in [N/m2] **
11160 IF VOL = 0 THEN EL = FNLAY(NUMDLAYER)
11170 IF VOL = 1 THEN EL = FNLAY(NVLAYER)
11200 RETURN
12000 REM calculation of the distance from the neutral axis to the bottom layer
12020 REM DS = Sustrate thickness in [m] **
12030 DISTANCE = (ES*DS*DS - EL*DL*DL)/(2*ES*DS + 2*EL*DL)
12100 RETURN
12200 REM Calculation of the second moment of inertia of SUBSTRATE and LAYER
12210 INS =((DS^3)/3 - (DS*DS*DISTANCE) + (DS*DISTANCE*DISTANCE))*WID
12220 INL =((DL^3)/3 + (DL*DL*DISTANCE) + (DL*DISTANCE*DISTANCE))*WID
12300 RETURN
12400 REM **calculation of NORMALIZED YOUNG'S MODULUS CHANGE **
12410 EOVERALL = (ES*INS+EL*INL)/(INS+INL)
12420 NYMC = (ES-EOVERALL)/ES
12430 RETURN
12440 REM Print results to crt
12490 A$ = "  ###.####     ###.####      ###.####   #.#####   #.#####    ##.####
= "
12500 IF KK = 1 THEN PRINT " " : PRINT " "
12505 IF KK = 1 THEN PRINT LABEL$ : PRINT " "
12510 IF KK = 1 THEN PRINT" El (GPa)   Eoverall(GPa)      Eexp      nymc      en
ymc          dd"
12520 PRINT USING A$;ELAYER,EEOVER,EE(KK),NYMC,ENYMC,DD
12700 RETURN
13500 REM MODIFIED for 3D slit cracks, elliptical indent bottom
13510 CR$ = " 3D slit cracks, MODIFIED, elliptical indent bottom"
13520 FC1 = .5*(PI*PI)*(1! - POISSON*POISSON):REM Fac1 is the prefactor, aligned
                                                slit cracks
13530 FC2 = (2!/PI) : REM Fac2 is a multiplicative factor associated with epsilo
n
13540 PER = (2!*RADIUS) + (2*DL) + (2*ELL*HD): REM Per is the perimeter of
                                the slit crack, ignoring the free surface
13550 S1 =  (2!*RADIUS*DL) - (.5*PI*HD*HD*KPRIME):  REM s is the area of the sli
t crack
13560 SSQ = S1*S1 : REM Ssq is the square of the crack area (slit crack)
13570 REM With lig = 1 , factor of 2.8 gives reasonable fit DEF FNLAY(X) = ES*(1
 - (2.8*X*FC1*FC2*SSQ)/PER): VOL = 1 : REM 3D modified slit
13580 DEF FNLAY(X) = ES*(1 - (X*FC1*FC2*SSQ)/PER): VOL = 1 : REM 3D modified sli
t
13590 SLOPE =  (FC1*FC2*SSQ)/PER: VOL = 1 : REM 3D modified slit
13600 RETURN
13610 REM
```

```
13620 REM
13630 REM Calculate for MODIFIED half ellipse cracks, elliptical indent bottom
13640 CR$ = "MODIFIED half ellipse cracks, elliptical indent bottom"
13650 REM Much better fit if lig = 0 rather than lig = 1
13660 FAC1 = (16!/3!)*(1! -POISSON*POISSON):  REM Fac1 is the prefactor, aligned
                                                 elliptical cracks
13670 FAC2 = (2!/PI) : REM Fac2 is a multiplicative factor associated with
                          epsilon
13680 PERIM = (2!*RADIUS*ELL) + (2*ELL*HD): REM Perim is the perimeter of
  a half-ellipse ignoring the free surface, but including indent ligament
13690 RP = 1!/PERIM
13700 A11  = ((PI/2!)*RADIUS*DL) - (.5*PI*HD*HD*KPRIME):  REM A11 is the area of
 a half-ellipse, corrected for indent ligament
13710 ASQ = A11*A11 : REM Asq is the square of the crack area (half-ellipse)
13720 DEF FNLAY(X) = ES*(1! - X*FAC1*FAC2*ASQ*RP) : VOL = 1 : REM modified HALF-
ELLIPSE cracks
13730 SLOPE = FAC1*FAC2*ASQ*RP : REM modified HALF-ELLIPSE cracks
13740 RETURN
13750 REM
13760 REM
13770 REM modified 3D cracks, edition II, elliptical indent bottom
13775 CR$ = "modified 3D cracks, edition II, elliptical indent bottom"
13780 FC1 = .5*(PI*PI)*(1! - POISSON*POISSON) :  REM Fac1 is the prefactor, alig
ned                                              slit cracks
13790 FC2 = (2!/PI) : REM Fac2 is a multiplicative factor associated with
                        epsilon
13800 PER = (2!*RADIUS + 2!*DL + 2*ELL*HD)
13810 RP = 1!/PER
13820 SA =  (2!*RADIUS*DL) - (.5*PI*HD*HD*KPRIME) :  REM s is the area
                               of the slit crack
13830 SSQ = SA*SA : REM Ssq is the square of the crack area (slit crack)
13840 GOSUB 14000 : REM Elliptic integral subroutine
13850 DEF FNLAY(X) = ES*(1! - (X*VV*FC1*FC2*SSQ*RP)) : VOL = 1 : REM  SLIT crack
s
13860 SLOPE = VV*FC1*FC2*SSQ*RP : REM Slope is the slope of the            delta
 E/Eo versus N data for SLIT cracks
13870 RETURN
13880 REM
13890 REM
14000  REM EVALUTATE ELLIPTIC INTEGRALS, ECCENTRICITY
14010 PI = 3.141592 : M = 0
14040 IF DL > RADIUS THEN RETURN
14060 F1 = (RADIUS*RADIUS - DL*DL)
14070 ECCEN = (SQR(F1))/RADIUS
14080 REM Power series approximation to elliptic integral of second kind in
        terms of the modulus m.  (See Dwight, Table of Integrals for series).
14090 KPRIME = SQR(1! - ECCEN*ECCEN)
14100 M = (1! - KPRIME)/(1! + KPRIME)
14110 T1 = PI/(2!*(1! + M))
14120 T3 = (M*M)/4
14130 T4 = M^4/(2*2*4*4)
14140 T5 = (9*(M^6))/(2*2*4*4*6*6)
14150 T6 = (3*3*5*5)*(M^8)/(2*2*4*4*6*6*8*8)
14160 ELL = T1*(1! + T3 + T4 + T5 + T6)
14180 FCC = SQR(1! - ECCEN*ECCEN)
14200 FACTOR = (2!/3!)*(FCC/ELL) : REM PRINT "factor = ";FACTOR
14207 VV =(16/(PI*PI)* FCC*ELL)
14210 REM FACTOR = 1!/(FCC*ELL) : REM PRINT "factor = ";FACTOR
14220 REM PRINT "dl = ";DL;"   radius = ";RADIUS:STOP
14300 RETURN
15500 REM PRINT RESULTS TO DISK FILE
15505 IF DPRI = 0 THEN RETURN
15510 FF$ = "crack.RES"
15520 OPEN FF$ FOR APPEND AS 2
15525 PRINT #2, CR$;L$
15530 FOR A = 1 TO SETS
```

```
15570   PRINT #2, USING AV$;AVEMIN(A,3);AVEMIN(A,4);AVEMIN(A,1);AVEMIN(A,2),AVEM
IN(A,5),AVEMIN(A,6)
15590 NEXT A
15600 PRINT #2, " "
15650 CLOSE
15660 RETURN
20000 DATA 6 : REM Sets, which is the number of data sets
21000 DATA 7,3,49, " 49 N loading indented both sides", 4.181e-5
21010 DATA 0.00612,0.0687,0.00101,0.000110,0.00081,1.138e-4,.219,3.223355e11
21020 DATA         0,        0 , 322.3355
21040 DATA        45,        0 , 322.2478
21060 DATA        45,       45 , 322.1164
21080 DATA        90,       45 , 322.0319
21100 DATA        90,       90 , 321.8348
21120 DATA       135,       90 , 321.5595
21140 DATA       135,      135 , 321.3719
23000 DATA 8,3,98, "98 N loading  indented on two sides", 5.944e-5
23010 DATA 0.012,0.0707,0.001,0.000144,0.000712,1.8505e-4,.206,3.348828e11
23020 DATA         0,        0 , 334.8828
23040 DATA        46,        0 , 334.6449
23060 DATA        46,       46 , 334.4863
23080 DATA       138,       46 , 334.2002
23100 DATA       138,      138 , 333.5011
23120 DATA       230,      138 , 333.1398
23140 DATA       230,      230 , 332.9058
23160 DATA       322,      230 , 332.3318
24000 DATA 3,3,196, " 196 loading indented on both sides",  8.39e-5
24010 DATA 0.012,0.0685,0.001000,0.000239,0.000522,3.224e-4,.208,3.339898e11
24020 DATA  0 ,  0 , 333.9898
24040 DATA  22 , 0 , 333.5575
24060 DATA  22 , 44 , 331.9211
27000 DATA 8,2,49, " 49 N loading indented on single side", 4.181e-5
27010 DATA 0.012,0.0693,0.001,0.000110,0.00081,1.138e-4,.207,3.341635e11
27020 DATA  0 ,  334.1635
27040 DATA  40 , 334.0537
27060 DATA  80 , 333.9270
27080 DATA 120 , 333.8173
27100 DATA 160 , 333.7864
27120 DATA 200 , 333.7188
27140 DATA 240 , 333.6119
27160 DATA 280 , 333.5192
30000 DATA 5, 2,98, "  98 loading  indented on one side", 5.944e-5
30100 DATA 0.012,0.06943,0.001014,0.000144,0.000870,1.8505e-4,.206,3.273381e11
30110 DATA         0 , 327.3381
30120 DATA        68 , 327.0228
30130 DATA       102 , 326.9290
30140 DATA       170 , 326.5768
30150 DATA       238 , 326.2183
33000 DATA 13,2,196, " 196 loading indented on one side",  8.39e-5
33010 DATA 0.012,0.0697,0.001005,0.000239,0.000766,3.224e-4,.215,3.328715e11
33020 DATA  0 ,  332.8715
33040 DATA  7  , 332.5756
33060 DATA  14 , 332.4626
33080 DATA  21 , 332.2899
33100 DATA  36 , 331.8183
33120 DATA  44 , 331.6822
33140 DATA  52 , 331.4366
33160 DATA  59 , 331.2575
33180 DATA  66 , 331.1215
33220 DATA  87 , 330.5878
33240 DATA  108, 330.0017
33260 DATA  129, 329.4656
33280 DATA  150, 328.7873
```

APPENDIX J. Normalized Young's modulus change calculation for eleven different crack geometry models based on rule of mixtures.

This program calculates the nomalized Young's modulus change as a function of crack number density and crack geometry models based on rule of mixtures composite layer model.

```
10 REM ** calculation of OVERALL MODULUS assuming 2-D limiting form of
      (Slit) cracks-Hasselmann, THREE LAYER COMPOSITE MODEL **
20 CLS:KEY OFF
25 PRI = 0 : LIG = 1 : LPRI = 1 : DPRI = 0
30 DIM EE(15), DIFF(15)
40 REM EE is the vector containing the experimental modulus data
42 FOR U = 1 TO 8 :  REM FOR U = 9 TO 11
45 GOSUB 9500 : REM Initialize avemin vector
50 FOR HHH = 1 TO 1
60 READ SETS  : REM Sets is the number of data sets
70 FOR GG = 1 TO SETS
80    READ NDATA, MODEL,LD,LABEL$, HD : REM hd is the half-diagonal indent
                length at load
100   READ WID,LENGTH,THICKNESS,DL,DS,RADIUS,POISSON,ES
110   GOSUB 1500  : REM Dl, Ds modification
120   GOSUB 14000 : REM EVALUTATE ELLIPTIC INTEGRALS, ECCENTRICITY
160   IF MODEL = 2 THEN GOSUB 10000 : REM Two layer model
180   IF MODEL = 2 THEN GOTO 870
200   FOR KK = 1 TO NDATA
205      GOSUB 9000 : REM Initialize for sums, get constants
210      GOSUB 1000 : REM Calculation of layer modulus (TOP and BOTTOM)
220      GOSUB 2000 : REM CALCULATION OF THE DISTANCE BETWEEN THE NEUTRAL AXIS
                      AND THE THE INTERFACE BETWEEN THE bottom LAYER AND
                      SUBSTRATE
240      GOSUB 3000 : REM CALCULATION OF THE SECOND MOMENT OF INERTIA OF TOP,
                      SUBSTRATE AND BOTTOM LAYER
280      GOSUB 4500 : REM Calculation of NORMALIZED YOUNG'S MODULUS CHANGE
320      GOSUB 4700 : REM Conversion of units for elastic modulus
360      GOSUB 4800 : REM Calculation of Experimental value of Normalized of
                         Normalized Young's modulus
500      IF PRI = 1 THEN GOSUB 5000 : REM PRINT RESULTS TO CRT
700   NEXT KK
800   IF PRI = 1 THEN GOSUB 8000 : REM Print summary results to CRT for data set
820 REM STOP
870 NEXT GG
900 RESTORE : REM Reset data pointer so that data can be reevaluated for
              different values of dl,ds
940 NEXT HHH
950 GOSUB 9700 : REM print out avemin vector to the crt
960 GOSUB 15500 : REM Print results to disk file
980 NEXT U
990 END
1000 REM **Calculation of layer modulus (TOP and BOTTOM) under 2-D Rectangular
        (slit) crack model **
1005 READ TIND,BIND,EE(KK)
1007 IF LIG = 1 THEN GOSUB 7000 : REM model as two cracks, omitted central "liga
ment where the
1008 REM                  indent impression appears
1010 REM WID = Width of the specimen in [m] **
1020 REM LENGTH = Length of the specimen in [m] **
1025 REM THICKNESS = thickness of the specimen in [m] **
1030 REM DL = Depth of the layer in [m] for the Vickers indentation**
1040 REM RADIUS =  Radius means Half of slit crack size in [m], which is half of
                   measured radial crack size, 2c **
1050 REM POISSON = undamaged Poisson's ratio of the specimen*
1060 NUMDTLAYER = TIND/(WID*LENGTH) :REM  **NUMDTLAYER stands for NUMBER density
     of top layer(mm-2), TIND represents number of indents on top surface
1065 NVTLAYER = TIND/(WID*LENGTH*DL) :REM
1070 NUMDBLAYER = BIND/(WID*LENGTH) :REM**NUMDBLAYER and BIND are NUMBER density
     of bottom layer(mm-2) and Number of indentations on the bottom
1075 NVBLAYER = BIND/(WID*LENGTH*DL) :REM
1080 NDSURFACE = NUMDTLAYER + NUMDBLAYER : REM **NDSURFACE represents total(T+B)
                                 number density of cracks (mm-2)**
1100 NDVOLUME = (TIND+BIND)/(WID*LENGTH*THICKNESS) : REM **NDVOLUME is
                        number density of cracks in whole specimen**
1120 REM ES = THE SUBTRRATE MODULUS IN [N/M2] **
```

```
1260 IF VOL = 1 THEN EB = FNLAY(NVBLAYER)
1400 RETURN
1500 REM Ds, Dl
1510 REM DL = DL - (DL/100)*(HHH - 1)
1520 IF MODEL = 2 THEN DS = THICKNESS - DL
1540 IF MODEL = 3 THEN DS = THICKNESS - (2!*DL)
1610 REM hD = HD - (HD/100)*(HHH - 1)
1990 RETURN
2000 REM **calculation of the distance from the neutral axis to the bottom layer
2020 REM DS = Sustrate thickness in [m] **
2030 DISTANCE = (ET*DL*DL + 2*ET*DL*DS + ES*DS*DS - EB*DL*DL)/(2*ET*DL + 2*ES*DS
 + 2*EB*DL)
2100 RETURN
3000 REM **Calculation of the second moment of inertia of TOP, SUBSTRATE and
          BOTTOM layer**
3005 INET =((DS-DISTANCE)*(DS-DISTANCE)*DL + (DS-DISTANCE)*DL*DL + (DL^3)/3)*WID
3010 INS =((DS^3)/3 - (DS*DS*DISTANCE) + (DS*DISTANCE*DISTANCE))*WID
3020 INB =((DL^3)/3 + (DL*DL*DISTANCE) + (DL*DISTANCE*DISTANCE))*WID
3100 RETURN
4500 REM **calculation of NORMALIZED YOUNG'S MODULUS CHANGE **
4600 RA1 = DL/THICKNESS : RA2 = DS/THICKNESS
4620 IF MODEL = 3 THEN EOVERALL = (ET*RA1) + (EB*RA1) + (ES*RA2)
4625 TOTAL = 2!*RA1 + RA2 : SUB = TOTAL - THICKNESS
4630 NYMC = (ES-EOVERALL)/ES
4640 REM PRINT "ES = ";ES;"  ET = ";ET;"  EB = ";EB : STOP
4656 REM PRINT "SUB = ";SUB : STOP
4690 RETURN
4700 REM Conversion of units for elastic modulus
4710 CONV = 1000000000#
4720 NDVV = NDVOLUME/CONV  : REM ** 1000000000 [mm3] = 1 [m3] **
4740 NDSS = NDSURFACE /1000000!  : REM ** 1000000 [mm2] = 1 [m2] **
4760 ESS = ES/CONV : EBB = EB/CONV : EEOVER = EOVERALL/CONV  : REM ** 1000000000
                              [N/m2] = 1 [GPa] **
4780 IF MODEL = 3 THEN ETT = ET/CONV
4790 IF MODEL = 2 THEN ELAYER = EL/CONV
4795 RETURN
4800 REM  Calculation of Experimental value of Normalized Young's modulus
4830 ENYMC = (ESS - EE(KK))/ESS
4840 IF ENYMC < > 0! THEN DD = (ENYMC - NYMC)/ENYMC : REM For the initial,
                        damaged value, enymc is zero
4860 DIFF(KK) = (EEOVER - EE(KK))/EE(KK) : DIFF(KK) = DIFF(KK)*DIFF(KK)
4870 REM IF KK = NDATA THEN PRINT DIFF(KK) : STOP
4880 SUM = SUM + DIFF(KK)
4885 IF KK = NDATA THEN AVE(GG) = SQR(SUM/(NDATA - 1!))
4900 IF KK = NDATA THEN GOSUB 5400 : REM Bookeeping on min sums
4990 RETURN
5000 REM Print results to crt
5100 A$ = " ###.####  ###.####   ###.####  ###.####  #.#####  #.#####  ##.#####"
5105 IF KK = 1 THEN PRINT " " : PRINT " "
5107 IF KK = 1 THEN PRINT LABEL$ : PRINT " "
5110 IF KK = 1 THEN PRINT" Et (GPa)  Eb (GPa)   Eov(GPa)  E exp      nymc     en
ymc      dd   "
5130 PRINT USING A$;ETT,EBB,EEOVER,EE(KK),NYMC,ENYMC,DD
5200 RETURN
5400 REM Bookeeping on min sums
5405 IF AVE(GG) > AVEMIN(GG,1) THEN RETURN
5420 AVEMIN(GG,1) = AVE(GG)
5440 AVEMIN(GG,2) = DL
5460 AVEMIN(GG,3) = LD
5480 AVEMIN(GG,4) = MODEL
5490 IF VOL = 0 THEN SLOPE = SLOPE*1000000!: REM 2D crack densities
5495 IF VOL = 1 THEN SLOPE = SLOPE*1E+09   : REM 3D crack densities
5500 AVEMIN(GG,5) = SLOPE
5520 AVEMIN(GG,6) = HD
5800 RETURN
7000 REM calculation, on two cracks, neglecting central ligament
```

```
7100 TIND = TIND*2! : BIND = BIND * 2! : LNIND = LNIND * 2!
7130 REM
7140 IF KK > 1 THEN RETURN
7150 RADIUS = (RADIUS - HD)/2! : REM hd = the half indent inpression (in meters
7200 RETURN
8000 REM Print summary results to CRT for data set
8010 TT = 0! :  REM TT is the thickness, computed from layer(s) + substrate
8020 PRINT " "
8030 PRINT "dl = ";DL;"   ds = ";DS;"
8040 IF MODEL = 2 THEN TT = DL + DS : PRINT "thick = ";TT;THICKNESS
8050 IF MODEL = 3 THEN TT = 2!*DL + DS : PRINT "thick = ";TT;THICKNESS
8070 PRINT "average sum = ";AVE(GG)
8190 RETURN
8200 REM 2D slit crack
8210 DEF FNLAY(X) = ES*(1 - (2! * PI* (1-POISSON^2) * X * RADIUS^2)) :VOL = 0
8212 SLOPE =  (2! * PI* (1-POISSON^2) * RADIUS^2)
8215 CR$ = "2D slit crack"
8220 RETURN
8250 REM DEF modified 2D slit cracks
8255 CR$ = "modified 2D slit cracks"
8260 DEF FNLAY(X) = ES*(1 - (2!*FACTOR * PI* (1-POISSON^2) * X * RADIUS^2))
8265 SLOPE = (2!*FACTOR * PI* (1-POISSON^2) * RADIUS^2)
8270 VOL = 0
8290 RETURN
8295 REM
8296 REM
8297 REM
8300 REM MODIFIED for 3D slit cracks
8305 CR$ = " 3D slit cracks, MODIFIED"
8310 FC1 = .5*(PI*PI)*(1! - POISSON*POISSON):REM Fac1 is the prefactor, aligned
                                              slit cracks
8320 FC2 = (2!/PI) : REM Fac2 is a multiplicative factor associated with epsilon
8330 PER = (2!*RADIUS + 2*DL) + (PI*HD): REM Per is the perimeter of
                          the slit crack, ignoring the free surface
8340 S1 =  (2!*RADIUS*DL) - (.5*PI*HD*HD):  REM s is the area of the slit crack
8350 SSQ = S1*S1 : REM Ssq is the square of the crack area (slit crack)
8360 REM With lig = 1 , factor of 2.8 gives reasonable fit DEF FNLAY(X) = ES*(1
- (2.8*X*FC1*FC2*SSQ)/PER): VOL = 1 : REM 3D modified slit
8370 DEF FNLAY(X) = ES*(1 - (X*FC1*FC2*SSQ)/PER): VOL = 1 : REM 3D modified slit
8380 SLOPE =  (FC1*FC2*SSQ)/PER: VOL = 1 : REM 3D modified slit
8390 RETURN
8396 REM
8397 REM
8400 REM Calculate for MODIFIED half ellipse cracks
8405 CR$ = "MODIFIED half ellipse cracks"
8407 REM Much better fit if lig = 0 rather than lig = 1
8410 FAC1 = (16!/3!)*(1! -POISSON*POISSON):  REM Fac1 is the prefactor, aligned
                                              elliptical cracks
8420 FAC2 = (2!/PI) : REM Fac2 is a multiplicative factor associated with
                           epsilon
8430 PERIM = (2!*RADIUS*ELL) + (PI*HD): REM Perim is the perimeter of        a
half-ellipse ignoring the free surface, but including indent ligament
8435 RP = 1!/PERIM
8440 REM PERIM = (2!*radius*ell) + 2!*(radius -(2!*hd) + PI*hd): REM Perim is th
perimeter of a half-ellipse ignoring the free surface, but including indent liga
ment
8450 A11  = ((PI/2!)*RADIUS*DL) - (.5*PI*HD*HD):  REM A11 is the area of a half-
ellipse, corrected for indent ligament
8460 ASQ = A11*A11 : REM Asq is the square of the crack area (half-ellipse)
8470 DEF FNLAY(X) = ES*(1! - X*FAC1*FAC2*ASQ*RP) : VOL = 1 : REM modified HALF-E
LLIPSE cracks
8480 SLOPE = FAC1*FAC2*ASQ*RP : REM modified HALF-ELLIPSE cracks
8490 RETURN
8496 REM
8497 REM
8500 REM HALF ELLIPSE CRACKS, UNMODIFIED
```

```
8505 CR$ = " HALF ELLIPSE CRACKS, UNMODIFIED "
8507 REM For lig = 0, -1.4 < dd < .5, for lig = 1 reasonable fit except for
         3-layer, 98 N load
8510 FAC1 = (16!/3!)*(1! - POISSON*POISSON):  REM Fac1 is the prefactor, aligned
                                                  elliptical cracks
8520 FAC2 = (2!/PI):REM Fac2 is a multiplicative factor associated with
                    epsilon
8530 PERIM = 2!*RADIUS*ELL : REM Perim is the perimeter of a half-ellipse
                                 ignoring the free surface
8540 REM PERIM = 2!*radius : REM Perim is the perimeter of a half-ellipse
                                 ignoring the free surface
8545 RP = 1!/PERIM
8550 AA =  (PI/2!)*RADIUS*DL :  REM AA is the area of a half-ellipse
8560 ASQ = AA*AA : REM Asq is the square of the crack area (half-ellipse)
8570 DEF FNLAY(X) =ES*(1 - (X*FAC1*FAC2*ASQ*RP)): VOL = 1:REM HALF-ELLIPSE crack
8580 SLOPE  =FAC1*FAC2*ASQ*RP :REM HALF-ELLIPSE crack
8590 RETURN
8596 REM
8597 REM
8600 REM  3D  SLIT CRACKS, UNMODIFIED
8605 CR$ = " 3D  SLIT CRACKS, UNMODIFIED "
8610 FC1 = .5*(PI*PI)*(1! - POISSON*POISSION): REM Fac1 is the prefactor, aligne
                                                  slit cracks
8620 FC2 = (2!/PI) : REM Fac2 is a multiplicative factor associated with
                     epsilon
8625 PER = 2*RADIUS + 2*DL : REM Per is the perimeter of the slit crack
8630 REM PER = 2!*(DL + 2!*RADIUS) : REM Per is the perimeter of the slit crack,
                                       incldуing the free surface
8635 RP = 1!/PER
8640 SS =  2!*RADIUS*DL :  REM s is the area of the slit crack
8650 SSQ = SS*SS : REM SSQ is the square of the crack area (slit crack)
8660 DEF FNLAY(X) = ES*(1! - (X*FC1*FC2*SSQ*RP)) : VOL = 1 : REM 3D SLIT CRACKS
8680 SLOPE = FC1*FC2*SSQ*RP : REM 3D SLIT CRACKS
8690 RETURN
8696 REM
8697 REM
8700 REM SHETTY CRACKS
8705 CR$ = " SHETTY CRACKS "
8707 REM For lig = 1, fitting is very poor (one - two orders of magnitude errors
         in terms of nymc
8710 FAC1 = (16!/3!)*(1! - POISSON*POISSON):  REM Fac1 is the prefactor, aligne
              elliptical cracks
8720 FAC2 = (2!/PI) : REM Fac2 is a multiplicative factor associated with
                      epsilon
8730 PERIM= (RADIUS *ELL) + DL - HD : REM Perim is the perimeter of half-ellipse
 ignoring the free surface, but including indent ligament
8735 RP = 1!/PERIM
8740 AREA = ((PI/4!)*RADIUS*DL - (HD*DL)): REM AREA area of a half-ellipse, corr
ected for indent ligament
8750 ASQ = AREA*AREA : REM Asq is the square of the crack area (half-ellipse)
8760 DEF FNLAY(X) = ES*(1! - (X*FAC1*FAC2*ASQ*RP)) : VOL = 1 :REM sketty cracks
8780 SLOPE = FAC1*FAC2*ASQ*RP :REM sketty cracks
8790 RETURN
8796 REM
8797 REM
8800 REM modified 3D cracks, edition II
8810 CR$ = "modified 3D cracks, edition II "
8820 FC1 = .5*(PI*PI)*(1! - POISSON*POISSON) :  REM Fac1 is the prefactor, align
ed                                                slit cracks
8830 FC2 = (2!/PI) : REM Fac2 is a multiplicative factor associated with
                     epsilon
8835 PER = (2!*RADIUS + 2!*DL + PI*HD)
8840 RP = 1!/PER
8850 SA =  (2!*RADIUS*DL) - (.5*PI*HD*HD) :  REM s is the area
                          of the slit crack
8860 SSQ = SA*SA : REM Ssq is the square of the crack area (slit crack)
```

```
8865 GOSUB 14000 : REM Elliptic integral subroutine
8870 DEF FNLAY(X) = ES*(1! - (X*VV*FC1*FC2*SSQ*RP)) : VOL = 1 : REM  SLIT cracks
8880 SLOPE = VV*FC1*FC2*SSQ*RP : REM Slope is the slope of the           delta
E/Eo versus N data for SLIT cracks
8890 RETURN
8896 REM
8897 REM
9000 REM Initialize for sums, get constants
9050 SUM = 0! : REM Sum is the sum of the residuals (difference between
                   and modeled values are the residuals).
9060 DD = 0! : TT = 0! :  REM Initialize dd value
9120 REM Crack functions
9240 IF U = 1 THEN  GOSUB 8200 : REM 2D slit crack
9260 IF U = 2 THEN  GOSUB 8250 : REM modified 2D slit cracks
9280 IF U = 3 THEN  GOSUB 8300 : REM 3D SLIT CRACK, MODIFIED
9300 IF U = 4 THEN  GOSUB 8400 : REM 3D MODIFIED half ellipse cracks
9320 IF U = 5 THEN  GOSUB 8500 : REM 3D HALF ELLIPSE CRACKS, UNMODIFIED
9330 IF U = 6 THEN  GOSUB 8600 : REM 3D SLIT CRACKS, UNMODIFIED
9340 IF U = 7 THEN  GOSUB 8700 : REM SHETTY cracks
9360 IF U = 8 THEN  GOSUB 8800 : REM modified 3D cracks, edition II
9365 REM Elliptical shaped indent cross-section
9370 IF U = 9 THEN  GOSUB 13500 : REM modified 3D slit, ellip hd
9380 IF U =10 THEN  GOSUB 13630 :  REM modified 3D half-ellipse, ellip hd
9390 IF U =11 THEN  GOSUB 13770 : REM modified 3D cracks, edition II
9400 RETURN
9490 RETURN
9500 REM Initialize avemin vector
9520 FOR WQ = 1 TO 6
9600   AVEMIN(WQ,1) = 99999.9 : AVEMIN(WQ,2) = 0!
9610 NEXT WQ
9690 RETURN
9700 REM
9705 IF LIG = 1 THEN L$ = "  with ligament (radius and ndensity revised)
9707 IF LIG = 0 THEN L$ = "  without ligament correction "
9720 AV$ =" ####     ##     ##.####^^^^         ##.###^^^^    ##.###^^^^   ##.###^^
^^"
9730 PRINT " " : PRINT " "
9732 IF LPRI = 1 THEN LPRINT " " : LPRINT " "
9735 PRINT CR$;L$
9736 PRINT ROM$
9737 IF LPRI = 1 THEN LPRINT CR$;L$
9738 IF LPRI = 1 THEN LPRINT ROM$
9740 PRINT"Load(N)  Layers   Min Ave Sum        Dl            Slope    hd "
9742 IF LPRI = 1 THEN LPRINT"Load(N)  Layers   Min Ave Sum        Dl           S
lope    hd "
9760 IF LPRI = 1 THEN LPRINT " "
9820 FOR A = 1 TO SETS
9840   PRINT USING AV$;AVEMIN(A,3);AVEMIN(A,4);AVEMIN(A,1);AVEMIN(A,2),AVEMIN(A,
5),AVEMIN(A,6)
9842  IF LPRI = 1 THEN LPRINT USING AV$;AVEMIN(A,3);AVEMIN(A,4);AVEMIN(A,1);AVEM
IN(A,2),AVEMIN(A,5), AVEMIN(A,6)
9860 NEXT A
9990 RETURN
10000 REM Two layer model
10040 GOSUB 14000 : REM Compute elliptic integrals
10060 FOR KK = 1 TO NDATA
10070     GOSUB 9000 : REM Initialize for sums, get constants
10080     GOSUB 11000 : REM Calculation of layer modulus
10140     GOSUB 12400 : REM calculation of NORMALIZED YOUNG'S MODULUS CHANGE
10180     GOSUB 4700  : REM Conversion of units for elastic modulus
10220     GOSUB 4800  : REM Calculation of Experimental value of Normalized of
                           Normalized Young's modulus
10260     IF PRI = 1 THEN GOSUB 12440 : REM PRINT RESULTS TO CRT
10300 NEXT KK
10390 IF PRI = 1 THEN GOSUB 8000 : REM Print summary results to CRT for data set
10400 REM STOP
```

```
10500 RETURN
11000 REM **Calculation of layer modulus under 2-D Rectangular(slit) crack model
11005 READ LNIND, EE(KK)
11007 IF LIG = 1 THEN GOSUB 7000 : REM model as two cracks, omitted central "lig
ament where the
11008 REM                  indent impression appears
11010 REM WID = Width of the specimen in [m] **
11020 REM LENGTH =  Length of the specimen in [m] **
11025 REM THICKNESS = thickness of the specimen in [m] **
11030 REM DL =  Depth of the layer in [m] for indentation**
11040 REM RADIUS is Half of slit crack size in[m], which is half of measured
                 radial crack size, 2c **
11050 REM POISSON = undamaged Poisson's ratio of the specimen*
11060 NUMDLAYER = LNIND/(WID*LENGTH) :REM  **NUMDLAYER stands for NUMBER
                                       density of layer(mm-2) **
11100 NDVOLUME = (LNIND)/(WID*LENGTH*THICKNESS) : REM **NDVOLUME is
                                       number density of cracks in whole specimen
11105 NVLAYER = (LNIND)/(WID*LENGTH*DL): REM
11120 REM ES  is substrate modulus in [N/m2] **
11160 IF VOL = 0 THEN EL = FNLAY(NUMDLAYER)
11170 IF VOL = 1 THEN EL = FNLAY(NVLAYER)
11200 RETURN
12000 REM calculation of the distance from the neutral axis to the bottom layer
12020 REM DS = Sustrate thickness in [m] **
12030 DISTANCE = (ES*DS*DS - EL*DL*DL)/(2*ES*DS + 2*EL*DL)
12100 RETURN
12200 REM Calculation of the second moment of inertia of SUBSTRATE and LAYER
12210 INS =((DS^3)/3 - (DS*DS*DISTANCE) + (DS*DISTANCE*DISTANCE))*WID
12220 INL =((DL^3)/3 + (DL*DL*DISTANCE) + (DL*DISTANCE*DISTANCE))*WID
12300 RETURN
12400 REM **calculation of NORMALIZED YOUNG'S MODULUS CHANGE **
12410 RA1 = DL/THICKNESS : RA2 = DS/THICKNESS
12420 EOVERALL = (EL*RA1) + (ES*RA2)
12430 NYMC = (ES-EOVERALL)/ES
12435 RETURN
12440 REM Print results to crt
12490 A$ = "  ###.####     ###.####      ###.####   #.#####   #.#####    ##.####
# "
12500 IF KK = 1 THEN PRINT " " : PRINT " "
12505 IF KK = 1 THEN PRINT LABEL$ : PRINT " "
12510 IF KK = 1 THEN PRINT" El (GPa)   Eoverall(GPa)      Eexp      nymc      en
ymc          dd"
12520 PRINT USING A$;ELAYER,EEOVER,EE(KK),NYMC,ENYMC,DD
12700 RETURN
13500 REM MODIFIED for 3D slit cracks, elliptical indent bottom
13510 CR$ = " 3D slit cracks, MODIFIED, elliptical indent bottom"
13520 FC1 = .5*(PI*PI)*(1! - POISSON*POISSON):REM Fac1 is the prefactor, aligned
                                                 slit cracks
13530 FC2 = (2!/PI) : REM Fac2 is a multiplicative factor associated with epsilo
n
13540 PER = (2!*RADIUS) + (2*DL) + (2*ELL*HD): REM Per is the perimeter of
                              the slit crack, ignoring the free surface
13550 S1 =  (2!*RADIUS*DL) - (.5*PI*HD*HD*KPRIME):  REM s is the area of the sli
t crack
13560 SSQ = S1*S1 : REM Ssq is the square of the crack area (slit crack)
13570 REM With lig = 1 , factor of 2.8 gives reasonable fit DEF FNLAY(X) = ES*(1
 - (2.8*X*FC1*FC2*SSQ)/PER): VOL = 1 : REM 3D modified slit
13580 DEF FNLAY(X) = ES*(1 - (X*FC1*FC2*SSQ)/PER): VOL = 1 : REM 3D modified sli
t
13590 SLOPE =  (FC1*FC2*SSQ)/PER: VOL = 1 : REM 3D modified slit
13600 RETURN
13610 REM
13620 REM
13630 REM Calculate for MODIFIED half ellipse cracks, elliptical indent bottom
13640 CR$ = "MODIFIED half ellipse cracks, elliptical indent bottom"
13650 REM Much better fit if lig = 0 rather than lig = 1
```

```
13660 FAC1 = (16!/3!)*(1! -POISSON*POISSON):  REM Fac1 is the prefactor, aligned
                                                elliptical cracks
13670 FAC2 = (2!/PI) : REM Fac2 is a multiplicative factor associated with
                          epsilon
13680 PERIM = (2!*RADIUS*ELL) + (2*ELL*HD): REM Perim is the perimeter of
  a half-ellipse ignoring the free surface, but including indent ligament
13690 RP = 1!/PERIM
13700 A11  = ((PI/2!)*RADIUS*DL) - (.5*PI*HD*HD*KPRIME):  REM A11 is the area of
 a half-ellipse, corrected for indent ligament
13710 ASQ = A11*A11 : REM Asq is the square of the crack area (half-ellipse)
13720 DEF FNLAY(X) = ES*(1! - X*FAC1*FAC2*ASQ*RP) : VOL = 1 : REM modified HALF-
ELLIPSE cracks
13730 SLOPE = FAC1*FAC2*ASQ*RP : REM modified HALF-ELLIPSE cracks
13740 RETURN
13750 REM
13760 REM
13770 REM modified 3D cracks, edition II, elliptical indent bottom
13775 CR$ = "modified 3D cracks, edition II, elliptical indent bottom"
13780 FC1 = .5*(PI*PI)*(1! - POISSON*POISSON) :  REM Fac1 is the prefactor, alig
ned                                                slit cracks
13790 FC2 = (2!/PI) : REM Fac2 is a multiplicative factor associated with
                          epsilon
13800 PER = (2!*RADIUS + 2!*DL + 2*ELL*HD)
13810 RP = 1!/PER
13820 SA =  (2!*RADIUS*DL) - (.5*PI*HD*HD*KPRIME) :  REM s is the area
                                 of the slit crack
13830 SSQ = SA*SA : REM Ssq is the square of the crack area (slit crack)
13840 GOSUB 14000 : REM Elliptic integral subroutine
13850 DEF FNLAY(X) = ES*(1! - (X*VV*FC1*FC2*SSQ*RP)) : VOL = 1 : REM  SLIT crack
s
13860 SLOPE = VV*FC1*FC2*SSQ*RP : REM Slope is the slope of the            delta
 E/Eo versus N data for SLIT cracks
13870 RETURN
13880 REM
13890 REM
14000  REM EVALUTATE ELLIPTIC INTEGRALS, ECCENTRICITY
14010 PI = 3.141592
14040 IF DL > RADIUS THEN RETURN
14060 F1 = (RADIUS*RADIUS - DL*DL)
14070 ECCEN = (SQR(F1))/RADIUS
14080 REM Power series approximation to elliptic integral of second kind in
        terms of the modulus m.  (See Dwight, Table of Integrals for series).
14090 KPRIME = SQR(1! - ECCEN*ECCEN) : REM KPRIME is identical to dl/radius
14092 REM RATOP = DL/RADIUS
14095 REM PRINT "dl/radius = "; RATOP;"  ";KPRIME
14100 M = (1! - KPRIME)/(1! + KPRIME)
14110 T1 = PI/(2!*(1! + M))
14120 T3 = (M*M)/4
14130 T4 = M^4/(2*2*4*4)
14140 T5 = (9*(M^6))/(2*2*4*4*6*6)
14150 T6 = (3*3*5*5)*(M^8)/(2*2*4*4*6*6*8*8)
14160 ELL = T1*(1! + T3 + T4 + T5 + T6)
14180 FCC = SQR(1! - ECCEN*ECCEN)
14200 FACTOR = (2!/3!)*(FCC/ELL) : REM PRINT "factor = ";FACTOR
14207 VV =(16/(PI*PI)* FCC*ELL)
14300 RETURN
15500 REM PRINT RESULTS TO DISK FILE
15505 IF DPRI = 0 THEN RETURN : REM dpri = 0 means "do not print results to disk
15510 FF$ = "ROM.RES"
15520 OPEN FF$ FOR APPEND AS 2
15525 PRINT #2, CR$;L$
15527 PRINT #2, ROM$
15530 FOR A = 1 TO SETS
15570   PRINT #2, USING AV$;AVEMIN(A,3);AVEMIN(A,4);AVEMIN(A,1);AVEMIN(A,2),AVEM
IN(A,5),AVEMIN(A,6)
15590 NEXT A
```

```
15600 PRINT #2, " "
15650 CLOSE
15660 RETURN
20000 DATA 6 : REM Sets, which is the number of data sets
21000 DATA 7,3,49, " 49 N loading indented both sides", 4.181e-5
21010 DATA 0.00612,0.0687,0.00101,0.000110,0.00081,1.138e-4,.219,3.223355e11
21020 DATA         0,        0 , 322.3355
21040 DATA        45,        0 , 322.2478
21060 DATA        45,       45 , 322.1164
21080 DATA        90,       45 , 322.0319
21100 DATA        90,       90 , 321.8348
21120 DATA       135,       90 , 321.5595
21140 DATA       135,      135 , 321.3719
23000 DATA 8,3,98, "98 N loading  indented on two sides", 5.944e-5
23010 DATA 0.012,0.0707,0.001,0.000144,0.000712,1.8505e-4,.206,3.348828e11
23020 DATA         0,        0 , 334.8828
23040 DATA        46,        0 , 334.6449
23060 DATA        46,       46 , 334.4863
23080 DATA       138,       46 , 334.2002
23100 DATA       138,      138 , 333.5011
23120 DATA       230,      138 , 333.1398
23140 DATA       230,      230 , 332.9058
23160 DATA       322,      230 , 332.3318
24000 DATA 3,3,196, " 196 loading indented on both sides",  8.39e-5
24010 DATA 0.012,0.0685,0.001000,0.000239,0.000522,3.224e-4,.208,3.339898e11
24020 DATA  0 ,  0 , 333.9898
24040 DATA  22 , 0 , 333.5575
24060 DATA  22 , 44 , 331.9211
27000 DATA 8,2,49, " 49 N loading indented on single side", 4.181e-5
27010 DATA 0.012,0.0693,0.001,0.000110,0.00081,1.138e-4,.207,3.341635e11
27020 DATA  0 ,  334.1635
27040 DATA  40 , 334.0537
27060 DATA  80 , 333.9270
27080 DATA 120 , 333.8173
27100 DATA 160 , 333.7864
27120 DATA 200 , 333.7188
27140 DATA 240 , 333.6119
27160 DATA 280 , 333.5192
30000 DATA 5, 2,98, "  98 loading  indented on one side", 5.944e-5
30100 DATA 0.012,0.06943,0.001014,0.000144,0.000870,1.8505e-4,.206,3.273381e11
30110 DATA         0 , 327.3381
30120 DATA        68 , 327.0228
30130 DATA       102 , 326.9290
30140 DATA       170 , 326.5768
30150 DATA       238 , 326.2183
33000 DATA 13,2,196, " 196 loading indented on one side",  8.39e-5
33010 DATA 0.012,0.0697,0.001005,0.000239,0.000766,3.224e-4,.215,3.328715e11
33020 DATA  0 ,  332.8715
33040 DATA  7  , 332.5756
33060 DATA  14 , 332.4626
33080 DATA  21 , 332.2899
33100 DATA  36 , 331.8183
33120 DATA  44 , 331.6822
33140 DATA  52 , 331.4366
33160 DATA  59 , 331.2575
33180 DATA  66 , 331.1215
33220 DATA  87 , 330.5878
33240 DATA  108, 330.0017
33260 DATA  129, 329.4656
33280 DATA  150, 328.7873
```

REFERENCES

1. B. A. Boley and J. H. Weiner, Theory of Thermal Stresses, John Wiley and Sons, Inc. New York 1960.

2. H. Ohira and R. C. Bradt, "Strength Distribution of a Quench-Strengthened Aluminosilicate Ceramic", J. Amer. Ceram. Soc., 71 [1]: 35-41, 1988.

3. W. P. Rogers, A. F. Emery, R. C. Bradt and A. S. Kobayashi, "Statistical Study of Thermal Fracture of Ceramic Materials in the Water Quench Test", J. Amer. Ceram. Soc., 70 [6]: 406-412, 1987.

4. M. Ashizuka, T. E. Easler and R. C. Bradt, "Statistical Study of Thermal Shock Damage of a Borosilicate Glass", J. Amer. Ceram. Soc., 66 [8]: 542-550, 1983.

5. D. P. H. Hasselman, "Crack Propagation under Constant Deformation and Thermal Stress Fracture", Int. J. Fract. Mech., 7: 157, 1971.

6. D. P. H. Hasselman, "Unified Theory of Thermal Shock Fracture Initiation and Crack Propagation in Brittle Ceramics", J. Am. Ceram. Soc., 52[11]: 600-604, 1969.

7. T.K. Gupta, "Strength degradation and crack propagation in thermally shocked Al_2O_3", J. Amer. Ceram. Soc., 55: 249, 1972.

8. J. P. Singh, J. R. Thomas and D. P. H. Hasselman, "Analysis of Effect of Heat-Transfer Variables on Thermal Stress Resistance of Brittle Ceramics measured by Quenching Experiments", J. Am. Ceram. Soc., 63[3-4]: 140-144, 1980.

9. P.F. Becher, "Transient Thermal Stress Behavior in ZrO_2-Toughened Al_2O_3", J. Amer. Ceram. Soc., 64: 37-39, 1981.

10. K. Kokoni, "Effect of Package Lid on the Thermal Shock Test of Glass-to-Metal Seal in Microelectronics", Am Ceram. Soc. Bull., 65: 1493-1497, 1986.

11. S. T. Buljan, J. G. Baldoni and M. L. Huckabee, "Si_3N_4-SiC Composites", Am. Ceram. Soc. Bull., 66[2]: 347-352, 1987.

12. W. D. Kingery, H. K. Bowen and D. R. Uhlmann, Introduction to Ceramics, 2nd ed., Chap. 16, John Wiley and Sons, New York, 1976.

13. W. D. Kingery, "Factors Affecting Thermal Stress Resistance of Ceramics Materials", J. Am. Ceram. Soc., 38[1]: 3-15, 1955.

14. J. C. Coppola and R. C. Bradt, "Thermal Shock Damage in SiC", J. Amer. Ceram. Soc., 56 [4]: 214-218, 1973.

15 IBM Packaging Technology, IBM Journal of Research and Development, Vol. 26, No. 3 1982.

16. D. Lewis and R. W. Rice, "Comparison of Static, Cyclic, and Thermal Shock Fatigue in Ceramic Composites", Ceram. Eng. Sci. Proc. 3[9-10], 714-721, 1982.

17. D. Lewis and R. W. Rice, "Thermal Shock Fatigue of Monolithic Ceramics and Ceramic - Ceramic Particulate Composites", Ceram. Eng. Sci. Proc., 2[7-8], 712-718, 1981.

18. J. P. Singh, K. Niihara, and D. P. H. Hasselman, "Analysis of Thermal Fatigue Behavior of Brittle Structural Materials", J. Mater. Sci., 16 : 2789-2797, 1981.

19. B. K. Sarkar and T. G. J. Glinn, Trans. Brit. Ceram. Soc., 69: 1285-1287, 1970.

20. K. T. Faber, M. D. Huang, and A. G. Evans, "Quantitative Studies of Thermal Shock in Ceramics Based on a Novel Test Technique", J. Amer. Ceram. Soc. 64: 296-301, 1981.

21. A. G. Evans and R. L. Jones, "Evaluation of a Fundamental Approach for the Statistical Analysis of Fracture", J. Amer. Ceram. Soc., 61, 156, 1978.

22. Y. Kim, W. J. Lee, and E. D. Case, "Thermal Fatigue in SiC Fiber Reinforced Aluminosilicate Glass Ceramic Composite", pp 479-486, in Metal and Ceramic Matrix Composites: Processing, Modeling and Mechanical Behavior, Edited by R. B. Bhagat, A. H. Clauer, P. Kumar and A. M. Ritter, The Minerals, Metals and Materials Society, 1990.

23. Y. Kim, W. J. Lee and E. D. Case, "Thermal Fatigue Behavior of Ceramic Matrix Composites: A Comparison Among Fiber Reinforced, Whisker Reinforced, and Monolithic Ceramics", pp 871-881 in Proceedings of the American Society for Composites, 5th Technical Conference, 1990.

24. W. J. Lee and E. D. Case, "Cyclic Thermal Shock in SiC Whisker/Alumina Composites", Mater. Sci. and Eng., A119: 113-126, 1989.

25. W. J. Lee and E. D. Case, "Thermal Fatigue in Polycrystalline Alumina", J. Mater. Sci., 25: 5043-5054, 1990.

26. F. Delale, "Critical Fiber Size for Microcrack Suppression in Ceramic-Fiber/Ceramic-Matrix Composites", Eng. Frac. Mech., 31 [1]: 145-155, 1988.

27. R. W. Davidge and T. J. Green, "The Strength of Two-Phase Ceramic /Glass Materials", J. Mat. Sci., 3: 629-634, 1968.

28. A. H. Heuer, N. Classen, W. M. Kriven and M. Ruhle, "Stability of Tetragonal ZrO_2 Particles in Ceramic Matrices", J. Amer. Ceram. Soc., 65: 642-650, 1982.

29. Y. Fu, A. G. Evans and W. M. Kriven, "Microcrack Nucleation in Ceramics Subject to a Phase Transformation", J. Amer. Ceram. Soc., 67 [9]: 626-630, 1984.

30. E. D. Case, K. M. Louie and A. G. Evans, "Statistical Analysis of Damage Induced by Water Drop or Water Jet Impact", J. Mat. Sci. Lett., 3: 879-884, 1984.

31. H. P. Kirchner and E. D. Issacson, "Residual Stresses in Hot-Pressed Si_3N_4 Grooved by Single-Point Grinding", J. Am. Ceram. Soc., 65: 55-60, 1982.

32. H. P. Kirchner, "Comparison of Single-Point and Multipoint Grinding Damage in Glass", J. Am. Ceram. Soc., 67: 347-353, 1984.

33. K. Matsushida, S. Kuratani, T. Okamoto and M. Shimada, "Young's Modulus and Internal Friction in Alumina Subject to Thermal Shock", J. Mat. Sci. Lett., 3: 345-348, 1984.

34. S. Nishijima, K. Matsushita, T. Okada, T. Okamoto and T. Hagihara, "Dynamic Young's Modulus and Internal Friction in Composite Materials", pp 143-151 in Nonmetallic Materials and Composites at Low Temperature 3, edited by G. Hartwig and D. Evans, Plenum Press, New York and London, 1986.

35. E. D. Case, J. R. Smyth and O. Hunter, Jr., "Microcrack Healing During the Temperature Cycling of Single Phase Ceramics", pp 507-530 in Fracture Mechanics of Ceramics, vol.5, edited by R. C. Bradt, A. G. Evans, D. P. H. Hasselman and F. F. Lange, Plenum Press, N.Y., 1983.

36. T. K. Gupta, "Crack Healing and Strengthening of Thermally Shocked Alumina", J. Am. Ceram. Soc., 59[5-6]: 259-262, 1976.

37. T. K. Gupta, "Instability of Cylindrical Voids in Alumina", J.

Am. Ceram. Soc., 61[5-6]: 191-195, 1978.

38. T. K. Gupta, "Kinetics of Strengthening of Thermally Shocked MgO and Al_2O_3", J. Am. Ceram. Soc., 59[9-10]: 448-449, 1976.

39. A. G. Evans and E. A. Charles, "Strength Recovery by Diffusive Crack Healing", Acta Met., 25: 919-927, 1977.

40. C. F. Yen and R. L. Coble, "Spheroidization of Turbular Voids in Al_2O_3 Crystals at High Temperatures", J. Amer. Ceram. Soc., 55[10]: 507-509, 1972.

41. F. F. Lange and K. C. Radford, "Healing of Surface Cracks in Polycrystalline Al_2O_3", J. Amer. Ceram. Soc., 53[7]: 420-421, 1970.

42. T. K. Gupta, "Crack Healing in Thermally Shocked MgO", J. Amer. Ceram. Soc., 58[3-4]: 143, 1975.

43. J. T. A. Roberts and B. J. Wrona, "Crack Healing in UO_2", J. Amer. Ceram. Soc., 56[6]: 297-299, 1973.

44. G. Bandyopadhyay and J. T. A. Roberts, "Crack Healing and Strength Recovery in UO_2", J. Amer. Ceram. Soc., 59[9-10]: 415-419, 1976.

45. G. Bandyopadhyay and C. R. Kennedy, "Isothermal Crack Healing and Strength Recovery in UO_2 Subjected to Varying Degrees of Thermal Shock", J. Amer. Ceram. Soc., 60[1-2]: 48-50, 1977.

46. R. N. Singh and J. L. Routbort, "Fracture and Crack Healing in (U,Pu)C", J. Amer. Ceram. Soc., 62[3-4]: 128-133, 1979.

47. Y. Ohya, Z. Nakagawa and K. Hamano, "Crack Healing and Bending Strength of Aluminum Titanate Ceramics at High Temperature", J. Amer. Ceram. Soc., 71[5]: c-232-c-233, 1988.

48. M. Tomozawa, K. Hirao and P. E. Bean, "Origin of Strength Increase of Abraded or Indented Glass upon Annealing", J. Amer. Ceram. Soc., 69[8]: c-186-c-188, 1986.

49. A. I. Bailey, "Friction and Adhesion of Clean and Contaminated Mica Surfaces", J. Appl. Phys., 32: 1407-1412, 1961.

50. R. B. Leonesio, "Fracture and Healing Effects in Mica Crystals", J. Am. Ceram. Soc., 55[9]: 437-439, 1972.

51. T. A. Michalske and E. R. Fuller, "Closure and Repropagation of Healed Cracks in Silicate Glass", J. Amer. Ceram. Soc., 68[11]: 586-590, 1985.

52. B. Stavrinidis and D. G. Holloway, "Crack Healing in Glass", Phys. Chem. Glasses, 24[1]: 19-25, 1983.

53. M. Inagaki, K. Urashima, S. Toyomasu, Y. Goto and M. Sakai, "Work of Fracture and Crack Healing in Glass", J. Am. Ceram. Soc., 68[12]: 704-706, 1985.

54. G. R. Pulliam, "Precipitation in Microscopic Cracks", J. Am. Ceram. Soc., 42[10]: 477-82, 1959.

55. D. H. Roach, S. Lathabai and B. R. Lawn, "Interfacial Layers in Brittle Cracks", J. Am. Ceram. Soc., 71[2]: 97-105, 1988.

56. R. L. Lehman, R. E. Hill, Jr. and G. E. Sigel, Jr., "Low-Temperature Crack Closure in Fluoride Glass", J. Amer. Ceram. Soc., 72[3]: 474-477, 1989.

57. M. K. C. Holden and V. D. Frechette, "Healing of Glass in Humid Environments", J. Amer. Ceram. Soc., 72 [11]: 2189-2193, 1989.

58. H. M. Chou and E. D. Case, "Time-Dependent Recovery of the Elastic Modulus in Thermally Shocked Polycrystalline Yttrium Iron Garnet (YIG)", Mat. Sci. Eng., 100: 7-14, 1988.

59. S. S. Manson, Chap. 7 in Thermal Stress and Low-Cycle Fatigue, McGraw-Hill, New York, 1966.

60. C. M. Cheng, "Resistance to Thermal Shock", J. Am. Rocket Soc., 21[6]: 147-153, 1951.

61. G. Simmons and H. Wang, pp 146, 328-329 in Single Crystal Elastic Constants and Calculated Aggregate Properties, A Handbook, The M.I.T. Press, Cambridge, 1971.

62. C. Kittel, p 142 in Introduction to Solid State Physics, 5th ed., John Wiley & Sons, New York, 1976.

63. L. D. Bentsen, D. P. H. Hasselman and R. Ruh, "Effect of Hot-Pressing Temperature on Thermal Diffusivity/Conductivity of SiC/AlN Composites", J. Am. Ceram. Soc. Comm., 66[3]: c40-c41, 1983.

64. P. F. Becher, "Effect of Water Bath Temperature on the Thermal Shock of Al_2O_3", J. Am. Ceram. Soc. Comm., 64[1]: c17-c18, 1981.

65. P. F. Becher, D. Lewis III, K. R. Carman and A. C. Gonzales, "Thermal Shock Resistance of Ceramics: Size and Geometry Effects in Quench Tests", Bull. Am. Ceram. Soc., 59[5]: 542-548, 1980.

66. J. P. Singh, Y. Tree and D. P. H. Hasselman, "Effect of Bath and

Specimen Temperature on Thermal Stress Resistance of Brittle Ceramics Subjected to Thermal Quenching", J. Mat. Sci., 16: 2109-2118, 1981.

67. F. P. Incropera and D. P. De Witt, Chap. 10 in Introduction to Heat Transfer, John Wiley & Sons, New York, 1985.

68. E. Hahne and U. Grigull, pp 403-424 in Heat Transfer in Boiling, Hemisphere Publishing Corporation, London, 1977.

69. J. R. Thome, Chap. 2 and 7 in Enhanced Boiling Heat Transfer, Hemisphere Publishing Corporation, New York, 1990.

70. R. W. Davidge, pp 4953-4956 in Encyclopedia of Materials Science and Engineering, vol. 7, Editor-in-chief M. B. Beaver, Pergamon Press, Oxford, 1986.

71. R. F. Cook, B. R. Lawn, T. P. Dabbs, and P. Chantikul, "Effect of Machining Damage on the Strength of Glass-Ceramic", J. Am. Ceram. Soc. Comm., 64[9]: c121-c122, 1981.

72. F. F. Lange, M. R. James, and D. J. Green, "Determination of Residual Surface Stresses Caused by Grinding in Polycrystalline Al_2O_3", J. Am. Ceram. Soc. Comm., 66[2]: c16-c17, 1983.

73. D. A. Krohn and D. P. H. Hasselman, "Effect of Abrasion on Strength and Thermal-Stress Resistance of a Soda-Lime-Silica Glass", J. Am. Ceram. Soc., 56[6]: 337-338, 1973.

74. D. Lewis III, "Effect of Surface Treatment on the Strength and Thermal Shock Behavior of a Commercial Glass-Ceramic", Am. Ceram. Soc. Bull., 58[6]: 599-605, 1979.

75. P. J. Berensen, "Experiments on Pool Boiling Heat Transfer", Int. J. Heat Mass Transfer, 5: 985-999, 1962.

76. B. Budiansky and R. J. O'Connell, "Elastic Moduli of A Cracked Solid", Int. J. Solids Structures, 12: 81-97, 1976.

77. A. Hoenig, "Elastic Moduli of a Non-Randomly Cracked Body", Int. J. Solids Structures, 15: 137-154, 1979.

78. N. Laws and J. R. Brockenbrough, "The Effect of Micro-Crack Systems on the Loss of Stiffness of Brittle Solids", Int. J. Solids Structures, 23[9]: 1247-1268, 1987.

79. D. P. H. Hasselman and J. P. Singh, "Analysis of Thermal Stress Resistance of Microcracked Brittle Ceramics", Am. Ceram. Soc. Bull., 58[9]: 856-860, 1979.

80. T. Yokobori and M. Ichikawa, "Elastic Solid with an Infinite Row of Collinear Cracks and the Fracture Criterion", J. Phys. Soc. Jpn., 19: 2341-2342, 1964.

81. W. R. Delameter, G. Herrmann and D. M. Barnett, "Weakening of an Elastic Solid by a Rectangular Array of Cracks", 43[3]: 74-80, J. Appl. Mech., Trans. ASME, 1975.

82. J. J. Mecholsky, Jr., S. W. Freiman and R. W. Rice, "Effect of Grinding on Flaw Geometry and Fracture of Glass", J. Am. Ceram. Soc., 60[3-4]: 114-117, 1977.

83. H. P. Kirchner, "Damage Penetration at Elongated Machining Grooves in Hot-Pressed Si_3N_4", J. Am. Ceram. Soc., 67[2]: 127-132, 1984.

84. T. J. Larchuk, J. C. Conway, Jr., and H. P. Kirchner, "Crushing as a Mechanism of Material Removal during Abrasive Machining", J. Am. Ceram. Soc., 68[4]: 209-215, 1985.

85. J. D. B. Veldkamp, N. Hattu and G. de With, "Deformation and Cracking during High Temperature Scratching of Some Brittle Materials", pp 121-144 in Fracture Mechanics of Ceramics, Vol. 5, edited by R. C. Bradt, A. G. Evans, D. P. H. Hasselman and F. F. Lange, Plenum Press, New York, 1983.

86. D. B. Marshall, pp 190-220 in Fracture in Ceramic Materials; Toughening Mechanisms, Machining Damage, Shock, edited by A. G. Evans, Noyes Publications, Park Ridge, New Jersey, 1984.

87. B. R. Lawn, A. G. Evans and D. B. Marshall, "Elastic/Plastic Indentation Damage in Ceramics: The Median/Radial Crack System", J. Am. Ceram. Soc., 63[9-10]: 574-581, 1980.

88. B. R. Lawn and M. V. Swain, "Microfracture Beneath Point Indentations in Brittle Solids", J. Mat. Sci., 10: 113-122, 1975.

89. B. R. Lawn and D. B. Marshall, "Hardness, Toughness and Brittleness: An Indentation Analysis", J. Am. Ceram. Soc., 62[7-8]: 347-350, 1979.

90. G. R. Anstis, P. Chantikul, B. R. Lawn and D. B. Marshall, "A Critical Evaluation of Indentation Techniques for Measuring Fracture Toughness: I, Direct Crack Measurements", J. Am. Ceram. Soc., 64[9]: 533-538, 1981.

91. B. R. Lawn and E. R. Fuller, "Equilibrium Penny-like Cracks in Indentation Fracture", J. Mat. Sci., 10: 2016-2024, 1975.

92. D. B. Marshall and B. R. Lawn, "Residual Stress Effects in Sharp Contact Cracking: Part I Indentation Fracture Mechanics", J. Mat. Sci., 14[8]: 2001-2012, 1979.

93. J. F. Kalthoff and D. A. Shockney, "Instability of Cracks Under Impulse Loads", J. Appl. Phys., 48[3]: 986-993, 1977.

94. A. G. Evans, "On Impact Damage in the Elastic Response Regime", J. Appl. Phys., 49[6]: 3304-3310, 1978.

95. E. D. Case, "Numerical Approximating Forms for the Dynamic Stress Intensity Factor", pp 211-222 in Fracture Mechanics of Ceramics, Vol. 7, edited by R. C. Bradt, A. G. Evans, D. P. H. Hasselman and F. F. Lange, Plenum press, New York, 1983.

96. E. Case and A. G. Evans, pp 404-415 in Fracture in Ceramic Materials: Toughening Mechanisms, Machining Damage, Shock, edited by A. G. Evans, Noyes Publications, Park Ridge, New Jersey, 1984.

97. E. D. Case and Youngman Kim, "The Effect of Surface Limited Microcracks on the Effective Young's Modulus of Ceramics: I. Analysis", Submitted to Mat. Sci. and Eng.

98. ASTM Standard C 203-85 "Standard test methods for breaking load and flexural properties of block type thermal insulation"

99. F. Forster, "Ein neues Messverfahren zur Bestimmug des Elastiziatmoduls und der Dampfung"(A New Method for Determination of Modulus of Elasticity and Damping), Zeitschrift fur Metallkunde, 29[4]: 109-115, 1937.

100. S. Spinner and W. E. Tefft, "A Method for Determining Mechanical Resonance Frequencies and for Calculating Elastic Moduli from These Frequencies", ASTM Proc., 61: 1221-1238, 1961.

101. E. Schreiber, O. L. Anderson, and N. Soga, Elastic Constants and Their Measurements, Chap. 4, McGraw-Hill, New York, 1974.

102. G. Pickett, "Equations for Computing Elastic Constants from Flexural and Torsional Resonant Frequencies of Vibration of Prism and Cylinder", ASTM Proc., 45: 846-865, 1945.

103. D. P. H. Hasselman, Tables for the Computation of Shear Modulus and Young's Modulus of Elasticity from Resonant Frequencies of Rectangular Prisms, Carborundum Co., Niagara Falls, NY, 1961.

104. J. B. Wachtman, Jr. and W. E. Tefft, "Effect of Suspension on Apparent Values of Internal Friction Determined by Forster's Method", Rev. Sci. Instrs., 29[6]: 517-520, 1959.

105. L. Rayleigh, pp253-83 in The Theory of Sound, vol.1, Dover Publication, New York, 1976.

106. J. V. Beck and K. J. Arnold, pp 234-247 in Parameter Estimation in Engineering and Science, Wiley Series in Probability and Mathematical Statistics, John Wiley & Sons, New York, 1977.

107. J. V. Beck, B. Blackwell and C. R. St. Clair, Jr., pp 290-294 in Inverse Heat Conduction; Ill-Posed Problems, Wiley-Interscience, New York, 1985.

108. B. L. Symonds, R. F. Cook and B. R. Lawn, "Dynamic Fatigue of Brittle Materials Containing Indentation Line Flaws", J. Mat. Sci., 18: 1306-1314, 1983.

109. A. G. Evans and E. A. Charles, "Fracture Toughness Determinations by Indentation", J. Am. Ceram. Soc., 59[7-8]: 371-372, 1976.

110. Y. Kim and E. D. Case, "Time-dependent Elastic Modulus Recovery Measurement on Thermally Shocked SiC fiber/Aluminosilicate Composites, Machinable Glass Ceramics and Polycrystalline Alumina", Submitted to J. Mat. Sci.

111. P. C. Paris and F. Erdogan, "A critical analysis of crack propagation laws", J. Basic Eng. Trans. ASME, series D, 85: 528-34, 1963.

112. R. G. Foreman, V. E. Kearney and R. M. Engle, "Numerical analysis of crack propagation in cyclic loaded structures", ibid, 89: 459-464, 1967.

113. S. Pearson, "Effect of mean stress in 12.6 mm aluminum alloy of high and low fracture toughness", Eng. Frac. Mech., 1: 213-33, 1968.

114. H. W. Liu, "Crack propagation in thin metal sheet under repeated loading", J. Basic Eng. Trans. ASME, series D, 83: 23-31, 1961.

115. B. Thomkins, "Fatigue crack propagation-an analysis", Phil. Mag., 18: 1041-66, 1968.

116. K. N. Raju, "An energy balance criterion for crack growth under

fatigue loading from consideration of energy of plastic deformation", Int. J. Fracture, 8: 1-14, 1972.

117. T. V. Duggan, "A theory for fatigue crack propagation", Eng. Frac. Mech., 9: 735-47, 1977.

118. N. E. Frost and J. R. Dixon, "A theory of fatigue crack growth", Int. J. Fracture, 3: 301-16, 1967.

119. L. P. Pook and N. E. Frost, "A fatigue crack growth theory", Int. J. Fracture, 9: 53-61, 1973.

120. W. Elber, "The significance of fatigue crack closure", ASTM STP 486, 230-42, 1971.

121. D. A. Krohn and D. P. H. Hasselman, "Static and cyclic behavior of a Polycrystalline Alumina", J. Am. Ceram. Soc., 54[4]: 208-11, 1972.

122. F. Guiu, "Cyclic fatigue of polycrystalline alumina in direct push-pull" J. Mat. Sci., 13: 1357-1361, 1978.

123. Susumu Horibe, "Cyclic fatigue crack growth from indentation flaw in Si_3N_4", J. Mat. Sci. Lett., 7: 725-27, 1988.

124. L. Ewart and S. Suresh, "Dynamic Fatigue Crack Growth in Polycrystalline Alumina under Cyclic Compression", J. Mat. Sci. Lett., 5: 774-78, 1986.

125. L. Ewart and S. Suresh, "Crack propagation in ceramics under cyclic loads", J. Mat. Sci., 22: 1173-1192, 1987.

126. T. Kawagubo and K. Komeya, "Static and cyclic fatigue behavior of a sintered Si_3N_4 at room temperature", J. Am. Ceram. Soc., 70[6]: 400-405, 1987.

127. C. P. Chen and W. J. Knapp, "Fatigue fracture of an alumina ceramic at several temperatures", 691-707, in Fracture Mechanics of Ceramics, vol. 2, edited by R. C. Bradt, D. P. H. Hasselman and F. F. Lange, Plenum press, New York, 1974.

128. A. G. Evans and E. R. Fuller, "Crack propagation in ceramic materials under cyclic loading conditions", Met, Trans., 5[1]: 27-33, 1974.

129. A. G. Evans, "Fatigue in ceramics", Int. J. Fracture, 16[6]: 485-498, 1980.

130. Susumu Horibe and Masae Sumita, "Fatigue behavior of sintered SiC; temperature dependence and effect of doping with aluminum",

J. Mat. Sci., 23: 3305-3313, 1988.

131. A. G. Evans, L. R. Russel and D. W. Richerson, "Slow crack growth in ceramic materials at elevated temperatures", Met. Trans. A, 6A[4]: 707-716, 1975.

132. D. Lewis III, "Cyclic mechanical fatigue in ceramic-ceramic composite-An Update", Ceram. Eng. Sci. Proc., 4[9-10]: 874-881, 1983.

133. K. M. Prewo, "Fatigue and stress rupture of silicon carbide fiber-reinforced glass-ceramic", J. Mat. Sci., 22: 2695-2701, 1987.

134. S. Suresh, L. X. Han and J. J. Petrovic, "Fracture of Si_3N_4-SiC whisker composites under cyclic loads", J. Am. Ceram. Soc., 71[3]: c-158-c-161, 1988.

135. A. A. Morrone, S. R. Nutt and S. Suresh, "Fracture toughness and Fatigue crack growth behavior of an Al_2O_3-SiC composite", J. Mat. Sci., 23: 3206-3213, 1988.

136. K. M. Prewo, "Tension and Flexural Strength of SiC fiber-reinforced Glass-Ceramics", J. Mat. Sci., 21: 3590-3600, 1986.

137. D. Lewis III, pp 487-496, in Fracture Mechanics of Ceramics, Vol.6, edited by R. C. Bradt, A. G. Evans, D. P. H. Hasselman and F. F. Lange, Plenum Press, N.Y., 1983.

138. F. H. Gillery and E. A. Bush, "Thermal Contraction of β-Eucryptite (Li_2O Al_2O_3 $2SiO_2$) by X-ray and Dilatometer Methods", J. Am. Ceram. Soc., 42: 175-177, 1959.

139. E. G. Wolff, "Thermal Expansion in Metal/Lithia-Alumina-Silica (LAS) Composites", Int. J. Thermophysics, 9[2]: 221-232, 1988.

140. D. H. Grande, J. F. Mandell and K. C. C. Hong, "Fiber/matrix bond strength studies of glass, ceramic, and metal matrix composites", J. Mat. Sci., vol. 23: 311-328, 1988.

141. R. L. Salganik, "Mechanics of Bodies with Many Cracks", Mech. Solids, 8[4]: 135-142, 1974.

142. T. Hoshide, T. Ohara and T. Yamada, "Fatigue Crack Growth from Indentation Flaws in Ceramics", Int. J. Fract., 37: 47-59, 1988.

143. A. Grossmuller, V. Zelizko and M. V. Swain, "Fatigue Crack Growth in Ceramics using a Compressive Loading Geometry", J. Mat. Sci. Lett., 8[1]: 29-31, 1989.

144. M. J. Reece, F. Guiu and M. F. R. Sammur, "Cyclic Fatigue Crack Propagation in Alumina under Direct Tension-Compression Loading", J. Am. Ceram. Soc., 72[2]: 348-352, 1989.

145. K. Chyung, G. H. Beall, and D. G. Grossman, "Microstructures and Mechanical Properties of Machinable Glass-Ceramics", pp 1167-1194, in Electron Microscopy and Structure of Materials, edited by G. Thomas. University of California Press, Berkeley, 1972.

146. Z. Strnad, pp 226-230, in Glass-Ceramic Materials (Glass Science and Technology; Vol. 8), Elsevier, New York, 1986.

147. A. B. Bhatia, Ultrasonic Absorption, Chap. 3, Oxford University Press, Oxford, 1967.

148. T. N. Tiegs and P. F. Becher, J. Am. Ceram. Soc., 70 [5]: C109-C111, 1987.

149. J. J. Brennan and K. M. Prewo, "Silicon Carbide Fiber Reinforced Glass-Ceramic Matrix Composites exhibiting High Strength and Toughness", J. Mat. Sci., 17: 2371-2383, 1982.

150. P. F. Becher, C. Hsueh, P. Angelini and T. N. Tiegs, "Toughening Behavior in Whisker-reinforced Ceramic Matrix Composites", J. Am. Ceram. Soc., 71 [12]: 1050-1061, 1988.

151. P. F. Becher and G. C. Wei, "Toughening Behavior in SiC Whisker-reinforced Alumina", ibid, 67 [12]: C267-C269, 1984.

152. D. R. Biswas and V. K. Pujari, "Verification of the Double-Torsion Equation by using Different Thickness Samples of a Machinable Glass-Ceramic", ibid, 64 [7]: C98-C99, 1981.

153. P. W. McMillan, Glass Ceramics, 2nd ed., p. 238, Academic Press, London, England, 1979.

154. R. A. Schapery, "Thermal expansion coefficients of composite materials based on energy principles", J. Comp. Mat., 2[3]: 380-404, 1969.

155. W. R. Manning and O. Hunter, Jr., "Elastic properties of Polycrystalline Yttrium Oxide, Holmium Oxide, and Erbium Oxide; High Temperature Measurements", J. Am. Ceram. Soc., 52: 492-496, 1969.

156. J. A. Haglund and O. Hunter, Jr., "Elastic Properties of Polycrystalline Monoclinic Gadolinia", J. Am. Ceram. Soc., 55: 327-330, 1973.

157. M. N. Ozisik, Heat Transfer, Chap. 6-8, McGraw-Hill, New York, 1985.

158. S. W. Churchill and H. H. S. Chu, "Correlating Equations for Laminar and Turbular Free Convection from a Vertical Plate", Int. J. Heat Mass Transfer, 18: 1323, 1975.

159. J. P. Holman, Heat Transfer, Fourth Edition, Chap. 5-7, McGraw-Hill, New York, 1976.

160. F. P. Incropers and D. P. De Witt, Introduction to Heat Transfer, Chap. 6-9, John Wiley & Sons, New York, 1985.

161. S. Whitaker, Elementary Heat Transfer Analysis, Pergamon, New York, 1976.

162. A. A. Zukauskas and A. B. Ambrazyavichyus, "Heat Transfer of a Plate in a Liquid Flow", Int. J. Heat Mass Transfer, 3: 305, 1961.

163. Astro Met Associates Inc. (A distributor of the Corning Glass products, Cincinnati, OH) provided technical data for Macor.

164. W. H. Gitzen, p 65 in Alumina as a Ceramic Material, American Ceramic Society, Columbus, OH, 1970.

165. Y. S. Touloukian, editor, pp 236-249 in Thermophysical Properties of High Temperature Solid Materials, vol. 6: Part I, Thermophysical Properties Research Center, Purdue University, 1967.

166. E. A. Farber and R. L. Scorah, "Heat Transfer to Water Boiling Under Pressure", Trans. ASME, 79: 369-384, 1948.

167. T. Hachisu, T. Sakai and K. Taguchi, "Transient Temperature Distribution in Circular Cylinders During Quenching", Heat Transfer; Japanese Research, 10[1]: 52-64, 1981.

168. M. N. Ozisik, Heat Transfer, Chap. 10, McGraw-Hill, New York, 1985.

169. J. P. Holman, Heat Transfer, Fourth Edition, Chap. 9, McGraw-Hill, New York, 1976.

170. Y. Kim, W. J. Lee, and E. D. Case, "The Measurement of the Surface Heat Transfer Coefficient for Ceramics Quenched into a Water Bath", Accepted for the publication in Mat. Sci. Eng.

171. Provided data by Manufacturer (Specialty Materials Division, Eagle-Picher Industries, Inc.)

172. K. K. Smyth and M. B. Magida, "Dynamic Fatigue of a Machinable Glass-Ceramic", J. Am. Ceram. Soc., 66[7]: 500 - 505, 1983.

173. N. Noda, Y. Matsunaga, T. Tsuji, and H. Nyuko, "Thermal Shock Problems of Elastic Bodies with a Crack", J. Thermal Stresses, 12: 369 - 383, 1989.

174. R. W. Hertzberg, p 282, figure 8.7 (e), Deformation and Fracture Mechanics of Engineering Materials, third ed., John Wiley & Sons, New York, 1989.

175. M. K. Ferber, P. F. Becher, and C. B. Finch, "Effect of Microstructure on the Properties of TiB_2 Ceramics", J. Am. Ceram. Soc., 66[1]: c-2 - c-4, 1982.

176. Ceramic Source, Vol. 1, p 351, 1985, The American Ceramic Society, Inc.

177. W. S. Durant and S. Mirshak, "Roughening of Heat Transfer Surfaces as a Method of Increasing Heat Flux at Burnout, Progress Report No. 1", U. S. Atomic Energy Commission Report DP-380, 1959, as cited in L. S. Tong, p 188 in Boiling Heat Transfer and Two-Phase Flow, John Wiley & Sons, Inc., New York, 1965.

178. W. S. Durant and S. Mirshak, "Roughening of Heat Transfer Surfaces as a Method of Increasing Heat Flux at Burnout", U. S. Atomic Energy Commission Report DPST-60-284, 1960, as cited in L. S. Tong, p 188 in Boiling Heat Transfer and Two-Phase Flow, John Wiley & Sons, Inc., New York, 1965.

179. Y. Kim, S. Gaynor, and E. D. Case, "The Effect of Surface Limited Microcracks on the Effective Young's Modulus of Ceramics: III. Experiment", Submitted to J. Mat. Sci.

180. D. P. H. Hasselman, "Effect of Cracks on Thermal Conductivity", J. Comp. Mat., 3: 403-407, 1978.

181. L. R. F. Rose, "On the Initial Motion of a Griffith Crack", Int. J. Frac., 12[6]: 829-841, 1976.

182. J. R. Willis, "Variational and Related Methods for the Overall Properties of Composites", Advances in Applied Mechanics, 21: 1-78, 1981.

183. E. D. Case, "The Effect of Microcracking on the Poisson's Ratio of Brittle Materials", J. Mater. Sci. 11: 3702-3712, 1984.

184. C. B. Ponton and R. D. Rawlings, "Review of Literature and Formulation of Standardized Indentation Toughness Equations", Mater. Sci. and Tech., 5: 865-872, 1989.

185. C. B. Ponton and R. D. Rawlings, "Application and Critical Evaluation of Standardized Indentation Toughness Equations", Mater. Sci. and Tech., 5: 961-976, 1989.

186. K. Niihara, R. Morena, and D. P. H. Hasselman, "Evaluation of K_{Ic} of Brittle Solids by the Indentation Method with Low Crack-to-Indent Ratios", J. Mat. Sci. Lett., 1: 13-16, 1982.

187. K. Niihara, "A Fracture Mechanics Analysis of Indentation-Induced Palmqvist Crack in Ceramics", J. Mat. Sci. Lett., 2: 221-223, 1983.

188. J. Lankford, "Threshold Microfracture during Elastic-Plastic Indentation of Ceramics", J. Mat. Sci., 16: 1177-1182, 1981.

189. J. Lankford, "Indentation Microfracture in the Palmqvist Crack Regime: Implications for Fracture Toughness Evaluation by the Indentation Method", J. Mat. Sci. Lett., 1: 493-495, 1982.

190. D. K. Shetty, A. R. Rosenfield, and W. H. Duckworth. "Indenter Flaw Geometry and Fracture Toughness for a Glass-Ceramic", J. Am. Ceram. Soc., 68 [10]: C-282-C-284, 1985.

191. D. K. Shetty, I. G. Wright, P. N. Mincer, and A. H. Clauer, "Indentation Fracture of WC-Co Cermets", J. Mat. Sci., 20: 1873-1882, 1985.

192. D. B. Marshall, "Controlled Flaws in Ceramics: A Comparison of Knoop and Vickers Indentation", J. Am. Ceram. Soc., 66: 127-131, 1983.

193. S. S. Smith and B. J. Pletka, "Indentation Fracture of Single Crystal and Polycrystalline Aluminum Oxide" pp. 189-209 in Fracture Mechanics of Ceramics, Vol 6., Edited by R. C. Bradt, A. G. Evans, F. F. Lange, and D. P. H. Hasselman., Plenum Press, New York, 1983.

194. P. F. Becher, C. Hsueh, P. Angelini and T. N. Tiegs, "Toughening Behavior in Whisker-Reinforced Ceramic Matrix Composites", J. Am. Ceram. Soc., 71[12]: 1050-1061, 1988.

195. D. B. Marshall and B. R. Lawn, "Flaw Characteristic in Dynamic Fatigue: The Influence of Residual Contact Stresses", J. Am. Ceram. Soc., 63[9-10]: 532-536, 1980.

196. E. R. Fuller, B. R. Lawn, and R. F. Cook, "Theory of Fatigue for Brittle Flaws Originating from Residual Stress Concentrations", 66[5]: 314-321, 1983.

197. C. C. Chiu and E. D. Case, "Influence of Quenching on Fracture Strength, Elastic Modulus, and Internal Friction of Glass Plates", Submitted to J. Mat. Sci.

198. E. D. Case and Youngman Kim, "The Effect of Surface Limited Microcracks on the Effective Young's Modulus of Ceramics: II. Crack Geometry Modification", Submitted to Mat. Sci. and Eng.

199. D. E. Wiley, W. R. Manning and O. Hunter, Jr., "Elastic Properties of Polycrystalline TiB_2, ZrB_2 and HfB_2 from Room Temperature to 1300 °K", J. Less-Common Metals, 18: 149-157, 1969.

200. F. W. Valdiek, "Electrical Resistivity, Elastic Modulus, and Debye Temperature of Titanium Diboride", J. Less-Common Metals, 12: 202-209, 1967.